UNIVERSITAT POLITÈCNICA DE VALÈNCIA

DEPARTAMENTO DE MÁQUINAS Y MOTORES TÉRMICOS

PARTIAL NEEDLE LIFT AND INJECTION RATE SHAPE EFFECT ON THE FORMATION AND COMBUSTION OF THE DIESEL SPRAY

DOCTORAL THESIS

Presented by:
  Michele Bardi

Supervised by:
  Prof. Raúl Payri Marín

Valencia, April 2014

Doctoral Thesis

PARTIAL NEEDLE LIFT AND INJECTION RATE SHAPE EFFECT ON THE FORMATION AND COMBUSTION OF THE DIESEL SPRAY

Presented by: Mr. Michele Bardi
Supervised by: Prof. Raúl Payri Marín

EXAMINING BOARD:

President: José Maria Desantes
Secretary: Octavio Armas
Examiner: Joaquin De la Morena

REVIEWING BOARD:

               Anil Bika
               Gilles Bruneaux
               José Hernandez

Valencia, April 2014

Resumen

La inyección directa de combustible representa uno de los puntos clave en el desarrollo de los motores Diésel. El atractivo de esta solución ha ido creciendo gracias al desarrollo paralelo en la tecnología de los equipos de inyección y en el conocimiento de la física involucrada en el proceso de formación y combustión del chorro.

En la presente tesis doctoral se estudia el efecto del levantamiento parcial de la aguja y del perfilado de la tasa de inyección mediante el empleo de un inyector multi-orificio.

El perfilado de la tasa de inyección se presenta hoy en día como una de las alternativas más llamativas a las estrategias de inyección múltiple. Sin embargo, su implementación ha sido obstaculizada por limitaciones tecnológicas. Un prototipo de inyector ha permitido llevar al cabo el presente estudio: en este inyector la aguja está acoplada directamente con un actuador piezo-eléctrico, garantizando un amplio control sobre la posición de la aguja, y permitiendo la realización de perfiles de inyección de forma controlada.

Distintos aspectos del desarrollo y de la combustión del chorro se investigaron a través de varios diagnósticos ópticos, en una novedosa maqueta de flujo continuo, que garantiza tener control en las condiciones de ensayo en un amplio rango (hasta 1000 K y 15 MPa). Adicionalmente, la caracterización hidráulica de la tobera permitió investigar el flujo interno en condiciones de levantamiento parcial de la aguja.

Los resultados destacaron que el levantamiento parcial de la aguja produce una reducción en el gasto másico y, también, una reducción en el área efectiva y un aumento en el ángulo de apertura del chorro. Además, en estas condiciones, se observó un incremento de la dispersión entre orificios y de las inestabilidades del flujo. Las vibraciones de la aguja producidas por la interacción con el flujo de combustible conjuntamente a la aparición de cavitación en el asiento de la aguja son indicadas como posibles causas de este comportamiento.

El perfilado de la tasa de inyección tiene un impacto sustancial sobre la fase premezclada de la combustión y sobre la posición del encendido. Además, los resultados comprobaron que las modificaciones en el flujo interno producidas por el levantamiento parcial de la aguja se ven reflejadas en una ligera reducción del tiempo de encendido. Por otro lado, analizando los datos experimentales con un modelo *1D* se observó que un aumento brusco en la tasa de inyección (perfiles de tipo *rampa* o *bota*) provoca una subida en el dosado relativo en la zona del *lift-off length*, y un consecuente aumento en la formación de hollín en la fase difusiva de la combustión.

Finalmente, el amplio rango de condiciones estudiadas en los ensayos sirvió para sacar conclusiones generales sobre la física del proceso de inyección/combustión y, en algunos casos, para obtener correlaciones estadísticas.

Resum

La injecció directa de combustible representa un dels punts clau en el desenvolupament dels motors Dièsel. L'atractiu d'aquesta solució ha anat creixent gràcies al desenvolupament en parallel que s'ha produït en la tecnologia dels equips d'injecció i en el coneixement de la física involucrada en el procés de formació i combustió del doll.

En la present tesi doctoral s'estudia l'efecte de l'aixecament parcial de l'agulla i del perfilatge de la taxa d'injecció mitjançant l'ús d'un injector multi-orifici.

El perfilatge de la taxa d'injecció es presenta a dia d'avui com una de les alternatives més cridaneres a les estratègies d'injecció múltiple. Això no obstant, la implementació d'aquest mètode ha sigut obstaculitzada per limitacions tecnològiques. Un prototip d'injector ha permès dur a terme el present estudi: en aquest injector l'agulla està acoblada directament amb un actuador piezoelèctric, la qual cosa garanteix un ampli control sobre la posició de l'agulla, i permet la realització de perfils d'injecció de forma controlada.

Es van investigar divers aspectes del desenvolupament i de la combustió del doll mitjançant diferents diagnòstics òptics, en una innovadora maqueta de flux continu, que garanteix tindre el control en les condicions d'assaig en un ampli rang (fins a $1000\,\text{K}$ i $15\,\text{MPa}$). Addicionalment, la caracterització hidràulica de la tovera va permetre investigar el flux intern en condicions d'aixecament parcial de l'agulla.

Els resultats van permetre destacar que l'aixecament parcial de l'agulla produeix una reducció de la despesa màssica i, també, una reducció de l'àrea efectiva i un augment de l'angle d'obertura del doll. A més a més, en aquestes condicions, es va observar un increment de la dispersió entre orificis i de les inestabilitats del flux. Com a possibles causes d'aquest comportament s'indiquen les vibracions de l'agulla prodïudes per la interacció amb el flux de combustible, juntament amb l'aparició de cavitació a la base de l'agulla.

El perfilatge de la taxa d'injecció té un impacte substancial damunt la fase premesclada de la combustió i sobre la posició de l'encesa. Finalment, els resultats van permetre comprovar que les modificacions en el flux intern produïdes per l'aixecament parcial de l'agulla es veuen reflectides en una lleugera reducció del temps d'encesa. D'altra banda, analitzant les dades experimentals amb un model *1D* es va observar que un augment brusc en la taxa d'injecció (perfils de tipus rampa o bota) provoca una pujada en el dosatge relatiu a la zona de lift-off length, i un conseqüent augment en la formació de sutja en la fase difusiva de la combustió.

Finalment, l'ampli rang de condicions estudiades en els assajos va servir per

a traure conclusions generals sobre la física del procés d'injecció/combustió i, en alguns casos, per a obtindre correlacions estadístiques.

Abstract

Fuel direct injection represents one of the key turning points in the development of the Diesel engines. The appeal of this solution has been growing thanks to the parallel advancement in the technology of the injection hardware and in the knowledge of the physics involved in the spray formation and combustion.

In the present thesis, the effect of partial needle lift and injection rate shaping has been investigated experimentally using a multi-orifice Diesel injector.

Injection rate shaping is one of the most attractive alternatives to multiple injection strategies but its implementation has been for long time impeded by technological limitations. A novel direct-acting injector prototype made it possible to carry out the present research: this injector features a mechanical coupling between the nozzle needle and the piezo-stack actuator, allowing a fully flexible control on the nozzle needle movement and enabling partial needle lift as well as the implementation of alternative injection rate shapes typologies. Different optical diagnostics were applied to study the spray development and combustion in a novel continuous flow test chamber that allows an accurate control on a wide range of thermodynamic conditions (up to 1000 K and 15 MPa). In addition, hydraulic characterization tests were carried out to analyze the fuel flow through the injector nozzle.

Partial needle lift has been found to affect the injection event, reducing the mass flow rate (as expected) but also causing a reduction in the effective orifice area and an increase on the spreading angle. Moreover, at this condition, higher hole-to-hole dispersion and flow instabilities were detected. Needle vibrations caused by the needle interactions with fuel flow and by the onset of cavitation in the needle seat are likely the causes of this behavior.

Injection rate shaping has a substantial impact on the premixed phase of the combustion and on the location where the ignition takes place. Furthermore, the results proved that the modifications in the internal flow caused by the partial needle lift are reflected on the ignition timing. On the other hand, the analysis of the experimental data through a *1D* spray model revealed that an increasing mass flow rate (e.g. *ramp* or *boot* injection rate profiles) causes an increase in the fuel-air equivalence ratio at the lift-off length and a consequent higher soot formation during the diffusive phase of the combustion. Finally, the wide range of boundary conditions tested in all the experiments served to draw general conclusions about the physics involved in the injection/combustion event and, in some cases, to obtain statistical correlations.

To my family

To Francesca

Acknowledgements

Long time has passed by since my first day at CMT. First as a pancho *and later as a PhD student, this place has become my second home. Looking back while approaching the finish line, I have to say that, apart from getting older, I learned a lot and not only about science and engines. All this things have been possible thanks to the unique combination of persons around me and I want to take this opportunity to express my gratitude to some of them.*

First of all, I have to say thanks to my supervisor Raúl Payri for his wise guidance in the development of this thesis and my formation as researcher and runner.

I want to express my thanks to the Departamento de Maquinas y Motores Térmicos, and in particular to Prof. Francisco Payri and Prof. José María Desantes for giving me the privilege of working in this world wide recognized research center.

I am very thankful also to Lyle Pickett and Luigi Allocca for tutoring me during my internships, in which I spent valuable time learning a lot in two of the best places working in the field of engine.

A special thanks go to the injection team*. In particular, thanks to Oscar, my PhD twin, a great colleague and friend; to Juan Pablo and Daniel, for the good time spent together and for their support during the last days of writing. Also, thanks to the other current or former PhD students of the group, Gabriela, Julien, Joaquin, Jorge, Pedro, Marcos, David and Giovanny, sharing always a good ratio of ideas and jokes. Thanks to Jose Enrique, whose expertize and skills in the lab are the only things above his jokes and to Jaime and Javi, always providing precious help and guidance anytime I needed it. Thanks to Francesco, Vincent, David, Moises and Alberto for their collaboration during the experiments and their patience when working with me.*

Also, I cannot forget to acknowledge Annalisa and Zolpho, my second family here in Valencia; Mario and Leonardo, unbeatable friends and flatmates and Colo, Spalla, Pucce, Marta, Giuse, Lodo, Coro and the other folks from PC.

Thanks to my parents and family for their continuous support through my entire life, no matter the distance.

My last thanks go to Francesca for being with me and for making me feel better.

Contents

List of Figures

List of Tables

Symbology

Greeks

α Constant used in *2C* methodology.

Δp Pressure difference, generally $p_i - p_a$.

Δx Difference between x_{SSI} and LOL_{av}.

ϵ Emissivity.

γ Spray axis angle (deviation from the orifice nominal axis).

λ Wavelenght or throttling ratio (defined in 5.2)

λ_{foot} *Foot* throttling ratio (defined in 5.2).

μ Dynamic viscosity (general).

μ_f Fuel dynamic viscosity.

ν_a Ambient gas cinematic viscosity.

ν_f Fuel cinematic viscosity.

ω Collection angle.

Φ_{eq} Fuel-air equivalence ratio.

ϕ_{visc} Total head losses.

ϕ_M Major losses.

ϕ_m Minor losses.

ρ Density (general).

ρ_f Fuel density.

ρ_a Ambient gas density.

σ Stefan-Boltzmann constant/Standard deviation.

θ Spray spreading angle.

θ_{av} Average spray spreading angle.

τ_{cf} First-stage ignition delay.

τ_i Injection delay.

τ_{SSI} Second-stage ignition delay.

Latins

2C   2-color optical pyrometry.

A   Area (general).

a, b Power-law constants

A_{eff} Effective area (defined in 3.2)

A_o Orifice outlet area.

A_p Pipe cross-sectional area

ADC   Analogue to digital converter.

CPF   Constant pressure flow facility.

CV   Control volume.

c   Speed of sound.

c_1, c_2 Constants in Plank's radiation law equation.

C_A Area coefficient (defined in 3.2)

C_d Discharge coefficient (defined in 3.2)

C_M Momentum coefficient (defined in 3.2)

C_v Velocity coefficient (defined in 3.2)

CIDI   Compression-ignition direct-injection.

D   Diameter (general).

D_0 Orifice outlet diameter.

D_i Orifice inlet diameter.

d_p Temperature probe diameter.

DBI   Diffused back-light illumination.

ECN   Engine Combustion Network

ECU   Electronic control unit.

ET   Energizing time.

E   Global activation energy.

E_m Signal output by a single pixel.

EOI   End of injection.

e   Absolute roughness.

FEM　　Finite elements method.

F　　Resulting force (general).

f　　Mixture fraction.

f_v　　Soot volumetric fraction.

fnl　　Full needle lift.

fps　　Frames per second.

g　　Gravitational acceleration.

I_{soot}　　Radiation power.

I_b　　Black body radiance.

KL　　*2C* derived flame optical thickness.

k–factor　Conicity factor of the orifice (Defined in Sec. 3.2).

k_{fric}　　Friction coefficient.

k_a　　Ambient gas thermal conductivity.

k_λ　　Soot volume fraction indicator.

LES　　Large eddy simulation.

LTC　　Low temperature combustion

L_o　　Orifice length.

L　　Optical path length (defined in Sec. 4.5).

LL　　Liquid phase penetration at evaporative conditions (liquid length).

LL_{av}　　Average liquid length.

LOL　　Lift-off length.

LOL_{av}　Average lift-off length.

m　　Mass (general).

$\dot{M}$　　Spray momentum flow.

$\dot{m}$　　Mass flow rate.

$\dot{M}_{th}$　　Theoretical momentum flow.

$\dot{M}_{av}$　　Average spray momentum flow.

$\dot{m}_{th}$　　Theoretical fuel mass flow rate.

$\dot{m}_{av}$　　Average steady mass flow rate.

m_{SSI}　　Fuel mass injected before the ignition.

Max Int Prof　Intensity profile (defined in Sec. 4.5)

n　　Normal vector.

OD_{DBI}　Optical depth obtained in *DBI* measurements.

OH_{peak}　*OH** chemiluminescence peak intensity.

p Pressure (general).

p_a Discharge pressure/pressure within the combustion chamber.

p_i Injection pressure.

p_{vap} Vapor pressure.

PDF   Probability distribution function.

PPCI   Partially premixed compression ignition.

PECU   Programmable engine control unit.

Re   Reynolds number.

ROI   Rate of injection.

r_e Entrance connecting radius of the orifice.

SOI   Start of injection/Injection delay.

S Spray tip penetration (general).

S_l Spray tip penetration at isothermal conditions.

S_v Spray tip penetration at evaporative conditions.

T Temperature (general).

T_a Temperature of the gas within the combustion chamber.

T_c Temperature of the injector holder coolant.

T_j Temperature of the thermocouple junction.

T_f *2C*-derived flame temperature.

T_s Temperature of the surface/wall (general).

ths_{OH} Threshold employed for the determination of the ignition delay in *OH** chemiluminescence imaging.

t_{open} Opening time (injection profile characteristic parameter defined 5.2).

u Flow velocity.

u_{eff} Effective velocity (defined in 3.2)

u_{th} Theoretical (Bernoulli's) velocity.

UHC   Unburned hydrocarbons.

UV   Ultraviolet.

v Local velocity.

$v_{f,av}$ Average fuel specific volume (defined in Sec.3.3).

V_s Spray total volume.

VCO   Valve closed orifice.

x Spray axial distance.

x_0 Virtual origin of the spray.

x_{SSI} Second-stage ignition nozzle distance.

Y_i Mass fraction of the component i.

z Piezometric height.

Z_{st} Stoichiometric mixture fraction.

Chapter 1

Introduction

1.1 General context

Diesel engines demonstrated indubitable strong points in terms of efficiency, reliability and adaptability. Despite the applications of this kind of engine spread over many fields (naval, electric generator, agriculture etc.), the automotive industry is one of the sector which boosted the most its development [1, 2]. The competitive market, together with the stringent emissions regulations imposed by the governments [3, 4], led Diesel engines to continuous improvements being nowadays one of the most efficient combustion engines [5].

Fuel direct injection represents one of the key turning points in the development of the Diesel engines: the idea of controlling the auto-ignition and the consequent combustion of a liquid spray injected in a reacting environment during a time scale of few milliseconds has been a challenging task for the engine community and pushed to a massive research in this field [6–8].

In this sense, the technological advancement reached in the hardware employed made available systems capable of performing fast and accurate fuel injections [9]; on the other hand, the many studies performed in the last decades allowed to gain a deep knowledge of the spray formation and combustion process [6, 10–12]. In spite of that, it is still difficult to assess with accuracy how a modification in the geometry of the nozzle, in the injector technology or in other boundary conditions affects the whole process. The small time/length scale involved in the phenomenon, the difficulty in controlling with accuracy the relevant boundary conditions and the intrinsic complexity of the atomization process that

is at the basis of the spray formation, are only few of the difficulties that characterize this study.

Currently, the primary and long term objective for researchers is to develop accurate predictive models capable of describing the injection/combustion event, with the aim of replacing (or at least at reducing) the experimental practice with numeric simulation or analytical models [13–16].

The complexity of these tasks moved researchers to investigate, each time in more detail, the phenomena involved in the injection process in order to provide modelers quantitative data to compare to the results of their simulations and to gain understanding of the mechanisms involved. To this end, in the last decade, several new specific diagnostics have been introduced also thanks to the introduction of new technology available: in this sense, the massive introduction of the optical diagnostics and of the digital acquisition systems gave a substantial step forward in the quality and quantity of data available for the analysis [8, 17].

In the research applied to direct injection Diesel engines, two main approaches can be identified:

- engine research, oriented to the understanding of the injection combustion within the engine;

- fundamental study, oriented to the study of the spray in simplified environments.

In the first case, the tests are performed in real Diesel engines with only slight modifications to gain optical access or to introduce specific probes: the results have immediate impact on the decisions to take during the engine calibration, since all the relevant phenomena are considered in the experiment [18–21]. However, in this approach, the unknowns that remain between the defined boundary conditions and the final results are many. To this end, the fundamental studies aim at investigating the single processes in order to gain knowledge and control on it, for example studying the spray development avoiding the combustion, or the fuel atomization avoiding the opening and closing transient. To this end, specific test chamber have been developed to study the spray in finely controlled boundary conditions: the injections are performed in a nearly quiescent environment, where the characteristics of the charge are known (e.g. ambient temperature, ambient density and oxygen concentration) and the interaction with the wall controlled or avoided. This purpose-designed facilities also have the fundamental advantage of being endowed with large accesses that simplify the implementation of the diagnostics. This second approach, therefore, is more oriented to the fundamental understanding of the process and the results provided have generally a

more general extent [22–25]. The work developed in the present thesis follows this second approach.

1.2 Objectives and methodology

The present thesis was born from the requirement from General Motors to evaluate an injector prototype by Continental. This injector features the so called direct-acting system, where a piezo-actuator (stack) is mechanically coupled with the injector needle, having direct control on its position: this technological achievement enables a fast and precise control on the position of the needle and, therefore, on the fuel flow through the injector nozzle [26]. In this way, without modifying the rail pressure, the fuel mass flow rate can be controlled, even in the short time scale of the injection event, enabling alternative injection rate profiles (*injection rate shaping*).

Injection rate shaping is one of the most attractive alternatives to multiple injection strategies since, theoretically, it allows to control the premixed as well as the diffusive phase of the combustion, avoiding the drawbacks deriving from the several opening/closing transient characterizing pilot and post injections [27–29]. In fact, multiple injection strategies present some important limitations:

- the hydraulic delay and the time needed for the injector to open and close define minimum injection time and dwell time between consecutive injection, limiting the flexibility of the strategy [30];

- the opening and, even more, the closing transient are characterized by poor atomization and, in some cases, by additional fuel injection due to the needle rebound, as observed by recent studies [30, 31].

The implementation of injection rate shaping, even though investigated theoretically, has been for a long time impeded by technological limitations. Therefore, although many researches have been oriented to the study of the injection event using conventional servo-hydraulic injectors, only few are discussing the effect of the partial needle lift on injection process and, to the author knowledge, none of them has been tested at real engine conditions.

The present thesis follows two main objectives:

- bringing forward the general understanding of the injection process by performing conventional tests over a wide range of test conditions employing the state of the art technology available in the department;

- taking advantage from the availability of the Continental *direct acting* prototype to understand the consequences and potentialities of the introduction of the needle position control in the injection system.

The different aspects of the injection process have been explored with an empirical approach, putting in parallel experimental measurements with previous results found in the literature or theoretical predictions. In particular, the tests performed can be divided in three main groups basing on their specific target:

- hydraulic characterization of the fuel flow through the nozzle;

- spray development in inert conditions;

- ignition and combustion characterization.

To this end, several diagnostics have been employed: it is worth to keep in mind, in this introduction, that most of the experiments were performed in a state of the art, optically accessible test chamber, enabling the application of different optical diagnostics to study the spray formation and combustion at real engine conditions [32]. This facility allowed to carry out the experiments with an improved control on the boundary conditions and, at the same time extending the space domain of the studies, thanks to the big size of the test chamber [25]. The present thesis, is the first presented at CMT-Motores Térmicos employing this high temperature high pressure test rig. The long experience gained at *CMT-motores térmicos* in the Diesel research [11, 12, 33, 34], together with the state of the art facilities and diagnostic systems available in the department [35], constituted a favorable starting point for this research, providing a fundamental methodological and analytical background to the research. Nonetheless, this thesis aspires to be an active part in this process for three main reasons:

- the importance of the research performed and the extent of the results obtained;

- the employment of new devices that allowed to learn their potentialities and improve their functionality (e.g. the constant flow combustion vessel);

- the careful use of the diagnostics employed, putting the emphasis on the methodologies followed to obtain the final data.

1.3   About this thesis

This thesis is organized in seven chapters including the present introduction (*Chapter 1*). In the second chapter, the injection process is discussed in the context of Diesel engine and the critical requirement are presented together with trends and technological development. Finally, the injector prototype used in the present work is described in this chapter.

As mentioned earlier, this work focuses on the fundamental study of the injection process: *Chapter 3* describes the theoretical background that represents the starting point of this work, and serves as a reference for the interpretation of the results obtained. To this end, the different processes taking place in the fuel injection are described including the flow through the nozzle, the liquid atomization/evaporation process and the combustion process. Finally, the studies found in literature about the effect of partial needle lift on Diesel injection are presented in a brief review.

The fourth chapter illustrates the experimental methodology followed in this work: the experiments performed are presented in details, on one side outlining the physical principles behind the measurements and, on the other, describing the specific measurements performed, discussing the hardware, the processing techniques and the information made available by each experiment.

Chapters 5 and *6* are devoted to the presentation of the experimental results. The fifth chapter presents all the results obtained in *inert* environment, that is, in tests where the combustion is prevented: the hydraulic characterization and the study of the liquid- and vapor-phase spray boundaries in isothermal and evaporative conditions [36–38]. Finally, the results related to this part are employed for the calibration of a *1D* model [39] that will be used for the interpretation of the results presented in the following chapter. Chapter six encompass the results obtained when studying the spray at reacting conditions: the autoignition of the spray is studied at different experimental conditions together with the diffusive flame development [40]. Characteristic parameters like ignition delay and lift-off length are presented and related to other measured (flame temperature and soot formation) and model derived (fuel to air equivalence ratio) quantities. In both chapters, particular emphasis is put on the effect that the partial needle lift and injection rated shaping have on the measured variables.

The last chapter (*Chapter 7*) draws the main conclusions of this thesis contrasting all the new information brought and indicating the possible directions in which to orient to future studies.

References

[1] MAJEWSKI, W. A. and M. K. KHAIR. *Diesel emissions and their control*. Society of Automotive Engineers, 2006.

[2] JOHNSON, T. V. "Review of diesel emissions and control". *International Journal of Engine Research* 10.5 (2009), pp. 275–285.

[3] *European Parliament and the Council of the European Union, Regulation (EC) No 595/2009*. June 2009.

[4] *Summary of current and historical light-duty vehicle emissions standards*. Tech. rep. 2010.

[5] HEYWOOD, J. "Internal combustion engine fundamentals". *Mc Graw Hill, Inc. -* (1998), pages.

[6] DEC, J. *A conceptual model of DI diesel combustion based on laser-sheet imaging*. Society of Automotive Engineers Warrendale, PA, 1997.

[7] SCHMIDT, D. P. and M. L. CORRADINI. "The internal flow of diesel fuel injector nozzles: A review". *International Journal of Engine Research* 2.1 (2001), pp. 1–22.

[8] LINNE, M. "Imaging in the optically dense regions of a spray: A review of developing techniques". *Progress in Energy and Combustion Science* 39.5 (2013), pp. 403–440.

[9] MENDEZ, S. and B. THIROUARD. "Using multiple injection strategies in diesel combustion: potential to improve emissions, noise and fuel economy trade-off in low CR engines". *Technology* 2013 (2008), pp. 04–08.

[10] FLYNN, P. F. et al. "Diesel combustion: an integrated view combining laser diagnostics, chemical kinetics, and empirical validation" (1999).

[11] GARCÍA, J. M. "Aportaciones al estudio del proceso de combustión turbulenta de chorros en motores diesel de inyección directa". PhD thesis. Valencia: E.T.S. Ingenieros Industriales. Universidad Politécnica de Valencia, 2004.

[12] GIMENO, J. "Desarrollo y aplicación de la medida de flujo de cantidad de movimiento de un chorro Diesel". PhD thesis. E.T.S. Ingenieros Industriales. Universidad Politécnica de Valencia, 2008.

[13] WRIGHT, Y., G. DE PAOLA, K. BOULOUCHOS, and E. MASTORAKOS. "Simulations of spray autoignition and flame establishment with two-dimensional CMC". *Combustion and Flame* 143.4 (2005), pp. 402–419.

[14] DESANTES, J. M., J. J. LOPEZ, J. M. GARCIA, and J. M. PASTOR. "Evaporative diesel spray modeling". *Atomization and Sprays* 17.3 (2007).

[15] HERNÁNDEZ, J., J. SANZ-ARGENT, J. CAROT, and J. JABALOYES. "Modelling of the auto-ignition angle in diesel HCCI engines through D-optimal design". *Fuel* 89.9 (2010), pp. 2561–2568.

[16] *Engine Combustion Network web-page*. last access 15/02/2014. URL: http://www.sandia.gov/ecn/.

[17] ZHAO, H. and N. LADOMMATOS. "Optical diagnostics for soot and temperature measurement in diesel engines". *Progress in Energy and Combustion Science* 24.3 (1998), pp. 221–255.

[18] NABI, M. N., M. S. AKHTER, and M. M. ZAGLUL SHAHADAT. "Improvement of engine emissions with conventional diesel fuel and diesel–biodiesel blends". *Bioresource Technology* 97.3 (2006), pp. 372–378.

[19] DOBER, G. et al. "The impact of injection strategies on emissions reduction and power output of future diesel engines". *SAE Paper* 2008-01-0941 (2008).

[20] LAPUERTA, M., O. ARMAS, J. J. HERNÁNDEZ, and A. TSOLAKIS. "Potential for reducing emissions in a diesel engine by fuelling with conventional biodiesel and Fischer–Tropsch diesel". *Fuel* 89.10 (2010), pp. 3106–3113.

[21] VALENTINO, G., L. ALLOCCA, S. IANNUZZI, and A. MONTANARO. "Biodiesel/mineral diesel fuel mixtures: Spray evolution and engine performance and emissions characterization". *Energy* 36.6 (2011), pp. 3924–3932.

[22] SIEBERS, D. "Liquid-phase fuel penetration in Diesel sprays". *SAE transactions* 107.3 (1998), pp. 1205–1227.

[23] PICKETT, L. M., D. L. SIEBERS, and C. A. IDICHERIA. "Relationship Between Ignition Processes and the Lift-Off Length of Diesel Fuel Jets". *SAE Paper* 2005-01-3843 (2005).

[24] PAYRI, F., V. BERMUDEZ, R. PAYRI, and F. SALVADOR. "The influence of cavitation on the internal flow and the spray characteristics in diesel injection nozzles". *Fuel* 83.4 (2004), pp. 419–431.

[25] BAERT, R., P. FRIJTERS, B. SOMERS, C. LUIJTEN, and W. DE BOER. "Design and operation of a high pressure, high temperature cell for HD diesel spray diagnostics: guidelines and results". *SAE Paper* 2009-01-0649 (2009).

[26]   FERRARI, A. and A. MITTICA. "FEM modeling of the piezoelectric driving system in the design of direct-acting diesel injectors". *Applied Energy* 99 (2012), pp. 471–483.

[27]   JUNEJA, H., Y. RA, and R. REITZ. "Optimization of injection rate shape using active control of fuel injection". *SAE Paper* 2004-01-0530 (2004).

[28]   CHARLES B. BRIGHT, J. C. G. "Very high speed rate shaping fuel injector". US7255290 B2. 2007.

[29]   KASTNER, O., F. ATZLER, C. JUVENELLE, R. ROTONDI, and A. WEIGAND. "Directly actuated piezo injector for advanced injection strategies towards cleaner diesel engines". *7th Int. symposium towards cleaner diesel engine TDCE*. 2009.

[30]   TANAKA, T., A. ANDO, and K. ISHIZAKA. "Study on pilot injection of DI diesel engine using common-rail injection system". *JSAE Review* 23.3 (2002), pp. 297–302.

[31]   MANIN, J., M. BARDI, L. PICKETT, R. DAHMS, and J. OEFELEIN. "Development and mixing of diesel sprays at the microscopic level from low to high temperature and pressure conditions". *THIESEL 2012 Conference on Thermo-and Fluid Dynamic Processes in Direct Injection Engines*. 2012.

[32]   PAYRI, R., J. M. GARCÍA-OLIVER, M. BARDI, and J. MANIN. "Fuel temperature influence on diesel sprays in inert and reacting conditions". *Applied Thermal Engineering* 35 (2012), pp. 185–195.

[33]   PAYRI, F. and J. DESANTES. *Motores de combustión interna alternativos*. Editorial Reverté, 2011.

[34]   SALVADOR, F. J. "Estudio teórico experimental de la influencia de la geometría de toberas de inyección Diesel sobre las características del flujo interno y del chorro". PhD thesis. Valencia: E.T.S. Ingenieros Industriales. Universidad Politécnica de Valencia, 2003.

[35]   *CMT-motores termicos web-page*. last access 15/02/2014. URL: http://www.cmt.upv.es/.

[36]   PAYRI, R., J. GIMENO, O. VENEGAS, and A. H. PLAZAS-TORRES. "Experimental and computational study of the influence of partial needle lift on nozzle flowin diesel fuel injectors". *Atomization and Sprays* 22.8 (2012).

[37]   PAYRI, R., J. GIMENO, M. BARDI, and A. H. PLAZAS. "Study liquid length penetration results obtained with a direct acting piezo electric injector". *Applied Energy* 106 (2013), pp. 152–162.

[38] PAYRI, R., J. GIMENO, J. P. VIERA, and A. H. PLAZAS. "Needle lift profile influence on the vapor phase penetration for a prototype diesel direct acting piezoelectric injector". *Fuel* 113 (2013), pp. 257–265.

[39] PASTOR, J., J. LÓPEZ, J. GARCÍA-OLIVER, and J. PASTOR. "A 1D model for the description of mixing-controlled inert diesel sprays". *Fuel* 87.13 (2008), pp. 2871–2885.

[40] MACIAN, V, R. PAYRI, S. RUIZ, M. BARDI, and A. H. PLAZAS. "Experimental study of the relationship between injection rate shape and Diesel ignition using a novel piezo-actuated direct-acting injector". *Applied Energy* 118 (2014), pp. 100–113.

Chapter 2

Direct injection in diesel engines

2.1 Introduction

Direct injection has been the most common method to introduce the fuel into the combustion chamber in Diesel engines [1]. This method has become the dominant technology in Diesel engines thanks to the substantial increase in efficiency and reduction in size of the engine head, consequent to the elimination of the pre-chamber. However, by definition, the fuel has to mix and ignite directly within the combustion chamber: this fact has represented the main drawback of this system pushing to a continuous innovation in the technology as well as in injection strategies. In this chapter, the fundamentals of direct injection are described highlighting the critical achievements that led to better performing injection systems. The short summary presented refers to a global understanding resulting from decades of research and well-established results obtained in the field of Diesel engines [1, 2].

2.2 Injection and combustion in *CIDI* engines

In compression-ignition direct-injection engines (*CIDI*) the fuel is directly injected into the combustion chamber: this fact creates a tide link between the injection event and the heat released during the combustion. A convenient way to describe this phenomenon is the representation presented in Fig. 2.1: using the same time reference (in this case, the start of the injector energizing) the fuel mass flow rate is plotted together with the apparent heat release rate (*AHRR*) that is obtained measuring the pressure in the chamber and applying the perfect gas law. The plot

presented is a sample case representing a typical single-injection at medium load conditions.
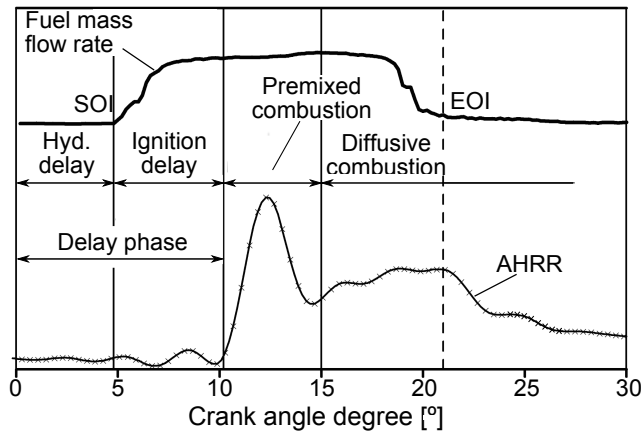
*Figure 2.1: Different phases of Diesel combustion and relationship between the apparent heat release rate (*AHRR*) and the fuel mass flow rate [3]. The start of the injection (*SOI*) and end of injection (*EOI*) are indicated on the mass flow rate curve.*

Three main phases are normally identified in the *AHRR* curve (Fig. 2.1):

1. *delay*. After the electric signal is sent to the injector a certain lapse of time has to pass before the first effects of the combustion are observed. This phase is divided into two main parts: the first part (the *hydraulic delay*) is the time the injector requires to make the injection begin; the duration of this period is mainly related to the injector technology while the conditions within the chamber and the injection pressure have only a second order effect. After the start of the injection (*SOI*), the fuel mixing process and some pre-reactions take place. During this phase, there are the concurrent effects of the fuel evaporation, reducing the temperature (and the pressure) in the chamber, and pre-reactions characterized by a weak amount of heat released. The competition between these opposite effects is reflected in Fig. 2.1 by the negative gradient appearing after the start of the injection. When the pre-reactions create the favorable conditions, exothermic reactions take place causing the first significant increase in the ambient pressure: this marks the end of the delay phase. Generally, the elapsed time between the start of the injection and the end of the delay phase is named ignition delay [4–6];

2. *premixed combustion*. After the onset of the first exothermic reactions, the temperature locally rises significantly and leads all the surrounding ignitable mixture to burn. This premixed combustion causes the high peak in the *AHRR* that is responsible for the harsh noise, typical of old Diesel engines. Once the premixed phase ends, if the fuel injection continues, the flame acquires steady features. Conventionally, the end of the premixed phase is generally identified with the local minimum that follows the premixed peak [3];

3. *diffusive combustion*. Once the premixed phase of the combustion has ended, the combustion develops certain features that are typical of the diffusive combustion and, most of all, the fuel burns at the same rate as it is injected. In this phase, the *AHRR* is relatively constant until the end of injection (*EOI*), when the *AHRR* suddenly drops.

With this simple description, the reader can distinguish the two main complications of direct injection in Diesel engines:

- the delay phase, which significantly extends the duration of the injection/combustion process, limits the maximum rotational speed of the engine and, to a certain extent, the control over the combustion process;

- the peak in the *AHRR* observed during the premixed combustion, on one side, causes a pressure wave that increases the noise and the mechanical stress to the engine, on the other, the rich mixture burned in this phase is responsible for the pollutant emissions (NO_x and soot) [7, 8]. The reduction of these emissions is nowadays the biggest challenge for Diesel engine development.

Even if visually the two weak points highlighted above can be described separately, they are linked to each other: in fact, the height of the *AHRR* peak reached in the premixed phase, is dependent on the fuel injected prior to combustion, and that is, among other things, a function of the delay.

Theoretically, the ideal injector would be able to inject without any delay and to control the mass flow rate during the injection: a slow mass flow rate during the ignition delay period, in order to reduce the premixed-phase peak and a high mass flow rate during the diffusive phase, in order to produce the needed power (c.f. Fig. 2.2).

Many path and solutions have been tried in the past decades for the improvement of the combustion in the Diesel engine, controlling the reactivity of the atmosphere in the chamber (e.g. introducing exhaust gases recirculation *EGR*) or
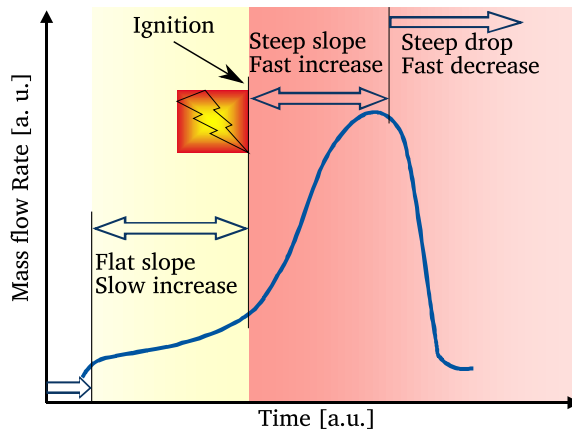
Figure 2.2: Ideal mass flow rate for CIDI *[9]*

modifying the reacting properties of the fuel (e.g. dual fuel strategies). Moreover, a constant effort has been done to improve the flexibility of the injection system and many important successes have been achieved. Due to the specific aim of this thesis, the next section has been focused on the presentation of the technology available in the current injection systems, in order to provide to the reader a clear background of the reasons as well as the objectives that are behind the study of the direct-acting injector.

2.3   Injection systems

The *common rail* is currently the most employed injection system in Diesel engines. Even if different injection systems have been used during the last decades (e.g. *pump injector*), the *common-rail* is currently employed for nearly the totality of the automotive applications and in most Diesel engines in general. In fact, at the current state of maturity, it is the system that matches the most the requirements of the automotive market [10]. In fact, due to the variability of the working conditions typical of this applications, it is required an extreme flexibility of the injection system.

Fig. 2.3 presents the main components and layout of a typical common-rail system [12]. A low pressure pump, generally placed in the fuel tank, feeds the fuel to the high-pressure pump. This second pump, mechanically connected to the engine, provides a certain fuel mass flow rate abundantly higher than the average fuel mass flow rate required by the engine. The fuel flow is directed
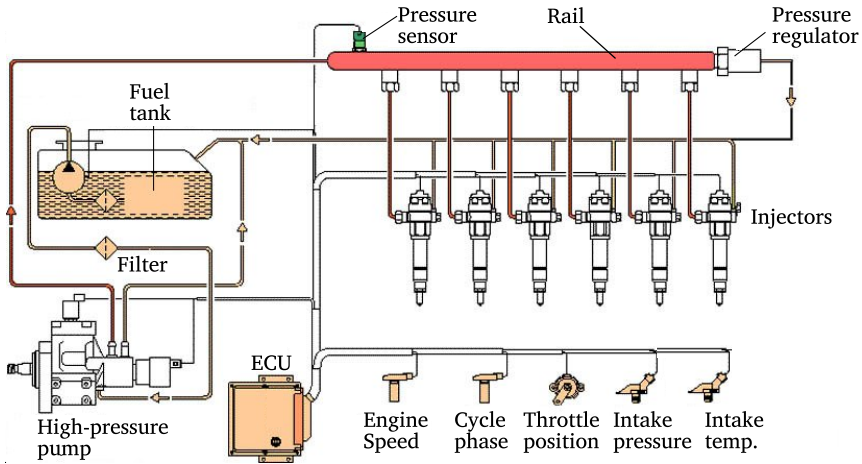
Figure 2.3: Components and layout of a typical common rail system [11].

to the rail, which is connected to the injectors. A flow valve, combined with a pressure sensor, controls the pressure of the fuel in the rail, directing the part of the fuel that is not injected to the fuel tank.

In this way, a relatively high fuel volume (rail and feeding pipes) is maintained at high and constant pressure. The rail acts like an accumulator limiting on the one hand, the fluctuations related to the high pressure pump and, on the other, the pressure drop occurring at the opening of one of the injectors [12, 13].

The injectors, connected to the rail through short high pressure lines (typically $10 - 20$ cm), are actuated independently by the engine control unit (*ECU*).

The fundamental advantage of the injection system is due to the fact that the rail pressure and the timing of the injection timing is completely decoupled from the engine working conditions and it is controlled electronically. In fact, the *ECU* is connected to a wide number of sensors, providing the information needed to understand the particular working condition of the engine. Therefore, the independent control on the rail pressure and injection timing allows to extend significantly the range of injection strategies and to adapt it to each different engine condition.

Therefore, the *common rail* system, with respect to other technologies, presents the following advantages:

- more control on the start and duration of the injection;

- accuracy on the injected mass;
- it releases the injection system from the working condition of the engine;
- it maximizes the control on the mass flow rate.

Moreover, the last development in injection technology increased the limit in the maximum injection pressure up to 300 MPa significantly increasing the capability of delivering fuel in a short time and indirectly enhancing the efficiency of fuel-air mixing [14].

The development of the common rail system pivots around the development of the injector: the next section describes the working principle of this fundamental device.

2.4   The common-rail injector

The injector certainly represents the most complex organ of the *common-rail* system. The elements composing a common-rail injector are presented in Fig. 2.4 and can be branched in the following main components:

- injector nozzle. The injector nozzle generally has several orifices, (typically 5 to 10 in automotive applications). In this element it is included also the needle, which has the function of controlling the fuel flow through the nozzle orifices;

- connecting rod. The connecting rod transmits the movement from the servo-actuated circuit to the nozzle needle. The top of needle pushes against the bottom part of this component;

- servo actuated system. This mechanism is composed of an actuator (in this case a solenoid actuator), a fuel valve and a control volume. This is the core of the injection and allows to generate the forces needed to move the needle effectively during the injection. The working principle of this mechanism is explained below.

The schematic presented in Fig. 2.5 illustrates the working principle of the servo actuated injector highlighting the different phases of the injection. The high pressure fuel, coming from the rail through the high pressure line, right after the entrance is divided into two channels: one goes down toward the nozzle and another goes to the control volume. The control volume, located at the top of the connecting rod, is endowed with two calibrated orifices: one connecting to the injector entrance and the other to the low pressure return line; the fuel

Fuel return line
Solenoid valve
High pressure feeding
Electric connection
Control volume
Auxiliary line
Main feeding line
Connecting rod
Nozzle needle
Nozzle
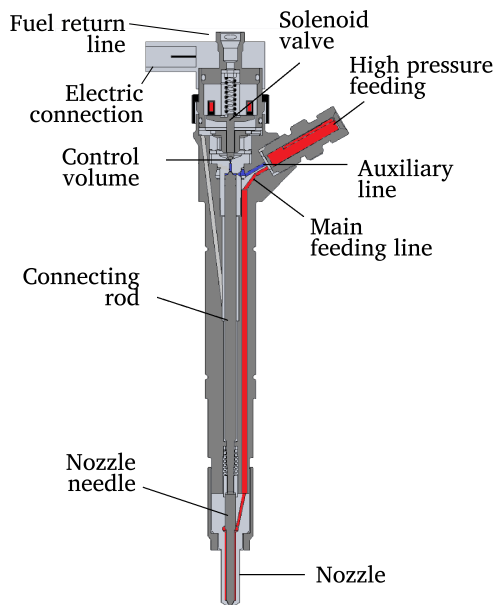
Figure 2.4: Global sketch of a solenoid activated common rail injector (Bosch CRI2.4 [15]).

flow through this second channel is controlled by the solenoid valve. When the solenoid is not activated (rest condition), the valve is closed and no flow can exit from the control volume. Consequently, the fuel pressure in the control volume is equivalent to the fuel pressure in the feeding line and, since the area at the top of the connecting rod is higher than that of the needle, the resultant force pushes the rod-needle toward the nozzle, closing the orifices. Even without pressure, this position is maintained by a pre-loaded spring that keeps the injector closed.

Once the solenoid is activated, the valve opens and the fuel flows through the outlet of the control volume: due to the specific designe of the calibrated orifices, the fuel flow generated through the control volume cause a significant decrease of the pressure in this region of the injector. As a consequence of that, the pressure at the top of the connecting rod is lower and the high pressure at the bottom of the needle cause the rod-needle system to go up. Once the needle is lifted the fuel can flow through the orifices and the injection starts. When the solenoid is deactivated, the flow through the control volume stops, causing the fuel pressure to rise again and leading the forces acting on the rod-needle system to the initial conditions. This pushes the needle down until its seat, blocking the fuel flow through the orifices, thus ending the injection.
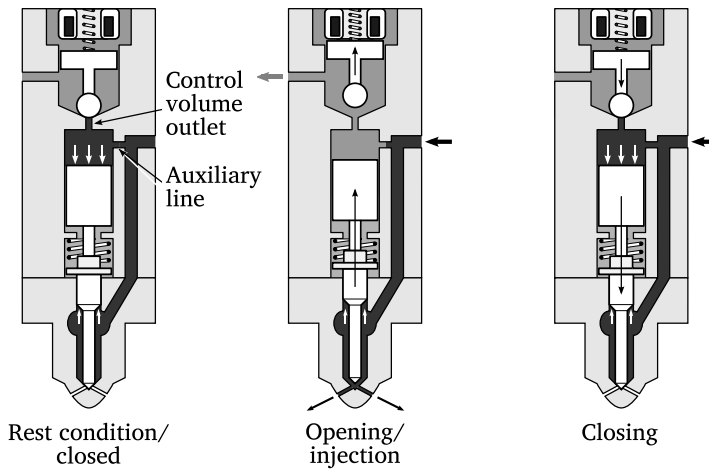
Figure 2.5: Working principle of a typical servo actuated common rail injector [16].

Different solutions have been implemented during the years, improving the accuracy and the rapidity of the injector actuation. In particular the reduction of the inertia of the needle-rod system and the effectiveness of the actuator allowed to reduce significantly the time lag between the electrical signal and the injection event, allowing the implementation of a higher number of injections during each cycle.

In this context, it is worth to mention the introduction, in newer generations injectors, of piezo-electric systems in substitution of the solenoid actuator [17, 18]: in this system, the new design of the servo hydraulic circuit combined with the introduction of a piezo-actuator allowed a substantial reduction of the inertia of the moving system composed by the needle-rod system and a consequent improvement of the injector dynamic response. In particular, the Bosch CRI3.1 piezo-actuated injector presents the elimination of the connecting rod, thanks to the introduction of an amplifier piston [18].

Fig 2.6 shows the internal components of this kind of injector: piezoelectric valve (which consists of a piezoelectric actuator, a hydraulic amplifier and a control valve), injector holder (high-pressure fitting, filter, fuel return to pump, injector body) and nozzle. The inner components of the piezoelectric valve are shown in detail in Fig.2.6-right. Unlike the typical solenoid injector, the control volume has three active orifices (an outlet orifice and two inlet orifices). The outlet orifice (OAZ) also works as an inlet orifice. On the other hand, the control volume is placed directly over the valve, which improves the dynamic response of the injector and facilitates the introduction of multiple injections (up to eight

1. High pressure fitting
2. Filter
3. Fuel return
4. Injector body
5. Piezo-electric actuator
6. hydraulic amplifier
7. Control valve
8. Nozzle

1. Piezo-electric actuator
2. Amplifier piston
3. Tube spring
4. Valve piston
5. Valve piston spring
6. Valve holder
7. Valve bolt
8. Control plate
9. Control volume
10. Needle

OB. Bypass orifice
OAZ. Inlet/outlet orifice
OZ. Inlet orifice

L1-L2-L3. Feed lines

Figure 2.6: Internal components of the Bosch CRI3.1 *piezo-electric actuated injector [18].*

consecutive injections). The maximum injection pressure that can be achieved by these injectors is 200 MPa.

When the actuator is activated it expands, displacing the amplifier piston, which compresses the fuel located between the lower part of the amplifier piston and the upper part of the command piston. The shape of the volume between the piezo-actuator and the amplifier piston amplifies the vertical displacement of the system, opening the upper seat of the control valve and closing the lower one (valve seat 1 opened and valve seat 2 closed). At these conditions, valve seat 1 opens and the decrease in the pressure in the control volume causes the movement of the needle and the consequent start of the injection.

When the actuator is deactivated, valve seat 1 closes due to the valve spring pre-load and the pressure on the upper part of the command piston is recovered as the fuel enters through the inlet orifice (*OZ*) and the outlet orifice (*OAZ*), because when valve seat 2 opens, it connects the inlet of the *OZ* orifice to the outlet of the *OAZ* orifice through *OB* orifice. Finally, the needle is pushed towards its seat, thus ending the injection process.

Finally, the recent introduction of balanced-valves in traditional solenoid actuators allowed this technology to endure in the market and they are nowadays being installed in many commercial engines [9]. In this last solution, the design of the valve enables a reduction in the force on the actuator caused by the hydrostatic pressure of the fuel (see sketch in Fig. 2.7): in this way, the spring precharge on the solenoid valve can be decreased with a consequent improvement of the injector actuation.
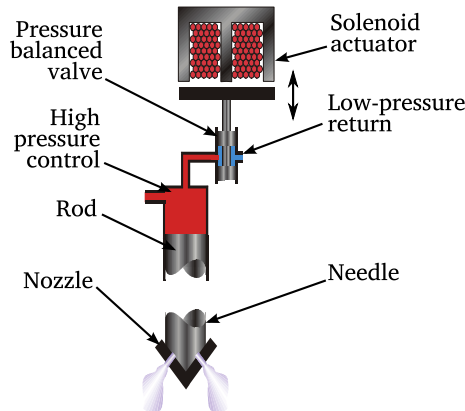
Figure 2.7: Sketch of the solenoid balanced valve system employed by Delphi in the DFI1 *concept [19].*

Despite the injector performances improved considerably, these injectors can work only in on/off mode, allowing a high control on the injection timing and duration, but leaving the shape of the mass flow rate profile a dependent parameter, related above all to the injection pressure. Even if the pressure in the rail is a well controlled parameter, it is difficult to adjust this quantity in cycle-to-cycle timing, and, even more, to have a control on it capable of modifying accurately the shape of the injection rate profile.

The injector prototype from Continental employed in this thesis features the control of the needle position as a method of controlling the injection mass flow rate. A brief overview of other solutions employed for the mass flow rate control in common rail injectors are presented in the next section.

2.4.1   Hydraulic amplified system

The hydraulic amplifier or piston amplifier system allows a partial modulation of the mass flow rate during the injection. This solution, called from Bosch Hydraulic

Amplifier Diesel Injection System (*HADIS* [9, 20]) has been adopted by different manufacturers (e.g. Bosch, Delphi) and allows the injection of fuel at two different fuel pressure levels: the rail pressure and a higher pressure obtained thanks to the action of a piston amplifier. The working principle of this injector is presented in Fig.2.8: in rest conditions both valves (needle and piston valves) are closed. In this condition the pressure of the fuel forces the needle against its seat and the spring pre-charge maintain the piston in a certain position. When the needle valve is activated, the pressure in the upper surface of the needle decreases and causes the start of the injection as in a conventional system. However, when the second valve is activated the piston is forced to move toward the needle and the particular shape of the piston causes an increase of the fuel pressure in the needle region, producing the pressure *amplification*. In this way two different pressure levels can be employed in the same injection event and with a rail pressure of only 135 MPa and actual injection pressure of 250 MPa can be obtained. However, the complication of the system, together with the limited flexibility generated, limited the appeal of this solution [21].
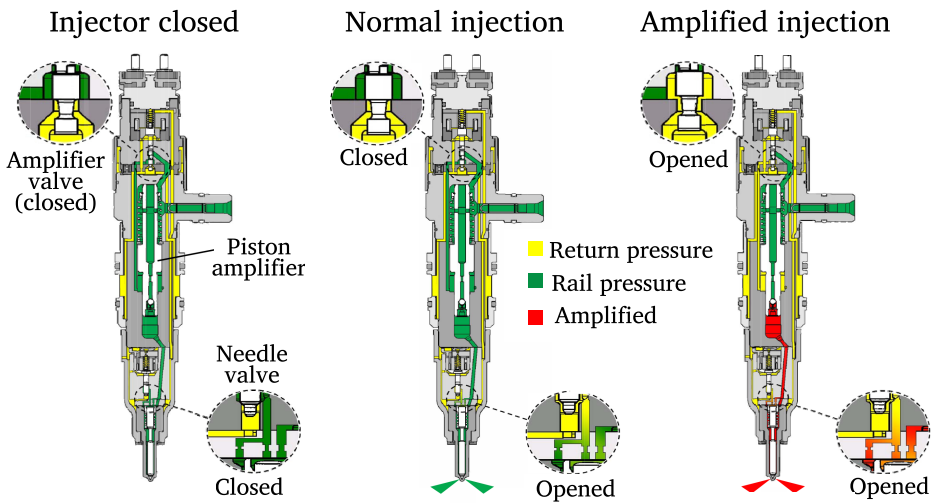
Figure 2.8: Working principle of the HADIS *system [9].*

A similar system has been adopted by Caterpillar in the so called *HEUI* system (hydraulically actuated, electronically controlled unit injector) [22]. In this system, a fuel high pressure pump is combined to the availability of high pressure oil. As in the previous system, the injector can work in non-amplified mode at the line fuel pressure, an in an amplified mode: in this case the amplifier piston is activated by the oil and its movement can be modulated thanks to the actuation

valve. The manufacturer claims a higher control on the injection with respect to previous systems: however, the implementation of this system is limited by the need of high pressure oil, that is normally not available in automotive vehicles [22, 23].

2.4.2   Delphi *DFI3*.

In comparison to conventional servo (solenoid or piezo) hydraulic technology, the direct acting system proposed by Delphi in their *DFI3* generation eliminates the usual four step servo hydraulic concept down to a single step: the direct actuation of the needle through a hydraulic amplifier by a piezo-ceramic actuator (Fig.2.9) [24].
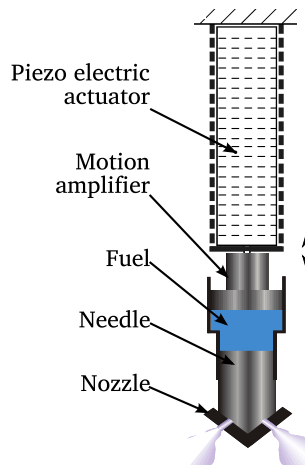
Figure 2.9: Direct acting injector designed by Delphi [25].

Unlike a servo controlled injector, the force change needed for needle opening is provided by a piezo-actuator that is decoupled from the rail pressure supply. It is therefore possible to adapt the force change delivered by the actuator electronically as required. The manufacturer claims that this system leads to an improved multiple injection capability. Moreover, this injector contains an internal volume of fuel and does not have any back-leak (low pressure fuel flowing to the return line). The absence of back-leak simplifies the installation and eliminates the need for fuel return lines and fuel coolers even when operating at 200 MPa. The manufacturer claims also that, thanks to this configuration, the maximum needle speed is increased (3 m/s against 1 m/s of the traditional injectors). Moreover, the needle

speed is not dependent on rail pressure and so it is maintained even at very low rail pressures [24–26].

2.5 The Continental direct-acting injector

In this thesis, the experiments were carried out using a direct-acting prototype injector designed by *Continental*. The Continental direct-acting injector (*CDA*) has the outstanding feature to set into motion the nozzle needle by direct coupling the piezo-electric actuator and the nozzle needle itself.

Opposite to the solution presented by Delphi, the *CDA*, provides a mechanical coupling between the piezo-stack and the nozzle needle through the introduction of a leverage system. The leverage system has the function to overcome the limited deformations of piezo-actuator, amplifying them and causing a larger displacement of the needle. The working principle of the injector is represented in the sketch in Fig. 2.10.

Therefore, the deformation of the actuator controls directly the opening of the needle unlike the existing servo-actuated fuel injection technologies which use an electro-hydraulic circuit generating pressure differences. Thereby, the limiting *open-close* working mode is extended to a variety of controlled needle movements. Both the intrinsic fast time-response of the piezo-stack actuator and the capability of the ECU to generate complex electrical signals, promise to control accurately the needle position and to throttle the fuel flow through changes of the electronic signal to the injector. Therefore, the conventional *square* injection rate profile could be easily modified, varying the mass flow rate during the injection.

Even though the concept is relatively simple, the development of this device has been pursued for a long time. The challenges in building a direct acting injector are several:

- to increase the order of magnitude of the displacement produced by the piezo-actuator, typically too low for the needle lift needed;

- to develop a system capable of supporting the forces related to the typical common-rail injection pressures;

- to extend as much as possible the range of conditions in which the injector can work properly.

The key feature of the *CDA* injector is the introduction of a lever amplifier that transfers the deformation of the actuator to the nozzle needle. Fig. 2.10 shows
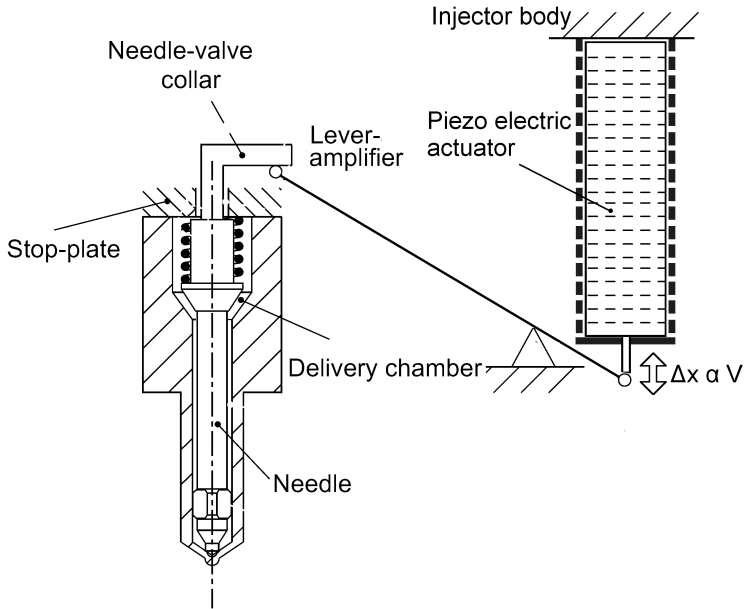
Figure 2.10: Scheme of the working principle of the CDA injector. A leverage system transfers and amplifies the deformation of the actuator to the needle collar [27].

a picture of the *CDA* injector with a sketch of the leverage system: applying a voltage to the piezo-stack, the push pin moves downward as a consequence of the actuator deformation; then, the leverage system actuates on the needle collar causing the needle lifting and the beginning of the injection. The position of the needle is *normally closed*: when no voltage is applied, the pre-load spring and the fuel hydrostatic pressure provide the force needed to close the injector.

Ferrari et al. [27] carried out a detailed study, modeling this type of injector entire mechanism in order to assess both the capabilities and the limitations of this novel system. In the study, they included a *FEM* sub-model predicting the piezo-actuator behavior developed by Altieri et al. [28]: the deformation of the actuator is related to the voltage applied, computing also the current absorbed, the heat produced and the hysteresis implied. The leverage mechanism and the injector needle assembly are carefully studied through a *0D* approach that takes into account the elastic deformation of the components. Among the many achievements of their work, the conclusions most related to the present study are reported below:

- the pressure of the fuel pushes the needle against the nozzle: this force, existing in rest condition and during the injection, is proportional to the rail pressure;

- the deformation of the elements composing the leverage system are significant and proportional to the force needed for the needle lift which is dependent on the injection pressure (as explained in the previous point). Therefore, if the injection pressure varies, the voltage applied to the piezo-stack needs to be adjusted to obtain the same needle lift (e.g. at higher injection pressure the voltage should be higher);

- the piezo-stack temperature has a significant impact on the injector performances: when the piezo-stack temperature increases, the related deformation of the actuator lowers. This means that the injector temperature control during tests has to be accurately controlled.

Some preliminary tests, revealed that the ramp up shape of the voltage signal has great effect on the injection, mostly related to the pressure of the fuel in the nozzle which *helps* the needle lift. However, this force is available only after the start of the injection, when the fuel flow causes the increase of the pressure within the nozzle sac.

Depending on the shape of the voltage ramp-up sent to the injector, the sudden increase of the nozzle sac pressure can cause instabilities in the needle position and therefore in the flow. For this reason, the injector manufacturer provided a map of the signals to apply, according to the boundary conditions. This map is implemented in a programmable *ECU* or *PECU*, dedicated to the control of the whole high pressure system.

The signals sent to the injector are characterized not only by a *top-hat* steady voltage, but also by a well defined ramp-up followed by a peak. As a consequence, the actuation of the piezo-stack will be referred in this thesis to the input parameter used in the *ECU*: the *Charge* % (*Ch*). This value, expressed as the percentage, defines the voltage applied to the piezo-stack and the shape of its curve. The *Ch* varies in a range between $0 - 115\%$: *Ch*=0% corresponds to no actuation, while $Ch = 100\%$ refers to the nominal maximum needle lift. Injecting at *Ch* over the nominal maximum is possible but only for short periods since it leads to the overheating of the piezo-stack.

From $Ch = 0\%$ to a certain value depending on the injection pressure (typically $40 - 50\%$) no injection is produced: within these limits the only result of the piezo-stack actuation is the clearance compensation of the mechanism and the deformation of the leverage system. For another charge-range, some fuel is

injected, but the needle position is not stable causing a fluctuating flow and high cycle-to-cycle dispersion.

References

[1]   HEYWOOD, J. "Internal combustion engine fundamentals". *Mc Graw Hill, Inc. -* (1998), pages.

[2]   PAYRI, F. and J. DESANTES. *Motores de combustión interna alternativos*. Editorial Reverté, 2011.

[3]   GARCÍA, J. M. "Aportaciones al estudio del proceso de combustión turbulenta de chorros en motores diesel de inyección directa". PhD thesis. Valencia: E.T.S. Ingenieros Industriales. Universidad Politécnica de Valencia, 2004.

[4]   PAYRI, R., F. SALVADOR, J. GIMENO, and J. DE LA MORENA. "Effects of nozzle geometry on direct injection diesel engine combustion process". *Applied Thermal Engineering* 29.10 (2009), pp. 2051–2060.

[5]   BRUNEAUX, G. "Development of optical diagnostic techniques to correlate mixing and auto-ignition processes in high pressure Diesel jets". *Oil and Gas Science and Technology-Revue de l'IFP* 63.4 (2008), pp. 461–477.

[6]   MANCARUSO, E. and B. M. VAGLIECO. "Optical investigation of the combustion behaviour inside the engine operating in HCCI mode and using alternative diesel fuel". *Experimental Thermal and Fluid Science* 34.3 (2010), pp. 346–351.

[7]   MAJEWSKI, W. A. and M. K. KHAIR. *Diesel emissions and their control*. Society of Automotive Engineers, 2006.

[8]   DEC, E. J. "Advanced compression-ignition engines-understanding the in-cylinder processes". *Proceedings of the Combustion Institute* 32.2 (2009), pp. 2727–2742.

[9]   DOHLE, U., S. KAMPMANN, T. WINTRICH, and C. HINRICHSEN. "Advanced Diesel Common Rail Systems for Future Emission Legislation". *International Conference on Automotive Technologies-ICAT*. 2004, pp. 109–113.

[10] FLAIG, U., W. POLACH, and G. ZIEGLER. "Common Rail System (CR-System) for passenger car DI diesel engines; Experiences with applications for series production projects". *SAE Paper* 1999-01-0191 (1999).

[11] PLAZAS, A. H. "Modelado unidimensional de inyectores common-rail Diesel". PhD thesis. Valencia: E.T.S. Ingenieros Industriales. Universidad Politécnica de Valencia, 2005.

[12] PAYRI, R., B. TORMOS, F. SALVADOR, and A. PLAZAS. "Using one-dimensional modelling codes to analyse the influence of diesel nozzle geometry on injection rate characteristics". *International journal of vehicle design* 38.1 (2005), pp. 58–78.

[13] BOEHNER, D. W. "Common rail injection system for commercial diesel vehicles" (1997).

[14] JOHNSON, J. E. et al. "Characteristics of 3000 bar Diesel Spray Injection under Non-Vaporizing and Vaporizing Conditions". *ICLASS* (2012).

[15] MANIN, J. "Analysis of Mixing Processes in Liquid and Vaporized Diesel Sprays through LIF and Rayleigh Scattering Measurements". PhD thesis. E.T.S. Ingenieros Industriales. Universitat Politécnica de Valéncia, 2011.

[16] GIMENO, J. "Desarrollo y aplicación de la medida de flujo de cantidad de movimiento de un chorro Diesel". PhD thesis. E.T.S. Ingenieros Industriales. Universidad Politécnica de Valencia, 2008.

[17] LEE, J. et al. "Effect of piezo-driven and solenoid-driven needle opening of common-rail diesel injectors on internal nozzle flow and spray development". *International Journal of Engine Research* 7.6 (2006), pp. 489–502.

[18] SALVADOR, F. J., A. H. PLAZAS, J. GIMENO, and M. CARRERES. "Complete modelling of a piezo actuator last-generation injector for diesel injection systems". *International Journal of Engine Research* 15.1 (2014), pp. 3–19.

[19] DOBER, G. et al. "The impact of injection strategies on emissions reduction and power output of future diesel engines". *SAE Paper* 2008-01-0941 (2008).

[20] BLESSING, M., G. KONIG, C. KRUGER, U. MICHELS, and V. SCHWARTZ. "Analysis of Flow and Cavitation Phenomena in Diesel Injection Nozzles and Its Effects on Spray and Mixture Formation". *SAE Paper* 2003-01-1358 (2003).

[21] BENAJES, J., R. PAYRI, S. MOLINA, and V. SOARE. "Investigation of the influence of injection rate shaping on the spray characteristics in a diesel common rail system equipped with a piston amplifier". *Journal of fluids engineering* 127.6 (2005), pp. 1102–1110.

[22] GLASSEY, S. and A. STOCKNER. "HEUI-A new direction for diesel engine fuel systems" (1993).

[23] MILLER, C. R., D. J. WALDMAN, and S. F. SHAFER. *Direct operated check HEUI injector*. US Patent 5,651,345. July 1997.

[24] SCHÖPPE, D. et al. "Delphi Common Rail system with direct acting injector". English. *MTZ worldwide* 69.10 (2008), pp. 32–38.

[25] DELPHI. *Direct acting light-duty diesel CR system*. Tech. rep. Delphi Automotive, 2008.

[26] WINTERBOURN, M., D. HOPLEY, C. SOTERIOU, and S. ZUELCH. "Development of the New Delphi Diesel Direct Acting Piezo Injector (DFI3) Using Simulation". *Thiesel* 5 (2008), p. 232.

[27] FERRARI, A. and A. MITTICA. "FEM modeling of the piezoelectric driving system in the design of direct-acting diesel injectors". *Applied Energy* 99 (2012), pp. 471–483.

[28] ALTIERI, L. and A. TONOLI. "Piezoelectric Injectors for Automotive Applications: Modeling and Experimental Validation of Hysteretic Behavior and Temperature Effects". *Journal of Dynamic Systems, Measurement, and Control* 135 (2013), pp. 011005–1.

Chapter 3

The Diesel Spray

3.1 Introduction

The development in the injection technologies has been pushed by three principal, sometimes concurrent, drivers: 1) the quality of the resultant spray and mixing process, 2) the accuracy in the control of the injection parameters and 3) the flexibility of the injection system oriented to the extension of the available range of injection strategies [1–3].

While the last two points are easy to understand and strongly related to the dynamic response of the injector, in order to take advantage from modifications or improvements in the spray formation, the dynamics of the fuel-air mixing and combustion should be completely understood. Moreover, the spray formation remains the real cornerstone of the success of the Diesel injection, staying at the base of the fuel-air mixing process and of the physical processes that determine the combustion.

Due to the implicit turbulent nature of the atomization process and to the transient character of the spray formation, the injection event is a very complex phenomenon that still eludes a deterministic description and pushes the scientific community to go beyond its limits; the length- and the time-scale characterizing the event are also adding difficulties in the implementation of the experimental techniques and the results obtained are often non-conclusive. In this panorama, the contributions to the spray understanding are extremely fragmented and not rarely contrasting between each other. Therefore, before starting with the presentation of the experimental work performed in this thesis, it is fundamental to

settle the basis by presenting a review of the current knowledge about the Diesel spray formation, mixing and combustion.

The aim of this chapter is to give a summary of the physics involved in the Diesel spray formation and combustion, starting from fundamentals and arriving to the role the boundary conditions have on the results. This chapter is divided in four sections, corresponding to four different topics:

- *internal flow*: starting from the rail and arriving to the nozzle orifice outlet, the fuel experiences several pressure drops that in some cases are also related to complex phenomena like cavitation and multi-phase flow [4];

- *spray formation and mixing process*: the liquid core breaks at the orifice outlet due to aerodynamic forces and surface instabilities, forming first ligaments and large droplets, and then completing the atomization process forming fine droplets. The formation of the spray and its spread over a certain angle allow the fuel to efficiently mix with the surrounding gases [5];

- *fuel combustion*: the high pressure and high temperature air surrounding the spray is entrained in the spray and provides the thermodynamic conditions needed for the auto-ignition. After the fuel ignition the combustion evolves passing from a premixed stage to a phase characterized by diffusive combustion [6, 7];

- *partial needle lift and injection rate shaping*: the injector studied in this thesis features a direct control on the needle position; the current knowledge about the interaction between the needle and the fuel flow through the nozzle and the spray formation will be presented in a brief review [8].

3.2   Internal flow

The fuel hydrostatic energy stored in the rail forces the fuel to flow through the injector and eventually to enter into the combustion chamber through the nozzle orifices. The knowledge of the related fluid-dynamics interests injector manufacturers and spray specialists, who constantly work to improve the efficiency of the injector design. The processes taking place in this phase fall in the forced internal flow category since the fuel is forced to move through the injector channels and valves by a pressure difference. The transformations involved are mainly variation in pressure and velocity, energy dissipation and in some case the formation of fuel vapor due to the presence of regions at very low pressure (*cavitation*) [9].

The fluid mechanics has been studied for years and a lot of models and equations have been developed to predict and analyze the flow in many different situations. A general introduction to the problem is given in the following section.

3.2.1 Forced internal flow

When a fluid is forced to move through channels or pipes by pressure differences, it is usually named *forced internal flow*.

The Bernoulli equation, that can be considered as a statement of the energy conservation equation applied to the flow of fluids, is generally presented as a starting point to face forced internal flow problems:

$$H = \frac{p}{g\rho} + \frac{1}{2g} u^2 + z = \text{const} \quad , \tag{3.1}$$

where H is the *total head*, p, u and z are respectively the pressure, the velocity and the elevation at a datum point, ρ is the fluid density and g the gravitational acceleration. In the Bernoulli equation three characteristic terms of the flow energy can be distinguished: the elevation z, the pressure head $p/g\rho$, and the dynamic pressure $1/2g\, u^2$. In this specific application, the *elevation* term is normally neglected since the elevation differences are modest, and even more when compared to the high pressure variations characterizing the fuel flow in common rail systems. Eq. (3.1) is true in case of ideal flow, where the transformation from potential to kinetic energy is complete without any viscous dissipation. In real transformations this dissipation cannot be neglected and therefore, starting from Eq. (3.1), the flow transformation from section 1 to section 2 can be written including the dissipation term ϕ_{visc}

$$\frac{p_1}{g\rho} + \frac{1}{2g} u_1^2 + \cancel{z_1} = \frac{p_2}{g\rho} + \frac{1}{2g} u_2^2 + \cancel{z_2} + \phi_{visc} \quad . \tag{3.2}$$

The term ϕ_{visc}, accounting the total viscous losses of the flow, is responsible of the head losses observed when a real fluid flows in a pipe. The determination of this term is always complex and many studies in the past were carried out to characterize it. The quantity ϕ_{visc} is the result of the sum of two terms,

$$\phi_{visc} = \phi_m + \phi_M \quad , \tag{3.3}$$

where ϕ_m and ϕ_M represent respectively the *minor* and *major* losses. The minor losses (ϕ_m) are related to sudden changes in the shape or in the direction of the channel driving the flow. In these cases, the fluid cannot completely follow the
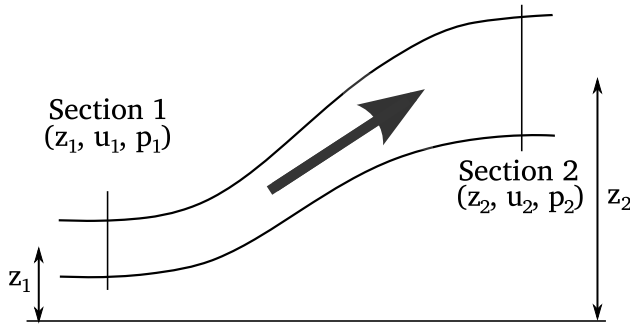
Figure 3.1: Schematic of the flow of a fluid through a pipe of variable section.

internal shape of the channel and a separation of the boundary layer may occur. This separation results in the apparition of a recirculation zone that restrains the flow in a smaller section, commonly called *Vena Contracta*. This restriction makes the flow speed up and then slow down around the *Vena Contracta* causing energy dissipation and eventually pressure losses. The minor losses are also called singular head losses and this term might be more suitable in injection related studies since these minor losses can actually be significant due to the complex geometry of the injector channels [10]. The pressure drop Δp_m related to a minor loss is normally expressed as

$$\Delta p_m = \xi \frac{\rho}{2} u^2 \quad , \tag{3.4}$$

where ξ is the minor loss coefficient. ξ ranges from 0 and upward: when $\xi = 0$ there is no loss, while $\xi = 1$ means that the pressure drop is equal to the dynamics pressure. Note that the minor loss coefficient can also be greater than 1 for some specific case.

Due to the extremely high fuel pressure employed in Diesel injection and the consequent high velocities reached, the fuel pressure locally assumes very low values in the recirculation zones. These values, in some cases, are lower than the vapor pressure p_{vap}, resulting in the phenomenon of the cavitation.

In order to predict accurately the head losses, the flow regime has to be identified to know which theory has to be applied in the studied case [11]. Two flow regimes are commonly identified: *laminar* and *turbulent*, which are distinguished for specific values of the Reynolds number [12]. The Reynolds number is a dimen-

sionless parameter that gives a measure of the ratio between inertial and viscous forces and it is defined as

$$Re = \frac{\rho\, u\, D}{\mu} \quad . \tag{3.5}$$

where D is the characteristic length (e.g. the diameter of the studied pipe) and μ the dynamic viscosity of the fluid. For cylindrical straight ducts, internal experimental observations show that the flow is laminar for values of Reynolds number below $Re \approx 2300$ and turbulent for values above $Re \approx 4000$. The interval $Re = 2300 - 4000$ is considered as a transition regime where both laminar and turbulent regimes are possible, depending on the pipe roughness. Nonetheless, care must be taken with respect to this definition because it appears to be valid only for fully developed flows: in fact, when there are changes in the pipe section, the perturbations in the flow are generated and protracted for a certain length (normally several diameters) called flow development length. This distance needed to get a stabilized flow also depends on the regime (laminar or turbulent) and, for each specific perturbation, needs different equations or coefficients to be studied. However, detailing the characteristics of the developing flow would go beyond the scope of this section.

On the other hand, the major losses are induced by the friction of the fuel on the channels wall and they depend on the length of the considered channel. The pressure drop Δp_M related to the major loss is defined

$$\Delta p_M = k_{fric} \frac{L}{D} \frac{\rho}{2} \bar{u}^2 \quad , \tag{3.6}$$

where k_{fric} is the friction coefficient, that depends on Re and wall relative roughness, while D is the section diameter. To evaluate the friction coefficient k_{fric}, the flow regime must be known; in the case of fully developed flow in laminar regime, the surface roughness can be neglected and k_{fric} is expressed as below:

$$k_{fric} = \frac{64}{Re} \quad . \tag{3.7}$$

In turbulent regime, the interaction between the fluid and the wall changes, as well as the velocity profile. In this case the surface roughness effect has to be taken into account expressing the friction coefficient by means of the following expression:

$$k_{fric} = f\left(Re, e/D\right) \quad , \tag{3.8}$$

where e/D is generally referred as the relative roughness, with e the absolute roughness and D the channel diameter. The Colebrooke's equation presents an analytical solution of the friction coefficient [13],

$$\frac{1}{\sqrt{k_{fric}}} = -2log\left(\frac{2.51}{Re\sqrt{k_{fric}}}\right) + \frac{e/D}{3.72} \quad . \tag{3.9}$$

Since k_{fric} appears on both sides of Eq. (3.9), it has to be solved by iteration; if Re, length and diameter of the channel, wall roughness, fluid density and mean velocity of the flow are known, the major losses can be calculated.

The theory presented for circular sections can be extended to other shapes using equivalent diameters D_{eq}. However, the calculation of the pressure drop for each single case lies outside the scope of this section, that is a qualitative presentation of the parameters that mainly affects the fuel flow in Diesel injection.

3.2.2 Upstream of the nozzle

Before reaching the injector nozzle, the fuel stored in the rail has to pass in the high pressure feeding line and then through the hydraulic circuit within the injector. In these transformations, the fuel normally does not experience important pressure losses, but the accurate design of this part has important consequences on the dynamic of the system. Normally, the feeding line internal diameter is about 3 mm, and its length depends on the injection system arrangement (for passenger cars varies between $300 - 700$ mm). The velocity of the fuel flow in the feeding pipe during the injection is typically $5 - 8$ m/s corresponding to a $Re \approx 10^4$. Calculating the pressure drop with the methodology presented in section 3.2.1 the pressure drop in the feeding line is expected to be less than 0.3 MPa. This value, compared with the total available pressure drop, typically of the order of 100 MPa, is negligible. However, the correct design of the feeding pipe is important: for example, the time required for a pressure wave to travel through the line is about $0.2 - 0.4 ms$, that is of the same order of magnitude of the injection duration [14]. Moreover, the propagation of pressure waves could have repercussions on the injection process as well as, in case of multi-injection strategies, on the following injection [10]. Subsequently, the fuel has to pass through the channels within the injector feeding the injector nozzle and, depending on the injector technology, the hydraulic circuit for the needle motion. Also in this case, the pressure losses are small when compared to the total pressure drop available and, moreover, they are very difficult to measure directly without using intrusive techniques.

Normally the fuel flow within the injector is estimated performing simulation with 1-D models [14, 15]. The characterization of the flow within the injector

becomes important in the phase of injector design when, for example, the size of the apertures of the control volume has to be decided. The correct design of the hydraulic circuit within the injector together with the reduction of the moving components inertia are the keys for a fast response of the injector [16]. Moreover, the design of the injector internal channels can generate pressure waves that are eventually reflected by oscillations of the mass flow rate. In the injector studied in this thesis, the needle movement is determined by the direct interaction between the piezo-electric actuator, the leverage mechanism, and the nozzle needle. Therefore, the exclusion of hydraulic circuits for the needle movement (at least for the needle lift) reduces the impact of the aforementioned design details.

3.2.3   Needle seat

The needle interference with the flow is traditionally considered limited or negligible, since in steady conditions the needle lift is sufficiently high to neglect its interference with the flow. In conventional injectors, save the transient phases at the start or the end of the injection, the needle is fully lifted, and the relatively wide cross-section area at the needle seat makes the restriction caused by the needle very low. However, due to the tendency in reducing the injection duration by separating the event in several pilot and post injections, the transient at intermediate needle lift are catching the attention of the engine community. In this sense, specific studies have been performed to assess the effect of the needle seat type on the spray development [17, 18].

Nowadays, there are two main typologies of needle seat types employed in commercial injectors: VCO (*valve closed orifice*) and *micro-sac*. As shown in Fig. 3.2, in the first typology, the orifices' inlet lay on the needle-nozzle contact surface, while in the second case, the sealing of the needle is performed in a specific contact-area between needle and nozzle upstream of the orifices, while the orifices' inlet is placed in a specific volume within the nozzle called *sac*. Because of the geometry, both solutions present the following advantages/drawbacks:

- the VCO nozzle has a faster response, since once the needle is lifted, the fuel flow directly through the orifices. However, during the opening/closing transients, the position of the needle strongly influences the fuel flow and it often results in asymmetric fuel flow and uneven distribution of the fuel around the nozzle [19];

- the micro-sac volume has been designed to prevent this problem. However, the residual fuel that, after the needle closing, remains into the sac is a problem because it can result in fuel dripping and consequent increase of

UHC and soot. For this reason, the size of the sac is strongly limited and the current tendency is to reduce its size [20];
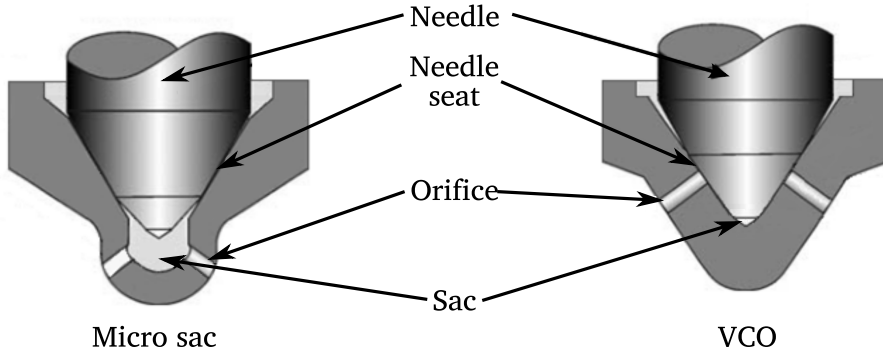
Figure 3.2: Example of two different needle seat types: micro-sac (left) and VCO (right).

The study of the flow upstream of the orifice has gained much importance in the last years due to the shortening of the injection timing, the multiple injection strategies and the availability of injectors able to control the needle lift: being the specific focus of this thesis the characterization of a direct acting injector, the discussion of the current state of the knowledge about this matter will be presented at the end of this chapter; after the global presentation of processing taking place during the injection event, the reader will more easily understand the partial needle lift phenomenon and its weight in the overall injection process.

3.2.4   Nozzle orifice

The nozzle orifices are the part of the nozzle where the fuel pressure is transformed in kinetic energy, accelerating the flow before entering into the combustion chamber. Each microscopic feature of the nozzle is strictly related to the diesel spray characteristics [13, 21, 22] and, therefore, to the mixing/combustion process. Even if the injector orifices used in the early injector generations were simple straight holes, direct injection system requirements have pushed researchers to produce different improvements in their shape in order to obtain the best performances in term of fuel delivery capability and mixing.

Fig. 3.3 defines schematically the main features of a typical orifice that can be found in a direct injection nozzle.
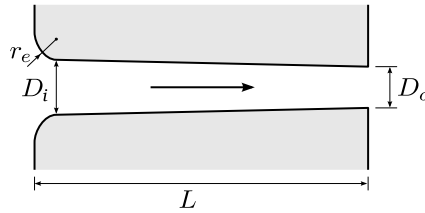
Figure 3.3: Geometric parameters to define the orifice of a direct injection nozzle.

The geometric parameters generally used in fluid mechanics applied to Diesel nozzle injectors are: inlet and outlet diameters, D_i and D_0 respectively, orifice length L, and entrance radius r_e. From these dimensions, some parameters can be defined, which characterize the shape of the nozzle's orifice and are dimensionless:

- length - diameter relation: L_o/D_0;
- entrance radius - inlet diameter: r_e/D_i;
- inlet - outlet diameter ratio: D_i/D_0.

This last ratio gives conicity or convergence (note that it can also be divergence) of the orifice, and it is equal to unity for cylindrical nozzles. To determine the convergence of an orifice, the *k–factor* is generally found throughout the literature and is defined as follows [23, 24]:

$$k\text{–}factor = \frac{D_i - D_o}{10\,[\,\mu\text{m}\,]}\;. \tag{3.10}$$

Nevertheless, this parameter presents the drawback of not taking into account the absolute outlet orifice diameter. For example, an orifice with $D_i = 210\,\mu$m and $D_o = 200\,\mu$m will have the same *k–factor* as another hole with $D_i = 110\,\mu$m and $D_o = 100\,\mu$m, while the geometrical areas and, as a result of that, the flow characteristics will be different.

In the short length of the nozzle orifices, the fuel pressure is converted in kinetic energy but also lost in viscous dissipation as discussed in section 3.2.1. As shown in Fig. 3.4, at the entrance of the orifice the abrupt change in the direction of the flow causes the detachment of the flow lines at the orifice inlet and the formation of recirculating regions between the orifice walls and the flow lines, the so called *vena contracta* (see Fig. 3.4). This detachment is the main cause of

Parameter	Typical values
D_0	$90 - 250\,\mu\text{m}$
L	$600 - 1000\,\mu\text{m}$
r	$10 - 50\,\mu\text{m}$
L/D_0	$4 - 10$
r/D_0	$0 - 0.3$
D_e/D_0	1-1.25
k–factor	$0 - 2.5$
Orifices No.	$5 - 10$

Table 3.1: Orifice parameters typical values for injectors employed in passenger cars.

Recirculation zone   Vena contracta
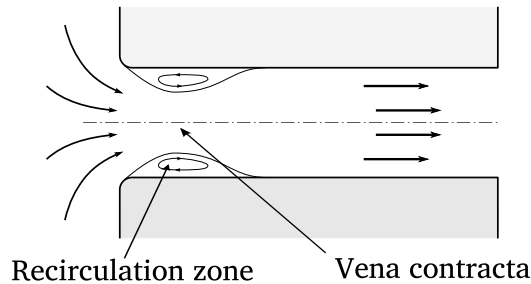
Figure 3.4: The nozzle orifice internal flow. The sketch shows the main features of the fuel flow through the nozzle orifice.

the head losses characterizing the flow through the orifice. The friction of the fuel on the orifice walls causes a further head loss that also contributes to the viscous dissipation of the flow. Nonetheless, care must be taken when attempting to calculate this value, since the discussion presented in section 3.2.1 is valid only for fully developed flows, which means after a certain distance in the pipe. When a fluid is traveling into a pipe, a sudden change of direction can produce local perturbations and it takes time (distance) for the boundary layer to be stabilized again. It is generally considered that it takes several diameters for the flow to be stable and, in the case of a typical nozzle orifice, it would be stable at high L/D (either D_i or D_0). This distance needed to get a stabilized flow also depends on the regime (laminar or turbulent) and would never be long enough in an injector's orifice, as this ratio is generally lower than $L/D \approx 10$. In practice, the length of

the orifice necessary to consider the flow as stable in the laminar regime is also function of the Reynolds number [25]:

$$\frac{L}{D} = 0.03 \, Re \ \text{ if } \ Re < 2300. \tag{3.11}$$

Other values of the coefficient in this equation can be found in the literature going from 0.03 to 0.06 [26]. In this formulation, for example, if $Re = 2000$ the length should be around 60 times the diameter D_i to consider the flow fully developed.

When the regime is turbulent ($Re > 4000$), the mixing intensity induced by the turbulence itself makes the necessary length shorter to get a developed flow. The formulation proposed by White [26] to calculate the length necessary to consider the flow stabilized in turbulent regime is

$$\frac{L}{D} = 4.4 \, Re^{1/6} \ \text{ if } Re > 4000. \tag{3.12}$$

As an example, for Reynolds number commonly used in the orifice of an injector ($10^4 < Re < 10^5$), the length should be between 20 and 30 times the orifice diameter to get a fully developed turbulent flow.

After this rough estimation of the flow characteristics in the orifice, it is clear that either in laminar or in turbulent regime condition the orifices used in Diesel injectors are long enough to completely develop the boundary layer. This means that in none of the cases the flow will be fully developed and, thus, the analysis of the flow in such orifices would require the following things to be taken into account:

- the behavior of the flow will be directly related to the geometry of the entrance of the orifice and will affect the flow characteristics, e.g., thickness of the boundary layer (or separation), local pressure losses, etc. In this way, the velocity profiles and head losses in the orifice will strongly depend on the flow behavior at the entrance;

- since the flow is not completely developed, the limits usually given to determine if the regime is either laminar or turbulent ($Re > 4000$) will not be valid [27]. As a consequence of that, the Reynolds number is not enough to characterize the flow regime and therefore the intensity of the turbulence;

- the fluid-mechanics theories based on fully developed flow cannot be applied in this case: for example, the velocity profiles at the orifice outlet will not be almost constant in the whole section of the orifice exit as it would be if flow were stabilized [28].

The separation of the boundary layer occurring at the orifice entrance causes a reduction in the static pressure in the recirculation: depending on the shape of the orifice and on the flow conditions, the static pressure can go down to the critical vapor pressure of the fluid forming fuel vapor bubbles that might be dragged through the orifice until the exit (cavitation). One of the first studies that commented the apparition of cavitation in the orifice has been presented by Bergwerk [21]. In this work, small transparent orifices have been used to observe the apparition of cavitation under certain conditions. Since then, a lot of studies have been performed to experimentally visualize cavitation with the aim of understanding the physics involved in the phenomenon and to determine its consequences on the spray formation. Suh and Lee [29] studied the effect of the orifice shape on cavitation using a planar transparent nozzle to image directly the flow within the orifice. The images obtained are useful to give a concrete overview of the phenomenon and its effect on the spray formation (see Fig. 3.5).
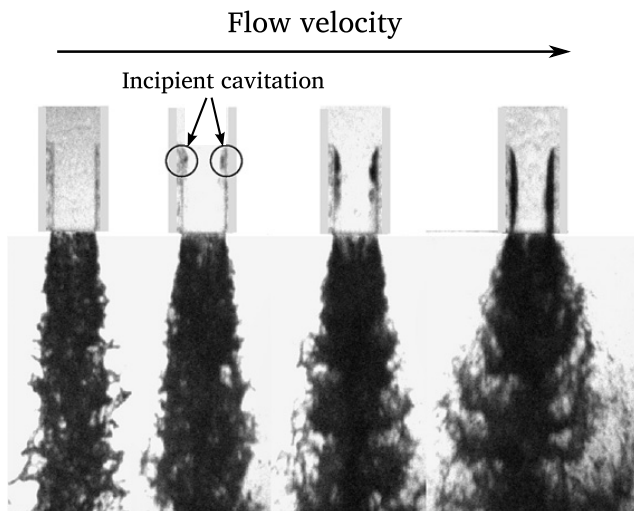
Figure 3.5: Formation of cavitation and effect on the spray formation [29].

Cavitation is a quite common issue in Diesel injector orifices due to the current trend in increasing the injection pressure. Generally, this phenomenon has a negative impact on the injector performances: in fact, the vapor bubbles act like an obstruction in the orifice, reducing the fuel mass flow rate; moreover, the spray formation is different whether the regime is cavitating or not, and the transition from one regime to the other is not easy to determine accurately. Finally, the bubbles formed in the recirculating region may collapse again in liquid fuel, due to the local increase of the static pressure: this process results in local pressure

waves that wear the wall of the orifice causing their deterioration. On the other hand, some recent studies associated the fuel cavitation in the nozzle orifice with the coking process (the formation of carbon derived particles within the nozzle orifice) [30, 31]: the vibrations derived from cavitation are considered one of the main inhibitors of this process.

Whether it is harmful or not, cavitation is generally not desired in fuel injector nozzles. For this reason, the shape of the orifice has been purposely designed to prevent the apparition of cavitation; to do so, convergent orifices and larger entrance radius have been manufactured as a response to the constant increase of the injection pressures. Such a shape also proved to keep the orifice cleaner due to a better internal dragging; despite their effectiveness, they started to be widely used only a few years ago due to the complexity in their manufacturing process [23, 32].

Influence of nozzle geometry on the internal flow

The internal geometry of the nozzle has a fundamental effect on the characteristics of the flow in the orifice. Even if, on one side, the accuracy in the amount of fuel injected is of primary importance, the capability of delivering as much fuel as possible is also fundamental. This section presents a qualitative overview of the relationship between orifice geometrical parameters and internal liquid flow.

Length - Diameter ratio - If there is no cavitation, an increase of the L/D ratio will induce higher losses due to friction against the walls and this will obviously obstruct the flow through the nozzle. Lichtarowitz et al. [33] compared several results obtained by researchers studying the flow under non-cavitating conditions and confirmed that the maximum discharge coefficient obtained at high Reynolds number was decreased as the L/D ratio was increased. On the other hand, the authors also pointed out that an excessive reduction of the L/D ratio ($L/D <$ 2) causes a reduction of the discharge coefficient due to the separation of the flow at the entrance making the effective area smaller. Moreover, the increase in the L/D ratio reduces the possibility of the formation of cavitation. In fact, the higher major head loss due to the increase of L/D brings as a consequence that, for similar discharge pressure and mass flow, the pressure at the orifice entrance is higher, thus leading to a lower probability of reaching the vapor pressure.

Convergence of the orifice - The convergence of the orifice is the relation between both inlet and outlet sectional areas. A convergent orifice has the outlet diameter smaller than the inlet one. In this kind of orifice the acceleration of the flow is not concentrated at the orifice inlet as in a cylindrical orifice, but it is distributed along the orifice length. For this reason, the mean velocity of the flow at

the entrance section will be lower than the outlet mean velocity for such an orifice. Therefore, the orifice convergence induces a higher increment of the static pressure at the orifice entrance leading to several consequences: first, a higher pressure at the entrance delays the apparition of cavitation (cavitation appears when the local absolute pressure is below the fuel vapor pressure p_{vap}). Secondly, a higher pressure in the entrance section means a lower pressure difference with the pressure upstream and thus, a diminution of the minor head loss at the entrance. Finally, the result of these two consequences has a direct effect on the injected mass. If the pressure loss is lower through the orifice, the mass flow rate is higher and, in the same way, the discharge coefficient as well. For these reasons and to better control the injection, almost all the nozzles implemented nowadays in Diesel engines use convergent orifices, some shapes are even able to cancel the possibilities of cavitation for all operating conditions [34, 35].

Entrance radius - The main cause of the head loss at the orifice entrance has been detailed previously as a separation of the boundary layer produced by the high velocity of the fuel combined with a sudden change of the direction of the flow. The introduction of a curvature at the entrance of the orifice helps mitigating the detachment of the boundary layer and the consequent *vena contracta*. Barrero showed that the introduction of a rounding to the edge at the orifice inlet reaches its maximum effect for $r_e/D_i \geq 0.2$: for this geometry, the head loss engendered in this area is considered as negligible [28]. This reduction of the pressure losses leads to higher values of the discharge coefficient but also to a diminution of the possibility of the apparition of cavitation [28]. This can be explained by a higher pressure at the entrance, due to smaller separation of the boundary layer and thus larger section area for higher r_e/D_i ratio.

The work published by Gimeno [36] treats the different aspects of the geometry as well as their influence on the flow at the outlet of the orifice. The reader may be interested in this thesis to find additional information concerning internal flow behavior. The high complexity of the internal flow oriented the researchers to introduce empirical parameters, with the aim of reaching a functional description of the flow.

The mass flow rate and the discharge coefficient

As discussed previously, the flow pattern at the orifice outlet can be either laminar or turbulent (Fig. 3.6).

The turbulence helps the momentum transfer from the axis of the orifice toward the walls, reducing the boundary layer all to the good of a more constant velocity profile. However, when cavitation occurs, the formation of fuel-vapor

Laminar   Turbulent
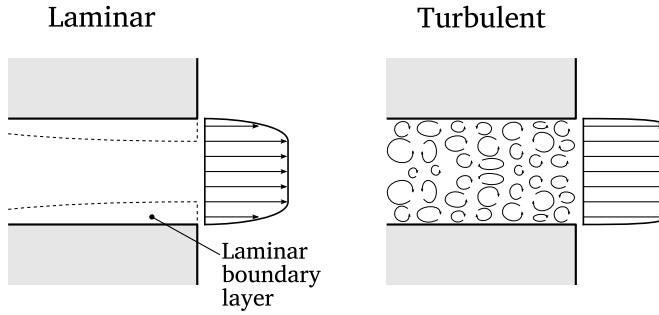
Figure 3.6: Scheme of the possible flow patterns through diese injector nozzles [36].

bubbles affects again the velocity profile increasing its inhomogeneities. Theoretically, the total flow through the orifice $\dot{m}$ can be described as

$$\dot{m} = \int_A \rho (V \cdot n) dA \ , \tag{3.13}$$

where $(V \cdot n)$ is the scalar product between the local velocity V and the normal vector of the differential area dA. Considering the axial component of the velocity u, Eq. (3.13) can be rewritten as

$$\dot{m} = \int_A \rho u dA \ . \tag{3.14}$$

As discussed earlier, it is not possible to know with accuracy the local axial velocity u. However, the limit case can be calculated considering a perfect fluid, which means constant density ($\rho = \rho_f$), $\mu_f = 0$ and consequently no boundary layer (where ρ_f and μ_f are respectively fuel density and dynamic viscosity). In this condition, Eq. (3.14) can be written in a simplified way,

$$\dot{m}_{th} = \rho_f u_{th} A_o \ , \tag{3.15}$$

being u_{th} the theoretical velocity obtained by the Bernoulli's equation considering a negligible variation in elevation ($z_1 = z_2$),

$$u_{th} = \sqrt{\frac{2(p_i - p_a)}{\rho_f}} \ , \tag{3.16}$$

where p_i and p_a are respectively the rail pressure and the back-pressure. Once the limit mass flow rate for a datum condition has been identified, the discharge coefficient C_d can be defined as the ratio between the real mass flow rate and the theoretical mass flow rate,

$$C_d = \frac{\dot{m}}{\dot{m}_{th}} \quad . \tag{3.17}$$

The discharge coefficient is of particular interest in injector nozzle characterization, since it relates measurable variables: in fact, $\dot{m}_{th}$ can be determined, being p_i and p_a known boundary conditions and A_o the geometrical area of the orifice; $\dot{m}$ is the real mass flow rate that, at steady conditions, can be experimentally determined (see 4.3). Finally, by the combination of equations (3.15) and (3.16) the real mass flow rate can be defined as a function of the boundary conditions and the discharge coefficient,

$$\dot{m} = C_d A_o \sqrt{2\rho_f (p_i - p_a)} \quad . \tag{3.18}$$

Eq. (3.18) stresses the dependence between the mass flow rate and the pressure difference at the two ends of the orifice. Moreover, the same equation underlines that the discharge coefficient C_d is an evaluator of the *efficiency* of the nozzle in delivering the fuel. Fig. 3.7 presents the discharge coefficient obtained for nozzles with different characteristics: one has a cylindrical shape and it is inclined to cavitate while the other one is not, due to its conical/convergent shape.
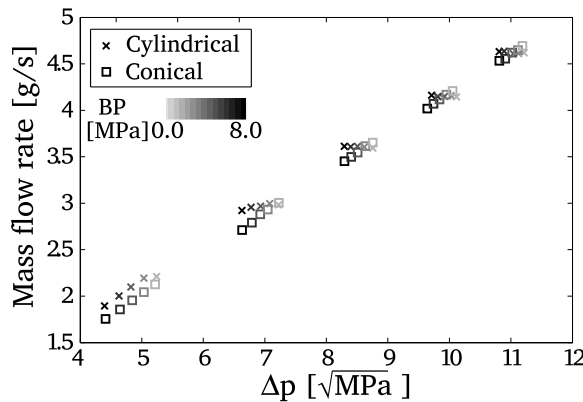
Figure 3.7: Mass flow rate obtained for two different nozzle types (cylindrical and conical) at various injection conditions [36].

When the cavitation is avoided, the mass flow rate dependence on $(p_i - p_b)^{1/2}$ is linear while, in the cylindrical nozzle, this linearity is preserved up to a certain limit, when mass flow rate stops growing. It is important to remark that the cavitation within the orifice constitutes a limitation in the performance of the injection in terms of mass flow rate and therefore in the injector capability of delivering fuel. The same concept is repeated by the plot in Fig. 3.8 presenting the C_d obtained for the same conditions presented in Fig. 3.7: the onset of cavitation causes a drastic decrease in the discharge coefficient.
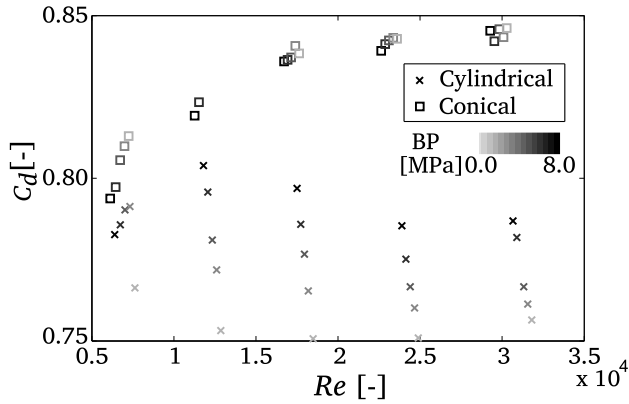
Figure 3.8: Discharge coefficient obtained for two different nozzle types (cylindrical and conical)at various injection conditions [36].

The spray momentum, C_A and C_v

The momentum of a moving object is the product of its mass and its velocity: a Diesel spray is composed by a number of droplets of different size moving at different velocities: in this case, it is preferable to talk of total momentum flux $\dot{M}$ that is defined as

$$\dot{M} = \int_A \rho v (v \cdot n) dA \ . \tag{3.19}$$

Again, for the particular case of the outlet section of the orifice, Eq. (3.19) can be simplified as

$$\dot{M} = \int_A \rho_f u^2 dA \ . \tag{3.20}$$

The momentum coefficient C_M is introduced to compare the theoretical momentum obtained using the Bernoulli velocity of the jet (u_{th}) to the measured momentum $\dot{M}$:

$$C_M = \frac{\rho_f u_{th}^2 A}{\dot{M}} \quad .$$

(3.21)

The momentum flux is a fundamental measurement since it is strictly related to the spray development. Naber and Siebers [37] carried out a comprehensive experimental study linking this parameter with spray penetration at different ambient conditions. Another important contribution has been given by Gimeno [36] performing a vast experimental characterization of the momentum flux of different injectors: in this work he stressed the relationship between momentum flux and spray penetration and included in the analysis the consequences of cavitation. In fact, the spray momentum flux, as the mass flow rate, is a measurable parameter (see Sec. 4.3) and the combination of this measurement with the mass flow rate enables the definition of other important quantities characterizing the fuel flow through the orifice. Payri et al. [38], after discussing the analytical difficulties in the determination of an exact velocity profile at the orifice outlet, proposed the following simplification: as shown by the sketch in Fig. 3.9, the complex problem of the flow at the orifice outlet is translated to a situation where the same mass flow rate is flowing with a flat velocity profile ($v = const$) through an equivalent area. The aforesaid velocity and area are normally called *effective velocity* u_{eff} and *effective area* A_{eff}. In many works [36, 39], this characterization has been performed and it proved to be accurate when correlated to the spray penetration, also in cavitating conditions.
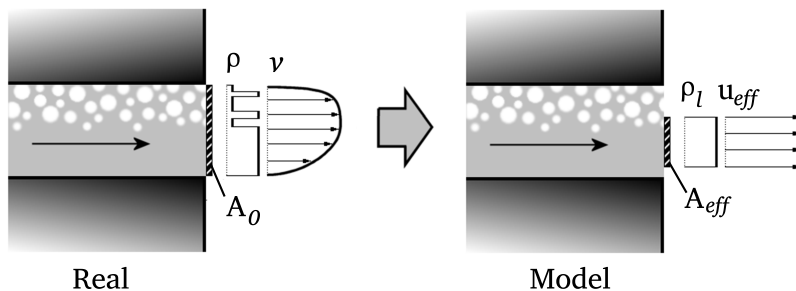
Figure 3.9: Effective area and effective velocity definition.

In this model, the mass flow rate and the momentum flux can be rewritten as

$$\dot{m} = A_{eff}\rho_f u_{eff} \ , \tag{3.22a}$$

$$\dot{M} = A_{eff}\rho_f u_{eff}^2 \ . \tag{3.22b}$$

Being the two terms on the left-hand side of the Eqs. (3.22a) and (3.22b) two measurable values and knowing ρ_f, the effective velocity and area can be determined:

$$u_{eff} = \frac{\dot{M}}{\dot{m}} \ , \tag{3.23a}$$

$$A_{eff} = \frac{\dot{m}^2}{\rho_f \dot{M}} \ . \tag{3.23b}$$

One of the advantages of this methodology is that, for this procedure, it is not necessary to know exactly the real outlet geometry and, at the same time, it gives important information on the flow behavior. As a consequence of that, two additional parameters can be defined, the velocity coefficient C_v and the area coefficient C_A,

$$C_v = \frac{u_{eff}}{u_{th}} \ , \tag{3.24a}$$

$$C_A = \frac{A_{eff}}{A_o} \ . \tag{3.24b}$$

Also in this case, by the measurement of the aforesaid parameters, it is possible to understand the behavior and the performances of the nozzle (see Fig.3.10).

Finally, combining the equations above, a relationship between the coefficients can be found,

$$C_d = \frac{\dot{m}}{\dot{m}_{th}} = \frac{\rho_f u_{eff} A_{eff}}{\rho_f u_{th} A_o} = C_v \ C_A \ . \tag{3.25}$$

3.3   Spray formation

The spray formation is the pillar of the direct injection in diesel engines: the mixing of the fuel with the surrounding air takes place suddenly and in a very
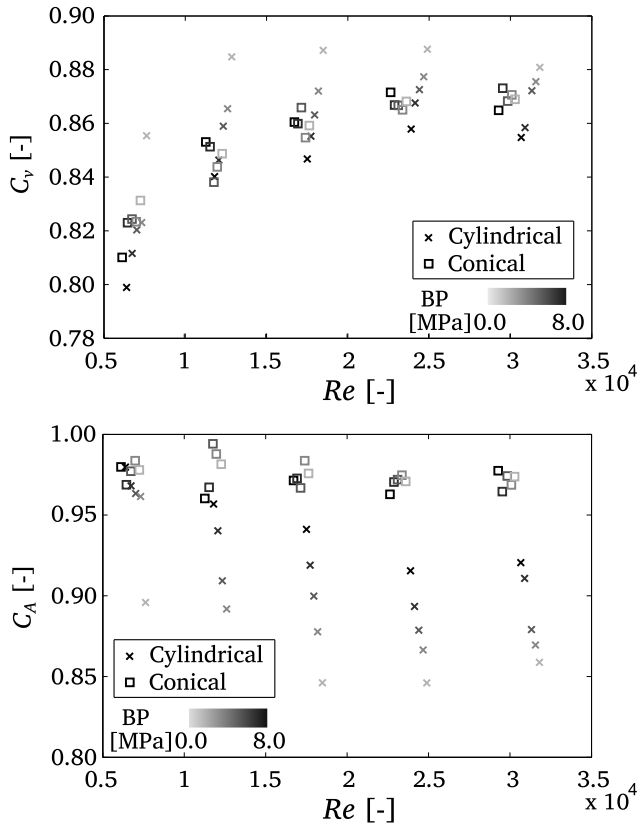
Figure 3.10: Velocity and area coefficients obtained for two different nozzle types (cylindrical and conical) at various injection conditions [36].

small volume. The correct prediction of its development and the understanding of its internal structure are the base for the improvement of the injection strategies. Although the efforts of the engine community in this sense have been strong and constant along the last decades, the atomization process still has many aspects to be understood and its prediction is strongly linked to empirical data.

In this section, an overview of the spray theory will be given, presenting the main conceptual ideas about the Diesel spray and the liquid atomization; moreover, some of the analytical approaches commonly employed for the spray prediction/understanding will be discussed.

The diesel spray is the complex result of the fuel atomization process. It is normally referred as spray the region starting from the orifice outlet in which the fuel is dispersed. The complex structure of the spray is described in the sketch of
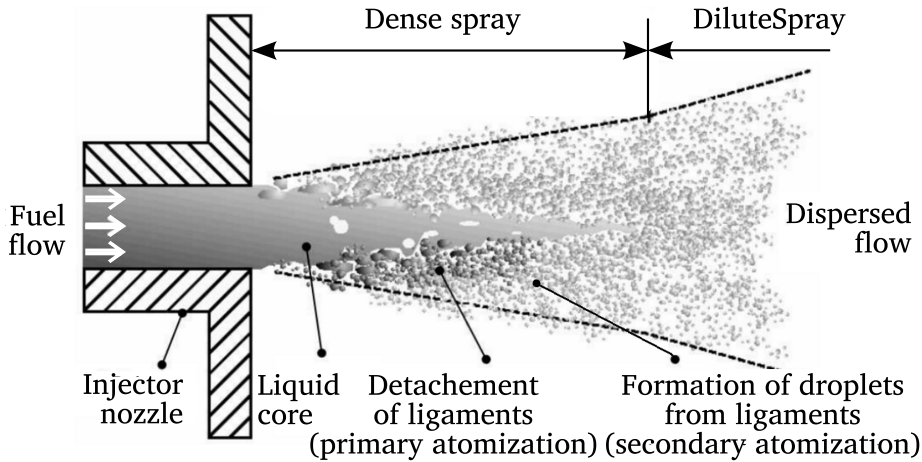
Figure 3.11: Structure of the Diesel spray.

Fig. 3.11: the first millimeters from the orifice outlet are characterized from an intact liquid core. Depending on the injection conditions it can be also observed the so called *intact surface*, a region of the spray (not longer than $1-1.5\,\mathrm{mm}$) where the liquid vein proceeds intact without forming any droplet. The aerodynamic instabilities at the liquid-gas boundaries, combined with the perturbations deriving from the turbulent flow, causes the separation of the liquid core with the formation of relatively large liquid structures called *ligaments*. These structures do not have a specific shape and are characterized by their direct origin from the liquid core: this first process is called primary atomization. Once detached from the liquid core, their relative velocity to the surrounding gas and the related viscous interaction lead the ligaments to a further aerodynamic instability, that breaks them in smaller formations. This process is repeated until the surface tension of the fluid is high enough to compensate the aerodynamic forces: this second part of the process is called secondary atomization.

Based on the optical depth and experimental approach that can be used for its study, the regions of the spray are also classified as *dense* and *dilute* region. The first, also called near field, as the name itself suggests, is the area close to the orifice outlet including the liquid core and ligaments where the spray is optically too dense to be studied using conventional optics: many studies related to this part of the spray have been performed using x-ray techniques [40–42] or ballistic imaging [43]; however the study of this region remains very difficult and the results obtained are sometime controversial [44]. The dilute region is normally referred to as the area where the atomization process is completed: in this

region the optical depth of the spray allows the implementation by means of conventional techniques [45, 46]. It is important to keep in mind that this is not a strict definition but it is rather used for descriptive purposes. Fig. 3.12, presenting the spray dense region obtained via ballistic imaging [43], is a good example to show that a rigid partitioning of the spray regions would be very difficult and unnecessary.
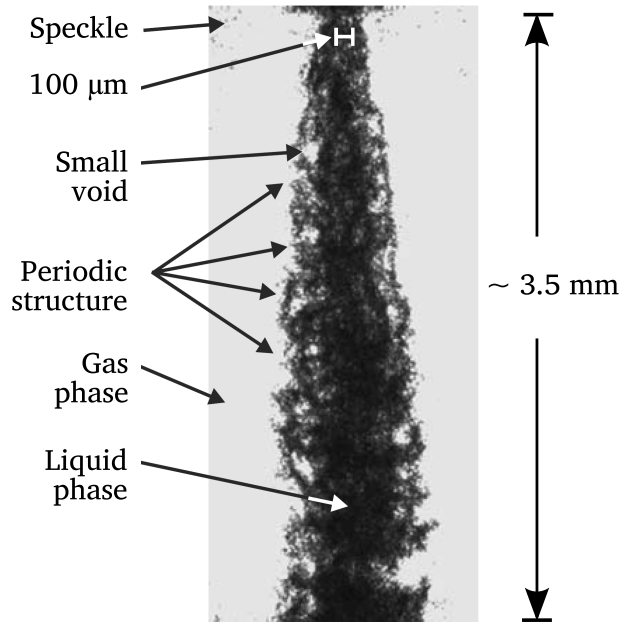
Figure 3.12: Spray image obtained via ballistic imaging [43].

3.3.1   Atomization process

The key of the efficient fuel-air mixing characterizing the Diesel spray is the atomization process taking place right out of the orifice. The disintegration of the liquid vein exiting from the orifice outlet is the result of interactions occurring at a microscopic scale, involving inertial forces, surface instabilities, aerodynamic interactions and surface tension. The main physical processes taking part in the fuel atomization are:

- the liquid surface tension: the resulting force causes the liquid vein to remain compact or to form droplets;

- surface instabilities: passing from forced- to free-flow, the liquid vein is in an unstable condition. This means that the surface tension resulting force is in equilibrium only if the cylindrical shape of the liquid vein is maintained. A minimum perturbation is amplified and causes the initial shape to disappear;
- the turbulence within the orifice: depending on the flow regime within the orifice the fuel may have a different level of radial velocities. The resulting inertial forces tend to spread the liquid in the chamber;
- aerodynamic interaction: the relative movement between the liquid and the surrounding gas causes friction forces that, among other things, are strongly dependent on the shape of the liquid vein.

It is important to realize that different forces control the breakup of jets from cylindrical orifices and their relative weight changes depending on the conditions. As a consequence of that, different regimes can be identified. For example, the aerodynamic forces will have a more substantial effect at high flow velocities. The atomization regime characterizing the Diesel spray has therefore to be intended as a particular case of breakup regime. The jet outlet velocity becomes a convenient quantity to introduce the different regimes, if all the other operating conditions are kept constant.
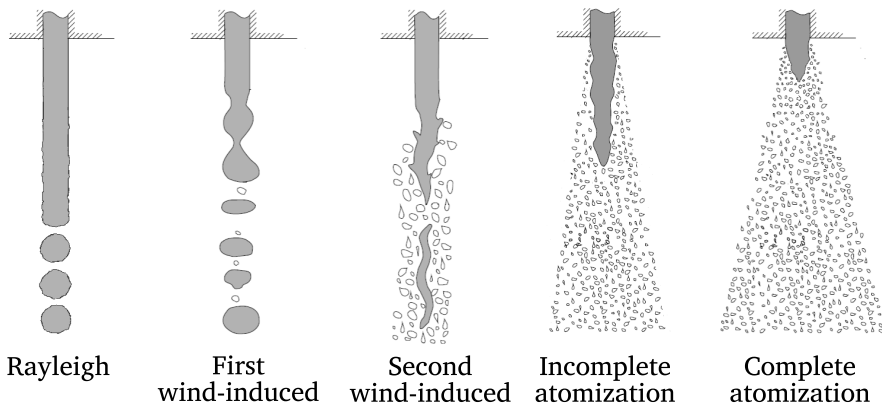
Figure 3.13: Schematic representation of the different atomization regimes [47].

Following the work presented by Reitz [47], the breakup regimes can be classified as follows:

- Rayleigh regime. This regime is observed at the lowest jet velocities. In this case the perturbations at the surface of the jet cause small deformations on the liquid surface. The surface tension amplifies these deformation until the liquid vein is separated in droplets, whose sizes are uniform and similar to the outlet orifice.

- First wind-induced regime. The effect of the first perturbation is amplified by the relative velocities between the jet and the surrounding ambient. In this way, the friction forces effect plays the same role of the surface tension and ease the droplets formation. In this regime the effect of the aerodynamic forces can be observed also in helical oscillation of the jet around its symmetry axis. In these first two regimes the droplets are pinched off from the end of the jet and their size is comparable to that of the orifice diameter.

- Second wind-induced regime. Increasing again the jet velocity, the initial perturbations are amplified by the aerodynamic forces and grow exponentially with time: this growth results in the formation of droplets of a size comparable to the wavelength of the initial perturbations. The formation of the droplet is, in this regime, closer to the orifice but still a certain distance is needed for the droplets to be formed.

- Atomization regime. The initial perturbations, combined with the aerodynamic forces, cause the droplets to form in the immediate proximity of the orifice and their size is, as in the second wind-induced regime, much smaller than the orifice diameter. In this case, the intact surface length is zero, which means that the surface is broken right at the orifice outlet. However, in the atomization regime the intact core can still be present. For this reason two atomization regimes are commonly indicated: incomplete- and complete atomization, whereas the intact core can be observed or not.

Grant and Middleman characterized the breakup regimes basing on the measured intact core length [48]. They noticed that the predominance of one force or the other is reflected on the behavior of this quantity (see Fig. 3.14). In the Rayleigh regime, after the first region of dripping, the intact core length increases gradually, since the jet velocity goes along with the gravitational forces and helps the liquid vein to extend farther from the outlet. Gradually the aerodynamic forces gain importance contrasting the aforesaid effect: when these two effects are balanced the intact core length reaches its maximum and this maximum is indicated to define the onset of the first-wind induced breakup. Therefore, the intact core length decreases until a local minimum is reached: at this point the droplets formed are strongly reduced in size, since they are a direct consequence

of the initial perturbation, and therefore more disintegration is needed to reach the jet core. Finally, this effect is balanced again by the increasing aerodynamic forces, causing a final reduction of the intact core length. The last part of the curve in Fig. 3.14-right is dashed because above a certain value of u the intact core length becomes difficult to measure especially at Diesel spray conditions.
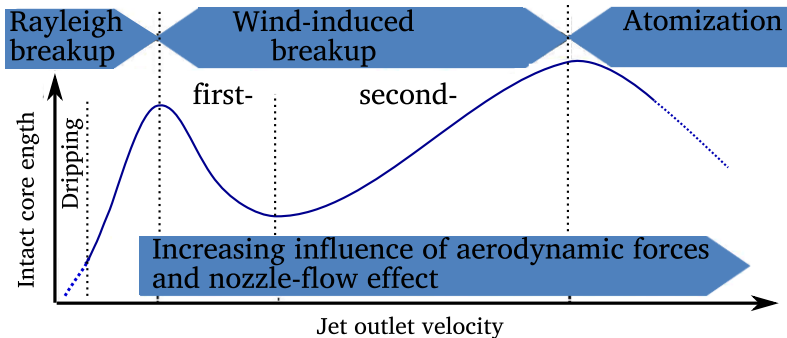
Figure 3.14: Qualitative relationship between velocity at the orifice outlet and intact core length [48, 49].

Up to this moment the regime classification has been presented referring only to the jet velocity at the orifice exit u_f. In the work presented by Reitz and Bracco [50], this classification is generalized starting from the linear stability analysis and introducing in the discussion dimensionless parameters. Thanks to their result it is possible to predict the break up regimes of atmospheric jet as well as fuel jets injected in a high density atmosphere. In the following paragraphs the dimensional analysis at the basis of their classification and the main outcome of their work are presented.

Dimensional analysis of the atomization process

Based on the information available in the literature, the parameters mainly affecting the atomization process can be pointed out:

- ambient density ρ_f [kg/m³]
- fuel density ρ_a [kg/m³]
- jet velocity (or relative velocity between fuel and air) u_{eff} [m/s]
- effective orifice diameter D_{eff} [m]
- fuel viscosity μ_f [kg/ms]
- surface tension σ [kg/m²]

As listed above, there are six parameters affecting the atomization process, and they contain three fundamental quantities (length, mass and time). As a consequence of that, following the π theorem of Buckingham [51], the influence of all the parameters above can be simplified using three dimensionless group of parameters. In general, the dimensionless parameters most employed in the literature are the density ratio ρ_a/ρ_f, the Reynold's number Re and one of the three following:

$$\text{Ohnesorge number: } Oh = \frac{\mu_f}{\sqrt{\rho_f \sigma D_{eff}}} \quad , \tag{3.26}$$

$$\text{Webber number: } We = \frac{\rho U^2 D_{eff}}{\sqrt{\rho_f \sigma D_{eff}}} \quad , \tag{3.27}$$

$$\text{Taylor number: } Ta = \frac{\rho_f}{\rho_a} \left(\frac{Re}{We} \right)^2 \quad . \tag{3.28}$$

Reitz and Bracco [50] classified the breakup regimes basing on the Ohnesorge number. This dimensionless number represents the ratio between the viscous forces and the liquid inertia combined with the surface tension.
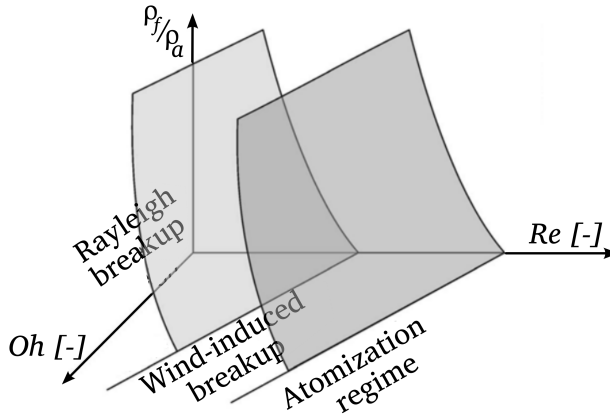
Figure 3.15: Qualitative separation of the atomization number using the three dimensionless parameters required by the Π theorem [50].

From the qualitative representation presented in Fig. 3.15, it is clear that the density ratio affects the atomization process only at its low values: this means that when the air density is low with respect to ρ_f this parameter has no effect on the atomization. For this reason it is usual to see this plot for a surface at iso-ρ_f/ρ_a,

as presented in Fig. 3.16: this representation presents the atomization regimes separation for high values of the density ratio.
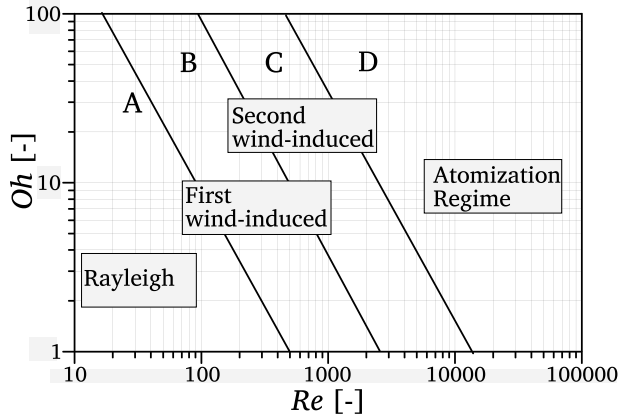
Figure 3.16: Separation of the atomization regimes for high values of the ratio ρ_f/ρ_a obtained by Fig.3.15 [50]

In Tab. 3.2, the equation proposed by Reitz [47] for the transition to the complete atomization regime is presented, where We_L and We_{amb} are respectively the Webber number for the liquid and the ambient. In this expression it has to be introduced the jet spreading angle: by means of this parameters the impact of the orifice geometry on the nozzle-flow is taken into account since they have an important impact especially for flow at high We [50]. In the literature other quantitative criteria can be found to separate the regimes, and they are listed in the Tab. 3.2 for reference.

The droplets formed by the liquid jet breakup (*primary breakup*) are still moving at high speed in a gaseous ambient: also in this case, the fate of the droplets will be decided by the same balance of forces described for the jet breakup, causing the so called *secondary breakup*. Due to the difference in shape (droplet instead of cylinder), the modality in which this process occurs is different. However, an accurate description of the secondary breakup would exceed the aim of this thesis. The reader who is interested in this information is invited to read the related works proposed in the bibliography [55–57].

3.3.2 Transient spray and 1-D spray approximation

The introduction to the diesel spray presented in the previous sections shows that, even under non-vaporizing conditions, in which the problem is undoubtedly a

Regime	Expression	Author
A-B	$We_g = 0.4$	Ranz [52]
	$We_g = 1.2 + 3.41Oh^{0.9}$	Sterling and Sleicher [53]
B-C	$We_g = 13$	Ranz [52]
C-D	$We_g = 40.3$	Meisse [54]
	$\dfrac{\rho_{amb}}{\rho_f} = \dfrac{\sqrt{A} - 1.15}{744} f(Ta)^{-2}$	Reitz [47]
	$f(Ta) = \frac{\sqrt{3}}{6}\left[1 - exp(-10Ta)\right]$	Reitz [47]

Table 3.2: Definition of the transition between atomization regimes, given by different authors.

two-phase flow, the droplets reach in a very short distance a dynamic equilibrium with the surrounding gas. Many works found in the literature demonstrated that this distance is so short that the whole spray can be analyzed from the point of view of the gas jet theory [58–61]. In this perspective the breakup process can be neglected and the droplets formed are so small that the heat transfer problem is reduced to a mixing issue. Consequently, non-reacting vaporizing Diesel sprays fit adequately in the *locally-homogeneous flow* description [62], which makes it possible to treat an *a priori* complicated two-phase problem from the point of view of single-phase flows.

In Fig. 3.17 the macroscopic features of the transient spray penetrating in the combustion chamber are shown: when the needle opens the spray starts penetrating in the chamber with a certain spreading angle. In a first stage the liquid and the vapor phase boundaries are very similar: the penetration is the same and the evaporation on the sides of the spray is negligible; when penetrating farther into the chamber, more air is entrained and the positive enthalpy balance causes the complete evaporation of the droplets at the sides of the spray: when the evaporation reaches the spray center line, the liquid phase stops penetrating and stabilizes around a certain value called *liquid length*; on the other hand, the vapor phase of the spray continues penetrating into the chamber [63, 64].

Among the conceptual models used to describe and predict the spray behavior, one of the most successful for its simplicity and its reliability is the so called
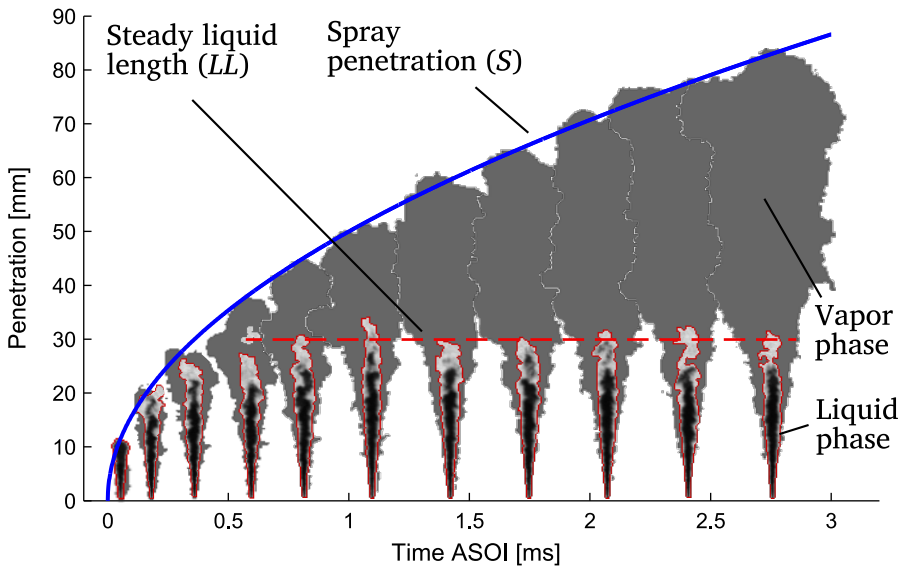
Figure 3.17: Liquid and vapor phase of the Diesel spray penetrating in a quiescent and non-reacting environment.

mixing limited model. The mixing limited model is a *1D* problem and can normally be applied to gas jet as well as to well atomized diesel spray. It presents advantages against the *0D* model, since it contains enough physics to have good accuracy in solving the problem, but also against CFD models, which, solving the conservation equations for small cells, tend often to miss the relationship between the macroscopic features of the spray and the boundary conditions.

Even though these kinds of models cannot be considered completely predictive, the interpretation they give to the spray allows to have a correct qualitative understanding of the effect of the boundary conditions on the spray development. Therefore, the theory underlying these models will be presented for two reasons: first, because it enable to explain in an analytical way the basis of the Diesel spray physics; second, because it is a valuable tool which will be employed for the interpretation and analysis of the experimental results.

This problem is largely analyzed in the literature. In these case, the approach chosen is the one presented by Pastor et al. [64]; this model's originality lays in the formulation of the conservation equations, which, as explained in Garcia's Ph.D thesis [65] solves the on-axis variables by using cross-sectional integrals and its transient formulation makes it possible to use the model for both constant and

also variable injection rate shapes; however, conceptually it is very similar to many other models that can be found in the literature [63, 66, 67].

In the mixing limited approach the fuel sprays are injected through a nozzle hole in a quiescent environment, where swirl or any other type of engine-induced air movement are not considered. The ambient volume is large enough, so that the spray evolution does not modify air conditions far away from the nozzle and there is no interaction with the walls of the chamber.
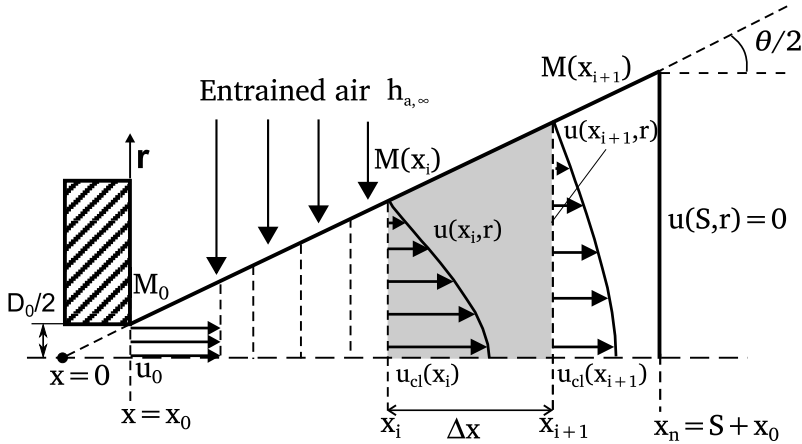
Figure 3.18: Schematic of the approach followed by the mixing limited model [64, 68].

Fig. 3.18 shows a sketch of the basic configuration of this type of problem: the fuel stream is assumed to have an uniform velocity profile at the nozzle exit; the ambient air enters in the spray from the side of the spray and its velocity has no component in the x-direction. The fuel flow exchanges momentum with the entrained air and sets it into movement while the spray increases in width with the axial distance. The spray cone angle (or spreading angle) θ defines this radial growth and it is an input to the model. Together with the nozzle diameter D_0, the spray angle defines the virtual origin of the spray (x_0), such that the following expression can be written:

$$x = x_0 = \frac{D_0}{2} \cdot \frac{1}{tan(\theta/2)} \quad . \tag{3.29}$$

However, in the context in which this model is normally used, the value of x_0 is negligible for the degree of precision requested. Due to the transient nature of

the general problem, the spray domain is axially divided into a number of cells with a certain thickness Δ_x spanning the whole spray cross-section. Each cell is limited by the inlet and the outlet sections (i and $i+1$, respectively) so that $x_{i+1} = x_i + \Delta_x$ (Fig. 3.18). At every time instant, the spray size is defined in terms of the tip penetration S, which is the farthest cell from the nozzle where the inlet velocity is different from zero and the outlet velocity is zero.

The following hypothesis are used to solve the model at each time instant t_i:

- the system is symmetric on the spray axis (e.g., no air swirl);

- a fully-developed turbulent flow is assumed, which means that self-similar radial profiles can be defined for the conserved variables (e.g., the ratio of any conserved variable divided by the center-line value does not depend on the axial coordinate). This is probably one of the major assumptions in the model, which is usually accepted for steady gas-jet or spray flows [69, 70]. Moreover, this hypothesis requires the flow to overlook the initial uniform radial profile: this incoherence in the hypothesis is solved fixing a distance at which the velocity profile is switched from one case to the other. This distance is generally physically interpreted as the *intact length* discussed earlier; in this model the profile is described by the following equation:

$$\frac{u(x,r)}{u_{cl}(x)} = \left[\frac{f(x,r)}{f_{cl}(x)}\right]^{1/Sc} = \left[\frac{h(x,r) - h_{a,\infty}}{h_{cl}(x) - h_{a,\infty}}\right]^{1/Pr} = exp\left[-k\left(\frac{r}{x}\right)^2\right] , \tag{3.30}$$

where u_{cl}, f_{cl} and $h_{cl} - h_{a,\infty}$ are the related quantities on the spray center line, k is a constant and Sc and Pr are the turbulent Schmidt and Prandtl numbers;

- locally-homogeneous flow is assumed [62], i.e., there exists a local equilibrium both in thermal and velocity conditions: this is one of the main consequences of the *mixing limited* assumption;

- pressure is assumed to be constant all over the spray and thus compressibility effects are neglected;

- local density is calculated under the assumption of ideal mixing,

$$\rho(x,r) = \frac{1}{\sum_i \left(\frac{Y_i(x,r)}{\rho_i(x,r)}\right)} , \tag{3.31}$$

where Y_i is the mass fraction of the mixture component i and ρ_i is the density for the pure component i at the mixture local temperature $T(x, r)$ and pressure p_a.

For each cell, the differential conservation equations of axial momentum, fuel mass and energy are

$$\dot{M}(x_i, t) - \dot{M}(x_{i+1}, t) = \frac{d}{dt}\left[\int\!\!\!\int_V \rho(x, r, t) \cdot u(x, r, t) \cdot dV\right] , \qquad (3.32a)$$

$$\dot{m}_f(x_i, t) - \dot{m}_f(x_{i+1}, t) = \frac{d}{dt}\left[\int\!\!\!\int_V \rho(x, r, t) \cdot f(x, r, t) \cdot dV\right] , \qquad (3.32b)$$

$$H(x_i, t) - H(x_{i+1}, t) = \frac{d}{dt}\left[\int\!\!\!\int_V \rho(x, r, t) \cdot \left(h(x, r, t) - h_{a,\infty}\right) \cdot dV\right]. \qquad (3.32c)$$

On the left hand-side of the previous equations there are expressions corresponding to the conserved property fluxes across the cell inlet (x_i) and outlet (x_{i+1}) surfaces. $\dot{M}$, $\dot{m}_f$ and H represents the axial momentum (related to u), fuel mass (related to f) and enthalpy (related to $h - h_{a,1}$) fluxes, respectively. On the right hand-side of the equations the terms representing the temporal variation of the volume integral to the whole cell appear, which quantifies the accumulation/de-accumulation process of the aforesaid quantities within a cell. The sub-indexes (i, $i + 1$) correspond to the spatial discretized coordinates ($x_{i+1} = x_i + \Delta x$), while super-indexes ($j, j + 1$) refer to the time variable ($t_{j+1} = t_j + \Delta t$). An implicit time discretization is used, so that temporal balances between t_j and t_{j+1} are expressed as

$$M_i^{j+1} - M_{i+1}^{j+1} = \frac{\int (\rho(x, r, t^{j+1})u(x, r, t^{j+1}) - \rho(x, r, t^j)u(x, r, t^j))dV}{\Delta t}, \qquad (3.33a)$$

$$m_{f,i}^{j+1} - m_{f,i+1}^{j+1} = \frac{\int (\rho(x, r, t^{j+1})f(x, r, t^{j+1}) - \rho(x, r, t^j)f(x, r, t^j))dV}{\Delta t}, \qquad (3.33b)$$

$$H_i^{j+1} - H_{i+1}^{j+1} = \frac{\int (\rho(x, r, t^{j+1})(h(x, r, t^{j+1}) - h_{a,\infty}) - \rho(x, r, t^j)(h(x, r, t^j) - h_{a,\infty}))dV}{\Delta t} .$$
$$(3.33c)$$

Finally, some of the parameters appearing in the equations can be measured experimentally, and therefore used as input to solve the model:

- momentum flux $\dot{M}$, mass flow rate $\dot{m}_f$ and enthalpy H at the orifice outlet; all these parameters can be obtained theoretically by correlations, but especially the first two of them, for a better accuracy, are preferred to be measured experimentally;

- the spray cone angle θ; due to the difficulty in measuring it directly and the limited accuracy of the available correlations, this parameter can be used as the only fitting parameter in the model;

- in order to calculate the other unknowns depending on the local density their relationship has to be made explicit. Formally, it is expressed as a function of the type $\rho = \rho(f)$, which falls into the category of the so-called state relationships. The function is known *a priori* and it relates the composition and thermodynamic conditions of pure fuel (conditions at the nozzle exit, sub-scripted as $f, 0$) and pure air (conditions sub-scripted as a, ∞), which may be constant (e.g. for a steady problem) or variable along time (e.g. for an internal combustion engine).

The reader can find further details on the model and on the solving procedure in the works presented by Pastor et al. [64] and Desantes et al. [68].

The model, following this relatively simple hypothesis, enables to investigate the details of the local fuel mixing and velocity within the spray. However, it is important to underline that many authors observed that in the *near region* the prediction of the models are not completely accurate, particularly at low ambient densities ($\rho_a \leq 20\,\mathrm{kg/m^3}$) [37, 64, 71]: Pastor et al. [64], like Hiroyasu et al. [71], explained that in this region the mixing limited hypothesis is not completely respected, due to the relatively big size of the droplets/ligaments and their high velocity. Differently, Naber and Siebers [37] claim that this behavior is due to the fact that in the first part of the injection the spray development is driven by the injected fuel, while the second is driven by the entrained air. A different interpretation has been given by Correas [72]: in his work he investigated the mass flow rate at the needle opening and observed that the linear behavior of the penetration can be related to the increasing mass flow rate. In this sense, Pickett et al., in a recent work [73], investigated the relationship between mass flow rate and spray penetration at start of the injection. In this works the authors highlighted on the one hand the high uncertainties linked to the mass flow rate measurements at this stage of the injection are reflected in a rough prediction of the penetration curve. Moreover, they observed that the shape of the spray cannot be described only by a single spray cone angle, and they introduced the definition of the *near field*-spreading angle and far-field spreading angle. Combining modifications to the mass-flow rate ramp-up with the introduction of the two-steps spreading angle, they have been able to obtain a better prediction of the spray penetration curve.

3.4   Spray characterization

Until now, the spray has been described from a physical point of view, trying to underline the processes behind the atomization and spray formation. In this section, a brief summary of the spray measurements performed and their characterization will be given.

Conventionally, the spray characterization is divided into two groups: macroscopic and microscopic, depending on the scale of the parameter observed. The macroscopic characterization investigates the global shape of the spray, while the microscopic characterization is focused on what it is "contained" within it.

3.4.1   Macroscopic characterization

The macroscopic characterization of the spray aims at understanding the global interaction of the spray with the surrounding air. The main parameters measured are:

- penetration;
- spreading angle;
- entrained air volume;
- liquid length;
- intact length.

Spray penetration
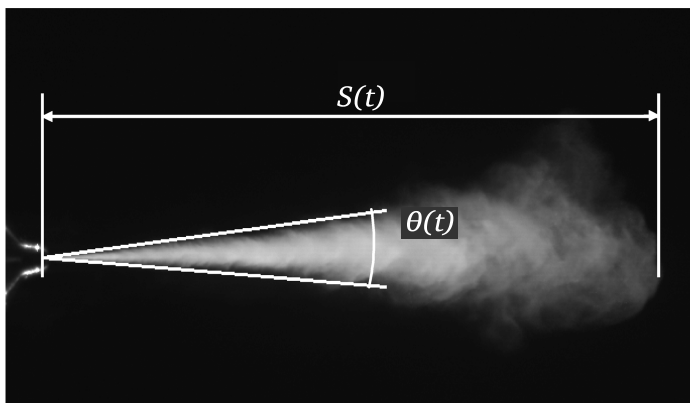
Figure 3.19: Spray penetration and spreading angle.

The definition of spray penetration (normally indicated with S) and spreading angle (θ) are indicated in Fig. 3.19. The penetration refers to the distance traveled by the spray tip into the combustion (or test) chamber, while the spreading angle is the opening angle included between the two sides of the spray. Even if conceptually it is very easy to understand the meaning of these two parameters, their definition is not always easy and, especially in the case of the spreading angle, small variations in the definition can cause substantial bias in the results. These parameters are widely studied due to their fundamental importance for the understanding of the spray dynamics and because, from the experimental point of view, their measurements are robust and relatively easy. From the wide number of studies that can be found in the literature, many correlation have been proposed to link the spray penetration and the boundary conditions such as the pressure drop through the orifice, the ambient density, the orifice diameter, etc.

Already in 1972, Hay and Jones [74] made a review of the correlations for spray penetration available in the literature at the time and highlighted as the best correlations the ones presented by Dent [75] and Wakuri et al. [76]. Apart from the constant applied to the relationship and other minor details, all the equations presented also in more recent works [17, 37, 60, 71, 72] are in the form

$$S \propto \rho_a^{-1/4} \Delta p^{1/4} an(\theta/2)^{1/2} D_0^{1/2} t^{1/2} \ . \tag{3.34}$$

Or, expressing the penetration as a function of the spray momentum $\dot{M}$ as

$$S \propto \rho_a^{-1/4} \dot{M}^{1/4} tan(\theta/2)^{-1/2} t^{1/2} \ . \tag{3.35}$$

The exponent of each parameter is obtained by the simple application of the dimensional analysis. Many authors also included the effect of the spreading angle [37, 72, 76]: Wakuri [76] was the first to include this parameter with proportionality $S \propto tan(\theta/2)^{-1/2}$; Dent [75], on the other hand, starting from the work presented by Forstall and Shapiro [77], included the effect of ambient temperature or, more precisely, the difference between the ambient and the nozzle tip temperature, adding the proportionality $S \propto (T_{nozz}/T_a)^{1/4}$. As mentioned earlier, the spray penetration in the first millimeters shows a different proportionality with the time. For this reason Hiroyasu and Arai [71] presented a penetration law split into two parts: one for transient or initial stage and a second for the *developed* spray, that has similar characteristics to the correlation seen in the previous

paragraph. The main characteristic of the first transient part is the linear proportionality between time and penetration. The two stages of the equation are:

$$S(t) = \begin{cases} 0.39\sqrt{\frac{2\Delta p}{\rho_f}}t & \text{if } t < t_b \;, \\ 2.95\rho_a^{-1/4}\Delta p^{1/4}D_0^{1/2}t^{1/2} & \text{if } t \geq t_b \;, \end{cases} \tag{3.36}$$

where t_b represents the time needed to reach the penetration at which the break up is completed, and it is defined as

$$t_b = 28.65\frac{\rho_f D_0}{(\rho_a \Delta p)^1/2} \;. \tag{3.37}$$

More recently, Naber and Siebers [37] developed a penetration law based on their experimental measurements and, as Hiroyasu and Arai, indicated two different behavior of the spray penetration. Moreover, they inserted in their penetration other flow parameters related to the internal flow (C_v and C_a) and, as Wakuri et al. [76], they included in the equation the spray spreading angle θ,

$$S(t) = \begin{cases} C_v\sqrt{\frac{2\Delta p}{\rho_f}}t & \text{if } t < t_b \;, \\ \frac{C_v^{1/2}(2C_a)^{1/4}}{a\tan\theta/2}\rho_a^{-1/4}\Delta p^{1/4}D_0^{1/2}t^{1/2} & \text{if } t \geq t_b \;. \end{cases} \tag{3.38}$$

In this case t_b is defined differently,

$$t_b = \frac{(2C_a)^{1/2}}{C_v a \cdot tan(\theta/2)}\frac{\rho_f D_0}{(\rho_{amb}\Delta p)^{1/2}} \;. \tag{3.39}$$

In the equation proposed by Naber and Siebers [37] the constant a is obtained by fitting the equations proposed to the their experimental data: the value obtained is $a = 0.66$.

Other authors obtained empirical correlation by the statistical analysis of the experimental data. For reference, the results obtained by Payri et al. by spray penetration measurement at isothermal conditions are reported [78]:

$$S \propto \rho_a^{-0.268}\dot{M}^{0.254}tan(\theta/2)^{-0.5}t^{0.513} \;. \tag{3.40}$$

The equation obtained by Payri et al. [78] remarks a good agreement between dimensional analysis and experimental measurements.

Spray spreading angle

The spreading angle θ is usually defined as the angle included by the lines fitting the two sides of the spray (Fig. 3.19). The spray spreading angle θ is a fundamental parameter driving the entrainment of air in the spray and determining the fuel evaporation and combustion process. After the first transient at the start of the injection, this angle stabilizes at a certain value: different correlations to predict the behavior of the spreading angle can be found in the literature.

One of the first characterization of the spreading angle has been presented by Ranz [52], relating $tan(\theta/2)$ with the boundary conditions,

$$tan\frac{\theta}{2} = \frac{4\pi}{A}\sqrt{\frac{\rho_f}{\rho_a}}F_t\left(\frac{\rho_a}{\rho_f}\frac{\sigma^2}{\mu_f^2 u_0^2}\right) \ ,$$

(3.41)

where F_t represents an analytical expression that, in the case of typical Diesel injection conditions, it reaches its limit value $F_t = 0.288$. However, this expression contains a constant (A) that needs to be tuned for the specific geometry of the orifice. Reitz and Bracco [79] carried out an extensive experimental study including several variation in the internal geometry. They concluded that the equation presented by Ranz predicts the behavior of the spreading angle with good accuracy and they used their database to introduce an analytical expression for the constant A,

$$A = 3 + \frac{L/D_0}{3.6} \ .$$

(3.42)

However, the definition given for A does not take into account neither the conicity of the orifice nor the curvature radius of the orifice inlet. Therefore, it gives good predictions for geometries that are similar to the one employed by Ranz [79] but loses its effectiveness when the geometry is changed more radically.

Hiroyasu and Arai [71] went forward performing a set of tests with parametric variation to the shape of the nozzle upstream of the orifice. Using a series of mini-sac injectors, they assessed the impact of a variation in the size of the sac. Basing on their experimental results, they defined the value of the spreading angle as

$$\theta = 83.5\left(\frac{L}{D_0}\right)^{0.022}\left(\frac{D_0}{D_s}\right)^{0.15}\left(\frac{\rho_a}{\rho_f}\right)^{0.26} \ ,$$

(3.43)

where D_s is the sac diameter. Other experimental studies proposed similar results, indicating the density ratio as the driving factor for the spreading angle [37, 80,

81]. In all these studies the injection pressure and the fuel viscosity have been found to have only a negligible effect. Kampman et al. [82], using different *VCO*-type nozzles, investigated the effect of the hydro-grinding level at the orifice inlet: the hydro-grinding is the process employed to increase the curvature radius at the orifice inlet. With their work, they proved that the higher the degree of hydro-grinding, the lower the spreading angle. Moreover, decreasing the hydro-grinding, a higher statistic dispersion of the measurements was observed. Recent studies related the cavitation phenomenon taking place within the orifice to an increment in the spreading angle: in this sense, Salvador [83] carried out an experiment comparing the spreading angle obtained with two different nozzles. The orifices of the two nozzles have similar outlet diameter but a different shape: one was conical and the other cylindrical. The results obtained showed that at low injection pressure, when none of the nozzles was cavitating, the spreading angle measured was the same. On the other hand, at high injection pressure, the spreading angle formed by the cylindrical nozzle was higher. The author concluded that the increment in the spreading angle observed was linked to the cavitation phenomenon, which was occurring only in the cylindrical nozzle. This effect has been confirmed by the investigations presented by Sou et al. [84] and Payri et al. [85], imaging simultaneously the flow within the orifice and the spray using transparent nozzles and microscopic imaging setup.

Observing the results found in the literature, the injection pressure have some effect on the spreading angle, but a general rule cannot be found since, probably, this effect is the result of many parameters all combined together, such as the nozzle seat type, the orifice inlet radius etc.

In general, the investigations carried out on the spreading angle, found an agreement on the main effects that determine the parameter: fuel/ambient density ratio, injector geometry and cavitation have been extensively proven to have an impact on the spreading angle. However, the quantification of these effect is still an open issue due, first of all, to the complexity of the phenomenon itself, that is the result of the combination of turbulence and aerodynamic instabilities; moreover, this specific measurement is particularly sensitive to many aspects of the experiments: the experimental technique employed, the details of the optical arrangement and the methodology employed for the image processing [86] affect the sensitivity of the experimental system and, therefore, the spray boundaries detected. Nonetheless, the definition of the spreading angle that is given is not always consistent: Naber and Siebers [37], for example, presented a definition of spreading angle based on the spray area calculation, while Pastor et al. [87] based their definition on the fitting of two lines on the spray boundary.

Liquid length

At evaporative conditions, the air entrained by the spray produces the progressive evaporation of the fuel: as a consequence of that, the spray liquid phase initially penetrates until it reaches a steady value (c.f. Fig. 3.17).

The liquid phase penetration or liquid length (*LL*) is a measurement commonly performed to characterize the mixing process of the Diesel spray [80, 88]; a simple definition of the liquid length can be given as the distance that the injected fuel has to penetrate in the chamber until its complete evaporation. In several studies on liquid phase penetration available in the literature [80, 88, 89] the dependence of the liquid length upon different parameters such as ambient temperature, ambient density, injection pressure, nozzle diameter and fuel type can be found. The behavior of the liquid length is generally well described using the *1D* mixing limited models, like the one from Pastor et al. [64] or by empirical correlations obtained by different authors in the literature [39, 90, 91]. For reference, the relationship obtained by dimensional analysis and implicit to the *1D* by Pastor et al. [64] is presented:

$$LL = \frac{K_p \cdot C_A \cdot D_0}{C_{mv} \cdot tan\left(\frac{\theta}{2}\right)} \, , \tag{3.44}$$

where K_p is a constant depending on ambient conditions, C_A is the area coefficient, D_0 is the orifice diameter, C_{mv} is a coefficient depending on the fuel and ambient properties, θ the spreading angle.

Intact length

The region right at the exit of the orifice is characterized by a very dense region and this region is characterized by an intact liquid core extending up to a certain distance. Even if this feature is listed in the macroscopic characteristics (it is undoubtedly a global feature of the spray) the length of the intact core can be less than 1 mm. This characteristic of the spray has been discussed from decades [47, 92]. Chehroudi et al. studied water sprays and they performed tests to characterize this quantity basing on the electrical conductivity of the intact core [93]. The qualitative relationship between the intact core length and the fuel velocity at the orifice outlet is represented in Fig. 3.14 [49].

The correct evaluation of this length is essential to understand the fundamentals of the spray break up: on one side, many researchers simulated the primary break-up via DNS method [94, 95] others focus their attention on the experimental measurement using commercial Diesel injectors. De la Morena, in his Ph.D.

thesis [96], performed a microscopic visualization of the spray and noticed that, at low injection pressure, the spray was characterized close to the orifice outlet by nearly 0° spreading angle and he named the length of this region *non-perturbed length*.

Even if their definition is very similar, the non-perturbated length has not to be confused with the intact surface length, since the last one only refers to the geometry of the spray while the first to the atomization process. In the same way Manin et al. [97] observed similar characteristics in a back illuminated setup: in this cases they observed also that in the *non-perturbed length* a transparent region was appearing in the spray, and they indicated that this phenomenon was related with the intact core (Fig. 3.20 left). In this field, an interesting study has been performed by Heilig et al. [98], who, taking advantage of the optical connectivity method, measured the transient intact liquid core obtained in a commercial multi-orifice injector (Fig. 3.20 right).
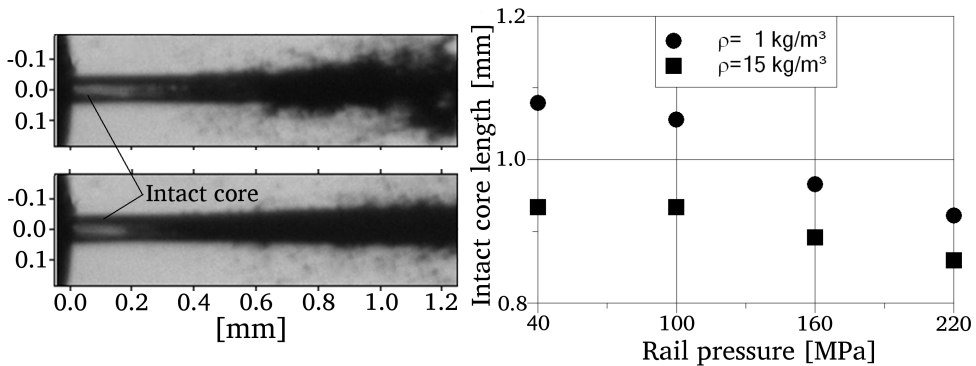
Figure 3.20: Intact core. Images obtained by Manin et al. [99] and intact core length measurements performed by Heilig et al. [98]

3.4.2 Microscopic characterization

The microscopic characterization aims at the understanding of what is within the spray boundaries. The information related to the microscopic characterization is fundamental for the development and validation of spray models and CFD simulations. However, the difficulties related to the Diesel spray measurements (high-temperature/pressure conditions, dense spray, very short time scale, etc.) make the access to these quantities a constant scientific/technological challenge.

The techniques developed in this field are therefore more complex than the ones used for the macroscopic characterization. In change, the accuracy of the

results is satisfactory and allows to measure variables that otherwise would be unknown.

Droplet size

Even if the droplet size is not affecting the spray evaporation (as a direct consequence of the mixing limited hypothesis), its measurement is important for the understanding of the atomization process and of the droplet-air momentum transfer (once combined with droplet velocity). On the other hand, the real droplet size involves a huge amount of information. The droplets formed, as a consequence of the turbulent nature of the atomization process, span over a wide range of diameters; the evaporation process (occurring also at ambient temperature) reduces the size of the droplets while traveling within the chamber. As a consequence of these facts, the droplet diameter cannot be treated as a deterministic measurement but it is convenient to use a statistical approach. The droplet size is therefore characterized by mapping the spray (in time and in space) and relating each point to an histogram. From the histogram, by representing the effective experimental measurement, the related *Probability Density Functions* are obtained. However, this characterization needs many hypothesis and leads to complex results and analysis; thus, it is addressed only to very specific studies. Moreover the analysis of the probability distribution function (*PDF*), generally, does not provide any crucial information, except regarding spray non-uniformity.

One solution normally employed to describe the atomization quality, is the definition of a characteristic diameter. This quantity can be defined in different ways depending on the application: Mugele and Evans [100] classified these definitions proposing a notation that nowadays is the most employed to indicate these parameters. Tab. 3.3 presents the notation together with the definitions.

Among the definitions given in Tab. 3.3, the most employed for Diesel spray studies is the D_{32}, also called *Sauter mean diameter* or D_{SMD}. The parameter, representing the average volume-surface ratio, is in fact an effective indicator of the relationship between the drag forces (related to the droplet surface) and the droplets inertia (related to the droplet mass). Moreover, it can be obtained directly by the application of imaging techniques: the *planar laser induced fluorescence* technique (PLIF) [101], and its derived techniques [102] relate the fluorescence signal, proportional to the droplet volume, to the scattering signal, that is a function of the droplet surface. From these two measurements the Sauter mean diameter is obtained as a direct result.

Another technique, normally employed for the determination of the droplet diameter, is the *Phase Doppler Particle Analyzer* that allows to determine the size

Notation	Dominant factors	Physical meaning	Formulation
D_{10}	Diameter	Avg. geometrical diameter	$\dfrac{\sum_i N_i D_i}{\sum_i N_i}$
D_{20}	Surface	Avg. surface area	$\left(\dfrac{\sum_i N_i D_i^2}{\sum_i N_i}\right)^{1/2}$
D_{30}	Volume	Avg. Volume / mass	$\left(\dfrac{\sum_i N_i D_i^3}{\sum_i N_i}\right)^{1/3}$
D_{32}	Volume/surface	Volume/surface ratio	$\dfrac{\sum_i N_i D_i^3}{\sum_i N_i D_i^2}$

Table 3.3: Definitions of mean diameters according to Mugele and Evans [100]

and the velocity of the droplets: even if it is considered more accurate than the PLIF methods, PDPA has the significant drawback of being a point-measurement, extending significantly the time required for the tests.

Several experimental studies have proposed correlations to relate D_{32} to the test conditions [103, 104]. For reference the correlation presented by Hiroyasu et al. [105] is presented, being one of the first that can be found in the literature,

$$D_{32} = k_{SMD}\Delta p^{-0.135}\rho_a^{0.121}\dot{m}_f^{0.131} \quad , \tag{3.45}$$

where k_{SMD} is a constant that is assumed to be $k_{SMD} = 0.38$. However, care must be taken with these correlations because large variations are obtained on the predictions, in part due to the weak amount of experimental data used to build the correlation. It is then hazardous to extend an expression to other nozzle shapes, diameters or injected fuels; they maybe used only as a starting point and adjusted to fit well the experimental data under consideration and as qualitative guidelines [106].

Velocity distribution

The characterization of the velocity field of the spray allows to evaluate and understand the process of air-fuel mixing. For this reason, many authors have investigated these parameters: most of them based their studies on the similitude

between Diesel spray and gas-jet proposed first by Adler and Lyn [107] that, as discussed earlier, it is accepted to describe in an accurate way the behavior of the steady spray at a certain distance from the orifice (in the *dilute region*) [37, 72, 108, 109]. However, an important difference lays between the gas-jet and the Diesel spray: in the first case the spreading angle is constant and it depends only on the proprieties of the fluids involved in the process, while, as discussed in 3.4.1, in the second case the geometry of the orifice and the gas density in the chamber have a significant effect. The first important consequence of the similitude between the gas-jet and the diesel spray is the similarity between radial velocity profiles, as seen in 3.3.2.

The radial velocity profiles can be then extended to concentration profiles by means of the Schmidt number (*Sc*) defined as the relationship between the diffusion of momentum and mass. Theoretical models allow to estimate these quantities as, for example, the one proposed by Spalding [110] and Desantes et al. [111]. These models show how the concentration and velocity profiles are characterized by two different zones: the first one, related to the intact length, where the variable studied remains constant; at a certain axial distance it starts the second zone where both the velocity and the concentration are proportional to $1/x$. The experimental tools available for these measurement are different: Rayleigh scattering [112] and Particle image velocimetry (PIV) allow to obtain entire maps of, respectively, the concentration and velocity fields [113]. The same PDPA technique is used to determine the velocity field and, when it is dedicated only to the particle velocity, it is also called LDV (laser doppler velocimetry).

3.5 Diesel spray combustion

This section will describe the details of the combustion process associated to the Diesel injection. This section can be divided in two parts, focused on the main phases of the Diesel combustion: the first describing the auto-ignition phase, strictly related to the formation of an ignitable mixture and the chemical reactions leading to the first peak of heat release, also called premixed phase; the second one presenting how the process after the combustion develops and a diffusive flame front is established.

3.5.1 Ignition process

The auto-ignition of the Diesel spray is a complex phenomenon that relates to each other the spray development, the air-entrainment, the liquid fuel evaporation, and the chemistry. This combination of processes is normally named *Diesel ignition*.

The chemical reactions start firstly in the regions of the spray where air-fuel ratio, temperature and ambient pressure have reached values suitable for ignition. All the key quantities are rapidly changing within the spray and, depending on their evolution, the chemical reactions will go one path or another. This fact links strictly the physics and the chemistry of the spray from the beginning.

The studies presented in the literature about Diesel ignition highlight many similarities to the ignition of a homogeneously premixed charge [114–117]. These works indicate the existence of a low intensity reaction stage before the main phase of the combustion. The heat release in this phase of the combustion is very low and, in many cases, it cannot even be appreciated. On the other hand, thanks to optically accessible test rigs, the imaging of the ignition enables to observe a distributed chemiluminescence light emissions occurring during this phase: these very weak light emissions can be observed only using intensified cameras and are distributed on the spray region. The evolution of their intensity and position has been the subject of many studies since it helps understanding the following development of the combustion [116, 117]. Lillo et al. [118], using a constant volume test rig, combined the chemiluminescence imaging with a Schlieren setup adding an optimized chamber pressure measurement: their results proved that the onset of the first chemiluminescence is captured by the camera, in the Schlieren imaging a variation in the spray global refractive index is detected. At the same time, the chamber pressure indication shows the first positive heat release: these results indicate that during the first chemiluminescence there is also a (weak) heat release. This first stage is followed by a sudden increase in the chemiluminescence signal and pressure, characterizing the beginning of the so called high-temperature reactions.

Higgins and Siebers [117], basing on their experimental data and on the combustion knowledge developed by Westrbrook et al. divided Diesel ignition into three phases [119]:

1. *physical induction period*: it includes the time up to the start of the simultaneous rise in pressure and chemiluminescence. During this time, the main driver is the physics involved in the spray formation described in 3.3.2: atomization, air entrainment and fuel evaporation. Fuel vaporization causes a decrease in the temperature in the spray region, inhibiting temporally the ignition chemistry; as the penetration and hot air entrainment continue, the fuel/air mixture temperature increases, overcoming the previous effect. In the regions where temperature reaches a certain value, the first stage of ignition begins: this represents the end of the physical induction period. However, it only means that the first stage ignition chemistry has become
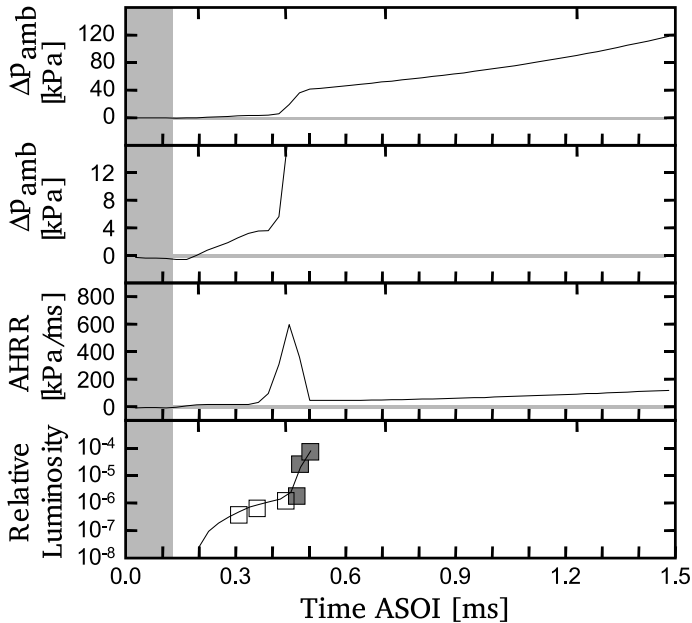
Figure 3.21: Pressure variation and apparent rate of heat release (AHRR) compared to the intensity captured by an intensified camera. The first and the second axes from the top, presents the same information with a different scale. The results were obtained in a constant volume vessel at $T_a = 1000\,\text{K}$ and $\rho_a = 14.8\,\text{kg/m}^3$, [117].

detectable and the demarcation between the physical induction period and the first stage of ignition depends somewhat on the sensitivity/resolution of the diagnostics used;

2. *first-stage ignition period*: it extends from the time of first detectable rise in pressure and chemiluminescence until rapid heat release begins, marking the start of the second stage ignition chemistry. The first stage ignition chemistry develops over a broad downstream region of the spray between the liquid length and the penetrating tip of the spray. The relatively uniform distribution of chemiluminescence in this region suggests a nearly uniform evolution of the first stage chemistry throughout the region. The average fuel-air mixture in this region is rich, with an equivalence ratio between three and four. Early in the first stage, chain-branching reactions consume fuel, producing radicals and releasing small quantities of energy that are responsible of the measured pressure increase and light emissions. However, as the temperature further increases due to both mixing and first-stage

chemistry, the temperature reaches levels ($\approx 750 - 900\,\text{K}$) where the dissociation of intermediate products back to reactants begins to occur. This reduces the chain branching, effectively decreasing the rate of fuel consumption, even if the temperature is higher. These intermediate-temperature dissociation-reactions, related to the decrease in the rate of pressure and chemiluminescence, rise in the later part of this stage. According to the spectra measured by Dec and Espey [116] in an optically accessible engine, the chemiluminescence observed in this phase is due mainly to the formation of formaldehyde (CH_2O) and CH radical, being the spectra similar to the ones obtained by Gaydon [120] in homogeneous mixture combustion. The total pressure rise during the first stage ignition is equal to approximately 10% of the pressure-rise, that ultimately occurs by the end of the premixed-burn phase. Due to the very low heat release observed, the chemiluminescence characterizing this phase of the ignition are also called *cool flames* [121].

3. *Second-stage ignition/premixed-burn period*: the beginning of significant heat release that leads into the sudden premixed-burn pressure-rise (see Fig. 3.21) marks the start of the second stage of ignition. This stage begins when, as a result of air entrainment and heat release from first-stage ignition, the temperature increases to a level where hydrogen peroxide (H_2O_2) dissociation reactions dominate the chemistry ($\approx 900\,\text{K}$), producing significant heat release. This process is the trigger for the premixed-burn. The dissociation of H_2O_2 produces the radical OH and its transition from excited- to ground-state produces the chemiluminescence emissions characteristic of this phase. During this last phase of the ignition, all the fuel that has formed an ignitable mixture before the second stage phase reacts causing the heat-release peak that is typical of the Diesel combustion. A local minimum follows the premixed-burn peak, marking the end of this stage and the beginning of the so called *diffusive flame*. The Fig. 3.22 presented by Higgins and Siebers [117] shows that apart from the intensity of the signal, the first and the second stage ignition are characterized by a different spatial distribution: in the first case the reactions are distributed in a wide part of the vaporized spray area, while in the second, it starts in nucleus normally characterized by rich mixture.

The ignition of the Diesel spray is critical for the global performances of the Diesel engine for different reasons:

- the peak in the heat release associated to the premixed-phase of the combustion is one of the main sources of noise of the engine;
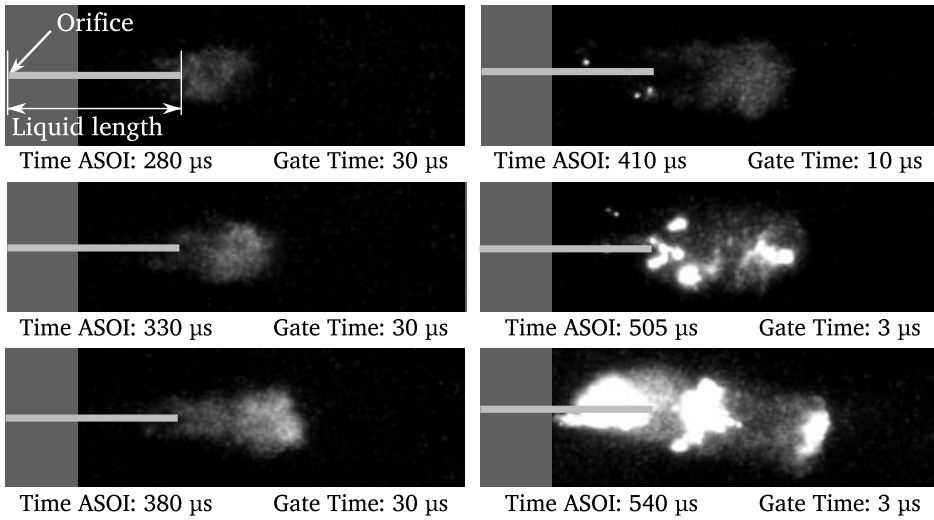
Figure 3.22: Image sequence of the ignition event obtained by Higgins and Siebers in [117] for the same test presented in Fig. 3.21. The position of the orifice and the liquid length are indicated on the images. The time refers to the start of the injection, and the gate time is reduced to balance the increase of the luminosity from the flame, and avoid the sensor saturation. The gray rectangle on the left of the image indicate the area that is not in the field of view of the camera.

- the high temperatures reached during this phase are responsible for NO_x production;

- the location where the ignition takes place strongly affects the subsequent evolution of the combustion.

The detailed knowledge of the parameters affecting the spray ignition timing is fundamental for the optimization of the engine performances and pollutant control. In the literature, different studies have been carried out to characterize the ignition timing under different boundary conditions [122–126]. One of the most representatives has been presented by Pickett et al. [121] performing experimental measurements in an optical accessible combustion vessel. Pickett et al. proposed a law basing on Arrhenius type equation,

$$\tau_{SSI} \propto \exp\left(\frac{E}{RT_a}\right)\rho_a^a Z_{st}^b \,, \tag{3.46}$$

where τ_{SSI} is the second stage ignition delay, E is the global activation energy of the reactions, R is the universal gas constant, and Z_{st} is the stoichiometric mixture fraction (depending on the fuel composition and on the oxygen content of the gas in the combustion chamber). Fitting the experimental data, they obtained the values of the constant included in the equation: $a = 1.3$, $b = 1.0$. The value of the E/R has been obtained experimentally by different authors [126, 127] and its value is around $5000 - 7000\,\mathrm{K}$. Injection pressure has only a secondary effect on the ignition: increasing the injection pressure, the fuel-air mixing is faster, and the favorable conditions for the ignition are reached in a shorter time as pointed out by [68, 91]. However, these variations are limited when compared to the effect of the oxygen concentration or the ambient temperature.

3.5.2 Diffusive phase

The premixed phase of the combustion ends with the formation of a diffusive flame front that expands the region where the auto-ignition occurred. The flame front moves, on one side downstream of the spray toward the spray tip, and, on the other, toward the nozzle until the balance between the flame front speed and the velocities within the spray is found. The transition from premixed- to diffusive-phase is not very clear and different interpretations might be found in the literature: even if it could be logical to think that the diffusive flame starts together with the premixed combustion, the results obtained by flame spectroscopy performed in an optical engine by Higgins et al. [128] have shown that the radiations typical of the diffusive combustion appear only in a second moment, close to the minimum in the apparent heat release rate (AHRR) showed in Fig. 2.1.

During this second phase of the combustion, the diffusive flame front is sustained by the convective supply of fuel that is provided by the inside of the spray. This phase continues until the end of the injection.

The understanding of the diffusive combustion phase of the Diesel spray has been the subject of many studies, and the sum of all these contributions is presented in the comprehensive works presented by Dec [129] and Flynn et al. [6]. The main regions characterizing the diffusive flame have been described by Dec [129] and can be observed in Fig. 3.23. Each region is characterized by significant differences in temperature and chemical composition of the mixture, but also by the chemical reactions occurring:

- the first region, corresponding to the zone starting from the nozzle, has the same features of the non-reacting spray. In fact, the reacting area is generally 'lifted' from the injector nozzle due to the very high speed of the fuel at the orifice outlet. As discussed for the inert spray (sec. 3.3.2), the fuel
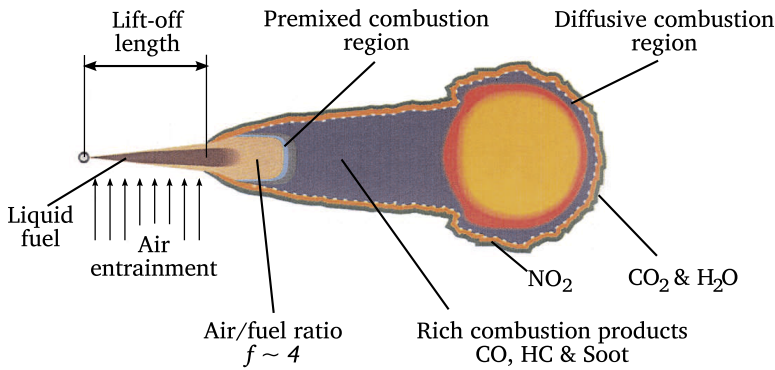
Figure 3.23: Conceptual model of the Diesel flame structure during the diffusive phase presented by Dec [129].

gradually mixes with the surrounding air, that is entering from its sides: this distance is needed because makes it possible to form an ignitable mixture with a proper f_{eq} and reach the correct balance between spray velocities and flame front speed. In fact, the air entrainment brings as a consequence the preparation of the fuel-air mixture, where the equivalence ratio is decreasing with the axial distance and the increase of the mixture temperature: both these facts contribute to extend the ignitable limits of the mixture and its adiabatic flame front speed. On the other hand the momentum transfer between the fuel and entrained air causes the velocities to decrease farther from the nozzle: summarizing, moving further from the nozzle, the conditions become more suitable for combustion. The length of this non-reacting region is normally called lift-off length (*LOL*) and its importance is described in the next section.

- starting from the *LOL* distance, the flame has the typical structure of a diffusion flame, being formed internally by products from partial combustion (unburnt hydro-carbons and soot) and surrounded by a reaction surface. On this surface the oxygen entrained by the spray mixes with the gases and converts them in water and carbon dioxide, completing the combustion reactions. The measurements performed by Dec and Coy [130] proved that these reactions take place in a very thin surface: they estimated this width to be about $120\,\mu$m. Dec and Canaan [131] observed experimentally that it is on this surface where most of the NO_x are formed, due to the high temperature characterizing this region. In the most downstream part of the

flame a vortex can be observed: this region is characterized by the highest concentration of soot and temperature.

- the third region is located between the first and the second region described above. In this region, the mixture is rich and all the oxygen entrained along the *LOL* reacts in this first premixed phase of the combustion [129]. However, since the mixture is very rich, the products formed in these reactions will constitute the fuel for the diffusive region. These products have the typical composition of a rich combustion: no oxygen, carbon monoxide, and partially burnt hydrocarbons that constitute the basis for the following soot formation.

The spatial description of the Diesel flame described by Dec, can also be understood tracking the path of a parcel of fuel injected in the chamber. This interpretation can be found in the work presented by Flynn [6].

Once injected in the chamber, the fuel atomizes and starts mixing with the entrained air; the hot air entrained increases the temperature of the fuel causing its evaporation until it approaches the premixed region (see Fig. 3.23). At this point the temperature is about 700 K while the equivalence ratio is about 4.

Passing through the premixed combustion region, the mixture formed is burnt increasing its temperature to about 1600 K. The rich local equivalent ratio causes the oxygen to react to completion leaving, as combustion products, principally carbon monoxide and short-chain non-saturated hydrocarbons (C_2H_2, C_2H_4 and C_3H_3). In his work, Flynn [6] hypothesizes that these intermediate composites successively react to from polyaromatic hydrocarbons that are the basis for the formation of soot. In this first reaction Flynn estimates a release of about the 15% of the total chemical energy of the fuel.

Later, the parcel enters in the diffusive region: the oxygen entrained in this region is completely employed for the diffusive reaction at the diffusive surface and, therefore, the oxygen content in this region is null. However, even if no heat release is supposed to occur in these regions, the combustion products derived from the diffusive surface are progressively entrained, modifying the mixture composition and increasing its temperature along the spray axis. As the parcel approaches the diffusive flame front, its temperature increases and at the same time the soot particles grow in size and number. Finally, when the parcel passes through the flame front, the oxygen reacts with the partial-combustion products and the combustion is completed releasing the remaining chemical energy: in the diffusive flame front region the maximum temperature is reached and estimations revealed that this temperature approaches the adiabatic temperature limit.

The diffusive flame front causes also the oxidation of the soot, due in part to the very high temperature reached and in part to the formation of the OH radical. This second fact has been observed first by Dec and Coy measuring the OH distribution via planar laser induced fluorescence (*PLIF*) [130] and confirmed in the work of Kosaka et al. where the OH radical distribution (via *PLIF*) and the soot [132] were imaged symultaneously. In these works the soot always appears surrounded by a layer of OH radicals and nearly no overlap is observed between these two regions. This fact entails that the OH radical formation is a fundamental step for the oxidation of soot. Concluding, the Diesel flame can be intended like a liquid jet of fuel that mixes with hot air providing the reactants for a rich premixed combustion; the products of this combustion are later fueling a diffusive flame [6]. It is interesting to observe that, in some ways, the early premixed phase of the combustion is surviving also during the diffusive phase in the *LOL* region. In this sense, Pickett et al. [121] performed an extensive study relating the ignition delay and the *LOL* obtained in a wide range of test conditions and concluded that these features of the combustion are strictly linked to each other. When the injection ends, the flame structure changes again, due to the increment of air entrainment at the end of injection as described by Musculus et al. in [133]. During this phase, also called *late combustion*, the diffusive region is completely surrounded by the diffusive reactions surface and the features of the air entrainment are modified radically. Due to the current trend in reducing the duration of the main injection and in increasing the ignition delay timing characteristics of *LTC* and *PPCI* strategies, the understanding of this phase gained the attention of many researchers: however, for more details on this last phase of the combustion the reader can see the work presented by Musculus et al. [7], in which it is presented an extensive review of the available experimental data to build a conceptual model more suitable to this kind of combustion, including the *late combustion* as a determining part.

3.5.3 Lift-off length

The separation between the orifice outlet and the reacting region or, in other words, the presence of the lift-off length, is a phenomenon that is characteristic of the partially premixed flames. The formation of the lift-off length has been firstly studied in turbulent gas-jets at ambient conditions. Peters [134] performed a detailed review of the data available in the literature and arrived to a scaling law that well fits most of the experimental data presented by Kalghatgi et al. [135]. In his equation, he relates the *LOL* to the average velocity at the nozzle outlet

(u_0), to the equivalent ratio (f), to the flame front velocity of the stoichiometric mixture at the condition tested $(s_l(f_{st}))$ and to the thermal diffusivity (α):

$$LOL = u_0 f_{st} \cdot \frac{\alpha}{s_l(f_{st})} \quad . \tag{3.47}$$

The lift-off length of the Diesel spray has been studied later: the first experimental observations available are from Winkhlofer [136] and Larsson [137] imaging directly the natural (unfiltered) flame luminosity. A step forward in the understanding of this parameter in Diesel combustion has been given by Siebers and Higgins [138]: they measured LOL in a constant volume combustion chamber. The study proposed has been fundamental for three different reasons:

1. the amount of parametric variations included in the measurements;
2. the use of a closed volume combustion vessel, which allowed to study the flame in open field (no interaction with the wall of the chamber) and nearly quiescent conditions; in this way it was improved the control on the parameters object of the study (ambient temperature, density etc.) excluding the potential influence of other factors such as swirl intensity or wall effects;
3. the methodology employed; differently from Winkhlofer and Larsson, measuring basing on the natural flame radiation, at the condition studied mainly due to soot incandescence, they based their measurements on the chemiluminescence of the OH* radical; the OH* radical is an exited transient state of the radical OH, and exists only for a very short time (some ps) before decaying to the ground state OH. The transition from OH* exited state to ground state OH is characterized by the emission of light under a well defined spectrum [112]: therefore, by using a specific filter, the OH* radiation can be easily imaged and separated by the rest of the flame radiation. As explained before, the formation of the soot precursors occurs in the premixed region , but the apparition of the first soot particles is shifted some millimeters downstream. On the other hand, this region is characterized by the consistent presence of the OH radical, due to the high rate of chemical reactions as evidenced by Dec and Coy [130]. Even if it is not quantitatively related to the OH mixture fraction, the OH* chemiluminescence imaging is a precise tool to determine the region where the OH is located.

In their work, it is proposed an empirical power-law equation (Eq. (3.48)), which assesses the influence of each test condition in a analytical expression (see Tab. 3.4).

$$LOL = u_0^a \, D_0^b \, \rho_a^c \, T_{amb}^d \, [O_2\%]^e \tag{3.48}$$

Quantity	Exponent	Exp. Value
Theoretical velocity (u_0)	a	1
Orifice diameter (D_0)	b	0.34
Ambient density (ρ_a)	c	-0.85
Ambient temperature (T_a)	d	-3.74
Oxygen vol. fraction ($O_2\%$)	e	-1

Table 3.4: Empirical coefficient by Siebers and Higgins [138, 139] obtained from a regression to their experimental data.

In addition, they proposed a new scaling law modifying the one proposed by Peters [134] and adding the effect of the spreading angle, which in turbulent gas jet is generally constant:

$$LOL = u_0 f_{st} \cdot \frac{\alpha}{s_l(f_{st}) tan(\theta)} \ . \tag{3.49}$$

From the results obtained by Siebers and Higgins [138] everything is similar to turbulent isothermal gas jet, apart from the effect of the orifice diameter: in turbulent gas jet it is not observed any influence, while for the Diesel spray it has a substantial effect. Siebers and Higgins explained that this difference is probably related to the non-isothermal nature of the Diesel spray upstream of the lift-off, affecting the whole chemistry in the premixed region.

The study of the LOL in Diesel spray allowed to understand one of the key steps of the soot formation in the Diesel combustion. In fact, the LOL determines the equivalent ratio in the premixed region and, therefore, the composition of the intermediate products within the diffusive region. Siebers and Higgins in [139] demonstrated that, if the equivalent ratio at the LOL is included between $1.8-2.2$, the soot production is nearly nonexistent: this fact is also in agreement with the results obtained in turbulent gas-jet by Peters [134], in which the non-sooting limit is found at $f \approx 2$.

3.6 Partial needle lift and injection rate shaping: a review

The combustion of the Diesel spray is a crucial process for controlling the pollutant emissions and the global performances of the whole Diesel engine. As

seen in the previous sections, Diesel combustion is controlled on the one hand by the conditions in the combustion chamber (oxygen content, ambient temperature and ambient density) and, on the other, by the injection parameters. In recent years, technological improvements in common-rail injectors have enabled the implementation of new injection strategies, including multiple pilot injection [140].

The injector studied in this thesis goes beyond this trend, featuring the direct control of the needle lift. This feature brings the promise of reducing the injection delay (the hydraulic circuit included in the servo-actuated injector is not needed) and to throttle the fuel flow by controlling the position of the needle lift. As a corollary of that, due to the fast response of the piezo-stack actuator, the needle lift can be varied in the fast time-scale characteristic of the injection event: therefore, injection rate shaping is enabled and advanced injection rate profiles could be obtained. In order to conclude this chapter, a review of the works found in literature about partial needle lift and injection rate shaping is presented.

One of the first works found in the literature discussing the effect of partial needle lift has been carried out by Favennac et al. [141]: in this work, the authors used a conventional servo-actuated injector fitted with a VCO nozzle; the needle lift was controlled by inserting at the top of the needle different gauges limiting the needle movement. The discharge coefficient obtained at different maximum needle lifts ($10, 25, 50, 100, 200, 300\,\mu\text{m}$) increases with Re until the onset of cavitation: at this point, the vapor bubbles formed obstruct the fuel flow causing the drop of the discharge coefficient. When the needle lift is reduced, the discharge coefficient diminishes as a consequence of a lower pressure upstream of the orifice. Moreover, they observed that the critical Re at which the cavitation collapse occurs is not dependent on the maximum needle lift allowed, indicating no interference between cavitation and partial needle lift. However, the compressive forces produced by the fuel pressure are suspected to deform the gauges especially at the lowest needle lifts tested, and consequently it puts partially into question the conclusions of the study. Moreover, they increased the Reynolds number only by modifying the back-pressure and no information is given about the effect of the injection pressure.

Arcoumanis et al. [142] studied the same problem with a totally different approach: by means of large-scale transparent nozzle they observed directly the formation of cavitation, gaining direct access to this information. Their results brought important insight about the formation and location of the cavitation: at high needle lift the vapor phase is situated in a well defined region close to te orifice inlet and it has a very stable behavior. Decreasing the needle lift, the width of the vapor layer gets smaller and at a certain point it disappears completely,

transformed in a cloud of fine vapor bobbles. Despite the significant difference observed in vapor formation, the cavitation onset is observed for the same value of k_{crit} disregarding the needle position. Badock et al. [143] gave a step forward imaging directly the cavitation phenomenon using a real-size single-hole nozzle and substituting part of the nozzle and the needle with transparent material. In this case the authors studied the effect of the needle only observing at the opening/closing transient position. Moreover, their setup enabled to observe also the spray formation and to study its relationship with the cavitation.

Miranda et al. [144] carried out a similar study using a transparent multi-hole VCO nozzle. In this case, the needle was fixed at different positions: they noticed that, for the same value of K, the cavitation area was lower at lower needle lift. Even though the range of injection pressure allowed by their transparent nozzle is considerably lower than the pressures employed in real injector, their setup allowed to obtain images of cavitation observing the orifice frontally: from this view, the cavitation appears to have a spiral shape, suggesting a large-scale rotational velocity of the flow (Fig. 3.24).
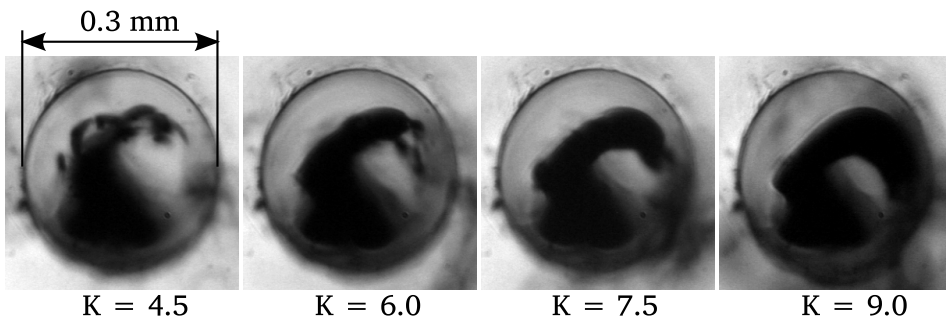
Figure 3.24: *Cavitation in transparent nozzle at different cavitation numbers: a view from the nozzle hole plane; $p_i = 1.5$ MPa [144].*

Blessing et al. studied the fuel flow in a multi-hole transparent nozzle at injection pressures relevant to the Diesel engine [145]. Combining their experimental results with *CFD* simulations performed with the code AVL-FIRE, they showed that, during the needle opening/closing, there is higher probability of formation of cavitation in the orifice. Moreover, the simulation performed using a *3D* mesh showed that the high flow velocities appearing in the needle seat at low needle lift cause turbulence in the nozzle sac and this is eventually reflected in pressure inhomogeneities in the sac and uneven flow through the orifices. However, this conclusion was supported only by computational results. When they compare the different nozzle geometries ($k - factor = -2.5, 0 and 2.5$) they observed that

the positive conicity of the orifice ($k-factor = 2.5$) was inhibiting the cavitation: despite the relatively high conicity at the needle closing, some cavitation was observed. Finally, they observed that the cavitation observed in the orifices is strongly linked to an increase in the spreading angle measured in the near field. Masuda et al. [146] with a experimental and computational study, proved that the opening/closing transient causes an increase of cavitation in the orifice and an increase in the spreading angle in the near field. In a similar study Lee et al. [147] compared a solenoid and a piezoelectric servo-actuated injectors, performing simulations of the internal flow: they observed that the faster needle lift occurring in the piezoelectric injector was causing a higher degree of cavitation in the nozzle needle during the opening and a consequent increase of the effective velocity. The near field spreading angle has been studied also by Manin et al. [99] performing high speed optical microscopy, but this time in a single- and axial-hole. Moreover, the geometry of the nozzle they where using was inhibiting cavitation at steady conditions, due to the orifice conicity ($k-factor = 2.5$) and a high degree of hydro-grounding. They found that for a relatively long transient at the start and at the end of the injection (about $0.2-0.4\,\mu$s, depending on the injection pressure) the near field spreading angle was higher that the one measured during the steady part of the injection.

Chiavola and Palmieri [148], investigating the consequences of short dwell-time injections, evaluated the effect of a radial component in the needle displacement motion in a multi-orifice micro-sac nozzle. They performed CFD simulations, and evaluated the velocity fields as well as the formation of fuel vapor due to cavitation. Among the most significant outcome of their works it is relevant to remind, in this review, that they obtained differences up to the 8% in the u_{eff} between orifices: most specifically the orifice toward which the needle was moving has the highest effective velocity and the opposite one, the lowest. Moreover, they found that these differences in the velocity profile were reflected in the cavitation pattern observed, which was different depending on the relative position of the orifices and the needle(see Fig. 3.25).

One of the last and most complete studies on the effect of partial needle lift, is presented in Martinez's PhD thesis [8]: in this work, the author starts with an experimental validation of the code implemented in OpenFoam [149] and investigates the effect of the partial needle lift in a multi-hole nozzle. The nozzle studied featured cylindrical orifices ($k-factor = 0$) and micro-sac nozzle seat type and therefore inclined to cavitate. The results obtained partially confirms what was found by previous authors and partially gave important new insight on the behavior of the flow at partial needle lift and the relationship between the restriction at the needle seat. More in details, his research highlighted the following aspects:
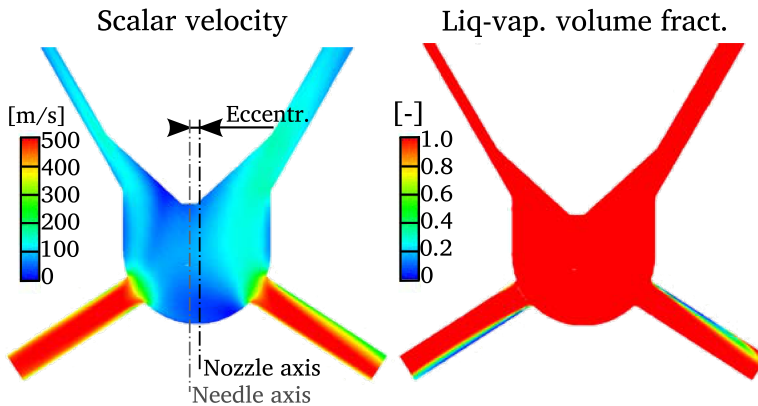
Figure 3.25: Scalar velocity and liquid-vapor volume fraction obtained applying an eccentricity to the nozzle needle (Chiavola and Palmieri [148])

- the acceleration of the flow occurring in the needle seat causes a higher degree of turbulence in the nozzle sac, and this fact causes differences in the flow at the orifices inlet;

- at low needle lift, the onset of cavitation can be observed in the needle seat as a consequence of the acceleration of the flow;

- the cavitation pattern modifies its shape and location depending on the needle lift, moving to the opposite side of the orifice due to the modification of the flow lines caused by the restriction at the needle seat (see Fig.3.26);

- the phenomenon described above has been observed in transient as well as in steady state simulations.

Stegemann et al. [150] carried out one of the few studies found in the literature presenting the macroscopic characterization of the Diesel spray produced by a direct acting injector. The injector prototype studied by Stegemann et al. featured the mechanical coupling between the piezoelectric actuator and the nozzle needle but no more details about the injector are given. However, the technology employed allowed only to control the position of the needle during the steady part of the injection and a slight control on the needle speed at the opening. After proving the capabilities of the system for controlling the mass flow rate, and measuring spray penetration and spreading angle in non-evaporative conditions, the following conclusions were drawn:
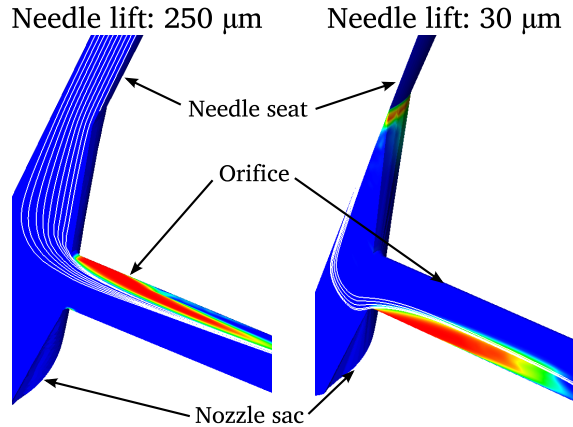
Figure 3.26: Partial needle lift effect on flow lines and cavitation formation (indicated by the red color); results obtained by Martinez [8].

- while at full needle lift the spray penetration was following the typical behavior described by Hiroyasu [71], at reduced needle lift the penetration was more difficult to predict; they observed features in the spray contours suggesting unsteadiness of the mass flow rate and related it with the likelihood of cavitation occurring in the needle seat;

- comparing two injections with the same mass flow rate but different injection pressure and needle lift (in the case with higher injection pressure the needle lift was lower) they observed that the penetration was similar in the two cases: they evinced that eventually the turbulence observed in the shape of the spray was not having any significant effect on the spray formation;

Blessing et al., in the above mentioned study [145], used the same nozzle to investigate the effect of rate shaping, using a piston amplifier common rail system (*APCRS*): the concept presented in Sec. 2.4 allows to modify the injection pressure during the injection and, consequently, to modify the injection rate profile. Testing the injector in an optically accessible engine showed that a reduction in the slope of the *ROI* at the needle opening enables important advantages for the premixed phase of the combustion: reducing the fuel amount injected during the delay phase, the temperature during the premixed phase was reduced, thus suggesting a reduction in NO_x emissions. However, the "shape-profile" capabilities of the APCRS system were weak and the results are limited only to a reduced range.

Junenja et al. [151] performed a computational study to understand the potential advantages of performing rate shaping. After calibrating their model with a regular injector, they modified the baseline rate shape used in the model and observed the evolution in fuel mixing/evaporation and combustion. Increasing the slope of the mass flow rate at the start of the injection, the NO_x produced during the premixed phase of combustion was considerably higher, due to the higher amount of fuel injected at that time. The soot formation analysis, (even though not included in the model, they studied the soot formation tracking its precursor, acetylene) revealed that decreasing ramp-up slope of the mass flow rate, the soot formation is reduced during premixed phase of the combustion, but during the diffusive phase the situation is the opposite. They stated that if the mass flow rate increases after the ignition, the LOL moves farther during the injection, but since the transient is relatively slow, the mixture at the lift-off region is richer than in other cases, causing a higher soot production.

References

[1] MAJEWSKI, W. A. and M. K. KHAIR. *Diesel emissions and their control*. Society of Automotive Engineers, 2006.

[2] JOHNSON, T. V. "Review of diesel emissions and control". *International Journal of Engine Research* 10.5 (2009), pp. 275–285.

[3] HEYWOOD, J. B. and O. Z. WELLING. "Trends in performance characteristics of modern automobile SI and diesel engines". *SAE International Journal of Engines* 2.1 (2009), pp. 1650–1662.

[4] SCHMIDT, D. P. and M. CORRADINI. "The internal flow of diesel fuel injector nozzles: a review". *International Journal of Engine Research* 2.1 (2001), pp. 1–22.

[5] LIN, S. and R. REITZ. "Drop and spray formation from a liquid jet". *Annual Review of Fluid Mechanics* 30.1 (1998), pp. 85–105.

[6] FLYNN, P. F. et al. "Diesel combustion: an integrated view combining laser diagnostics, chemical kinetics, and empirical validation" (1999).

[7] MUSCULUS, M. P. B., M. P. C., and L. M. PICKETT. "Conceptual models for low-load, single-injection, EGR-diluted, partially premixed low-temperature DI diesel combustion". *Progress in Energy and Combustion science* (2013).

[8]   Martínez López, J. "Estudio Computacional De La Influencia Del Levan-
      tamiento De Aguja Sobre El Flujo Interno Y El Fenómeno De La Cavitación
      En Toberas De Inyección Diesel". PhD thesis. E.T.S. Ingenieros Industri-
      ales. Universidad Politécnica de Valencia, 2013.

[9]   Schmidt, D. P. and M. L. Corradini. "The internal flow of diesel fuel
      injector nozzles: A review". *International Journal of Engine Research* 2.1
      (2001), pp. 1–22.

[10] Salvador, F. J., A. H. Plazas, J. Gimeno, and M. Carreres. "Complete
      modelling of a piezo actuator last-generation injector for diesel injection
      systems". *International Journal of Engine Research* 15.1 (2014), pp. 3–19.

[11] Stokes, G. G. *On the effect of the internal friction of fluids on the motion
      of pendulums*. Vol. 9. Pitt Press, 1851.

[12] Reynolds, O. "An experimental investigation of the circumstances which
      determine whether the motion of water shall be direct or sinuous, and of
      the law of resistance in parallel channels." *Proceedings of the Royal Society
      of London* 35.224-226 (1883), pp. 84–99.

[13] Colebrook, C. F. "Turbulent Flow in Pipes, with particular reference to
      the Transition Region between the Smooth and Rough Pipe Laws." *Journal
      of the ICE* 11.4 (1939), pp. 133–156.

[14] Salvador, F., J. Gimeno, J. D. la Morena, and M. Carreres. "Using one-
      dimensional modeling to analyze the influence of the use of biodiesels
      on the dynamic behavior of solenoid-operated injectors in common rail
      systems: Results of the simulations and discussion". *Energy Conversion
      and Management* 54.1 (2012), pp. 122–132.

[15] Bianchi, G. M., S. Falfari, M. Parotto, and G. Osbat. "Advanced model-
      ing of common rail injector dynamics and comparison with experiments".
      SAE transactions 112.3 (2003), pp. 55–72.

[16] Coppo, M., C. Dongiovanni, and C. Negri. "Numerical analysis and ex-
      perimental investigation of a common rail-type diesel injector". *Journal
      of engineering for gas turbines and power* 126.4 (2004), pp. 874–885.

[17] Payri, F., V. Bermudez, R. Payri, and F. Salvador. "The influence of cavi-
      tation on the internal flow and the spray characteristics in diesel injection
      nozzles". *Fuel* 83.4 (2004), pp. 419–431.

[18] Gavaises, M., A. Andriotis, D. Papoulias, N. Mitroglou, and A.
      Theodorakakos. "Characterization of string cavitation in large-scale
      Diesel nozzles with tapered holes". *Physics of fluids* 21 (2009), p. 052107.

[19] BAE, C., J. YU, J. KANG, J. KONG, and K. O. LEE. "Effect of nozzle geometry on the common-rail diesel spray". *SAE Paper* 2002-01-1625 (2002).

[20] POTZ, D., W. CHRIST, and B. DITTUS. "Diesel nozzle-the determining interface between injection system and combustion chamber". *Thermo-and Fluid-dynamic Processes in Diesel Engines: Selected Papers from the THIESEL 2000 Conference Held in Valencia, Spain, September 13-15, 2000*. Springer Verlag. 2002, p. 133.

[21] BERGWERK, W. "Flow pattern in diesel nozzle spray holes". *Proceedings of the Institution of Mechanical Engineers* 173.1 (1959), pp. 655–660.

[22] BOGUE, D. "Entrance effects and prediction of turbulence in non-Newtonian flow". *Industrial & Engineering Chemistry* 51.7 (1959), pp. 874–878.

[23] POTZ, D., W. CHRIST, and B. DITTUS. "Diesel nozzle-the determining interface between injection system and combustion chamber". *Thermo-and Fluid-dynamic Processes in Diesel Engines: Selected Papers from the THIESEL 2000 Conference Held in Valencia, Spain, September 13-15, 2000*. Springer Verlag. 2002, p. 133.

[24] PAYRI, R., C. GUARDIOLA, F. SALVADOR, and J. GIMENO. "Critical cavitation number determination in diesel injection nozzles". *Experimental Techniques* 28.3 (2004), pp. 49–52.

[25] SCHLICHTING, H., J. KESTIN, H. SCHLICHTING, and H. SCHLICHTING. *Boundary-layer theory*. Vol. 539. McGraw-Hill New York, 1968.

[26] WHITE, F. M. *Fluid mechanics, WCB*. 1999.

[27] GRAVESEN, P., J. BRANEBJERG, and O. S. JENSEN. "Microfluidics-a review". *Journal of Micromechanics and Microengineering* 3.4 (1993), p. 168.

[28] RIPOLL, A. B. and M. P.-S. SÁNCHEZ-PASTOR. *Fundamentos y aplicaciones de la Mecánica de Fluidos*. McGraw-Hill Interamericana de España, 2005.

[29] SUH, H. K. and C. S. LEE. "Effect of cavitation in nozzle orifice on the diesel fuel atomization characteristics". *International Journal of Heat and Fluid Flow* 29.4 (2008), pp. 1001–1009.

[30] ARGUEYROLLES, B., S. DEHOUX, P. GASTALDI, L. GROSJEAN, et al. "Influence of injector nozzle design and cavitation on coking phenomenon". *Small* 2013 (2007), pp. 09–03.

[31] TANG, J. et al. "Coking Phenomena in Nozzle Orifices of DI-Diesel Engines". *SAE International Journal of Fuels and Lubricants* 2.1 (2009), pp. 259–272.

[32]   SOTERIOU, C., M. LAMBERT, S. ZUELCH, and D. PASSEREL. "The flow characteristics of high efficiency Diesel nozzles with enhanced geometry holes". *Proc. THIESEL International Conference on Thermo-and Fluid Dynamic Processes in Diesel Engines. Valencia, Spain*. 2006.

[33]   LICHTAROWICZ, A., R. DUGGINS, and E. MARKLAND. "Discharge coefficients for incompressible non-cavitating flow through long orifices". *Journal of Mechanical Engineering Science* 7.2 (1965), pp. 210–219.

[34]   MACIÁN, V, V. BERMÚDEZ, R. PAYRI, and J. GIMENO. "New technique for determination of internal geometry of a diesel nozzle with the use of silicone methodology". *Experimental techniques* 27.2 (2003), pp. 39–43.

[35]   PAYRI, R., F. SALVADOR, J. GIMENO, and J. DE LA MORENA. "Study of cavitation phenomena based on a technique for visualizing bubbles in a liquid pressurized chamber". *International Journal of Heat and Fluid Flow* 30.4 (2009), pp. 768–777.

[36]   GIMENO, J. "Desarrollo y aplicación de la medida de flujo de cantidad de movimiento de un chorro Diesel". PhD thesis. E.T.S. Ingenieros Industriales. Universidad Politécnica de Valencia, 2008.

[37]   NABER, J. and D. SIEBERS. "Effects of gas density and vaporization on penetration and dispersion of diesel sprays". *SAE Paper* 960034 (1996).

[38]   PAYRI, R., J. GARCIA, F. SALVADOR, and J. GIMENO. "Using spray momentum flux measurements to understand the influence of diesel nozzle geometry on spray characteristics". *Fuel* 84.5 (2005), pp. 551–561.

[39]   PAYRI, R., F. SALVADOR, J. GIMENO, and L. ZAPATA. "Diesel nozzle geometry influence on spray liquid-phase fuel penetration in evaporative conditions". *Fuel* 87.7 (2008), pp. 1165–1176.

[40]   YUE, Y., C. F. POWELL, R. POOLA, J. WANG, and J. K. SCHALLER. "Quantitative measurements of diesel fuel spray characteristics in the near-nozzle region using X-ray absorption". *Atomization and sprays* 11.4 (2001).

[41]   MACPHEE, A. G. et al. "X-ray imaging of shock waves generated by high-pressure fuel sprays". *Science* 295.5558 (2002), pp. 1261–1263.

[42]   KASTENGREN, A. and C. POWELL. "Spray density measurements using X-ray radiography". *Proceedings of the Institution of Mechanical Engineers, Part D: Journal of Automobile Engineering* 221.6 (2007), pp. 653–662.

[43]   LINNE, M., M. PACIARONI, T. HALL, and T. PARKER. "Ballistic imaging of the near field in a diesel spray". *Experiments in fluids* 40.6 (2006), pp. 836–846.

[44] LINNE, M. "Imaging in the optically dense regions of a spray: A review of developing techniques". *Progress in Energy and Combustion Science* 39.5 (2013), pp. 403–440.

[45] BRUNEAUX, G. "Liquid and vapor spray structure in high-pressure common rail diesel injection". *Atomization and Sprays* 11.5 (2001).

[46] PICKETT, L. M. et al. "Relationship Between Diesel Fuel Spray Vapor Penetration/Dispersion and Local Fuel Mixture Fraction". *SAE International Journal of Engines* 4.1 (2011), pp. 764–799.

[47] REITZ, R. D. "Atomization and other breakup regimes of a liquid jet". PhD thesis. Princeton Univ., NJ, 1978.

[48] GRANT, R. P. and S. MIDDLEMAN. "Newtonian jet stability". *AIChE Journal* 12.4 (1966), pp. 669–678.

[49] SCHNEIDER, B. M. "Experimentelle Untersuchungen zur Spraystruktur in transienten, verdampfenden und nicht verdampfenden Brennstoffstrahlen unter Hochdruck". *Ph. D. Thesis* (2003).

[50] REITZ, R. and F. BRACCO. "Mechanisms of breakup of round liquid jets". *Encyclopedia of fluid mechanics* 3 (1986), pp. 233–249.

[51] BUCKINGHAM, E. "Model experiments and the form of empirical equations." *Trans. ASME.* 1915.

[52] RANZ, W. E. "Some experiments on orifice sprays". *The Canadian Journal of Chemical Engineering* 36.4 (1958), pp. 175–181.

[53] STERLING, A. M. and C. SLEICHER. "The instability of capillary jets". *J. Fluid Mech* 68.3 (1975), pp. 477–495.

[54] MIESSE, C. "Correlation of experimental data on the disintegration of liquid jets". *Industrial & Engineering Chemistry* 47.9 (1955), pp. 1690–1701.

[55] PILCH, M. and C. ERDMAN. "Use of breakup time data and velocity history data to predict the maximum size of stable fragments for acceleration-induced breakup of a liquid drop". *International Journal of Multiphase Flow* 13.6 (1987), pp. 741–757.

[56] HAN, J. and G. TRYGGVASON. "Secondary breakup of axisymmetric liquid drops. I. Acceleration by a constant body force". *Physics of fluids* 11 (1999), p. 3650.

[57] GUILDENBECHER, D., C. LÓPEZ-RIVERA, and P. SOJKA. "Secondary atomization". English. *Experiments in Fluids* 46.3 (2009), pp. 371–402.

[58]   ARCOUMANIS, C., J. WHITELAW, and K. WONG. *Gaseous simulation of diesel-type sprays in a motored engine*. Tech. rep. Warrendale, PA; Society of Automotive Engineers, 1989.

[59]   HIROYASU, H. "Experimental and theoretical studies on the structure of fuel sprays in diesel engines". *ICLASS-91, Gaithersburg, USA* (1991), pp. 17–31.

[60]   WAN, Y. and N. PETERS. "Scaling of spray penetration with evaporation". *Atomization and sprays* 9.2 (1999).

[61]   IYER, V., J. ABRAHAM, and V. MAGI. "Exploring injected droplet size effects on steady liquid penetration in a Diesel spray with a two-fluid model". *International Journal of Heat and Mass Transfer* 45.3 (2002), pp. 519–531.

[62]   FAETH, G. "Evaporation and combustion of sprays". *Progress in Energy and Combustion Science* 9.1 (1983), pp. 1–76.

[63]   MUSCULUS, M. and K. KATTKE. "Entrainment waves in diesel jets". *SAE International Journal of Engines* 2.1 (2009), pp. 1170–1193.

[64]   PASTOR, J., J. LÓPEZ, J. GARCÍA-OLIVER, and J. PASTOR. "A 1D model for the description of mixing-controlled inert diesel sprays". *Fuel* 87.13 (2008), pp. 2871–2885.

[65]   GARCÍA, J. M. "Aportaciones al estudio del proceso de combustión turbulenta de chorros en motores diesel de inyección directa". PhD thesis. Valencia: E.T.S. Ingenieros Industriales. Universidad Politécnica de Valencia, 2004.

[66]   SIEBERS, D. L. "Scaling liquid-phase fuel penetration in diesel sprays based on mixing-limited vaporization". *SAE Paper* 1999-01-0528 (1999).

[67]   DESANTES, J. M., J. J. LOPEZ, J. M. GARCIA, and J. M. PASTOR. "Evaporative diesel spray modeling". *Atomization and Sprays* 17.3 (2007).

[68]   DESANTES, J., J. PASTOR, J. GARCIA-OLIVER, and J. PASTOR. "A 1D model for the description of mixing-controlled reacting diesel sprays". *Combustion and Flame* 156.1 (2009), pp. 234–249.

[69]   BORÉE, J., N. ATASSI, G. CHARNAY, and L. TAUBERT. "Measurements and image analysis of the turbulent field in an axisymmetric jet subject to a sudden velocity decrease". *Experimental thermal and fluid science* 14.1 (1997), pp. 45–51.

[70]   MUNIZ, L. and M. MUNGAL. "Effects of heat release and buoyancy on flow structure and entrainment in turbulent nonpremixed flames". *Combustion and Flame* 126.1 (2001), pp. 1402–1420.

[71] HIROYASU, H. and M. ARAI. "Structures of fuel sprays in diesel engines". *SAE transactions* 99.3 (1990), pp. 1050–1061.

[72] CORREAS, D. "Estudio teórico-experimental del chorro libre diesel isotermo". PhD thesis. Tesis doctoral, Depto. de Máquinas y Motores Térmicos, Universidad Politécnica de Valencia, España, 1998.

[73] PICKETT, L. M., J. MANIN, R. PAYRI, M. BARDI, and J. GIMENO. "Transient rate of injection effects on spray development". *SAE Paper* 2013-24-0001 (2013).

[74] HAY, N. and P. JONES. *Comparison of the various correlations for spray penetration*. Society of Automotive Engineers, 1972.

[75] DENT, J. *A basis for the comparison of various experimental methods for studying spray penetration*. Society of Automotive Engineers, 1971.

[76] WAKURI, Y., M. FUJII, T. AMITANI, and R. TSUNEYA. "Studies on the penetration of fuel spray in a diesel engine". *Bulletin of JSME* 3.9 (1960), pp. 123–130.

[77] FORSTALL, W. and A. SHAPIRO. "Momentum and mass transfer in coaxial gas jets". *J. Appl. Mech.* 72 (1950), pp. 399–408.

[78] PAYRI, R., F. J. SALVADOR, J. GIMENO, and V. SOARE. "Determination of Diesel Spray Characteristics in Real Rngine In-Cylinder air Density and Presure Conditions". *Journal of Mechanical Science and technology* 19 (2005), pp. 2040–2052.

[79] REITZ, R. and F. BRACCO. "On the dependence of spray angle and other spray parameters on nozzle design and operating conditions". *SAE Paper* 790494 (1979).

[80] DESANTES, J., J. PASTOR, R. PAYRI, and J. PASTOR. "Experimental characterization of internal nozzle flow and diesel spray behavior. part II: Evaporative conditions". *Atomization and sprays* 15.5 (2005), pp. 517–543.

[81] DELACOURT, E., B. DESMET, and B. BESSON. "Characterisation of very high pressure diesel sprays using digital imaging techniques". *Fuel* 84.7 (2005), pp. 859–867.

[82] KAMPMANN, S., B. DITTUS, P. MATTES, and M. KIRNER. "The influence of hydro grinding at VCO nozzles on the mixture preparation in a DI diesel engine". *SAE transactions* 105.3 (1996), pp. 1329–1339.

[83] SALVADOR, F. J. "Estudio teórico experimental de la influencia de la geometría de toberas de inyección Diesel sobre las características del flujo interno y del chorro". PhD thesis. Valencia: E.T.S. Ingenieros Industriales. Universidad Politécnica de Valencia, 2003.

[84]   SOU A.AND MAULANA, M., K. ISOZAKI, S. HOSOKAWA, and A. TOMIYAMA. "Effects of nozzle geometry on cavitation in nozzles of pressure atomizers". *Journal of Fluid Science and Tachnology* 3 (2008), pp. 622–632.

[85]   PAYRI, R., J. GIMENO, P. MARTÍ-ALDAVI, and O. VENEGAS. "Study of the influence of internal flow on the spray behavior under cavitating conditions using a transparent nozzle". *ICLASS 2012* (2012).

[86]   MACIAN, V, R. PAYRI, A. GARCIA, and M. BARDI. "Experimental Evaluation of the Best Approach for Diesel Spray Images Segmentation". *Experimental Techniques* 36.6 (2012), pp. 26–34.

[87]   PASTOR, J. V., J. ARRÈGLE, and A. PALOMARES. "Diesel Spray Image Segmentation With a Likelihood Ratio Test". *Appl. Opt.* 40.17 (June 2001), pp. 2876–2885.

[88]   SIEBERS, D. "Liquid-phase fuel penetration in Diesel sprays". *SAE transactions* 107.3 (1998), pp. 1205–1227.

[89]   ANEJA, R. and J. ABRAHAM. "How far does the liquid penetrate in a diesel engine: Computed results vs. measurements?" *Combustion Science and Technology* 138.1-6 (1998), pp. 233–255.

[90]   MYONG, K., M. ARAI, H. SUZUKI, J. SENDA, and H. FUJIMOTO. "Vaporization characteristics and liquid-phase penetration for multi-component fuels". *SAE Paper* 2004-01-0529 (2004).

[91]   PAYRI, R., J. M. GARCÍA-OLIVER, M. BARDI, and J. MANIN. "Fuel temperature influence on diesel sprays in inert and reacting conditions". *Applied Thermal Engineering* 35 (2012), pp. 185–195.

[92]   BRACCO, F. *Modeling of engine sprays*. Tech. rep. Princeton Univ., NJ (USA). Dept. of Mechanical and Aerospace Engineering, 1985.

[93]   CHEHROUDI, B., S. CHEN, F. BRACCO, and Y. ONUMA. *On the intact core of full-cone sprays*. Tech. rep. Instrument Society of America, Research Triangle Park, NC, 1985.

[94]   LEBAS, R., T. MENARD, P. BEAU, A. BERLEMONT, and F.-X. DEMOULIN. "Numerical simulation of primary break-up and atomization: DNS and modelling study". *International Journal of Multiphase Flow* 35.3 (2009), pp. 247–260.

[95]   FUSTER, D. et al. "Simulation of primary atomization with an octree adaptive mesh refinement and VOF method". *International Journal of Multiphase Flow* 35.6 (2009), pp. 550–565.

[96] DE LA MORENA, J. "Estudio de la influencia de las características del flujo interno en toberas sobre el proceso de inyección Diesel en campo próximo". PhD thesis. Universidad Politécnica de Valencia, 2011.

[97] MANIN, J., M. BARDI, L. PICKETT, R. DAHMS, and J. OEFELEIN. "Development and mixing of diesel sprays at the microscopic level from low to high temperature and pressure conditions". *THIESEL 2012 Conference on Thermo-and Fluid Dynamic Processes in Direct Injection Engines*. 2012.

[98] HEILIG, A., M. KAISER, and F. DINKELACKER. "Near Nozzle High-Speed Measurements of the Intact Core for Diesel Spray". *ICLASS* (2012).

[99] MANIN, J., M. BARDI, L. PICKETT, and R. PAYRI. "Boundary condition and fuel composition effects on injection processes of diesel sprays at the microscopic level". *ILASS Europe* 2013-457 (2013).

[100] MUGELE, R. and H. EVANS. "Droplet size distribution in sprays". *Industrial & Engineering Chemistry* 43.6 (1951), pp. 1317–1324.

[101] JICHA, M., J. JEDELSKY, J. OTAHAL, and J. SLAMA. "Influence of some geometrical parameters on the characteristics of effervescent atomization". *ILASS Europe* (2002).

[102] KRISTENSSON, E. et al. "Analysis of multiple scattering suppression using structured laser illumination planar imaging in scattering and fluorescing media". *Opt. Express* 19 (2011), pp. 13647–13663.

[103] DIGIORGIO, F., D. LAFORGIA, and V. DAMIANI. "Investigation on drop size distribution in the spray of a five-hole vco nozzle at high feeding pressure". *SAE transactions* 104.3 (1995), pp. 205–219.

[104] ARREGLE, J. and J. V. PASTOR. "The influence of injection parameters on diesel spray characteristics". *SAE Paper* 1999-01-0200 (1999).

[105] HIROYASU, H., M. ARAI, and M. TABATA. "Empirical equations for the Sauter mean diameter of a Diesel spray". *SAE Paper* 890464 (1989).

[106] PAYRI, R., L. ARANEO, J. SHAKAL, and V. SOARE. "Phase doppler measurements: system set-up optimization for characterization of a diesel nozzle". *Journal of mechanical science and technology* 22.8 (2008), pp. 1620–1632.

[107] ADLER, D. and W. LYN. "The evaporation and mixing of a liquid fuel spray in a diesel air swirl". *Proceedings of the Institution of Mechanical Engineers, Conference Proceedings*. Vol. 184. 10. SAGE Publications. 1969, pp. 171–180.

[108] PRASAD, C. V. and S. KAR. "An investigation on the diffusion of momentum and mass of fuel in a diesel fuel spray". *Journal of Engineering for Power* 99 (1977), p. 225.

[109]   Desantes, J., R. Payri, F. Salvador, and A. Gil. "Development and validation of a theoretical model for diesel spray penetration". *Fuel* 85 (2006), pp. 910–917.

[110]   Spalding, D. B. *Combustion and mass transfer: a textbook with multiple-choice exercises for engineering students*. Pergamon Press Oxford, 1979.

[111]   Desantes, J., R. Payri, J. Garcia, and F. Salvador. "A contribution to the understanding of isothermal diesel spray dynamics". *Fuel* 86.7 (2007), pp. 1093–1101.

[112]   Espey, C., J. E. Dec, T. A. Litzinger, and D. A. Santavicca. "Planar laser Rayleigh scattering for quantitative vapor-fuel imaging in a diesel jet". *Combustion and Flame* 109.1 (1997), pp. 65–86.

[113]   Cao, Z.-M., K. Nishino, S. Mizuno, and K. Torii. "PIV measurement of internal structure of diesel fuel spray". *Experiments in fluids* 29.1 (2000), S211–S219.

[114]   Hurn, R. and K. Hughes. "Combustion characteristics of diesel fuels as measured in a constant-volume bomb". *SAE transactions* 6 (1952), pp. 24–35.

[115]   Kamimoto, T., H. Yokota, and H. Kobayashi. *Effect of high pressure injection on soot formation processes in a rapid compression machine to simulate diesel flames*. Tech. rep. Society of Automotive Engineers, Warrendale, PA, 1987.

[116]   Dec, J. and C. Espey. "Chemiluminescence imaging of autoignition in a DI diesel engine". *SAE Paper* 982685 (1998).

[117]   Higgins, B., D. Siebers, and A. Aradi. "Diesel-spray ignition and premixed-burn behavior". *SAE Paper* 2000-01-0940 (2000).

[118]   Lillo, P., L. Pickett, H. Persson, O. Andersson, and S. Kook. "Diesel Spray Ignition Detection and Spatial/Temporal Correction". *SAE International Journal of Engines* 5.3 (2012), pp. 1330–1346.

[119]   Westbrook, C. K. et al. "The effects of pressure, temperature, and concentration on the reactivity of alkanes: Experiments and modeling in a rapid compression machine". *Symposium (International) on Combustion*. 1998, pp. 371–378.

[120]   Gaydon, A. *The spectroscopy of flames*. Chapman & Hall London, 1957.

[121]   Pickett, L. M., D. L. Siebers, and C. A. Idicheria. "Relationship Between Ignition Processes and the Lift-Off Length of Diesel Fuel Jets". *SAE Paper* 2005-01-3843 (2005).

[122] AGGARWAL, S. "A review of spray ignition phenomena: present status and future research". *Progress in Energy and Combustion Science* 24.6 (1998), pp. 565–600.

[123] KOBORI, S., T. KAMIMOTO, and A. ARADI. "A study of ignition delay of diesel fuel sprays". *International Journal of Engine Research* 1.1 (2000), pp. 29–39.

[124] BRUNEAUX, G. "Development of optical diagnostic techniques to correlate mixing and auto-ignition processes in high pressure Diesel jets". *Oil and Gas Science and Technology-Revue de l'IFP* 63.4 (2008), pp. 461–477.

[125] HERNÁNDEZ, J., J. SANZ-ARGENT, J. CAROT, and J. JABALOYES. "Ignition delay time correlations for a diesel fuel with application to engine combustion modelling". *International Journal of Engine Research* 11.3 (2010), pp. 199–206.

[126] PAYRI, R., F. SALVADOR, J. GIMENO, and J. DE LA MORENA. "Influence of injector technology on injection and combustion development - Part 2: combustion analysis". *Applied Energy* 88.4 (2011), pp. 1130–1139.

[127] BENAJES, J., R. PAYRI, M. BARDI, and P. MARTI-ALDARAVI. "Experimental characterization of diesel ignition and lift-off length using a single-hole ECN injector". *Applied Thermal Engineering* 58.1-2 (2013), pp. 554–563.

[128] HIGGINS, B. and D. SIEBERS. "Measurement of the flame lift-off location on DI diesel sprays using OH chemiluminescence". *SAE Paper* 2001-01-0918 (2001).

[129] DEC, J. *A conceptual model of DI diesel combustion based on laser-sheet imaging*. Society of Automotive Engineers Warrendale, PA, 1997.

[130] DEC, J. and E. COY. *OH radical imaging in a DI diesel engine and the structure of the early diffusion flame*. Tech. rep. Sandia National Labs., Albuquerque, NM (United States), 1996.

[131] DEC, J. E. and R. E. CANAAN. "PLIF Imaging of NO Formation in a DI Diesel Engine1". *SAE Paper* 980147 (1998).

[132] KOSAKA, H. et al. "Simultaneous 2-D imaging of OH radicals and soot in a diesel flame by laser sheet techniques". *SAE Paper* 960834 (1996).

[133] MUSCULUS, M., T. LACHAUX, L. PICKETT, and C. IDICHERIA. "End-of-injection over-mixing and unburned hydrocarbon emissions in low-temperature-combustion diesel engines". *SAE Paper* 2007-01-0907 (2007).

[134] PETERS, N. *Turbulent combustion*. Cambridge university press, 2000.

[135] KALGHATGI, G. T. "Lift-off heights and visible lengths of vertical turbulent jet diffusion flames in still air". *Combustion Science and Technology* 41.1-2 (1984).

[136] WINKLHOFER, E. "An experimental database for diesel spray combustion". *Symposium (International) on Combustion*. Vol. 26. 2. Elsevier. 1996, pp. 2541–2547.

[137] LARSSON, A. "Optical studies in a DI diesel engine". *SAE transactions* 108.4 (1999), pp. 2137–2155.

[138] SIEBERS, D. L. and B. HIGGINS. "Flame lift-off on direct-injection diesel sprays under quiescent conditions". *SAE Paper* 2001-01-0530 (2001).

[139] SIEBERS, D. and B. HIGGINS. "Effects of injector conditions on the flame lift-off length of DI diesel spray". *Thermo-and fluid Dynamic Processes in Diesel Engines* (2000), pp. 253–277.

[140] MENDEZ, S. and B. THIROUARD. "Using multiple injection strategies in diesel combustion: potential to improve emissions, noise and fuel economy trade-off in low CR engines". *Technology* 2013 (2008), pp. 04–08.

[141] FAVENNEC, A.-G. and D. FRUMAN. "Effect of the needle position on the cavitation of Diesel injectors". *Proceedings of the 3rd ASME-JSME Joint Fluids engineering conference* FEDSM99-7044 (1999).

[142] ARCOUMANIS, C., H. FLORA, M. GAVAISES, N. KAMPANIS, and R. HORROCKS. "Investigation of cavitation in a vertical multi-hole Diesel injector". *SAE Paper* 1999-01-0524 (1999).

[143] BADOCK, C., R. WIRTH, A. FATH, and A. LEIPERTZ. "Investigation of cavitation in real size diesel injection nozzles". *International Journal of Heat and Fluid Flow* 20.5 (1999), pp. 538–544.

[144] MIRANDA, R., H. CHAVES, U. MARTIN, and F. OBERMEIER. "Cavitation in a transparent real size VCO injection nozzle". *Proceedings of ICLASS, Sorrento Italy* (2003).

[145] BLESSING, M., G. KONIG, C. KRUGER, U. MICHELS, and V. SCHWARTZ. "Analysis of Flow and Cavitation Phenomena in Diesel Injection Nozzles and Its Effects on Spray and Mixture Formation". *SAE Paper* 2003-01-1358 (2003).

[146] MASUDA, R. "Validation of diesel fuel spray and mixture formation from nozzle internal flow calculation". *SAE Paper* 2005-01-2098 (2005).

[147] LEE, J. et al. "Effect of piezo-driven and solenoid-driven needle opening of common-rail diesel injectors on internal nozzle flow and spray development". *International Journal of Engine Research* 7.6 (2006), pp. 489–502.

[148] CHIAVOLA, O. and F. PALMIERI. "Modeling needle motion influence on nozzle flow in high pressure injection system". *SAE Paper* 2007-01-0250 (2007).

[149] GUIDE, O. U. "Version 16". *Chicago, IL: SPSS Inc* (1990).

[150] STEGEMANN, J., J. SEEBODE, J. BALTES, C. BAUMGARTEN, and G. MERKER. "Influence of throttle effects at the needle seat on the spray characteristics of a multihole injection nozzle". *ILASS Europe* (2002).

[151] JUNEJA, H., Y. RA, and R. REITZ. "Optimization of injection rate shape using active control of fuel injection". *SAE Paper* 2004-01-0530 (2004).

Chapter 4

Materials and methods

4.1 Introduction

In this thesis, a prototype injector was used to study the effect of partial needle lift and injection rate shaping on the injection/combustion event: the novelty of the injector design, as well as the lack of exhaustive information in literature about the phenomena studied, underlined the need of performing an extensive experimental characterization of the injector.

The injector has been studied under different aspects: the rate of injection (*ROI*) and of momentum (*ROM*) have been measured to assess the general features of the injector and to investigate the hydraulic behavior of the nozzle at partial needle lift. However, the central part of this work is focused on the study of the spray formation and development in inert and reacting conditions employing a wide range of optical diagnostics.

The aim of this chapter is to give an accurate description of the experimental approach, presenting the principles of methodologies employed together with the details of the arrangements and processing followed to obtain the final data. The main experimental diagnostics applied can be divided in three groups based on the focus of the measurement:

- internal flow: these measurements aim at the understanding of the flow within the nozzle, before the fuel exits from the nozzle. This group includes rate of injection and rate of momentum measurements, and the hydraulic characterization of the nozzle that can be obtained by the combination of these two techniques [1];

- spray development and evaporation: in this phase the macroscopic features of the spray were studied. Spray penetration has been measured at isothermal (S_l) and evaporative conditions (S_v) detecting the liquid and the vapor phase contours of the spray. Other characteristic parameters, like liquid length (LL), spray spreading angle (θ) and spray axis inclination (γ), were measured and used for the analysis. In order to focus the attention on the spray development, in these tests the combustion was avoided by injecting the spray in nitrogen atmosphere [2, 3];

- spray ignition and flame development: this last group of tests was focused on the characterization of the spray combustion at Diesel-like condition [4]. First- and second-stage ignition delay (respectively τ_{cf} and τ_{SSI}) were analyzed together with the characteristic parameters of the diffusive phase of the combustion: lift-off length (LOL), flame temperature and soot distribution. To this end, *CH** and *OH** radicals chemiluminescence imaging was combined with the two-color optical pyrometry (*2C*).

While the internal flow was studied in test rigs devoted to each specific measurement, the latter two groups of tests can be classified as *optical diagnostics* and were performed in an optically accessible high-temperature high-pressure vessel [5].

This chapter is structured in five sections. The first section presents the fuel high pressure system, that is the common element of all the tests performed. The second one details the test rigs employed for the hydraulic characterization (mass flow rate and spray momentum). The third section addresses the description of the high-temperature high-pressure facility employed for the optical diagnostics, while the fourth section details these diagnostics by presenting the optical arrangements and the processing methods employed. The last section presents an overview of the parametric variations performed.

4.2   Injection system

The fuel is supplied to the injector by a common-rail system constituted by a high pressure pump (Bosch *CP4*), two conventional rails mounted in line and a flow regulator mounted on the second one (Fig.4.1). The choice of mounting two rails was made in order to solve problems with high-pressure fittings and, at the same time, to increase the volume of the high pressure system reducing the fluctuation due to the pump cycles. The system was adapted to laboratory use and features temperature control. This is necessary because of two reasons: the first one is to
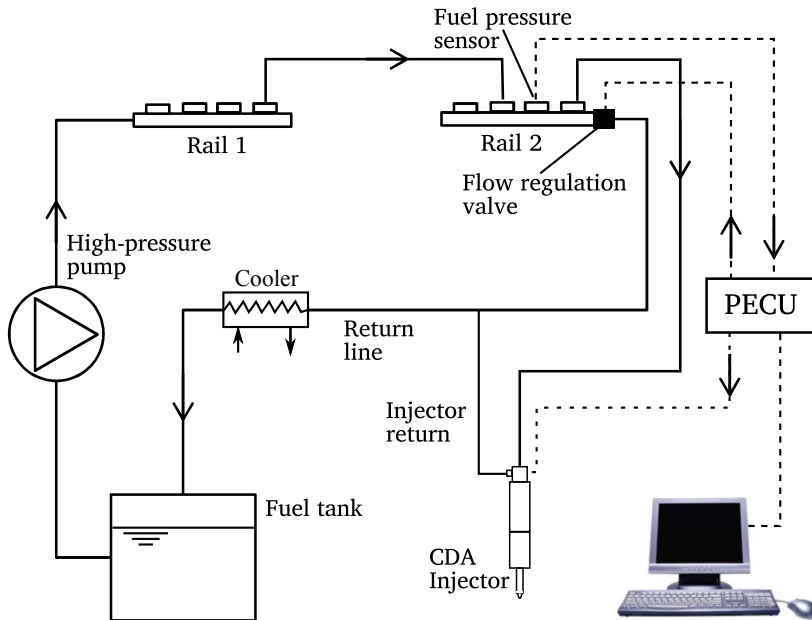
Figure 4.1: Sketch of the fuel high pressure system together with the injector and the PECU.

have all the variables under control while experiments are performed, the second one is the fuel injection amount, which is very low, thus there is a high proportion returning to the fuel tank, causing a gradual temperature rise. This is avoided using a well designed intercooler placed between the returning lines and the fuel tank.

A programmable engine control unit (*PECU*) was used to control all the settings of the injection system: on one side, a closed loop was formed by the pressure sensor and the flow regulation valve, installed in the rail and controlling the pressure in the rail (injection pressure or p_i); on the other hand, the *PECU* was mapped with the shape of the electrical signal (voltage signal) to be sent to the injector at the different condition tested. This last point is of particular importance to optimize the control on the *CDA* as discussed in Sec. 2.5.

The direct acting injector used in this study (see Sec.2.5) is fitted with a 7-hole nozzle: the orifices are equally separated and oriented with 156° opening angle, and they have outlet diameter $D_0 = 156\,\mu$m and *k–factor* = 1.5. All the nominal features of the injector are listed in Tab. 4.1. Even though the *CDA* injector is able to control the needle position, the exact needle lift and its relationship with the

controlled parameter *charge* (*Ch*) could not be determined. Not being possible to measure the real needle lift, the hydraulic characterization was employed to quantify the relationship between mass flow rate and piezo-stack charge.

The temperature of the piezo-actuator was controlled endowing all the facilities used for the tests with a liquid cooled injector holder, keeping the temperature of the liquid constant (343 K) by means of a closed loop PID.

Injector features	
Brand	*Continental*
Nozzle seat type	*micro-sac*
Number of orifices	7
Spray included angle [°]	158
Outlet diameter [mm]	0.156
k-factor[I]	*1.5*
Discharge coefficient	*0.81*[II]

Table 4.1: Nominal features of the CDA injector nozzle.

Finally, commercial Diesel fuel was used (EU standard EN590) with 812 kg/m³ density and 1.9 mm²/s kinematic viscosity (at 343 K). A sketch of the injection system employed is presented in Fig. 4.1.

4.3   Internal flow characterization

The experimental characterization of the internal flow is based on the measurement of the fuel mass flow rate (rate of injection or *ROI*) and spray momentum flux (rate of momentum or *ROM*). Combining these two direct measurements, important flow variables can be obtained, such as the flow effective velocity at the hole outlet (u_{eff}) and the effective flow area (A_{eff}). Moreover, several coefficients necessary for further spray analysis are measured: discharge coefficient (C_d), velocity coefficient (C_v) and area coefficient (C_a). These variables have already been presented in Sec. 3.2. The test rigs employed in these measurements are presented in the following section.

[I]Defined in Sec. 3.2.

[II]Nominal value. The discharge coefficient will be determined for each test condition experimentally.

4.3.1   Rate of injection measurement

The purpose of these tests is to determine the rate of injection curve. The equipment used allows to measure and record the data, describing the chronological evolution of the fuel mass flow rate during an individual injection event.

Mass flow rate measurements are carried out using the Injection Rate Discharge Curve Indicator (IRDCI) which uses the Bosch method [6]; it is known as the long tube method and it is the most widely used instrument for that purpose, due to the good dynamic response for capturing the mass flow signal, offering high efficiency. Fig. 4.2 illustrates the mass flow rate equipment. The measuring principle is based on the theory of pressure wave propagation in a liquid column.
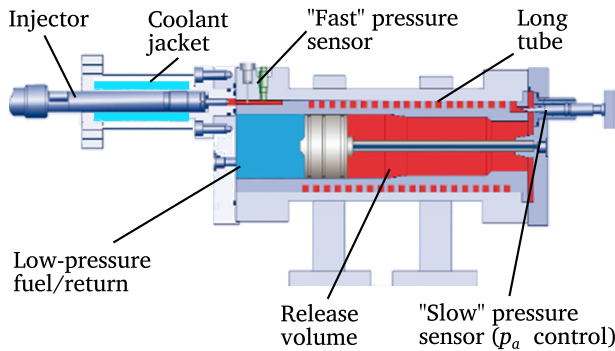
Figure 4.2: Sketch of the injection rate discharge curve indicator and the main parts composing the apparatus.

The injector is located in the cooled injector holder (as shows Fig. 4.2) and it discharges the fuel within the IRDCI, whose internal volume is comprised by a long tube and a deposit. At testing conditions, the whole internal volume is filled with fuel in order to have an accurate control on the pressure wave propagation. The pressure within the IRCDI is adjusted to simulate the pressure within a real engine combustion chamber (p_a) through a flow valve controlled by a PID, which guaranties controlled and steady pressure conditions before the start of the injection.

The beginning of the injection process generates a pressure wave that travels with a velocity equal to the speed of sound, from the nozzle tip to a small fuel deposit where it is damped. The pressure wave causes a pressure variation that is related to the liquid flow velocity by the Allievi equation (Eq. (4.1)) valid for a simple pressure wave in steady flows,

$$\Delta p = c \, \rho_f \, u \ , \tag{4.1}$$

where Δp is the pressure increment due to the injection with respect to the steady pressure, c is the fuel speed of sound, ρ_f is the fuel density and u is the liquid fuel velocity at the orifice outlet. This pressure variation is registered by a piezoelectric sensor located as close as possible to the nozzle tip (approximately, 33 mm from the nozzle tip) for two reasons: to avoid a delay between the injection event and the acquisition time and to avoid friction attenuation effects that could affect the measurement. Therefore, the injector must be placed directly on the tube with constant diameter, avoiding any extra volume that could perturb the wave propagation generated by the injection. The propagation wave moves towards the fuel deposit that has the function of limiting the global pressure increase during the injection event; when the wave reaches the deposit inlet, the higher transverse area generates a reflected wave that travels in the direction opposite to the main wave. In order to avoid any interaction between the original and the secondary waves, that could perturb the real signal, the length of the tube should be designed adequately. The calculation of the pipe length is done assuming that the reflected wave reaches the pressure sensor after the injection event finishes.

The signal directly obtained with this equipment is a pressure measurement proportional to the instantaneous mass flow rate; thus, the injection rate is obtained as

$$\dot{m}(t) = \frac{A_p \Delta p}{c} \quad , \tag{4.2}$$

where $\dot{m}$ is the injection rate, A_p is the tube cross-sectional area and Δp is the pressure increment measured during the injection.

The advantage of the Bosch method is the simplicity of the apparatus needed, not containing any moving elements or electro-mechanic actuators, and the robustness of the method: in fact, the injection rate is obtained directly by the pressure increment measurement in the tube and the only parameter necessary is the speed of sound in the fluid at the testing conditions. The speed of sound depends on the composition, pressure and temperature of the fuel and must be determined by specific tests.

With the purpose of corroborating the total injected mass quantity obtained with the IRDCI, a scale is placed downstream of the device. All the fuel flow passing through the apparatus, is measured with a balance during a certain time; that value should correspond to the integral of the mass flow rate for the correspondent number of injection events. To obtain a good estimation of the experimental errors, several repetitive measurements were carried out at the same test point (energizing time, rail pressure, and back-pressure), and it was found that it was less than 0.6% ($\sigma < 0.6\%$), as is explained in details in [7]. The signal

produced by the piezoelectric sensor was passed through a charge amplifier and then recorded by an analogue to digital converter (ADC) working at high acquisition rate (100 kHz). The *ROI* signal is recorded together with the instantaneous rail pressure, the voltage and the intensity of the energization signal are used to control the needle movement. For each test conditions 50 injection events were recorded in order to obtain a reliable indication of the average value and of the shot-to-shot dispersion [7]. Moreover, a characteristic mass flow rate value $\dot{m}_{av}$ was obtained for each test conditions, calculating the average of the measured variable $\dot{m}$ along the steady part of the injection for an interval of $2 - 2.7$ ms after the start of the injection (*ASOI*).

4.3.2   Rate of momentum measurement

The spray momentum for all the *CDA* orifices was measured in a specific device designed at CMT-Motores Térmicos. The spray momentum rate meter (*SMM*) is fully described in Gimeno's Ph.D. thesis [1].
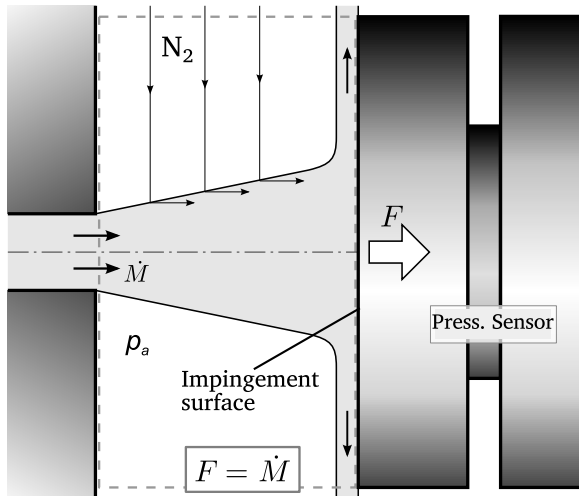
Figure 4.3: Scheme of the experimental setup used for the momentum flux measurements.

The measuring principle of the *SMM* is illustrated in Fig. 4.3. The final part of the orifice and the direction of the fuel flow are depicted on the left part of the figure; the piezo-electric sensor is on the right side and its impingement surface is placed perpendicular to the orifice axis (and therefore, to the fuel flow). This sensor measures the force applied by the diesel spray on the impingement surface.

In order to theoretically describe the measurement, a control volume between the nozzle and the sensor is indicated (*CV*). Neglecting the contribution of the gravitational acceleration, it can be assumed that within this volume there is a uniform ambient pressure. Moreover, in the control volume there are quiescent conditions and the momentum of the surrounding gas is assumed to be zero. Taking into account the last assumptions and considering that the fuel deflected is perpendicular to the axis direction, the total force produced by the spray impact on the impingement surface *F* can be written as

$$F = \frac{\partial}{\partial t} \int_{CV} \rho v \, d\varpi + \dot{M} \quad. \tag{4.3}$$

where $d\varpi$ is the differential of the surface surrounding the control volume *CV*, and ρ and v, in this case, are respectively the local density and velocity of the mixture passing through the control volume surface. The first term on the right side of Eq. (4.3) takes into account the momentum variations within the *CV* (accumulation) and $\dot{M}$ represents the momentum flux at the orifice outlet. Assuming steady state conditions, the accumulation term is canceled and Eq.(4.3) can be simplified in the expression below:

$$F = \dot{M} \quad. \tag{4.4}$$

This assumption is always true when the sensor frontal area and position are selected so that the spray area is much smaller than the impingement surface and the fuel is deflected perpendicularly to the spray axis.

In Fig. 4.4 a global sketch of the *SMM* is presented: the spray is injected into a chamber that can be pressurized with nitrogen to simulate the discharge pressure typical of typical Diesel engine conditions (up to 8 MPa). The pressure is controlled manually by the user, acting either on a release valve or feeding more nitrogen into the chamber. The impact force is measured with a calibrated piezo-electric pressure sensor placed at about 6 mm from the orifice outlet: reminding the hypothesis of quiescent conditions in the chamber, $\dot{M}$ is expected to be independent on the axial location; however, a too large distance would require an excessive impingement surface to guarantee the hypothesis of perpendicular deflection, while too short separation would cause excessive wear of the impingement surface and interaction with other sprays in case of multi-orifice nozzle.

The *SMM* is designed to test with both axial-hole and conventional multi-hole injectors, featuring different possibilities for the respective location of the injector and the sensor. In the case of the *CDA* (7-hole nozzle), the injector and the sensor
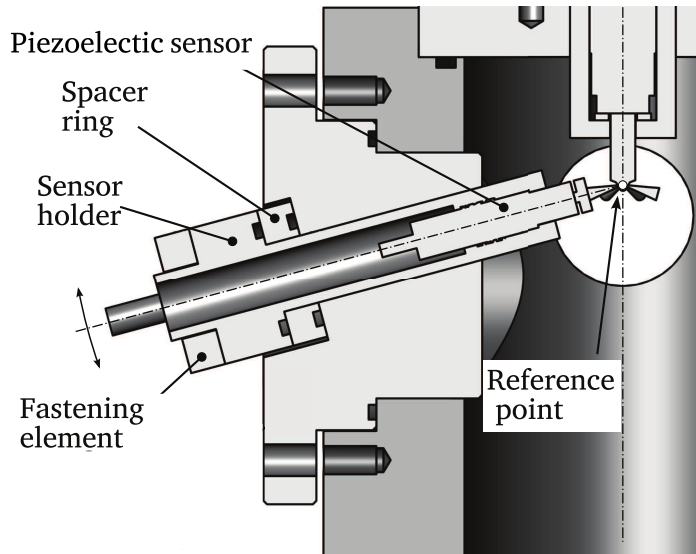
Figure 4.4: Sketch of the test rig used spray momentum rate measurement.

were placed as illustrated in Fig. 4.4 and each orifice was tested rotating the injector around its axis.

As for the mass flow rate, the signal produced by the piezoelectric sensor was passed through a charge amplifier and then recorded by an *ADC* at 100 kHz, as for the *ROI* tests. The momentum signal is recorded together with the instantaneous rail pressure, the voltage and the intensity of the energization signal controlling the needle movement. For each test conditions, 50 injection events were recorded in order to obtain a reliable indication of the average value and of the shot-to-shot dispersion. The details of the averaging methodology and the signal treatment are described by Payri et al. in [7]. As for *ROI* measurements, a characteristic spray momentum value $\dot{M}_{av}$ was obtained for each test conditions, calculating the average of the the measured variable $\dot{M}$ along the steady part of the injection: also in this case the interval chosen is between 2 and 2.7 ms *ASOI*.

4.4 High-temperature and high-pressure test rig

A novel high-temperature and high-pressure test chamber, capable of mimicking the Diesel in-cylinder conditions at the time of injection, was used to enable the application of different optical diagnostics. Following the convention presented by Baert et al. [5], the test rig is classified as a constant-pressure flow (*CPF*)

facility since the Diesel-like conditions are reached by means of a continuous flow of high temperature high pressure gas through the test chamber.

Compared to other facilities, this test rig has the unique feature of obtaining nearly quiescent and steady thermodynamic conditions in the test section, providing an important reduction in the time required for the tests and an improved control on the boundary conditions. The chamber is endowed with three large windows (128 mm in diameter) placed orthogonally to give full optical access to the test section. In Tab. 4.2 the main features of the test rig are summarized.

Facility type	*CPF*
Chamber diameter [mm]	200
Chamber height [mm]	250
Window diameter [mm]	128
Max. pressure [MPa]	150
Max. Temperature [K]	1000
Max. density (at 900 K) [kg/m^3]	53
Main heater power [kW]	30
Gas velocity [m/s]	<0.3

Table 4.2: Main features of the optical accessible high-temperature high-pressure facility.

In order to work properly, the test chamber has to be completed with the other auxiliary component forming the facility. The facility is composed of four parts: gas compressors, gas heaters, test vessel and control system. A global sketch of the layout is shown Fig. 4.5. The gas, stored by volumetric compressors in high pressure reservoirs, flows continuously through the test chamber. Electrical heaters, placed upstream of the chamber, increase the temperature of the gas flowing through the test section at the desired temperature. The control system is a closed loop PID that adjusts both the pressure in the chamber and the power of the heaters to obtain the test conditions required for the experiments. Further details about each part of the facility are given in the following sections.

4.4.1   Gas circuit

The facility relies on the continuous flow of high-pressure high-temperature gas through the test chamber. To this end, the test chamber is framed in a circuit that, in first place, provides the gas feeding to the test chamber, but also, enables an accurate control of the test conditions.
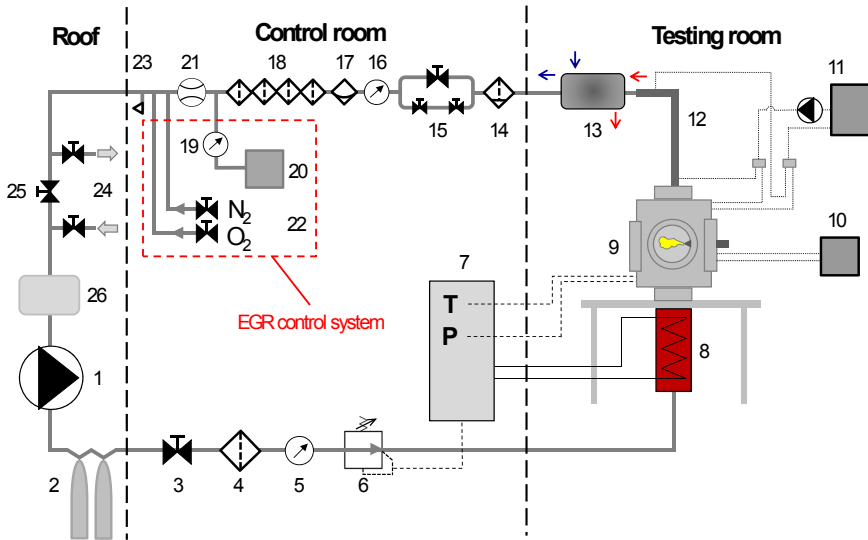
Figure 4.5: Sketch of the facility layout. The main components of the test rig facility are presented together with the path followed by the continuously flowing gas. 1) air compressors, 2) high pressure tanks, 3) main valve, 4) high pressure filter, 5) pressure gauge 6) pressure regulator 7) PLC control system 8) main heater, 9) test chamber, 10) injector cooling system, 11) test rig cooling system, 12) heat exchanger, 13) heat exchanger 14) high pressure filter with drain, 15) flow regulation valve, 16) pressure gauge, 17) centrifugal filter, 18) group of 4 low pressure filters, 19) pressure gauge, 20) broadband O_2 sensor, 21) flow meter, 22) oxygen/nitrogen reintegration, 23) low pressure drain, 24) open circuit valve ext, 25) open circuit valve int, 26) low pressure tank.

Two volumetric compressors work in parallel and provide a continuous feeding of maximum $70\,\mathrm{Nm^3/h}$; each compressor is composed by two parallel modules that can be activated independently: in this way the gas flow can be incremented from 0 to $70\,\mathrm{Nm^3/h}$ in four discrete steps. The design of the compressors guarantees negligible variation (lower than 10%) in the output flow when the pressure downstream is varied.

Two high pressure tanks (total volume $0.1\,\mathrm{m^3}$) receive the gas from the compressors and allow to partially decouple the output of the compressors from the gas entering the test chamber. This fact allows temporary variation of the gas flow through the test chamber during the test rig operations without acting on the compressors.

To avoid over-heating of the resistance constituting the main heaters, a minimum gas flow is needed. The regulation of the gas-flow through the chamber and the chamber pressure are controlled by two valves, one upstream and one downstream of the chamber. The upstream pressure reducer (Tescom $44-1300$) is operated by the control module, that adjusts its actuation to match the set-point pressure configured by the user with the pressure measured by a piezo-resistive sensor within the chamber. This valve performs a fine regulation maintaining constant the pressure within the chamber independently from the gas flow.

The second valve, placed downstream of the chamber, is manually regulated by the user, based on the reading of a thermal mass flow rate meter (Brooks $5800S$) placed downstream of the chamber. In practice, once the setpoint pressure has been reached, the flow regulation needs only small adjustments to compensate changes in the temperature of the gases or the thermal dilatation of the flow control valve.

Important components of the gas circuit are the two heat-exchangers, needed to reduce the temperature of the gas right at the chamber exit (Fig. 4.5 n. 12 and 13). A tubular counter-current heat-exchanger is placed right at the chamber outlet and it is encharged to reduce the gas temperature to about 150°C: this temperature is below the temperature limit provided by the high pressure pipes data sheet and therefore their mechanical resistance is guaranteed. The second heat exchanger, shell and tube type, is placed further downstream and its function is to further reduce the gas temperature at a health safe limit (about 40°C).

The facility is also designed to simulate *EGR* conditions. To this end, the circuit can be set in two different configurations by acting on the open/closed loop valves (see Fig. 4.5) in order to control the oxygen content within the chamber:

- open loop: this configuration enables testing with atmospheric air at 21% oxygen. Atmospheric air will be fed to the compressors while the test rig outlet will be discharged. In this case, the gas composition is not measured since it is considered to be constant.

- closed loop: in this case the oxygen concentration can be reduced to test with an oxygen concentration ranging between $0-21\%$. When testing in closed loop, the discharged gas is recirculated: the gas oxygen content is measured through a broadband lambda sensor placed downstream of the test chamber and it can be adjusted adding either pure nitrogen or air by the reintegration system.

4.4.2 Heating system

The extreme thermodynamic conditions reached in the chamber require very high performances in terms of heating power and thermal insulation. The test rig is equipped with three different heating components:

- main heater: It is placed right upstream of the chamber and it is comprised by two electric heating modules (Leister model $L10000DF$) of 15 kW maximum power each. The two heaters are three-phase powered and are mounted in cascade along the gas flow. The heating element is composed of several coiled wires of resistive material, mounted in a ceramic structure where the flow is forced to pass through (Fig. 4.6). The maximum temperature of the gas allowed at the heater outlet is 1173 K, due to the melting limit of the coils. The power fed to the resistances is controlled by the control module, which through a PID matches the output temperature to the set-point selected by the user. At these extreme conditions, the temperature of the coils is the real limiting factor of the heater and it is the result of the balance between the heat power supplied by the coils and the heat power exchanged with the flowing gas by convection-radiation: hence, a decrease in the gas flow causes a reduction of the heat transferred to gas, leading to a dangerous increase of the coil temperature.
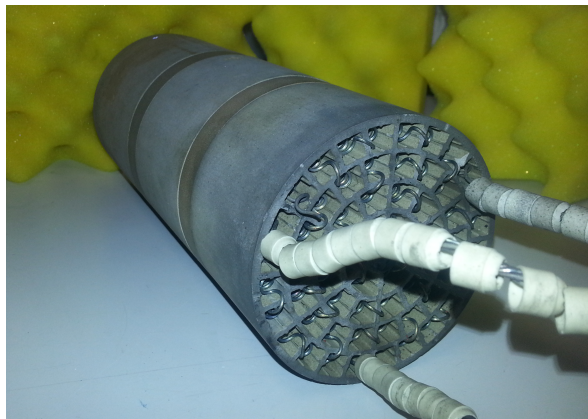
Figure 4.6: Picture of one module of the main heaters. The picture shows the ceramic structure, the resistive coils and the three electric connections.

- chamber liner: the important difference in temperature between the gas within the chamber and the room temperature causes significant heat losses

through the chamber walls that are finally reflected as temperature gradi-
ents within the chamber. To reduce this effect, a heating liner (3 kW) sur-
rounds the inner chamber of the test rig, increasing the temperature of the
walls of the chamber. At the same time, a double layer configuration has
been designed to improve the thermal insulation of the chamber and limit
the temperature of the outer walls of the test rig. The inner walls have
the function of *containing* the hot gas of the test section, avoiding any gas
flow at the outer walls surface. On the other hand, the outer walls have
the structural function of bearing the forces derived from the high pressure
of the gas contained. The same double-layer configuration is used for the
windows.

• the bottom heater: even though the gas flow is constant, in these high
density-high temperature conditions the buoyancy and the temperature
stratification in the chamber must not be neglected. To avoid this prob-
lem and to increase the temperature homogeneity in the test section, an
electric heater is placed in the bottom of the chamber (Fig. 4.7). This
heater supplies 2.5 kW and it is controlled manually by the user.
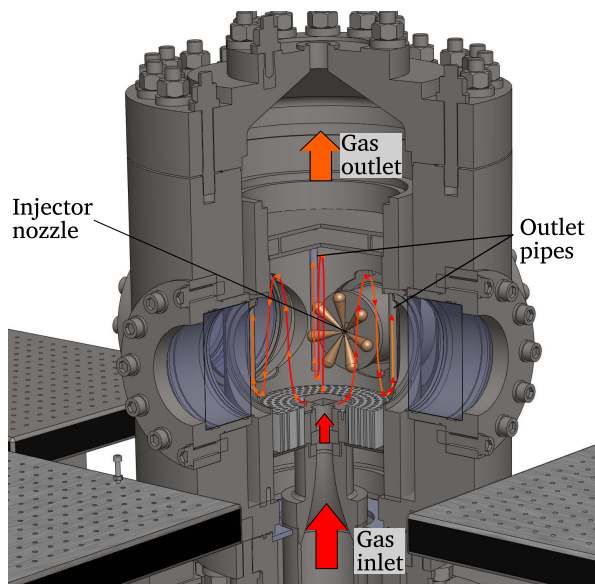
*Figure 4.7: Section view of the test chamber. The test chamber is presented together
with the lines representing the gas flow.*

4.4.3 Test chamber

The test chamber is the core of the test rig. The chamber has to accomplish different requirements:

- support high inner pressures up to 15 MPa and manage a high temperature gas flow (up to 1000 K);

- obtain a wide volume (about 6 L) in which the thermodynamic conditions are spatially and temporally steady;

- guarantee a complete optical access to the chamber to enable the application of the highest range of optical diagnostics.

Keeping in mind the three points above, most of the characteristics of the chamber already described can be justified: the double layer configuration, the liner and bottom heater and the thickness of the outer shell and windows. In this section, further characteristics of the test chamber will be discussed more in detail. Three large round windows (128 mm diameter) are placed orthogonally to give full optical access to the test section (c.f. Fig. 4.7 right). The material used is fused silica, a high purity quartz which combines high mechanical characteristics with optical properties. The big size of the test chamber (200 mm diameter) and the conical shape of the wall behind the injector nozzle minimize spray-wall interaction and allow studying spray development in free field-like conditions.

The gas-flow through the test chamber has been optimized in order to obtain the best compromise in terms of temperature homogeneity and gas-spray interaction. To improve the temperature homogeneity within the chamber, the velocities of the gas have to be high in order to limit the wall boundary layer and maintain the test section at high temperature. On the other hand, to study the spray in free-field-like conditions, the velocities have to be low. In Fig. 4.7 a sketch of the chamber is shown: the gas inlet is a reverse-cone diffuser placed in the bottom; due to its lower density the inlet gas goes toward the upper part of the chamber; then, after a small cool down due to the heat-exchange with the surrounding walls, the gas is forced to move toward the only available outlets, which are placed close to the walls in the bottom of the chamber. The position of the outlets in the bottom of the chamber improves heating efficiency, since it extracts the gas in a relatively cold position. The sealing between the different components of the chamber is provided by O-rings: to avoid these components to be damaged by the high temperature several cooling channels have been designed close to the sealing elements.

4.4.4   Temperature control

Thermocouples are normally considered simple and low-cost devices to measure temperature with good accuracy in steady environments. However, corrections are necessary when thermal radiation exchange is significant. Thermal radiation at ambient temperature is negligible but becomes more significant as the temperature of the gas and of the surrounding wall increases.

In the case of the measurements performed in the *CPF*, the heat-exchange by radiation (between the thermocouple junction and the surrounding walls) cannot be neglected, since the wall temperatures is about $80 - 100 \, \mathrm{K}$ lower than the ambient gas temperature and the radiation term is proportional to the forth power of the temperature [8]. To account for radiation errors, a probe consisting of different thermocouple diameters is used to define the required radiation corrections.

The ratio between the heat exchanged by convection and the heat exchanged by radiation varies depending on the thermocouple diameter. The measurement aims to estimate the real temperature of the gas and follows the indications of Michalski in [9]. The real gas temperature T_a is obtained using three *K-type* thermocouples, sheathed with the same material but with different diameters. The temperature in a small volume of the chamber is measured simultaneously by the three probes. Assuming that the chosen volume is small enough to consider the three probes surrounded by gas at the same temperature, the method described by Pitts et al. [10] can be applied by extrapolating the temperature to a (theoretical) $0 \, \mathrm{mm}$ diameter probe, solving the equation

$$T_a = T_j + \frac{\sigma \epsilon \nu_a}{0.56 k_a} \cdot \frac{d_p^{0.55}}{u^{0.45}} \cdot \left(T_j^4 - T_s^4 \right) \;\; , \tag{4.5}$$

with T_j the junction temperature, T_s the temperature of the surrounding walls, d_p the probe diameter, σ the Stefan-Boltzmann constant, ϵ the probe emissivity, u the flow velocity at the location of the measurement and ν_a and k_a respectively the kinematic viscosity and the thermal conductivity of the ambient gas. Using probes of the same material (same emissivity), and considering that the gas properties are the same for the three probes, T_a can be expressed as

$$T_a = T_j + K \cdot \left(T_j^4 - T_s^4 \right) \;\; , \tag{4.6}$$

being T_s the temperature of the chamber walls and K a constant defined as

$$K = \frac{\sigma \epsilon \nu_a}{0.56 k_a} \cdot \frac{d_p^{0.55}}{U^{0.45}} \; . \tag{4.7}$$
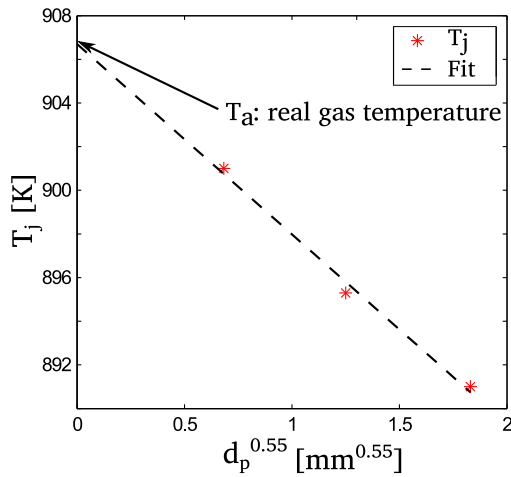
Figure 4.8: Real ambient temperature calculation. The fit of Eq. (4.8) to the simultaneous measurements of the three probes allow to extrapolate the real ambient temperature.

Considering the last term of the Eq. (4.6), a further approximation can be done assuming that the variation between the measurement of the probes with different diameters is typically lower than 10 K and, therefore, that the variation reflected in the term $\left(T_j^4 - T_s^4\right)$, can be neglected.

Thus, the problem is therefore simplified to the following equation:

$$T_a = T_j + K_1 \cdot d_p^{0.55} \, , \tag{4.8}$$

with K_1 a constant factor. The final result is obtained searching the best fit to Eq. (4.8) for the three pairs of values (T_j and d_p) coming from the three simultaneous measurements and extrapolating the equation to the theoretical 0 mm diameter probe.

4.4.5 Nozzle temperature control

Considering the relatively low frequency of the injections during the experiments in the hot spray facility, the temperature of the fuel is mainly determined by the nozzle temperature. To this end, the nozzle temperature was measured using a dummy-injector with a thermo-couple introduced into the nozzle sac. The coolant temperature is the setpoint value assigned to the PID controlling the injector cooling system, which practically coincides with the coolant temperature at the injec-

tor holder inlet. The dummy injector is a regular common-rail injector with some modifications: the orifice has not been drilled in the nozzle, a hole has been drilled axially in the needle and the upstream part has been adapted to insert a thin thermocouple. The thermocouple can slide all along the injector axis until getting in contact with the very tip of the internal region of the nozzle (the sac). A scheme of the injector dummy is represented on the left hand side of Fig. 4.9. Even if this device is not able to inject fuel, it can provide important information about the temperature inside the injector body. Moreover, the fuel flow, occurring during the tests with the real injector it is considered to have just a minor impact over the injector temperature, and the fuel temperature will be mainly driven by the temperature of the nozzle.
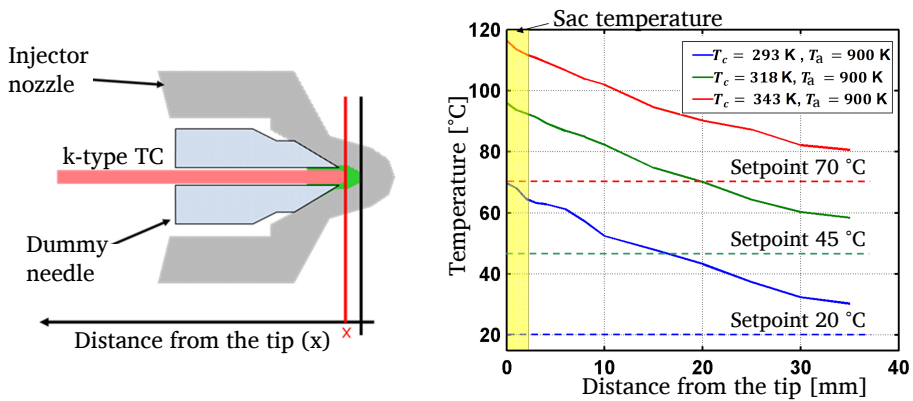
Figure 4.9: Nozzle temperature measurement. Sketch of the dummy injector (left) and results of the temperature measurement along the injector axis (right).

The temperature measurements performed, are considered not only a qualitative measurement but also a good approximation of the real temperature of the fuel within the injector body at the moment of the injection. In this experiment, the temperature was measured along the injector axis for three different coolant temperatures. The ambient temperature chosen in these tests ($T_a = 900\,\text{K}$) is intermediate to the ones used in the test matrix (870 and 950 K). The temperature was measured in different positions: moving along the injector axis, and considering the distance x as the distance between the thermocouple junction and the injector tip, the temperature has been measured for x spanning from 0 (thermocouple touching the injector tip) to 35 mm.

4.5 Optical diagnostics

In this section the optical diagnostics applied to the study of the *CDA* are presented, focusing on the details of the optical arrangements and the processing techniques applied.

4.5.1 Mie scattering

Mie scattering imaging technique is widely used by the engine community for the visualization of the fuel spray liquid phase. Basically, this technique consists in illuminating the fuel droplets with a light source and collecting the light scattered with a camera: the scattering phenomenon, related to the interaction between the light and transparent particles of sizes including the typical fuel droplet diameter, is described by Mie theory and it is called Mie scattering [11]. In the literature several examples of use and calibration of this technique can be found [12–14].

Generally, the spray is illuminated by a light source (continuous or pulsed) and the camera captures the intensity of the light scattered by the droplets composing the spray. This technique is used to detect the liquid phase boundary, since the fuel evaporation yields a severe reduction of the intensity of the light scattered due to the transition from Mie to Raileigh scattering regime [11]. A good Mie scattering optical setup enable to detect a signal in all the spray region where non-vaporized fuel is still existent. Mie scattering technique was used in this thesis to characterize the transient spray liquid phase boundaries in non-evaporative and evaporative conditions.

When testing at low ambient temperature ($T_a \approx 400\,\mathrm{K}$), the fuel evaporation is negligible and, for the length scale relevant to this study, the liquid phase boundaries overlap the whole boundary of the spray. However, when T_a is progressively increased, fuel evaporation becomes important and a significant difference appears between liquid- and vapor-phase boundaries, separating the spray penetration from the liquid length (see Sec. 3.3.2).

As a consequence of that, Mie scattering technique make it possible to measure either spray penetration (S_l) or liquid length (LL) depending on the range of ambient temperature tested. The sharp images of the spray obtained with the Mie setup at low ambient temperatures allow a precise detection of the spray contours: this is considered one of the most favorable conditions to measure the spray spreading angle θ.

Optical arrangement

Even if Mie scattering is a relatively simple technique, the quality of the results strongly depends on the details and the settings of the optical arrangement [14].

The availability of a fast CMOS camera (Phantom V12.0) enabled to study the transient phenomena, such as the early penetration of the jets, and to have a better understanding of the transient features characterizing the spray.

In these tests, different experimental arrangements have been used in order access more information about the spray formation.

With the aim of studying the formation of all the sprays, most of the tests have been performed with the optical configuration shown in the sketch in Fig 4.10: a relatively wide angle lens (Nikon 50 mm) and a large image format ($512x512$) were set to obtain images centered on the injector nozzle; a Xe-arc light source was connected to two optical fibers pointing, through the frontal window of the test-chamber, to the test-section. Two collimators were used to control the cone angle of the light coming from the optical fibers and to improve the homogeneity of the illumination.

The wide field of view required for these tests allows an overall description of the injection event and enables the comparison between the different sprays; however, this setup pays as a drawback a reduction in the frame acquisition rate. For this reason, additional tests have been carried out modifying the optical configuration: the field of view was restricted to only one spray, using a different lens (Carl Zeiss 100 mm) and reducing the size of the image ($124x436$); in this case the spray was illuminated head-on, in order to ensure the maximum brightness of the spray tip. For reference, the tests performed in this arrangement will be referred as *1-spray* configuration to indicate the difference from the previous *7-spray* configuration.

The substantial reduction in the field of view in the *1-spray* configuration gives a double advantage, one in terms of spatial image resolution (the *pix/mm* ratio can be increased) and the other in therms of acquisition rate: in fact, the fast-cameras are normally limited in speed by the maximum amount of pixels that can be read per second; when the frame resolution is reduced, the frames acquired per second can be incremented.

In the *1-spray* configuration, the area to be illuminated is smaller an therefore more light can be concentrated on the spray studied. As a consequence of that, the camera will receive more scattered light, allowing a reduction in the shutter time of the camera with a positive effect on the sharpness of the resulting images In fact, long shutter times lead the spray contour to be blurred, especially in the first transient, when the spray leading edge moves particularly fast. Finally, by
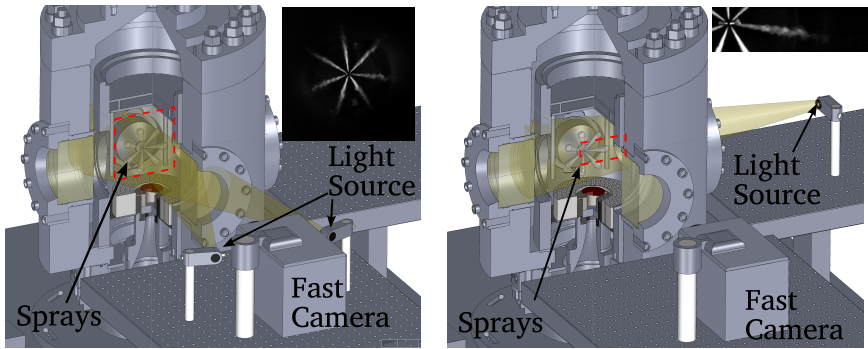
Figure 4.10: Optical arrangement employed for Mie scattering. 7-spray visualization (left) 1-spray visualization (right); the field of view in the two cases is indicated by the red dashed rectangle.

focusing the illumination on only one spray, a further corroboration of the results was accomplished testing the robustness of the measurements with two different optical setups [14].

A third configuration (*micro*) was also employed to track some very fast transient features of the spray: in this case, the image resolution was strongly reduced (64*x*64) with a consequent substantial increase in the frame rate (320 *kfps*). The image was centered on the nozzle tip allowing to include in the image the first mm of all the sprays. Even if the *pix/mm* ratio was not sufficient to study microscopic features of the spray, the setup allowed to characterize the first transient penetration and to have a detailed description of fast transient features characterizing the spray. In Tab. 4.3 all the details of the Mie scattering setup are listed.

Image processing

Image processing is one of the most important steps of the data analysis and many methods can be found in the literature [12, 15, 16]. After a review on the literature, the approach proposed by Siebers in [12] was chosen for its computational simplicity and its robustness. The steps followed in the image processing are summarized below:

1. *background subtraction*: the image acquired right before the start of injection is arithmetically subtracted to the spray images, in order to remove reflections and background artifacts.

2. *image sectorization*: in order to analyze each spray individually, the image has been divided in 7 sectors (Fig. 4.11);

	7-spray	1-spray	micro
Camera	Phantom V12.0 - CMOS sensor		
Light Source	Double Xe-arc source		
Lens	Nikon - Nikkor	Zeiss-Macro	Nikon-Nikkor
Lens features	50 mm - $f/1.8$	100 mm - $f/2.0$	50 mm - $f/1.8$
Pixel/mm	6.2	11.3	6.2
Image size [pix]	$512x512$	$152x512$	$64x64$
Image size [mm]	$82x82$	$13x45$	$10x10$
Frame rate [fps]	20000	68000	320000
Shutter time [μs]	24.0	8.0	1.5
Test repetitions	10	8	5

Table 4.3: Details of the different Mie scattering optical arrangements.
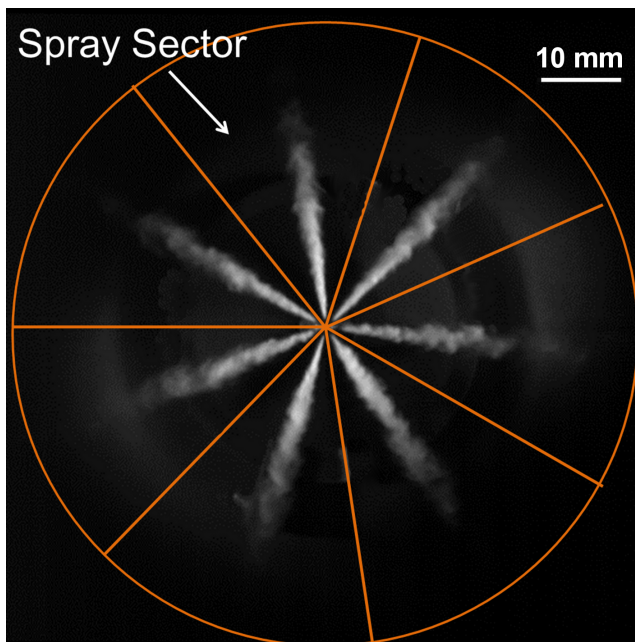
Figure 4.11: Image sectorization. In order to process each spray separately, the image is divided in sectors corresponding to each spray.

3. *image segmentation*: the contour of each spray is obtained using a variable threshold *ths*. The threshold is calculated as the 3 % of the dynamic range of the sector;

4. *connectivity algorithm*: applying the threshold the image is binarized. The connectivity algorithms [16] are employed to distinguish between the spray and the artifacts due to sensor noise;

5. *spray boundary*: the spray boundary is finally obtained as the contour of this area.
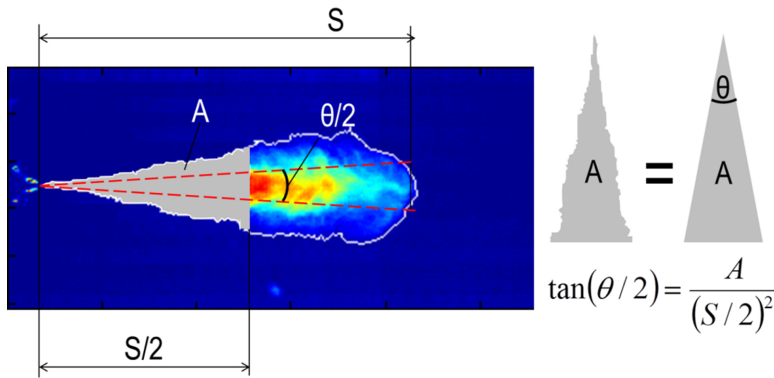
Figure 4.12: Spray penetration and spreading angle definition employed for non vaporizing spray.

The spray boundaries were analyzed to extract the spray macroscopic parameters: spray penetration and spreading angle were calculated using the method based on the spray area calculation described by Naber and Siebers [2] at low temperature conditions: in this method, as depicted in Fig. 4.12, the penetration is defined as the median of the distance from the injector tip, of the pixel boundaries contained within an arc of $\theta/2$. The spray spreading angle θ is defined by building the isosceles triangle of height $S/2$ and area A, as below:

$$tan\left(\frac{\theta}{2}\right) = \frac{A}{(S/2)^2} \cdot \tag{4.9}$$

Since each parameter depends on the other, their calculation shapes an iterative procedure.

Under evaporative conditions the spreading angle cannot be calculated correctly, due to the strong evaporation at the side of the spray. For this reason, it is

preferred to define the spray penetration as the leading edge of the spray bound-
ary and the spreading angle obtained as the angle included between the two lines
fitting the contours on the sides of the spray (Fig. 4.13).
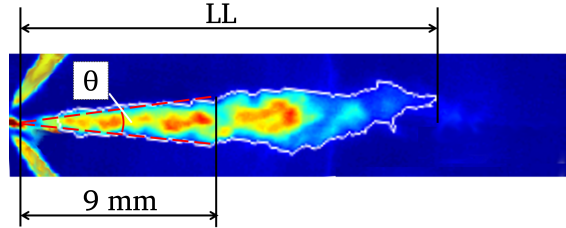
*Figure 4.13: Spray penetration and spreading angle definition employed for vapor-
izing spray.*

Data averaging

In order to asses robust conclusions about the experiments, several test repetitions
were performed for each test condition. Due to the characteristic shot-to-shot
dispersion of the results and the varying (but measured) delay existing between
the trigger and the beginning of the camera recording, the dispersion in the results
makes the data analysis difficult. For this reason a rolling average approach was
used to filter the data. The steps followed by the method are described below.

At each instant (image) x_i of a datum test, the measured quantity value y_i
(penetration or spreading angle) is obtained for each spray. The average value
y_m at the instant t_m is obtained following the procedure below:

- all the data falling within the interval $t_m \pm t_w/2$ are considered. The optimal
  time window t_w was chosen for each different test mainly depending on the
  acquisition rate and test repetitions;

- a linear fit to the data in the interval is performed obtaining a characteristic
  line;

- the value of y_m is obtained as the point on the line corresponding to the
  instant t_m.

This algorithm is repeated moving t_m along the time line with $10\,\mu s$ time steps;
finally, the average curve is obtained (solid line on Fig. 4.14). The rolling average
is applied to calculate the average penetration of either each single spray or the

7-spray average penetration including in the calculation above alternatively the data from only one spray or all of them.

As mentioned earlier the time window width t_w is optimized per each configuration: for the *7-spray* tests, the frame rate is lower than in the other cases and therefore, to smooth the experimental noise, a larger time window had to be been chosen ($t_w = 150\,\mu s$). In the *micro* configuration the frame rate was very high and much more data per time unit were available: the time window in this case was considerably reduced ($t_w = 40\,\mu s$). In the *1-spray* configuration an intermediate time window width was chosen ($t_w = 110\,\mu s$).

Moreover, in order to have a characteristic value for liquid length (LL_m) and spreading angle (θ_m) at each test condition, average parameters are extracted averaging the raw data falling between 2.0 and 2.7 ms ASOI. The interval is chosen in order to avoid the transients at the beginning and at the end of the injection: in this way the characteristic value obtained is more representative of an ideal steady spray [17].
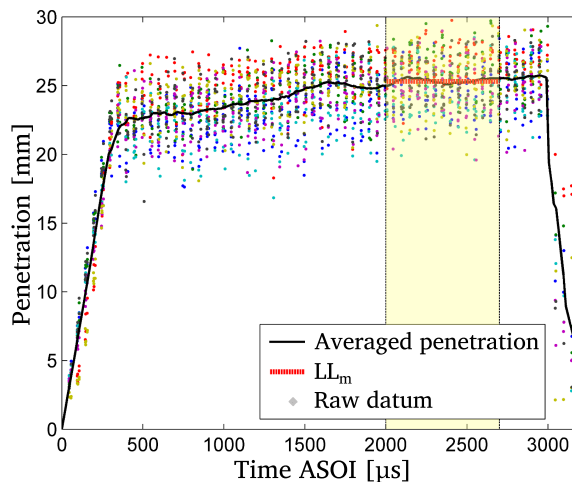
Figure 4.14: 7-spray averaging process applied to a sample test condition; the different colors refer to the different sprays. $T_a = 950\,K$, $\rho_a = 19.2\,{}^{kg}\!/m^3$, $p_i = 60\,MPa$, $ch = high$

4.5.2 Schlieren imaging

The Schlieren imaging technique was employed to characterize the spray vapor phase boundaries at evaporative conditions.

This technique is able to detect gradients in the refractive index of a transparent medium [18]. The technique relies on the deviation of a light beam produced when light passes through non-homogeneous fluids: when a beam of parallel rays of light is directed into the region of interest, the refractive index gradient will cause the deviation of some rays. Placing a spherical lens to collect the beam, only the parallel rays will converge to the focus point of the lens, while the others will have some offset: at that point, the rays deviated can be identified. For example, the use of a diaphragm at the focus point allows to clip the deviated rays and the regions characterized by refractive index gradient will appear with a lower intensity, producing eventually a shadowgraphic image.

A conventional Schlieren single-pass arrangement [2, 19] could not be used to study simultaneously the seven-sprays of the *CDA* injector, due to the impossibility to make the parallel beam pass through the injector holder. To solve this problem, the choice was oriented to a double-pass Schlieren setup using a high-temperature mirror [20]. This solution implies, on the one hand, a complication in the equipment required (compared to a simple Schlieren setup) and, on the other, it allows to obtain multi-spray images as in the Mie scattering tests, improving the quality (and quantity) of the information provided.

Optical arrangement

The main difference characterizing the optical arrangement for a double-pass Schlieren setup is the fact that the rays are passing two times through the test section, being reflected by a mirror placed right behind the test section. Since the light is reflected by the mirror toward the same direction it is coming from, a beam-splitter is required to complete the setup and reflect the image to the camera.

A scheme of the optical setup is represented in Fig. 4.15. This scheme shows the path of the light throughout the whole setup including the high pressure and high temperature vessel. The yellow translucent beam represents light before reaching the mirror and the orange beam represents light after high temperature mirror reflection. The beam-splitter is used to reflect the light coming from the test chamber to the high speed camera. Both the single point light source and the Fourier filtering diaphragm are purposely located at the focal point of *Lens B*.

The filtering or discarding device utilized in this setup consists of an adjustable diameter diaphragm centered in the focal point of the lens. This would fall in the category of a circular type cut-off device, which performs symmetrically if everything is properly aligned. The diaphragm opening diameter is adjustable so that it is possible to set the sensitivity of the setup. The single point source needed for

a Schlieren setup is obtained employing *lens A* focusing the light coming from the light source into a small and concentrated single point. The reduced size of this point is fundamental as it is directly related to the quality of the collimated beam. Only one lens for collimating and collecting (Lens B) was employed in order to reduce the length of the test area to the minimum possible, thus maximizing the collection angle.
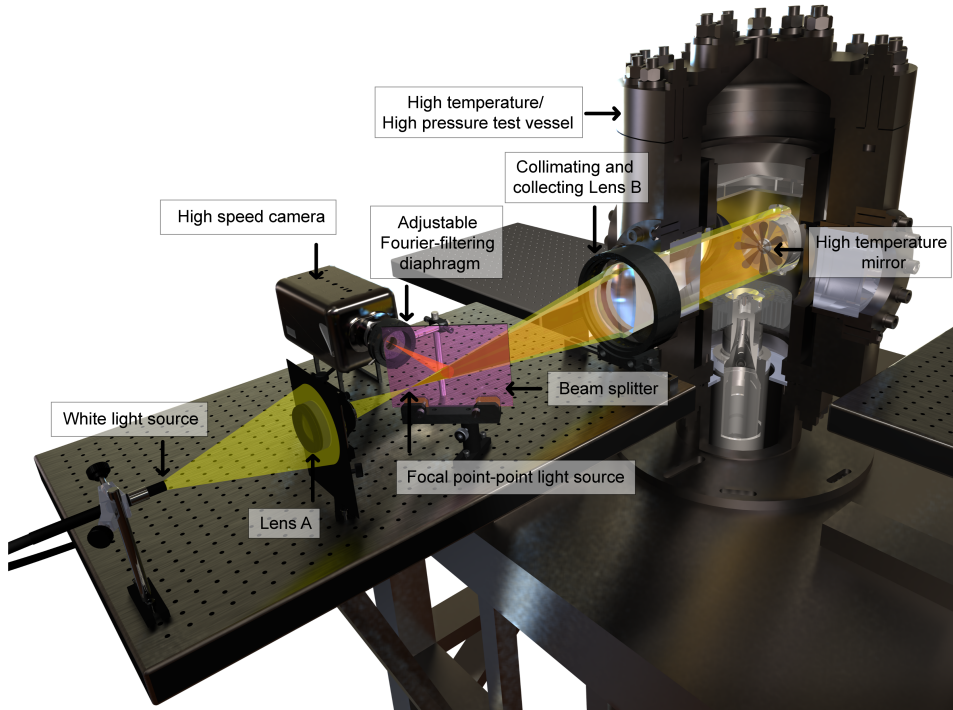
Figure 4.15: Optical arrangement employed for Schlieren imaging.

The acquisition was performed with a fast-camera: as mentioned before, a compromise between the image resolution and the acquisition rate has to be found, being the two setting dependent on each other. In this case, the image size obtained (608x608) is the result of a slight sacrifice in the acquisition speed (15000 *fps*). Nevertheless, the acquisition rate was considered to be enough for the vapor penetration rates involved and the field of view obtained permits the visualization of vapor up to almost the maximum permissible by the window diameter which is 128 mm.

A last remark has to be made about the high temperature mirror installed inside the vessel. This reflecting surface has to resist a very high temperature

environment being at the same time coupled to a metal surface and stressed by
the pressure waves related to the combustion when testing at reacting conditions.
The solution found was to use a fine polished stainless steel surface bolted directly
in the injector holder. This solution has been designed especially for these tests
that have been a valuable test bench [21].

Camera	Phantom V12.0 CMOS sensor
Light source	STORZ Xenon NoVA 300
Camera lens	Nikon 50 mm
Lens A	Nikon 50 mm
Lens B	TSI 450 mm
Beam splitter	Edmund Optics 50:50
Mirror	Custom made
Image size [pix]	608 x 608
Image size [mm]	114 x 114
Frame rate [*fps*]	15.000
pix/mm	5.3
Test repetitions	15

Table 4.4: Details of the optical setup and devices employed in the Schlieren arrangement.

Image processing

For the image segmentation, it was used the same approach followed in Mie scattering tests: the image was separated in sectors to process each spray separately, the background subtraction was applied and a black and white image was obtained using a scaled threshold as in Mie scattering. However, the images obtained in Schlieren are characterized by features that required to modify the processing routine used for the Mie images. Observing the image reported in Fig. 4.16 some considerations can be done:

- the spray appears darker than the background, therefore an inversion of the image and of the background is convenient;

- the head of the three bolts holding the mirror appear as dark spots in the image. Therefore, the sprays interfering with this bolts will not be processed to avoid erroneous measurements;

- the temperature/density gradient related to the turbulent flow appears in the background and cause fluctuations over a wide range of counts

level. Connectivity algorithms have been modified to obtain accurate spray boundaries.

As for the *LL* calculation, the vapor phase penetration (S_v) was calculated as the leading edge of the spray boundaries while the spray spreading angle was calculated, but due to the strong uncertainties related to the boundary detection at the side of the spray and their significant influence on the results, this datum was discarded preferring the spreading angle measured via Mie scattering.
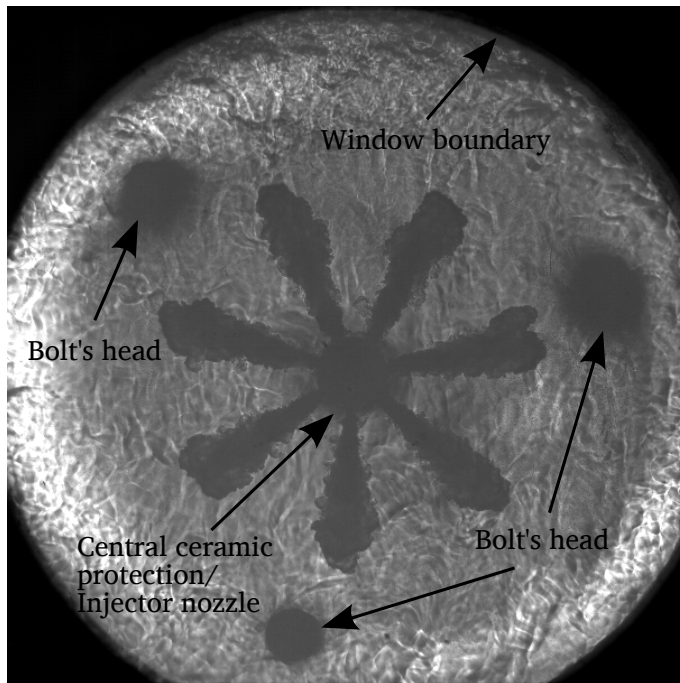
Figure 4.16: Sample image obtained from the Schlieren setup. The injector nozzle, the bolts' head and the window boundary are indicated.

Data averaging

The penetration data measured via Schlieren technique are averaged with the same method employed for the data from Mie scattering. Only some details were modified to improve the accuracy of the results. The time window t_w used in the rolling average is reduced to $100\,\mu s$ compensating the higher number of repetitions (in this case 15). Moreover, as mentioned earlier, the bolts (and other stains appearing on the mirror surface) prevent parts of the spray to be processed

accurately: preferring the accuracy of the results to their quantity, the decision to take only four of the seven sprays was taken, choosing only the sprays that was possible to process correctly through the entire test plan.

4.5.3   Diffused back-light illumination (*DBI*)

The previous tests are effective to characterize the spray macroscopic features but no information is given about the movements along the direction perpendicular to the image plane. The partial needle lift is expected to increase asymmetries in the fuel flow within the nozzle. As shown by Martinez [22] in a micro-sac configuration the perturbations caused by the needle increase the fuel velocity and modify the velocity profile at the orifice inlet Fig. 3.26: the expected spray asymmetries could be observed only on the plane laying on the orifice and the injector axis. Therefore, further tests were performed to image the spray from the lateral windows: to do that, the spray studied was isolated by deflecting the other sprays with specifically designed injector cap (Fig. 4.17).

The new configuration allows to implement the optimized diffused back-light illumination setup, developed by Ghandhi et al. [23] and applied for spray measurements by Manin et al. [24]. In this configuration, the fast camera points to the injector from one of the lateral windows, while a synchronized high-speed LED was placed at the opposite side of the test chamber (Fig. 4.17).
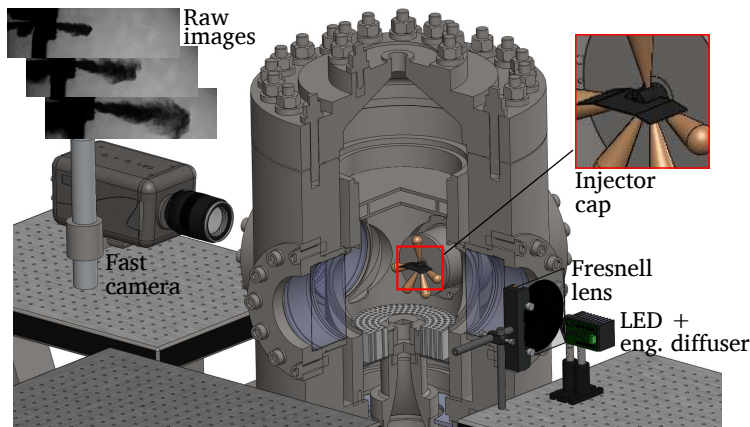
Figure 4.17: Optical arrangement employed for the DBI *setup. Par of the sprays are deflected to study effectively only one spray.*

An engineered diffuser is used to make the background illumination uniform without reducing the light intensity (more than 90% transmission) and the Fresnel

lens collimates the light to enhance illumination efficiency [23]. The details of the technique are described by Manin et al. [24].

The LED is driven by the camera shutter and the duration of the pulse is about 50 ns. The images have been acquired by means of a CMOS high-speed camera (*Phantom V12*). The camera was equipped with a 100 mm f /2.0 objective. The exposure time was set to 3 μs but the effective exposure time is driven by the LED pulse 50 ns. Fig. 4.17 represents the combustion vessel together with the optical setup.

This optical arrangement allows to capture sharp spray images: the short LED pulse duration permits to catch fast fluctuations in the spreading angle and/or spray axis variation that otherwise would be missed. Moreover, the images obtained give important information about the light extinction through the spray: the Beer-Lambert law, describing the extinction of light travelling into turbid media, allows to obtain from the images acquired two-dimensional optical density (OD_{DBI}) maps, implementing the equation below:

$$OD_{DBI} = -ln\left(\frac{Im_i}{Im_{bg}}\right) .$$

(4.10)

The results obtained with this calculation cannot be considered a quantitative measurement of the extinction, since the optics collect a relatively large amount of forward scattering [24]: however, this measurement can give important information about the spray morphology and, therefore, it was calculated and named OD_{DBI}, where the subscript *DBI* underlines the methodology (and the limitations) related to the measurement.

The spray axis angle γ was defined as the angle included between the nominal orifice axis and the line connecting the orifice outlet and the spray centroid (weighted on the OD_{DBI}): the same rolling average technique employed for Mie scattering tests was applied to this parameter.

4.5.4 *CH* and OH* chemiluminescence*

Chemiluminescence is a chemical phenomenon consisting in a light emission due to the decay of a molecule from an excited state to a lower energy level. *CH** and *OH** decay to ground-state radicals have a well-defined chemiluminescence spectrum that permits identifying the emitting molecule [25, 26]. The natural emission of light of the *CH** radicals (432 nm) was studied using the methodology described by Dec and Espey in [26]. Dec and Espey showed that *CH** is an excellent marker for the characterization of the first-stage of the Diesel ignition (*cool flames*). Its timing and location can give precious information and, in

their experiments, *CH** chemiluminescence appeared to be a fair witness of auto-ignition.

The combustion process ensues with fuel breakdown, followed by the first significant heat release and an eventual first soot formation occurring on the peak of premixed flame. This chemiluminescence lasts in rich areas of the jet during the whole combustion event but it is soon hidden by early soot radiations, being about three orders of magnitude brighter [27].

Many studies in the literature relate the high-temperature Diesel reactions to the formation of *OH* radicals, indicating that their formation takes place in nearly stoichiometric regions [28, 29]. Gaydon showed that the spectrum emitted by *OH** decay has its most important peak at 306 nm [25]. Therefore, first- and second-stage Diesel ignition can be characterized by the study of *CH** and *OH** chemiluminescence [30, 31].

Optical arrangement
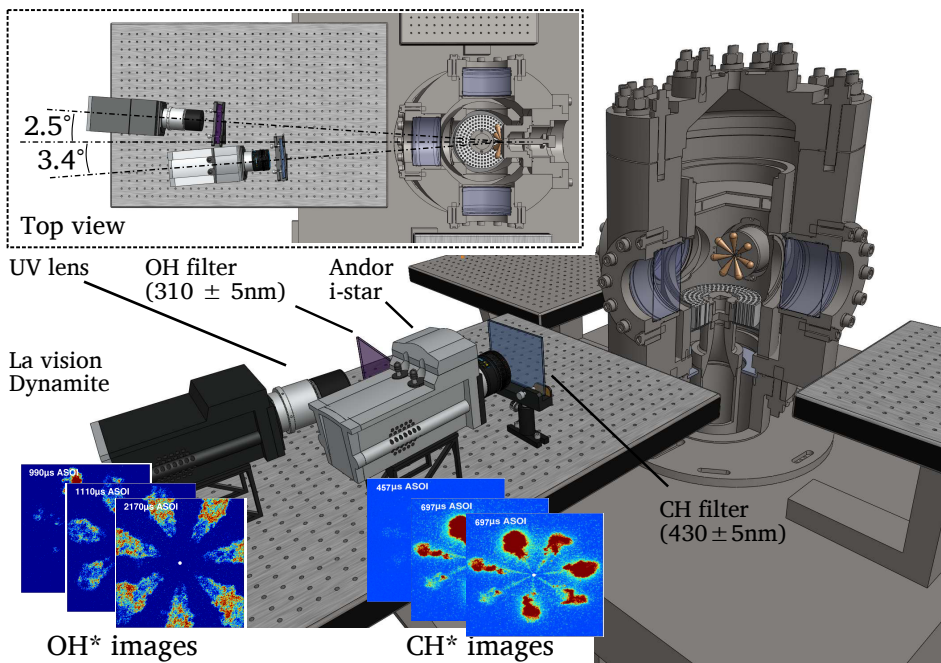
Figure 4.18: Sketch of the experimental setup employed for CH* *and* OH* *radicals chemiluminescence.*

The chemiluminescence of the radicals investigated was studied filtering the natural flame light emissions with narrow band pass filters: a 430 ± 5 nm filter

	CH*	OH*
Camera	Andor - Istar	La Vision - Dynamight
Sensor type	ICCD	ICCD
Lens	Nikon - Nikkor	B. Halle Nacht - U.V.
Lens features	50 mm - f/1.8	100 mm - f/4 U.V. glass
Pixel/mm	4.72	6.12
Image size [pix]	512 x 512	512 x 512
Image size [mm]	108x108	83x83
Gating time [μs]	20	20
Test repetitions	5	5
Filtering [nm]	430 ± 5	310 ± 5
Intensifier gain	Maximum	Max. at the ignition and reduced when the flame gets brighter

Table 4.5: Details of the optical setup employed for CH* *and* OH* *radicals chemiluminescence.*

was used to separate the *CH** emissions (at 432 nm); on the other hand, the emissions from *OH** radicals (at 306 nm) were acquired using a 310 ± 5 nm filter: this radiation, falling in the UV range, required the use of specific optics. In order to have enough sensitivity to capture correctly the chemiluminescence signals, two intensified CCD cameras (ICCD) were employed to image simultaneously *CH** and *OH** radicals' chemiluminescence: from this point forward, the camera devoted to image the *CH** emissions will be referred as *CH* camera* and the one used for imaging the *OH** emissions, *OH* camera*. A sketch of the configuration is presented in Fig. 4.18 and the related details are presented in Tab. 4.5.

A delay generator was used for two reasons:

- to compensate the different internal delay of the cameras and therefore to guarantee a simultaneous recording;

- to acquire images at different instant from the start of injection performing a time sweep along the injection event (still imaging) [30].

The delay increment setting of the delay generator was adjusted to increase the time resolution of the acquisition when it was considered to be convenient. During the ignition phase, time steps as short as 20 μs were employed, while during the diffusive (and more steady) phase of the combustion the delay step was increased with a maximum of 200 μs. The intensifier gating time was fixed for the two cameras at 20 μs to improve the accuracy of the data in the time

domain and 5 repetitions for each time step were performed to average the shot-to-shot variation and to have an understanding of the repeatability of the tests.

The low emissions of the *CH** radical, together with the need of catching the very beginning of the cool flames, have made light efficiency a primary issue. For this reason, the two cameras were visualizing directly the combustion, avoiding the use of a beam splitter or a chromatic mirror that would reduce the light efficiency of the system. Therefore, a small angle had to be included between the camera's and the injector's axes (Fig. 4.18) requiring a geometrical correction of the images which was included in the processing. The cameras' intensifier gain was set to its maximum, to make sure to catch the very beginning of the radicals' emissions.

After the second stage ignition, soot incandescence generally leads the *CH** camera sensor to saturation: being the signal acquired not related to *CH** chemi-luminescence anymore, the acquisition of *CH* camera* was stopped to avoid over-charging the intensifier. Due to the shorter wave length recorded by *OH* camera*, the overlap of *OH** signal and soot incandescence is very low [25]. Moreover, as shown by Higgins and Siebers in [32], a fundamental information about the diffusive phase of the combustion can be obtained imagin *OH** after the ignition, since it allows measuring the flame lift-off length (*LOL*). In the cases characterized by very intense *OH** emissions (e.g. $O_2\% = 21\%$), to avoid sensor overcharges, the gain of the intensifier was lowered after the ignition continuing the image acquisition.

Image processing and analysis

Due to the number of conditions tested and the amount of information contained in each single image, it is necessary to develop a processing technique capable of condensing the information and simplifying the analysis of the results. In the following section, the approach used and the variables introduced in the data analysis are described.

Contour maps

Three-variables plots were created by drawing contour maps on time-axial position axes. This graphic illustration of the results consists in the simultaneous presentation of the intensity recorded (color map) together with the axial position [I] (Y-axis) and temporal data (X-axis), so that an entire image sequence can be described on a single plot.

The intensity contour maps are obtained following a well-defined procedure:

[I]Even though observing Fig.4.19 the distance from the nozzle might be called *radial* distance, it is preferred to use the adjective *axial* referring to the spray development to avoid confusion.
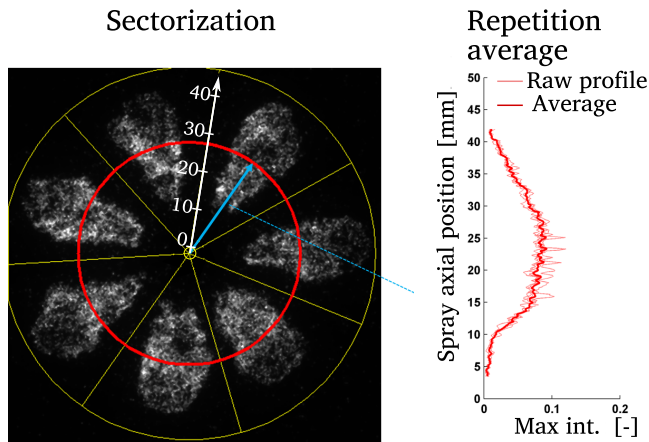
Figure 4.19: Steps to obtain the contour maps. Sectors delimitation (left); Max Int Prof *for the sector indicated by the arrow (right). The light colors represent the single-shot datum while the solid lines indicate the average over the repetitions.*

- geometrical correction: it is applied to the images to compensate the off-axis orientation of the cameras;

- average filter: a gaussian-filter ($6x6$ pix) is applied to the raw images to reduce the noise caused by the cameras' intensifier;

- image sectorization: the spray-sectors are delimited in the raw image, as in Mie scattering process (Fig. 4.19), and analyzed separately;

- intensity profile determination: an axial intensity profile is obtained for each spray sector seeking the pixel with the highest intensity (counts number) at each distance from the nozzle (Fig. 4.19, right);

- repetition average: the intensity profiles obtained (one per spray) are averaged over the 5 repetitions (Fig. 4.19, right), obtaining a characteristic axial profile per spray per time step;

- spray average: the characteristics intensity axial profiles obtained for the different sprays are averaged obtaining a global characteristic profile for each time step (*Max Int Prof*);

The adjective *radial*, in fact, will be used, when decribing spray features, referring to the direction perpendicular to the spray axis (Fig.3.18.

- contour map: the *Max Int Prof* vectors obtained for each time step are put together in a single contour map with on the X-axis the time after the start of the injection (*ASOI*) and the axial position and the color scale representing the chemiluminescence intensity on the Y-axis (Fig. 4.20).

Due to the image acquisition method, most of the tests focuses only on a specific time window: the time domain of the acquisition is represented on the contour maps by vertical black lines (see Fig. 4.20).

The same procedure was applied to *CH** and *OH** images: the prefix *CH* and *OH* will be used for reference when presenting the results.
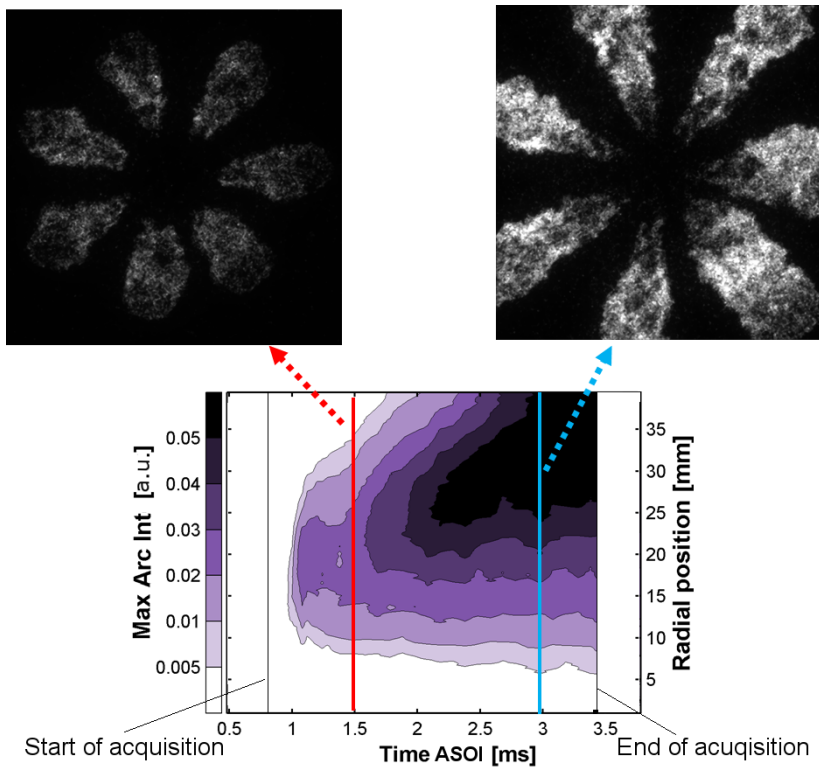
Figure 4.20: Steps to obtain the contour maps. Comparison between contour maps and raw images. The vertical black lines represent the start and the end of the camera acquisition period.

Ignition characterization

The first- and second- stage ignition delays were defined based on the appearance of, respectively, *CH** and *OH** radicals.

Due to the very low intensity of the *CH** chemiluminescence, the time elapsed between the start of the injection and the first onset of the *CH** emissions (cool flames), τ_{CF}, was defined as the first instant at which the signal is above the sensor noise level. On the other hand, the second-stage ignition, named in this work τ_{SSI}, was defined following the observations by Lillo et al. [33, 34] and based on the intensity time evolution during the combustion. In Fig. 4.21, the parameter *Max Int* (corresponding the maximum of the *Max Int Prof* at each instant) obtained for all the tests performed is presented on a single plot: the X-axis for each case is shifted arbitrarily in order to separate different groups of test conditions. The plot shows clearly that the curves are always characterized by a steep increase followed by a peak and a flat region. Even though oxygen concentration is the main driver for the value of this peak in *OH** chemiluminescence intensity (OH_{peak}), other authors showed that it is also related to other boundary conditions and it is representative of the premixed phase of the Diesel combustion [35]. In order to obtain coherent results, the differences in peak intensity observed were taken into account calculating a specific threshold for each test condition using as reference the intensity at the peak OH_{peak}. Finally, the threshold used for τ_{SSI} calculation, ths_{OH}, was obtained as

$$ths_{OH} = \frac{OH_{peak}}{2} \quad .$$ (4.11)
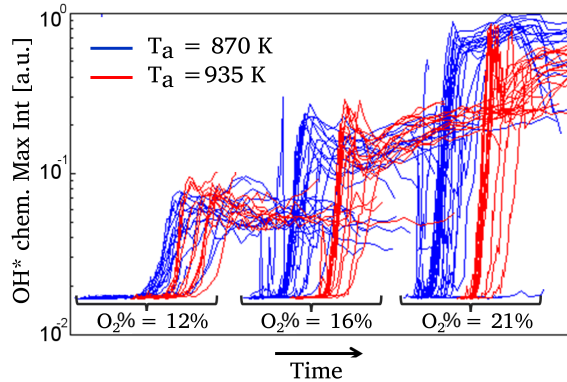
Figure 4.21: OH* max. int. *vs time for the different conditions tested. Each line corresponds to a different test condition. Different oxygen concentration and temperature are shifted on the x-axis to separate the different groups and show the different behaviors.*

In this way, for a datum test condition, the following quantities are calculated:

- first-stage ignition delay (τ_{CF}): the instant at which the first detectable *CH** chemiluminescence signal appears;

- second-stage ignition delay (τ_{SSI}): the instant at which the variable *Max Int* exceeds *ths_{OH}*;

- *OH** chemiluminescence peak height *OH_{peak}*: *OH** chemiluminescence intensity peak value reached right after the *OH** signal appearance;

- ignition location x_{SSI}: axial distance corresponding to the *OH_{peak}*;

- fuel mass injected before the second-stage ignition (m_{SSI}): it represents the fuel mass injected (obtained in *ROI* measurements) until the second stage ignition τ_{SSI}.

Time resolved and time averaged lift-off length

The filter used by the *OH* camera* (310 ± 5 nm) rejects most of the soot incandescence radiations allowing to study the *OH** location also during the diffusive phase of the combustion. In particular, this fact enables the measurement of the lift-off length (*LOL*) for each spray. The transient lift-off length was obtained using the same intensity threshold *ths_{OH}* employed for the calculation of the τ_{SSI}, following the idea suggested by Lillo et al. [33]; then, the value of the *LOL* was defined as the shortest axial distance at which *Max Int Prof* exceeds *ths_{OH}*.

However, the measurement of the transient lift-off length suffers relatively high uncertainties due to the high shot-to-shot dispersion of the results and to a relatively low signal to noise ratio in the lift-off length region. In order to obtain a more robust characterization, time averaged images were captured with the *OH* camera* extending the intensifier gating time [32]. To this end, it was decided to identify the time window corresponding to the steady part of the combustion of most of the conditions tested. The interval selected is $0.9 - 1.5$ ms ASOI which excludes the ignition and the end-of-injection transients.

The *OH** time averaged images were processed following the method described by Siebers [36] for each spray sector: after filtering the image with a gaussian filter ($3x3$ pix), two intensity profiles are obtained calculating the maximum intensity at each axial position in the upper and lower half of the image (Fig. 4.22). The lift-off length was determined by finding the distances between the orifice outlet and the first axial locations above and below the spray center-line with intensity greater than 50% of the intensity peak shown in (Fig. 4.22, right-bottom). The average of these two axial distances is defined as the lift-off length. Considering the dependence of the peak value on ambient/injection boundary
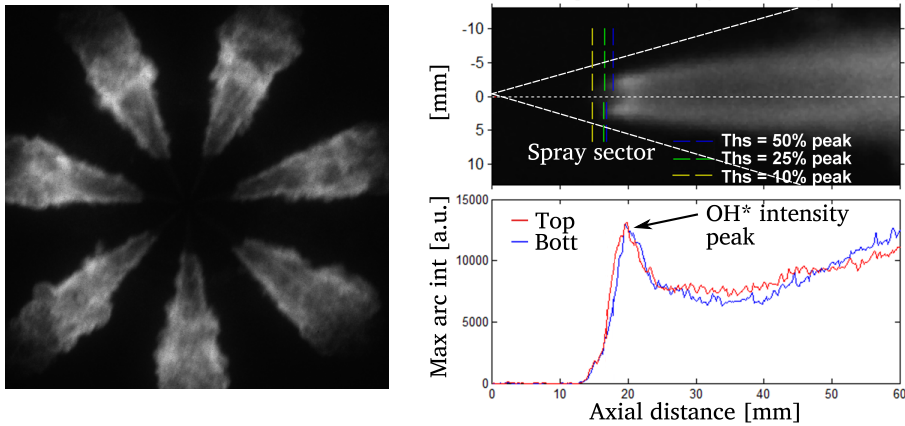
Figure 4.22: LOL definition. Left: sample raw time averaged image and determination for each spray sector. Right: the intensity profiles extracted from the two halves of the image (right top) are used for the determination of the reference peak and then the time averaged LOL. The color dashed lines indicate the different lift-off obtained changing the threshold.

conditions, the lift-off length threshold was obtained calculating the peak value for each combination of them, following the approach below:

- for each condition tested, the images from all the test repetitions were used to obtain a single average-image;

- a characteristic intensity profile was extracted averaging the upper and lower intensity profiles (see Fig. 4.22) of the average image and, finally, the threshold was scaled to the 50% of the peak observed in this curve.

In Fig. 4.22 right-top, the colored dashed lines indicate the *LOL* calculated for a sample image scaling the threshold to a different percentage of the peak: the separation between the *LOL* values obtained underlines the important effect that the threshold definition and the method used have on the final results [35].

4.5.5 2-color optical pyrometry (2C)

Soot formation and flame temperature are two fundamentals quantities concerning the Diesel flame, since they are strongly related to the amount of soot and NO_x in the exhaust [37–39].

The 2-color optical pyrometry (2C) is a well-known technique for the characterization of the flame temperature and soot distribution. The technique relies on the acquisition of synchronized images of the flame, filtering the light at different wave lengths. Assuming that during the diffusive phase of the Diesel combustion soot incandescence is dominating the natural luminosity of the flame, the quantitative determination of the light intensity at two different wave lengths allows to characterize the incandescence spectrum and, eventually, to determine the soot related *KL* and temperature. Even though the technique is relatively simple, the analysis of the results have to take into account the intrinsic limitation of the technique: the most important one is that the 2*C* is a line-of-sight technique, and consequently the derived variables have intrinsic uncertainties due to the unknown distribution of the quantities along the radiation path length. Furthermore, the high number of uncertainties related to the optical setup and the measuring principle may also affect the results. In this section, the principle of the technique will be presented along with the details of the optical setup and of the calculations performed.

2C fundamentals

The *2C* measurement bases on the light emissions derived from soot particles incandescence: this fact is particularly suitable for Diesel combustion studies since soot incandescence dominates the flame radiation emission during most of the heat release period [40] and therefore, flame images recorded by means of conventional non-filtered techniques are basically soot radiation images. As seen in Sec. 3.3.2, the heat transfer within the spray is so efficient that no temperature gradients are expected between soot particles and the surrounding gas. The experimental measurements carried out by Matsui et al. [41] demonstrated that temperature difference between soot particles and the true flame (gas phase) is negligible for diesel flame conditions, since differences between gas and soot temperature are expected to be less than 1 K: as a consequence of that, the measured soot temperature should provide a very close estimate of the flame temperature.

The fundamental assumption of the 2*C* is that the radiation intensity from a soot cloud with uniform spatial distributions of temperature and particles, depends only on the wavelength, the temperature and the amount of soot within the flame. This statement can be translated into the following mathematical equation

$$I_{soot}\left(\lambda, T_f, f_v, L\right) = I_b\left(\lambda, T_f\right) \cdot \epsilon\left(\lambda, f_v, L\right) \quad . \tag{4.12}$$

being I_{soot} the total soot radiation power per unit area, solid angle and wavelength are obtained as the product of the black-body radiance I_b (at the same

temperature T_f and wavelength λ) and the emissivity ϵ. The latter parameter depends on the wave length and the amount of soot, which can be quantified by means of the soot volumetric fraction f_v, and the radiation path length L through the flame. The black-body radiance can be obtained from Planck's radiation law:

$$I_b\left(\lambda, T_f\right) = \frac{1}{\lambda^5} \frac{c_1}{\left[\exp\left(\frac{c_2}{\lambda T_f}\right) - 1\right]} \quad, \tag{4.13}$$

where c_1 and c_2 are constants ($c_1 = 1.1910439 10^{-16}$Wm^{2}sr^{-1} and $c_2 = 1.43881 0^{-2}$mK). Additionally, the Bouguert-Lambert law defines ϵ for homogeneous poly-dispersed aerosols, assuming the hypothesis that multiple scattering is negligible [42],

$$\epsilon\left(k_\lambda, L\right) = 1 - \exp\left(-k_\lambda \cdot L\right) \quad, \tag{4.14}$$

where k_λ is the soot extinction coefficient, averaged over the path length L. The former coefficient depends on both the soot volume fraction f_v and optical properties. The coefficient k_λ is obtained following a semi-empirical approach, rewriting the previous equation as

$$\epsilon\left(k_\lambda, L\right) = 1 - \exp\left(-\frac{k_{soot} \cdot L}{\lambda^\alpha}\right) \quad, \tag{4.15}$$

where k_{soot} is a variable proportional to the soot volume fraction and λ is the wavelength of the radiation, it is usually expressed in μmand α is a constant. Zhao et al. [43] carried out a discussion on this issue, and state that $2C$ results are less dependent on α if visible wavelengths are selected. If this range of the spectrum is chosen, they conclude that $\alpha = 1.39$ can be assumed for most fuels.

However, the optical path length L is unknown and no matter the accuracy of the calculation of k_λ, without this quantity the equation cannot be solved. To overcome to these difficulties, the dependence of the emissivity on the soot amount within the optical path is usually expressed in terms of the product $KL = k_{soot}L$ or, in some cases [42, 44], $f_v L$. KL accounts for the total soot contribution along the radiation path length, either due to an optically thin highly-sooting flame, or to an optically thick low-sooting one. Combining equations (4.12) and (4.13) with Eq.(4.15), the dependence of soot radiation power (I_{soot}) on temperature, soot and wavelength can be made explicit in the expression below:

$$I_{soot}\left(\lambda, T_f, KL\right) = \left[1 - exp\left(-\frac{KL}{\lambda^\alpha}\right)\right] \frac{1}{\lambda^5} \frac{c_1}{\exp\left(\frac{c_2}{\lambda T}\right) - 1} \quad, \tag{4.16}$$

The working principle of the 2-color method relies on the measurement of the radiation of the same soot sample at two different wavelength: finally, the radiation power measured by the two sensors can be written as system of equations

$$I_1 = I_{soot}(\lambda_1, T_f, KL) \ , \tag{4.17a}$$
$$I_2 = I_{soot}(\lambda_2, T_f, KL) \ , \tag{4.17b}$$

from which the temperature T_f and the soot amount in terms of KL can be obtained. The measurement of the soot radiance can be performed by the simple use of a single photo-sensors. However, the state of the art CCD cameras have enough accuracy and sensitivity to be employed in this measurement, behaving, as a matter of fact, as an array of photo-sensors.

The use of scientific cameras allows to obtain two-dimensional images of the flame temperature and soot distribution. In fact, the measurement of the radiation is performed by each single pixel, which would produce a signal E_m:

$$E_m = \int_\lambda \int_\omega \int_A Q(\lambda) I_{soot}(\lambda, T, KL) \, \mathrm{d}A \mathrm{d}\omega \mathrm{d}\lambda \ , \tag{4.18}$$

where $Q(\lambda)$ is the detector spectral transfer function, A is the area of the sooting flame within the field of view of the detector and ω is the solid angle subtended by the detector area. In order to simplify the expression in Eq.(4.18) the following hypothesis can be made [44]:

- the detector size is small compared to the distance from the soot cloud: this fact brigs as a consequence that I_{soot} is independent of the solid angle ω;

- across the detection area A, the derived properties are constant, being the measured variables T_f and KL averaged over the field of view of the pixel. This hypothesis is acceptable in the case of *2C* imaging due to the high spatial resolution offered by a CCD sensor;

- the soot radiance measurement is related only to a particular wavelength: this aspect is guaranteed by the use of interference filters with narrow bandwidths. It was estimated that, for conventional 10 nm bandwidth filters, such as those used in this study, the error induced by this assumption is about ±10 K in temperature and less than ±2% in $f_v L$ [42].

Assuming the above mentioned hypothesis, the camera sensor response for a specific wave length $E_{m,\lambda}$ can be expressed as

$$E_{m,\lambda} = C_\lambda I_{soot}\left(\lambda, T, KL\right) \quad , \qquad (4.19)$$

where C_λ is a constant that takes into account the three integral variables (A, ω and λ). This parameter has to be calculated by means of the calibration of the system against a known radiation source.

Optical arrangement and calibration

Top view
Red filter
650 ± 5 nm
PCO
SensiCam
Phantom
V 12.0
Green filter
550 ± 5 nm
Beam
Splitter
50:50
Transient combustion images
1-spray
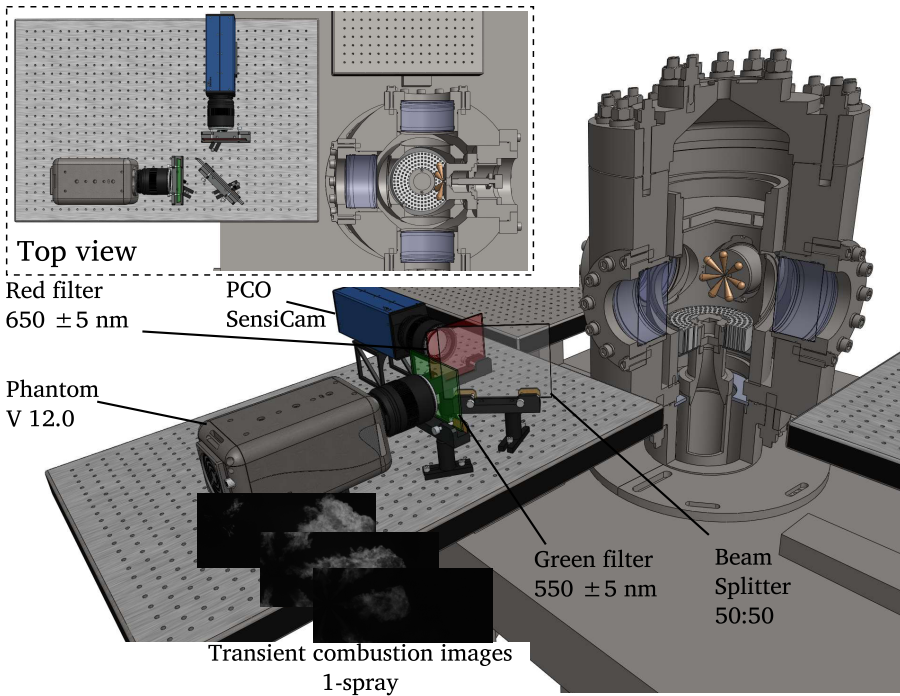
Figure 4.23: Sketch of the experimental setup employed for 2-color pyrometry.

The optical arrangements employed for *2C* measurements is presented in Fig.4.23: two cameras were used to image the flame simultaneously. In this way, the image deformation problems deriving from the use of a stereoscope [38] were avoided, taking advantage from the full resolution of each camera sensor. In a double camera setup, it is recommended to have the same optical configuration for the two cameras [38]: for this reason, similar lenses were employed in order to have the most similar collection angle for both the cameras.

The cameras were selected considering their signal to noise ratio and reliability. Taking into account the availability in the department at the time of the experiments, a CCD sensor PCO Sensicam was coupled to a CMOS sensor Phantom V12.0 fast-camera. Since only one of the two camera allows fast-acquisition, both cameras were used as *slow* cameras, performing still imaging.

Likewise in radical chemiluminescence imaging, a delay generator synchronizes the two cameras and adjusts the phase between the image acquisition and injection event. Also in this case, the time step was adjusted depending on the phase of the combustion, ranging from a minimum of $20\,\mu s$ to a maximum of $200\,\mu s$.

The field of view and the image resolution were the same for both cameras and a beam splitter 50 : 50 was used to have exactly the same view of the spray without including any angle.

Finally, two narrow-band interference filters (10FWHM) were mounted in order to improve the accuracy of the signal with central wave length at 550 nm and 650 nm. The details of the optical arrangement are presented in Tab. 4.6.

	Green	**Red**
Camera	Phantom V 12.0	PCO SensiCam
Sensor type	CMOS	CMOS
Lens	Zeiss - Macro	Sigma - Zoom
Lens features	$100\,mm$ - $f/4.0$	$24-70\,mm$ - $f/2.8$
Pix/mm	13.1	13.1
Image size [pix]	768 x 256	768 x 256
Image size [mm]	$59x19$	$59x19$
Gating time [μs]	12	12
Test repetitions	5	5
Filtering [nm]	550 ± 5	650 ± 5

Table 4.6: Details of the optical setup in the 2-color optical pyrometry.

Considering the accuracy needed in the information gathered by the camera, a high pix/mm was preferred in order obtain more measurements per area unit. To this end, it was chosen to study only one spray, maintaining the same image size.

As discussed above, the camera has to perform a quantitative measurement of the radiance of the flame. To relate the counts indicated by the camera to the light emitted by the flame, a calibration of the optical setup was performed studying the response of the camera sensor against a known light source.

A tungsten-ribbon calibrated lamp was used as reference (Osram-Wi17G): this device is provided together with the luminance data of a determined region of the lamp, detailed with the related spectrum. This information is given for different values of current applied to the lamp: in this way, the calibration curve for the filtered parts of the spectrum can be obtained. To this end, maintaining the same optical setup employed in the experiments, the calibrated lamp was positioned in the region normally occupied by the flame and the intensity recorded by the two cameras was studied to obtain the calibrated curves. The details of the calibration process is described by Payri et al. [38].
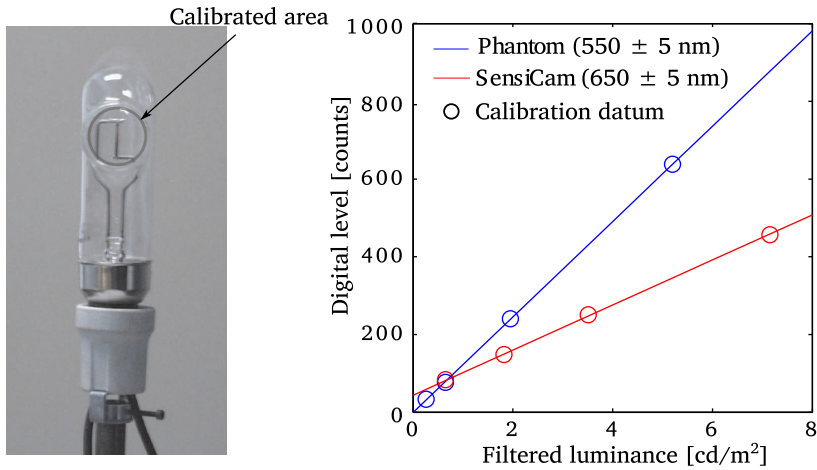
Figure 4.24: 2C *calibration process. Picture of the tungsten-ribbon calibrated lamp (left), and calibration curves obtained for the two cameras at the configuration employed in the tests (right).*

Image processing and analysis

The processing applied to the *2C* images can be divided in three different steps: image overlapping, *2C* algorithm application and data post processing.

As discussed earlier, the cameras were arranged to simultaneously capture images of the same region of the chamber with the same *pix/mm*, in order to assure a pixel to pixel correspondence between the two images. However, some slight movements of the cameras might occur during the tests: to compensate these movements, a translation was applied to each set of images (each test conditions). In a first step, some reference points were identified in the two images using a covariance detector [45]; afterward, the translation to be applied was calculated based on the relative location of the reference points in the two images.

The *2C* algorithm was solved for all the pixels of the image Eq. (4.19) through an iterative process. Flame temperature and *KL* maps were therefore obtained with the same spatial resolution of the raw images.

As observed for the *CH*/OH** chemiluminescence, the huge amount of information provided by these results needs to be condensed to enable an effective analysis of the data. In this case, the same process followed in the chemiluminescence images (see Sec. 4.5.4) was applied starting from the temperature and *KL* maps and obtaining the relative *contour maps*. The only difference among the two processing is that for the 2*C* only one spray was studied, and therefore the spray average was not performed.

4.6 Test conditions and parametric variations

The two main objectives of the selected test matrix are: 1) to obtain a well-defined picture of the parameters affecting the phenomena studied and 2) to target the thermodynamic conditions relevant to current Diesel engines. For this second reason, boundary conditions were modified in a significant range of values. In this thesis the boundary conditions will be divided in two groups: ambient parameters, namely density, temperature and oxygen concentration of the gas in the test chamber (indicated respectively by the symbols ρ_a, T_a and O_2%) and injection parameters rail pressure (p_i), piezo-stack charge (*Ch*) and injection rate shape.

The hydraulic characterization was performed to investigate the internal flow but also to understand the behavior of the injector itself: many values of the needle lift controlling parameter (*charge* or *Ch*) were tested at different combinations of p_i and p_a. The results obtained from these measurements were used to define 14 reference injection cases, each a different combination of p_i, *Ch* and the injection rate shape.

The optical diagnostics were applied to all the *reference* injection cases under various in-chamber ambient conditions. Isothermal tests were studied via Mie scattering at 300 K while liquid- and vapor-phase penetration were measured varying both T_a (870 and 950 K) and p_a ($3.5 - 5.0 - 6.5$ MPa). In order to match the same ambient densities in isothermal and evaporative tests, the ambient pressure was adjusted using real gas state equations [46]. In these tests, combustion was prevented using pure nitrogen atmosphere to focus the diagnostics on the spray development.

On the other hand, the combustion related experiments were carried out replicating the same in-chamber conditions mentioned above, but at different oxygen concentrations ($O_{2\%} = 12 - 16 - 21\%$) simulating the effect of *EGR*. Another

difference inherent to the test performed at reacting conditions is due to a limitation in the fuel injected mass. To limit the combustion-related pressure wave, the injected mass was limited at 50 mg: for this reason, the injection duration at reacting conditions was calculated keeping constant the total mass injected. The resultant injection duration is included in between $1.5 - 3.3$ ms.

In addition to the main boundary conditions listed above, in some case more parametric variations were performed to understand specific phenomena. For clarity, it has been preferred to present these variations directly in the results section.

A final remark has to be made about the ambient temperature tested during the radical chemiluminescence imaging tests: due to a partial failure of the test facility the maximum temperature was limited. The test matrix of these tests was therefore modified reducing the T_a for the high temperature case from 950 to 935 K.

Parameter	Values
Ambient Temperature (T_a) [K]	$300 - 870 - (935)950$
Ambient pressure - isoth. (p_a) [MPa]	$3.5 - 5.0 - 6.5$
Ambient pressure - evap. (p_a) [MPa]	$1.7 - 2.0 - 2.3$
Injection pressure (p_i) [MPa]	60 - 150 MPa
Injection shape	*square - boot - ramp*
Charge (for square shape) (*Ch*)	*high - med - low*
Injection duration [ms]	3.2^{I}
Coolant temperature (T_c) [K]	343
Oxygen Concentration (O_2%)	$0 - 12 - 16 - 21\%$

Table 4.7: Parametric variations summary.

References

[1] GIMENO, J. "Desarrollo y aplicación de la medida de flujo de cantidad de movimiento de un chorro Diesel". PhD thesis. E.T.S. Ingenieros Industriales. Universidad Politécnica de Valencia, 2008.

[2] NABER, J. and D. SIEBERS. "Effects of gas density and vaporization on penetration and dispersion of diesel sprays". *SAE Paper* 960034 (1996).

[I]Only for tests at inert conditions; at reacting environment the injection duration was adjusted to keep the inject quantity constant at 50 mg.

[3]   SÁNCHEZ, J. J. L. *Estudio teórico-experimental del chorro libre diesel no evaporativo y de su interacción con el movimiento del aire*. Reverté, 2005.

[4]   GARCÍA, J. M. "Aportaciones al estudio del proceso de combustión turbulenta de chorros en motores diesel de inyección directa". PhD thesis. Valencia: E.T.S. Ingenieros Industriales. Universidad Politécnica de Valencia, 2004.

[5]   BAERT, R., P. FRIJTERS, B. SOMERS, C. LUIJTEN, and W. DE BOER. "Design and operation of a high pressure, high temperature cell for HD diesel spray diagnostics: guidelines and results". *SAE Paper* 2009-01-0649 (2009).

[6]   BOSCH, W. "Fuel Rate Indicator Is a New Measuring Instrument for Display of the Characteristics of Individual Injection". *SAE Paper* 660749 (1966).

[7]   PAYRI, R., F. J. SALVADOR, J. GIMENO, and G. BRACHO. "A new methodology for correcting the signal cumulative phenomenon on injection rate measurements". *Experimental Techniques* 32.1 (2008), pp. 46–49.

[8]   INCROPERA, F. P., A. S. LAVINE, and D. P. DEWITT. *Fundamentals of heat and mass transfer*. John Wiley & Sons Incorporated, 2011.

[9]   MICHALSKI, L., K. ECKERSDORF, J. KUCHARSKI, and J. MCGHEE. "Temperature Measurement, John Wiley & Sons". *Chichester, Great Britain* - (2001), pages.

[10]   PITTS, W. M. et al. "Temperature uncertainties for bare-bead and aspirated thermocouple measurements in fire environments". *ASTM Special Technical Publication* 1427 (2003), pp. 3–15.

[11]   MIE, G. "Beiträge zur Optik trüber Medien, speziell kolloidaler Metallösungen". *Annalen der physik* 330.3 (1908), pp. 377–445.

[12]   SIEBERS, D. "Liquid-phase fuel penetration in Diesel sprays". *SAE transactions* 107.3 (1998), pp. 1205–1227.

[13]   PAYRI, R., F. SALVADOR, J. GIMENO, and L. ZAPATA. "Diesel nozzle geometry influence on spray liquid-phase fuel penetration in evaporative conditions". *Fuel* 87.7 (2008), pp. 1165–1176.

[14]   PICKETT, L. M., C. L. GENZALE, J. MANIN, L. MALBEC, and L. HERMANT. "Measurement uncertainty of liquid penetration in evaporating diesel sprays". *ILASS Americas* 2011-111 (2011).

[15]   PASTOR, J. V., J. ARRÈGLE, and A. PALOMARES. "Diesel Spray Image Segmentation With a Likelihood Ratio Test". *Appl. Opt.* 40.17 (June 2001), pp. 2876–2885.

[16] MACIAN, V, R. PAYRI, A. GARCIA, and M. BARDI. "Experimental Evaluation of the Best Approach for Diesel Spray Images Segmentation". *Experimental Techniques* 36.6 (2012), pp. 26–34.

[17] PAYRI, R., J. GIMENO, M. BARDI, and A. H. PLAZAS. "Study liquid length penetration results obtained with a direct acting piezo electric injector". *Applied Energy* 106 (2013), pp. 152–162.

[18] SETTLES, G. S. *Schlieren and shadowgraph techniques: visualizing phenomena in transparent media*. Springer Verlag, 2001.

[19] DESANTES, J., R. PAYRI, F. SALVADOR, and A. GIL. "Development and validation of a theoretical model for diesel spray penetration". *Fuel* 85 (2006), pp. 910–917.

[20] PASTOR, J. V., R. PAYRI, J. M. GARCIA-OLIVER, and F. J. BRICENO. "Analysis of transient liquid and vapor phase penetration for diesel sprays under variable injection conditions". *Atomization and Sprays* 21.6 (2011).

[21] PAYRI, R., J. GIMENO, J. P. VIERA, and A. H. PLAZAS. "Needle lift profile influence on the vapor phase penetration for a prototype diesel direct acting piezoelectric injector". *Fuel* 113 (2013), pp. 257–265.

[22] MARTÍNEZ LÓPEZ, J. "Estudio Computacional De La Influencia Del Levantamiento De Aguja Sobre El Flujo Interno Y El Fenómeno De La Cavitación En Toberas De Inyección Diesel". PhD thesis. E.T.S. Ingenieros Industriales. Universidad Politécnica de Valencia, 2013.

[23] GHANDHI, J. B. and D. M. HEIM. "An optimized optical system for backlit imaging". *Review of Scientific Instruments* 80.5 (2009), pages.

[24] MANIN, J., M. BARDI, and M. PICKETT L. "Evaluation of the liquid length via diffused back-illumination imaging in vaporizing Diesel sprays". *COMODIA* 6 (2012).

[25] GAYDON, A. *The spectroscopy of flames*. Chapman & Hall London, 1957.

[26] DEC, J. and C. ESPEY. "Chemiluminescence imaging of autoignition in a DI diesel engine". *SAE Paper* 982685 (1998).

[27] PICKETT, L. M. et al. "Comparison of diesel spray combustion in different high-temperature, high-pressure facilities". *SAE Paper* 2010-01-2106 (2010).

[28] DEC, J. and E. COY. *OH radical imaging in a DI diesel engine and the structure of the early diffusion flame*. Tech. rep. Sandia National Labs., Albuquerque, NM (United States), 1996.

[29] DEC, J. *A conceptual model of DI diesel combustion based on laser-sheet imaging*. Society of Automotive Engineers Warrendale, PA, 1997.

[30] PAYRI, R., F. SALVADOR, J. GIMENO, and J. DE LA MORENA. "Effects of nozzle geometry on direct injection diesel engine combustion process". *Applied Thermal Engineering* 29.10 (2009), pp. 2051–2060.

[31] PAYRI, R., J. M. GARCÍA-OLIVER, M. BARDI, and J. MANIN. "Fuel temperature influence on diesel sprays in inert and reacting conditions". *Applied Thermal Engineering* 35 (2012), pp. 185–195.

[32] HIGGINS, B. and D. SIEBERS. "Measurement of the flame lift-off location on DI diesel sprays using OH chemiluminescence". *SAE Paper* 2001-01-0918 (2001).

[33] LILLO, P., L. PICKETT, H. PERSSON, O. ANDERSSON, and S. KOOK. "Diesel Spray Ignition Detection and Spatial/Temporal Correction". *SAE International Journal of Engines* 5.3 (2012), pp. 1330–1346.

[34] BARDI, M. et al. "Engine Combustion Network: comparison of spray development, vaporization, and combustion in different combustion vessels". *Atomization and Sprays* 22.10 (2012), pp. 807–842.

[35] BENAJES, J., R. PAYRI, M. BARDI, and P. MARTI-ALDARAVI. "Experimental characterization of diesel ignition and lift-off length using a single-hole ECN injector". *Applied Thermal Engineering* 58.1-2 (2013), pp. 554–563.

[36] SIEBERS, D. and B. HIGGINS. "Effects of injector conditions on the flame lift-off length of DI diesel spray". *Thermo-and fluid Dynamic Processes in Diesel Engines* (2000), pp. 253–277.

[37] HUESTIS, E., P. A. ERICKSON, and M. P. MUSCULUS. "In-cylinder and exhaust soot in low-temperature combustion using a wide-range of EGR in a heavy-duty diesel engine". *Training* 2013 (2007), pp. 12–05.

[38] PAYRI, F., J. V. PASTOR, J. M. GARCÍA, and J. M. PASTOR. "Contribution to the application of two-colour imaging to diesel combustion". *Measurement Science and Technology* 18.8 (2007), p. 2579.

[39] MANCARUSO, E. and B. M. VAGLIECO. "Optical investigation of the combustion behaviour inside the engine operating in HCCI mode and using alternative diesel fuel". *Experimental Thermal and Fluid Science* 34.3 (2010), pp. 346–351.

[40] PICKETT, L. and D. L. SIEBERS. "Soot in diesel fuel jets: effects of ambient temperature, ambient density, and injection pressure". *Combustion and Flame* 138 (2004), pp. 114–135.

[41] MATSUI, Y., T. KAMIMOTO, and S. MATSUOKA. "A study on the time and space resolved measurement of flame temperature and soot concentration in a DI diesel engine by the two-color method". *SAE Paper* 790491 (1979).

[42] DiSTASIO, S. and P. MASSOLI. "Influence of the soot property uncertainties in temperature and volume-fraction measurements by two-colour pyrometry". *Measurement Science and Technology* 5.12 (1994), p. 1453.

[43] ZHAO, H. and N. LADOMMATOS. "Optical diagnostics for soot and temperature measurement in diesel engines". *Progress in Energy and Combustion Science* 24.3 (1998), pp. 221–255.

[44] MUSCULUS, M. P. B. "Measurements of the Influence of Soot Radiation on In-Cylinder Temperatures and Exhaust NOx in a Heavy-Duty DI Diesel Engine". *SAE Paper* 2005-01-0925 (2005).

[45] VEDALDI, A. and B. FULKERSON. *VLFeat: An Open and Portable Library of Computer Vision Algorithms*. 2008.

[46] PENG, D.-Y. and D. B. ROBINSON. "A New Two-Constant Equation of State". *Industrial & Engineering Chemistry Fundamentals* 15.1 (1976), pp. 59–64.

Chapter 5

Results and discussion: internal flow and spray development

5.1   Introduction

The results related to the internal flow and spray development experiments are presented and discussed in this chapter. After a first assessment of the *CDA* injector performances, the hydraulic characterization results are presented to show the effect of partial needle lift on the internal flow parameters. Afterward, results from macroscopic spray characterization at isothermal and evaporative conditions are presented and discussed. Finally a *1D* spray model [1] and statistical correlations are employed to understand the impact of the different test conditions putting the focus on the relationship existing between the needle lift position and the spray development.

5.2   Hydraulic characterization

The hydraulic characterization results are presented first, analyzing *ROI* and *ROM* separately: *ROI* measurements are studied to investigate the *CDA* performances in terms of *flow-throttling* capabilities and time response; moreover, the *ROI* results will also be employed to define the *reference* injection cases studied in the following experiments. On the other hand, the spray momentum meter enabled to study separately the sprays of the multi-hole nozzle enabling the hole-to-hole dispersion analysis [2]. Finally, the combination of the two measurements ($\dot{m}_{av}$

and $\dot{M}_{av}$) enables the calculation of the effective flow velocity and area at the orifice outlet together with the related coefficients (C_v and C_A) [3].

5.2.1   Rate of injection

In these first comparisons the effect of injection pressure and partial needle lift on *ROI* is shown for conventional *top-hat* or *square* injection rate profiles.

Fig. 5.1 shows the *ROI* of the *CDA* injector measured under different test conditions. The characteristic shape of the *top-hat* injection can be divided into three stages: two transient parts, related to the needle opening and closing, and a period in between, in which the mass flow rate is relatively steady [4].
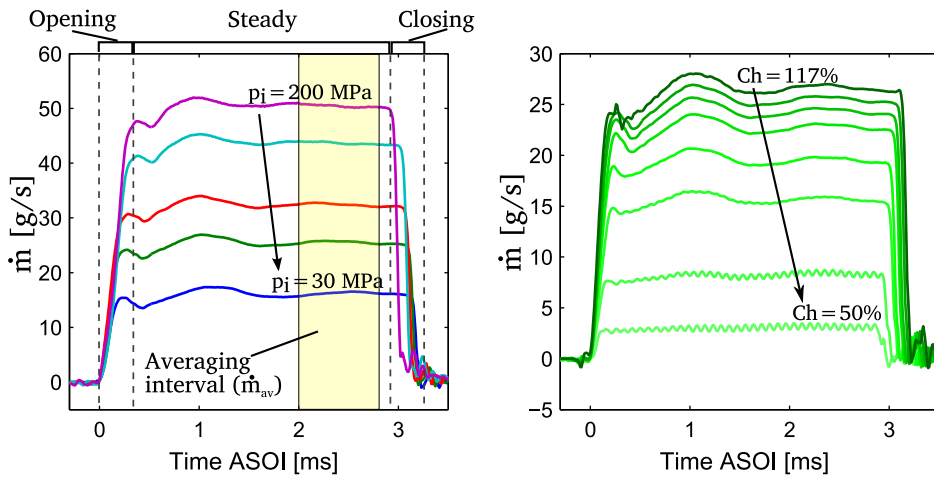
Figure 5.1: *ROI measurements at different test conditions. The opening and closing transients are indicated together with the averaging interval. Effect of p_i at* Ch = 100% *(left) and effect of* Ch *at p_i* = 60 MPa*(right); p_a* = 5 MPa.

The mass flow rate decreases with a reduction in either the injection pressure or *Ch*. Even if expected, the dependence of the *ROI* on the injector charge (Fig. 5.1-right) is the first important result found in this thesis: a reduction of the injector charge successfully controls the needle position, producing a progressive reduction in the mass flow rate.

The characteristic parameters have been obtained from each injection averaging the measurements performed in the interval indicated in Fig. 5.1. A global description of the *ROI* measurements is given in Fig. 5.2, where the average mass flow rate $\dot{m}_{av}$ is presented at different combinations of p_i and *Ch*. For each injection pressure, $\dot{m}_{av}$ increases with *Ch* and the variations in mass flow rate obtained

when varying *Ch* are of the same order as the variations obtained with p_i. However, this effect gets smaller as the injector charge gets higher and, above a certain charge value, $\dot{m}_{av}$ tends to a plateau: considering that higher injector charge means higher needle lift, when the flow area through the needle seat is sufficiently large not to affect the fuel flow, the entire pressure drop is concentrated in the nozzle orifice [4].

Another important aspect observed at high injection pressure, is that the range of *Ch* at which the injector works is reduced: this fact is related to the deformations of the leverage mechanism, that at high pressure conditions are more significant (see Sec. 2.5). The higher resultant of the hydrostatic forces when p_i is increased prevents the needle to lift, requiring a higher piezo-actuation (*Ch*). A similar behavior emerged from the computational studies of Ferrari et al. in [5]: below a certain charge, the needle does not move, preventing the injection to start [5].
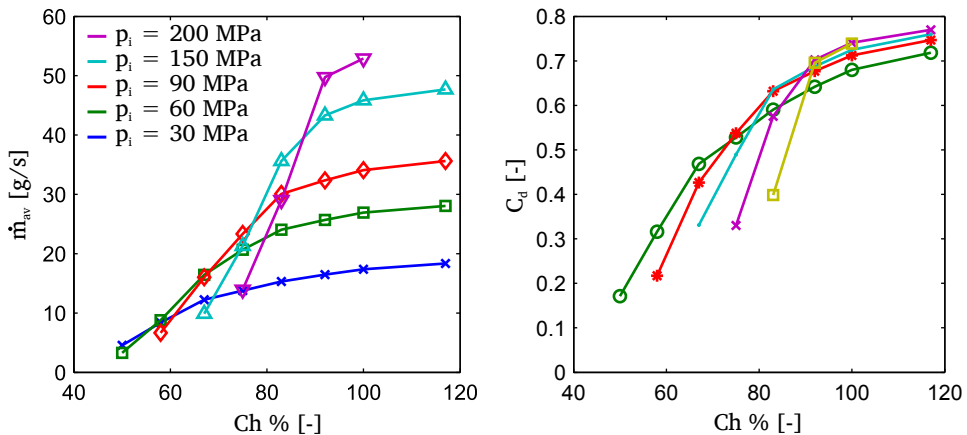
Figure 5.2: Average mass flow rate ($\dot{m}_{av}$) at different injector charge (Ch); $p_a = 5\,\text{MPa}$.

The right plot in Fig. 5.2 shows the discharge coefficient C_d for most of the conditions tested. C_d decreases significantly with *Ch* and the values obtained at low charge are significantly smaller than those found by other authors for Diesel injection nozzles ([3, 6]). According to the definition given in Sec. 3.2, C_d includes all the head losses from the rail to the orifice outlet; in this way, the unusual decrease of C_d is not related only to the nozzle orifices but also to the flow through the needle seat. This fact indicates a significant throttling effect of the needle and a consequent decrease of the effective pressure in the nozzle sac.

The relationship between *Ch* and $\dot{m}_{av}$ is not linear and it seems to depend on the value of p_i tested. In order to evaluate the effect of the charge on the mass flow rate, the non-dimensional parameter λ was introduced,

$$\lambda = \frac{\dot{m}_{av}}{\dot{m}_{av,fnl}} \quad , \tag{5.1}$$

where $\dot{m}_{av}$ is the steady mass flow rate for a specific test condition and $\dot{m}_{av,fnl}$ is the average mass flow rate obtained at the same test conditions, but at the nominal maximum needle lift (corresponding to $Ch = 100\%$).

The information provided by λ is fundamental, since it is the mathematical expression of the needle throttling effect, and this will be particularly useful in the following results analysis.

Fig. 5.3 shows the trend of λ versus the injection pressure at different values of *Ch*. At high values of *charge* ($Ch > 90\%$), the λ assumes similar values at different injection pressures. However, when *Ch* is reduced, the resultant needle throttling depends on p_i: this fact, again, is due to the resultant force of the hydrostatic pressure on the needle. Throttling the flow at the needle seat, the pressure in the nozzle sac decreases, subtracting *lifting* force to the needle and affecting the deformation of the leverage mechanism.
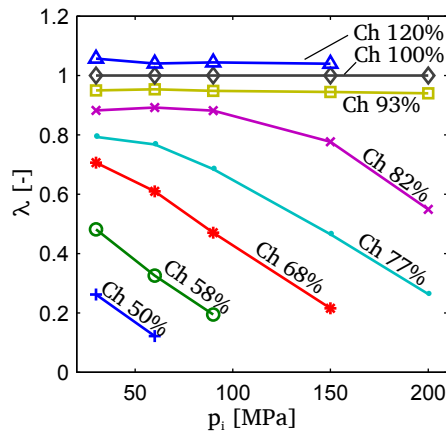
Figure 5.3: Needle throttling effect (λ) at different test conditions.

5.2.2   Needle opening

The analysis of the injector opening allows to better understand the injector behavior [7].

In Fig. 5.4-left the *CDA* rate of injection is compared to the one of a conventionl piezo servo-actuated injector. The comparison shows that the *ROI* ramp up of the servo actuated injector is faster and this difference is even more evident at high injection pressure. Moreover, the effect of p_i on the ramp up is the opposite in the two cases: a higher injection pressure causes a faster *ROI* ramp up for the conventional injector, while for the *CDA*, the ramp-up is slower (at least for the first part of the ramp). In a servo-actuated injector the movement of the needle is due to the effect of p_i: the higher the injection pressure, the stronger is the force moving the needle. On the other hand, the needle of the *CDA* is moved as a consequence of the direct actuation of the piezo, and the fuel pressure is forcing the needle against the nozzle seat also during the injection. Therefore, higher injection pressures mean higher forces against the needle movement and higher deformation of the leverage system [5].
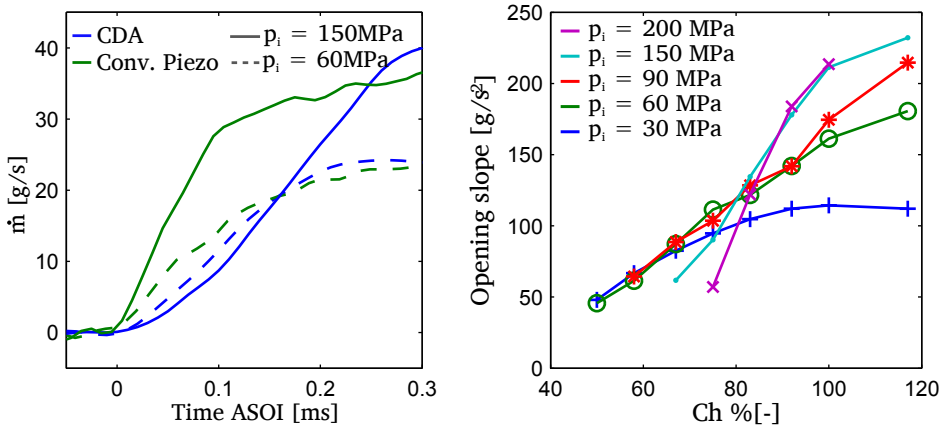
Figure 5.4: ROI at the start of the injection. Comparison of the ROI of the CDA (at the maximum nominal charge*) and a conventional piezo-injector (left) and effect of the test conditions on the slope of the ROI curve at the start of the injection (right).*

In order to enable a comparison among the different cases, the opening slope was calculated at each test condition performing a linear fitting of the *ROI* curve during the ramp-up, in the interval between 10 and 80% of $\dot{m}_{av}$. The results, plotted in Fig. 5.4-right, confirm the substantial impact of *Ch* on this measurement, while the impact of the injection pressure is noticeable only above a certain value of *Ch*.

The dwell-time between the electrical signal to the injector and the effective start of the injection (injection delay or τ_i) is also affected by the test conditions.

The injection delay increases at higher injection pressure and at lower *charge* (Fig. 5.5-left). Also in this case, the trend is the opposite of what is observed in conventional servo-actuated injectors, as noticed by other authors [8, 9]. A deeper analysis reveals that τ_i is mostly related to the energization profile sent to the injector: crossing the injection delay results with the related energization curves (voltage versus time), the voltage corresponding to the start of the injection can be obtained. The plot at the right hand side of Fig. 5.5 shows that, at a specific injection pressure, τ_i is mainly dependent on the voltage applied. In other words, at each injection pressure there is a voltage threshold that allows the needle to move and consequently the injection to start. This is consistent with the fact that the actuator has to compensate the hydrostatic forces and the related deformation of the leverage system.
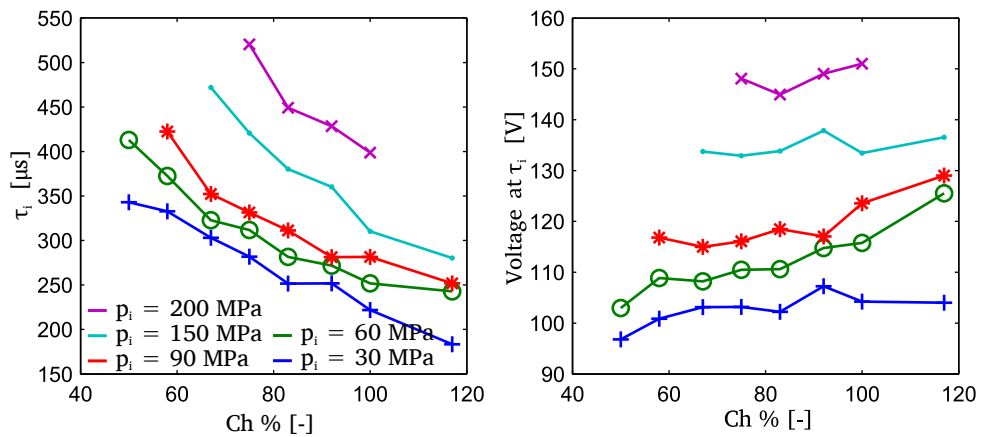
Figure 5.5: Injection delay analysis. τ_i under different test conditions (left) and energization voltage at the start of the injection (right).

An accurate control on the amount of fuel injected is a paramount requirement for an injector. Fig. 5.6 shows the shot-to-shot standard deviation obtained at different test conditions. As the needle is throttling the fuel flow, the accuracy on the injected mass decreases. This effect is more pronounced at higher injection pressure, remarking the problems related to the needle control at these conditions. In this case, the relationship between shot-to-shot standard deviation and p_i is similar to conventional injectors: increasing the injection pressure the accuracy of the injector increases as well [10]. However, this behavior is observed only at high needle lift ($\lambda \approx 1$): when the injector charge is reduced, the higher standard deviation is measured at higher pressure as a consequence of the more difficult control of the needle position at these conditions.
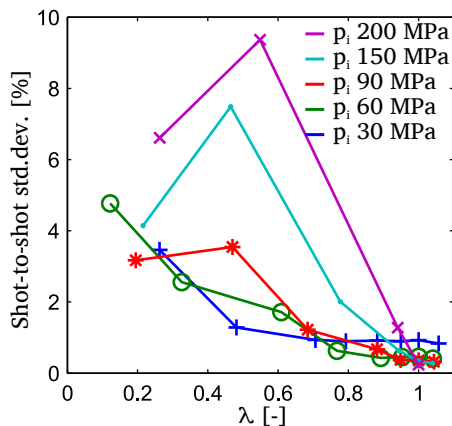
Figure 5.6: Relative standard deviation of the total mass injected for long injections; $ET = 3.0$ ms, $p_a = 5$ MPa.

5.2.3 Injection rate shaping

One of the breakthrough features of this injector is the capability of performing rapid variations in the needle position, even when compared to the short time-scale of the Diesel injection, in other words, to perform injection rate shaping. The plots in Fig. 5.7 show results obtained applying two different energization profile types. In the first case (Fig. 5.7-left), the ramp-up slope of the energization signal was reduced: as expected, this change is reflected on the *ROI* curve by a reduction in the mass flow rate ramp-up slope. This injection profile will be referred as *ramp* profile.

In the second case, a two-step energization profile was tested, setting a lower tension in the first part of the injection and targeting the *ROI* obtained at $Ch = 100\%$ in the final part. Also in this case, the *ROI* reflects the changes applied to the energization signal and a significant reduction in the mass flow rate is observed during the first stage of the injection. This injection profile shape will be referred as *boot* profile and it is divided into two stages based on the related mass flow rate: the first one is called *foot* stage, while the second is referred as *leg* stage.

In order to characterize these non-conventional injection rate profiles, two shape-parameters were defined:

- *opening time* (t_{open}). It is used to describe the ramp shaped injection profiles. It is defined as the time elapsed between the start of the injection and

the moment at which the *ROI* reaches the 90% of its steady value. This parameter can be quantified also for the *square* case;

- *foot rate* (λ_{foot}). It is used to quantify the *ROI* during the *foot* stage. Similarly to the parameter λ defined in Eq. (5.1), it is the ratio between the mass flow rates measured during the *foot* and *leg* stages. In the *square* case $\lambda_{foot} = 1$.
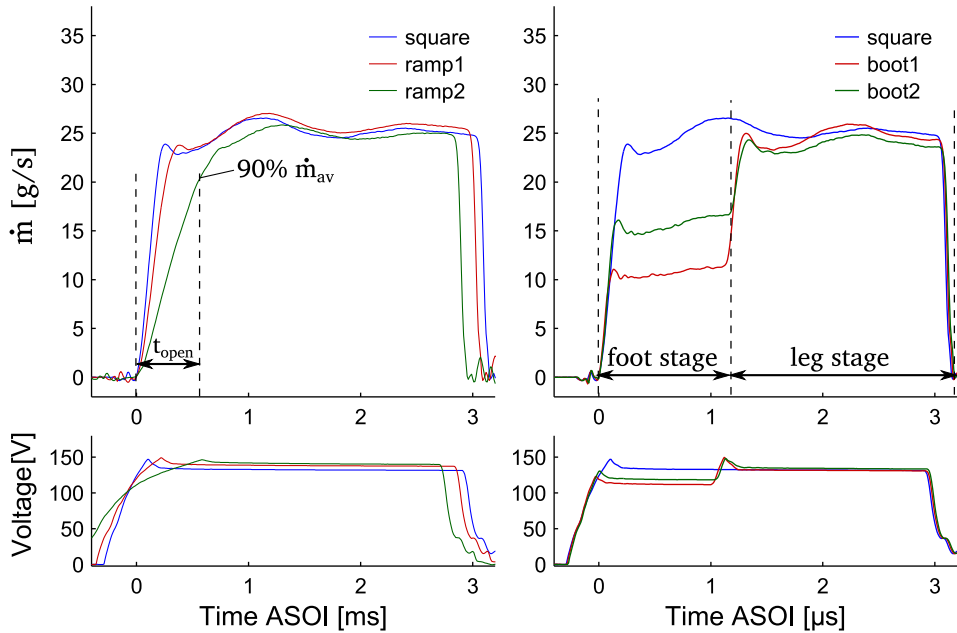
Figure 5.7: Alternative injection rate profiles. Ramp *(left) and* boot *(right) shaped ROI; in the bottom of the plots the energization signal is shown: the* square *shaped injection obtained at the same injection pressure and* Ch $= 100\%$ *is plotted for reference;* $p_a = 5$ MPa*,* $p_i = 60$ MPa

5.2.4   Rate of momentum

The spray momentum flux measurement is the second step necessary to complete the hydraulic characterization of the injector. Moreover, as explained in Sec. 4.3, the rate of momentum (*ROM*) can be measured for each single spray separately, allowing to understand the hole-to-hole dispersion at the different test conditions [11]. However, the seven-spray average better represents the injector behavior and, therefore, the results will refer to the seven-sprays averaged value $\dot{M}_{av}$, leaving the hole-to-hole dispersion analysis to a specific discussion.

The *ROM* curves presented in Fig. 5.8 have similarities to the ones seen in *ROI* measurements: the spray momentum flux decreases with either p_i or *Ch*. Therefore, these results are a further insight to the relationship between *Ch* and needle lift. More specific evaluation will be enabled by the analysis in the next section presenting area and velocity coefficients.
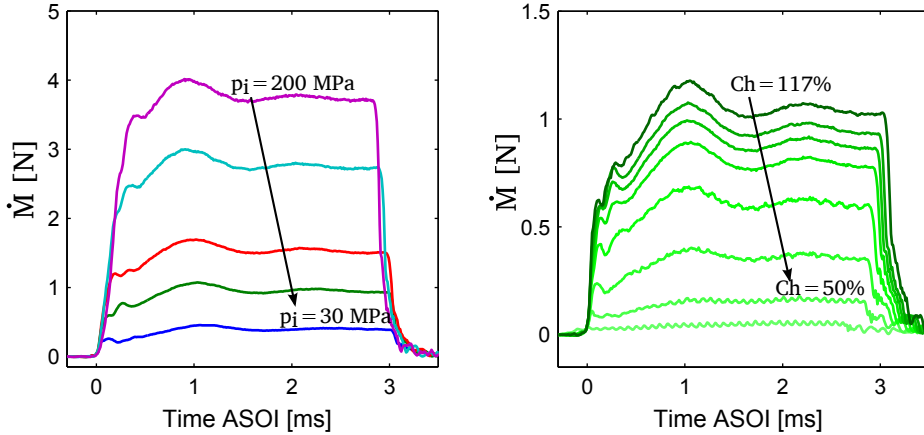
Figure 5.8: ROM measurements at different test conditions. Effect of a variation in p_i at full needle lift (left) and in Ch at $p_i = 60$ MPa (right); $p_a = 5$ MPa.

Fig. 5.9 shows the time averaged spray momentum flux ($\dot{M}_{av}$) as a function of the injector charge for all the rail pressures tested. The plot confirms the similarities with *ROI* results; in order to evaluate the relationship between *Ch* and the spray momentum, as previously done for *ROI* results, a non-dimensional parameter was defined:

$$\lambda_{ROM} = \frac{\dot{M}_{av}}{\dot{M}_{av,\ 100\%}} \quad , \tag{5.2}$$

where $\dot{M}_{av,\ 100\%}$ is the time averaged *ROM* obtained for the same test conditions at the nominal maximum needle lift (corresponding to *Ch* = 100%). The left plot of Fig. 5.9 shows that, as for the mass flow rate, the injector charge does not have a clear relationship with the spray momentum, as the *Ch* impact on $\dot{M}_{av}$ is non-linear and strongly dependent on p_i; as concluded after *ROI* analysis, this is due to the piezo-stack behavior and mechanical deformation of the leverage system.
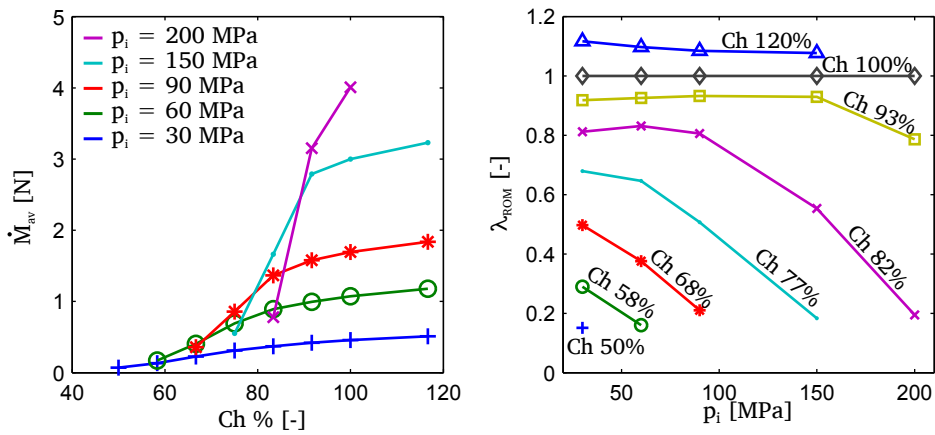
Figure 5.9: Time averaged spray momentum flux (left) and relative variation in $\dot{M}_{av}$ related to a variation in Ch (λ_{ROM})(right); $p_a = 5$ MPa.

5.2.5 Hydraulic characterization results

By the combination of the mass flow rate and momentum flux measurements, it is possible to estimate the effective velocity and area at the orifice outlet together with the related coefficients C_v and C_A [3].

The effective velocity decreases with λ (Fig. 5.10), accordingly to the hypothesis presented before of a decrease in the nozzle-sac pressure.

However, the analysis of the velocity and area coefficients in Fig. 5.11, shows an interesting feature: both quantities decrease with λ and show only a second order variation when modifying the injection pressure. This fact means that a reduction in either the needle lift or the injection pressure has a similar effect on the global mass flow rate, but different effects on the flow through the orifices. Considering that the high *k-factor* of the orifices (1.5) combined with the rounded orifice inlet prevents cavitation in the orifice at conventional test conditions [3, 12], it is expected only a slight influence of injection pressure on C_A. The effect of *Ch* (or λ) suggests that the modification in the flow caused at partial needle lift is propagated through the nozzle sac and reflected in the flow through the orifice outlet.

Moreover, the sensibility of the area coefficient to λ decreases when λ increases: this means that the variations in the fuel flow due to the needle throttling have greater effect on the area coefficient when the needle lift is small. In fact, at these conditions the fuel velocities in the nozzle seat increases significantly affecting the velocity profile at the orifice inlet. The different effect that *Ch* and p_i

have on the fuel flow will be the key to understand the results presented in the next section describing the spray development.

These results are in agreement with the computational work performed by Martinez [13], focused on the study of the fuel flow within the nozzle at reduced needle lift: the results showed that the acceleration of the fuel caused by the needle throttling changes the flow pattern at the orifice inlet.
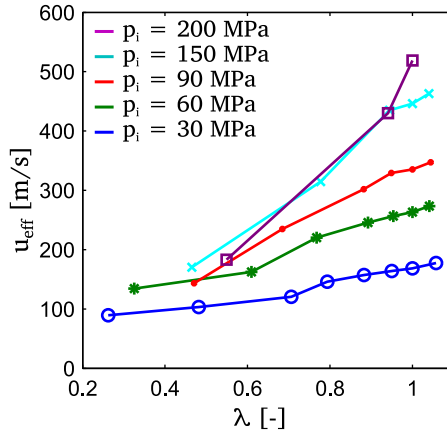
Figure 5.10: Results of the hydraulic characterization. Effective velocity (u_{eff}) (left) and velocity coefficient (C_v)(right) under different test conditions; $p_a = 5$ MPa.

5.2.6 Reference injection conditions

After performing the hydraulic characterization, a set of reference injections was selected to be studied in the following experiments. In order to have a global picture of the different capabilities of the injector, two injection pressures were included, representative of typical low ($p_i = 60$ MPa) and high ($p_i = 150$ MPa) rail pressure conditions. Three different injector *charges* for each p_i were chosen to represent the full needle lift case ($Ch = 100\%$) and two partial needle lifts: for each pressure the lowest stable needle lift ($Ch = low$) together with an intermediate one ($Ch = med$) were studied. The injection rate shaping capabilities of the injector were included in the test matrix choosing the profiles presented in 5.2.3:

- two *boot* profiles at different values of λ_{boot};
- two *ramp* profiles adjusting the opening slope (the parameter t_{open}).

Each injection profile was tested at both values of p_i mentioned earlier. Tab. 5.1 the details of the reference injections presents.
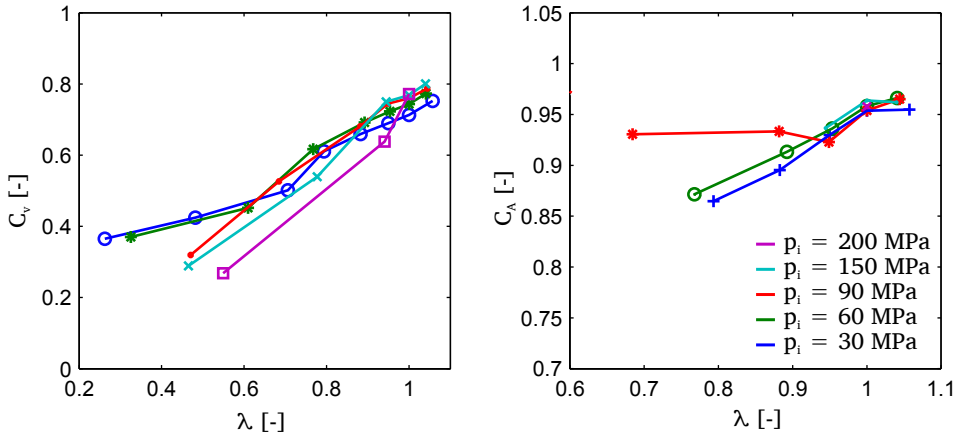
Figure 5.11: Results of the hydraulic characterization. Velocity coefficient (C_v) (left) and area coefficient (C_A)(right) under different test conditions; $p_a = 5$ MPa.

p_i [MPa]	Shape [−]	Ch [−]	Ch_{ref} [−]	λ [−]	λ_{boot} [−]	t_{open} [ms]	C_d [−]	C_v [−]	C_A [−]
	square	100	*high*	1	1	0.21	0.70	0.68	1.00
60	*square*	75	*med*	0.76	1	0.19	0.52	0.54	0.97
	square	50	*low*	0.58	1	0.17	0.40	0.41	0.95
	square	100	*high*	1	1	0.25	0.74	0.76	0.99
150	*square*	90	*med*	0.89	1	0.23	0.65	0.59	0.98
	square	85	*low*	0.77	1	0.19	0.56	0.53	0.96
60	*boot1*	100	*high*	1	0.4	-	-	-	-
	boot2	100	*high*	1	0.6	-	-	-	-
150	*boot1*	100	*high*	1	0.4	-	-	-	-
	boot2	100	*high*	1	0.6	-	-	-	-
60	*ramp1*	100	*high*	1	-	0.34	-	-	-
	ramp2	100	*high*	1	-	0.67	-	-	-
150	*ramp1*	100	*high*	1	-	0.52	-	-	-
	ramp2	100	*high*	1	-	1.1	-	-	-

Table 5.1: Reference injections features. The hydraulic coefficients were measured at $p_a = 5$ MPa.

The total duration of the injections had to be modified for the optical diagnostics carried out at reacting conditions, in order not to exceed the maximum injected fuel mass allowed by the test chamber (Sec. 4.6): in these cases, the only parameter modified is the total energizing time, keeping constant the other features of the injection. Finally, even if the tests were performed at different values of p_a, this quantity will not be included to define the reference injection cases, since its influence is negligible [14].

5.3 Spray development at isothermal conditions

Mie scattering imaging is a powerful technique for the study of the Diesel spray since it gives direct and reliable information about the spray development. The simple observation of the images provides paramount insights for the spray understanding.

Even if the parameters extracted in these tests are normally reduced to spray penetration and spreading angle, the information available in the images is much wider: for example, the definition of the aforesaid parameters can be adjusted in order to orient the investigation over different features of the spray. Moreover, the images themselves are maps of the light scattered by the sprays and, even if it is difficult to relate this signal to quantitative measurements, they give fundamental insight about the evaporation process.

As introduction to this section, Mie scattering images obtained at different ambient temperatures (keeping constant ρ_a and all the other injection parameters) are compared.

In Fig. 5.12, the raw images (presented in color map) highlight that at higher T_a the intensity gradients characterizing the spray boundaries are reduced. This phenomenon is related to the increasing fuel evaporation that at higher ambient temperature gets more intense and reduces the average droplet diameter [15]. In fact, the Mie signal is proportional to the surface of the droplets and consequently, to the square of the droplet diameter. In particular, the evaporation affects the resulting Mie image decreasing the intensity in the periphery regions where the mixing rate is higher (c.f. to Fig. 5.12) [1].

To have a better understanding of the effects of T_a on the Mie scattering images in Fig. 5.13, the digital level profile measured along the spray axial and radial directions are presented (see Fig. 5.12). The plot shows that the spray penetration still appears as a robust measurement until 600 K, since the intensity transition at the spray tip is steep and the threshold employed has a limited impact on the penetration measurement; this fact is also justified by the mixing rate at the spray tip,
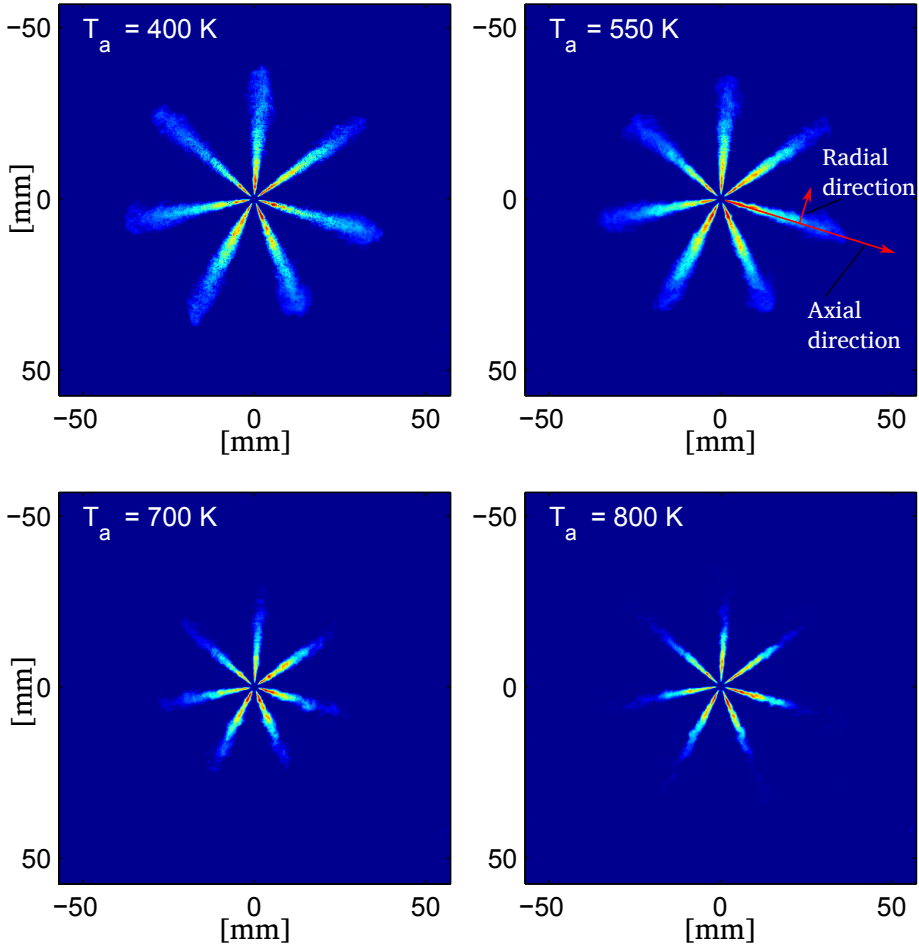
Figure 5.12: Comparison of Mie images at different T_a and constant density acquired at 750 µs ASOI; $p_i = 60$ MPa, $\rho_a = 19.2$ kg/m³, Ch = high. The axial and radial direction are indicated.

that is typically low for the Diesel spray [16] and therefore the fuel evaporation is limited.

On the other hand, a further increase of T_a causes the complete evaporation of the fuel at a certain distance from the orifice: this distance is normally referred as *liquid length* (*LL*) and, in this region, the gradient in intensity has a different aspect [17–19]. The bottom-right plot of Fig. 5.13 shows that the uncertainty due to the intensity threshold selected for the penetration is limited and, moreover, that this sensitivity increases with ambient temperature.
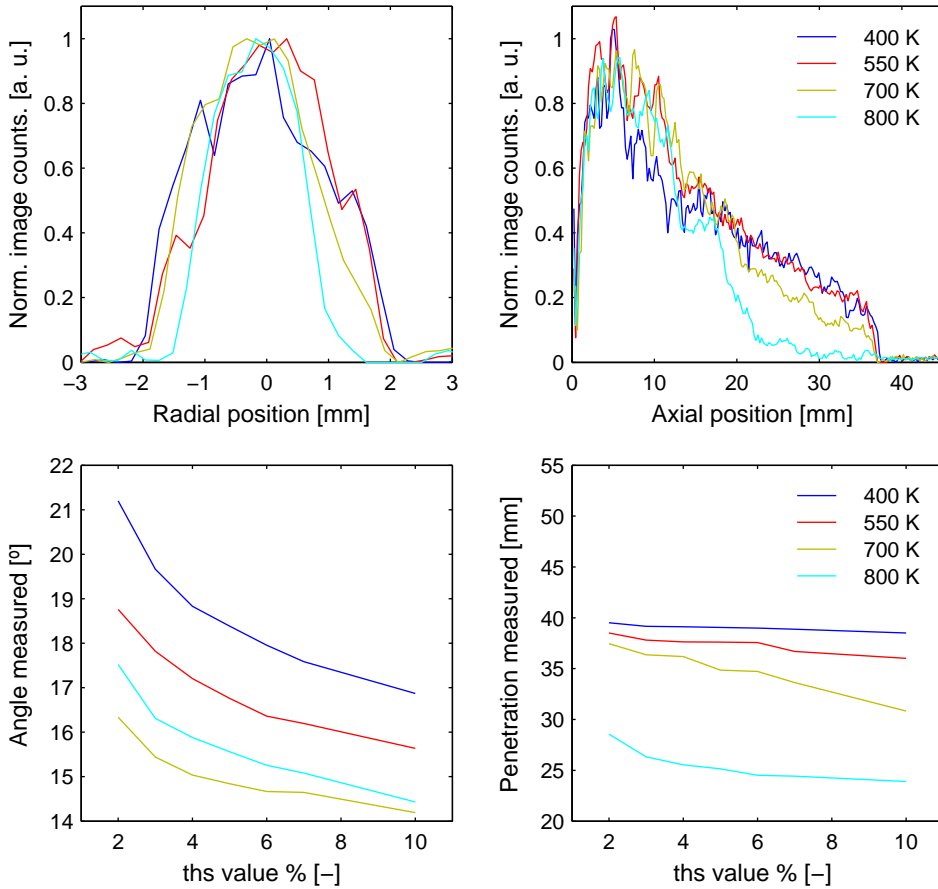
Figure 5.13: Radial (left) and axial (right) intensity profiles referred to the images of Fig.5.12 at different T_a and constant density; $\rho_a = 19.2\,\mathrm{kg/m^3}$, $p_i = 60\,\mathrm{MPa}$, Ch = high.

Another macroscopic parameter commonly measured in Mie imaging is the spreading angle θ. This parameter, crucial for the spray mixing process and representing the geometrical aspect of the spray, has a substantial impact on the air entrainment. Even though the definition of θ is conceptually simple, its implementation is a very delicate process, since slight changes in its definition cause important variation in the results [20, 21].

The radial intensity profile in the region typically chosen to calculate the spreading angle (Fig. 5.13-top-left) is not as steep as the axial profile; in addition, due to the definition of the parameter itself, an equivalent bias in the radial position of the boundaries has a bigger impact on the value of θ than it would have on the value of the penetration.

The bottom-left plot of Fig. 5.13 shows clearly a substantial sensitivity of the spreading angle to the threshold employed, regardless of the temperature tested. Consequently, the measurement θ is not considered quantitative since it is too sensitive to the arbitrary definition of the intensity threshold defining the spray boundaries [22].

Finally, an important outcome from Fig. 5.13 has to be highlighted: the tests performed at $T_a = 400\,\mathrm{K}$ show less sensitivity to the threshold selection for the penetration measurement and, when comparing the results of spreading angle, θ measured at 400 K is higher. This last aspect is particularly important because, assuming that the spray pattern is the same (or at least similar) at different temperatures, the variations in the measurement of the spreading angle are due to the evaporation of the droplets in the periphery of the spray (partial or complete) [1] and the consequent miss-detection of the optical setup. Therefore, in the next section, most of the results will be presented at 400 K [23].

5.3.1 Penetration and spreading angle

The effect of boundary conditions on the spray penetration (S_l) and spreading angle (θ) measured via Mie scattering are analyzed in this section. Even though the measurements were extracted from each spray separately, they will be generally presented as seven-spray average. Differently, if the results are related to only one spray, it will be specified.

Effect of ambient parameters

The effect of the T_a on the spray penetration S_l was studied testing different ambient temperatures while keeping constant the rest of the boundary conditions. Since it has been largely demonstrated that the ambient density (ρ_a) is the driving

parameter for the spray penetration [24–26], the ambient pressure was adjusted for each T_a in order to maintain constant ρ_a [27].

As expected, the effect of ambient temperature on the spray penetration is limited (c.f. figure 5.14) since the key parameters determining the penetration were kept constant in the comparison (spray momentum and ambient density) [23–25]. However, the plot shows a subtle consistent trend, indicating a slight decrease in spray penetration with increasing temperature. Keeping in mind what was discussed in the previous section, the differences observed (about 5 mm) cannot be related to a sensitivity matter, since they are well over the range of uncertainty due to the threshold selection (the result plotted are referred to *ths* = 2%). Therefore, the differences observed have to be related to some difference in the spray development: the reduction in droplet size due to the evaporation at higher temperature may ease the momentum transfer from the fuel to the surrounding air. This effect is important especially in the first millimeters of the spray penetration in which the velocities gradients are higher [23]. The plot presented in Fig. 5.14-right confirms that the differences in penetration observed are mainly related to the first millimeters, while, after a certain distance, the penetration rate is the same for all the cases. The only exception is the case $T_a = 700 \, \text{K}$: in this case, at a certain distance ($S_l > 50$ mm) S_l stops growing as a consequence of the complete evaporation of the spray. This observations are consistent with the work presented by Payri et al. testing an single-axial hole nozzle injector [23].

Having the ambient temperature an important effect on the sensitivity of the spreading angle measurement (c.f. Fig. 5.13), the related comparison would not be reliable and, therefore, it is not presented.

Ambient density is a critical parameter for the spray development [24, 28, 29] and it affects both spray penetration and spreading angle. Fig. 5.15 reflects this behavior and indicates that an increase in ρ_a causes a slower spray penetration and an increase of θ: a higher density of the gas entrained requires more kinetic energy to complete the momentum transfer and, thus the spray penetrates slower. Furthermore, the spray penetration measured at the lowest density ($\rho_a = 15.2 \, \text{kg/m}^3$) puts even more in evidence a feature that, in different proportion, characterizes all the curves: the penetration rate at the beginning is increasing as a consequence of an increase in mass flow rate. This phenomenon has a significant impact on the spray penetration.

Effect of injection parameters

When different injection pressures are tested, the effects over the spray penetration are readily apparent. Fig. 5.16 illustrates that, as expected, an increase
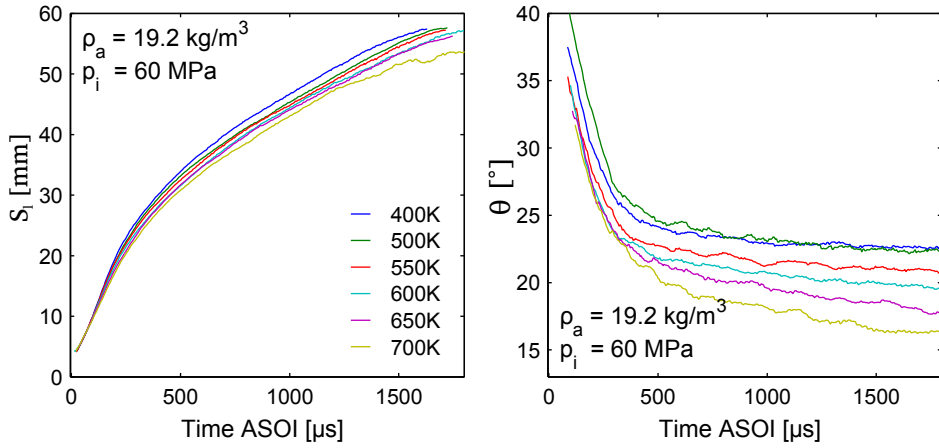
Figure 5.14: *Effect of T_a on the spray penetration (left) and spreading angle (right); $\rho_a = 25.0\,\mathrm{kg/m^3}$, $p_i = 60\,\mathrm{MPa}$, Ch = high.*
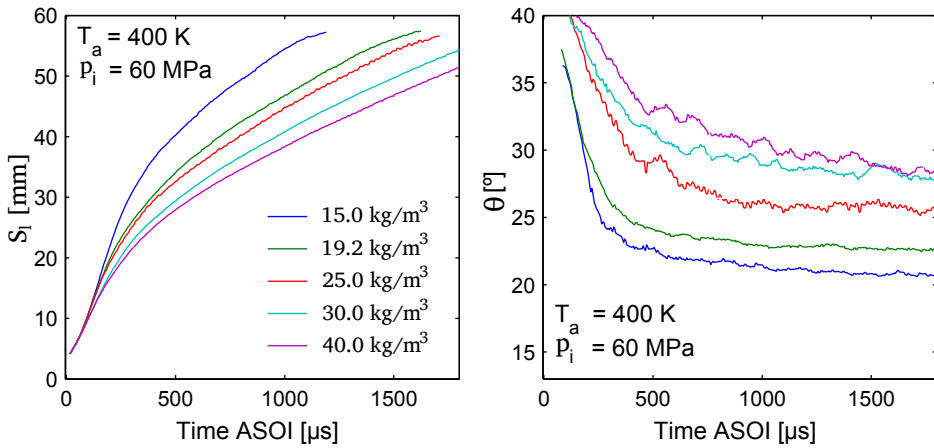
Figure 5.15: *Effect of ρ_a on the spray penetration (right) and spreading angle (left); $T_a = 400\,\mathrm{K}$, $p_i = 60\,\mathrm{MPa}$, Ch = high.*
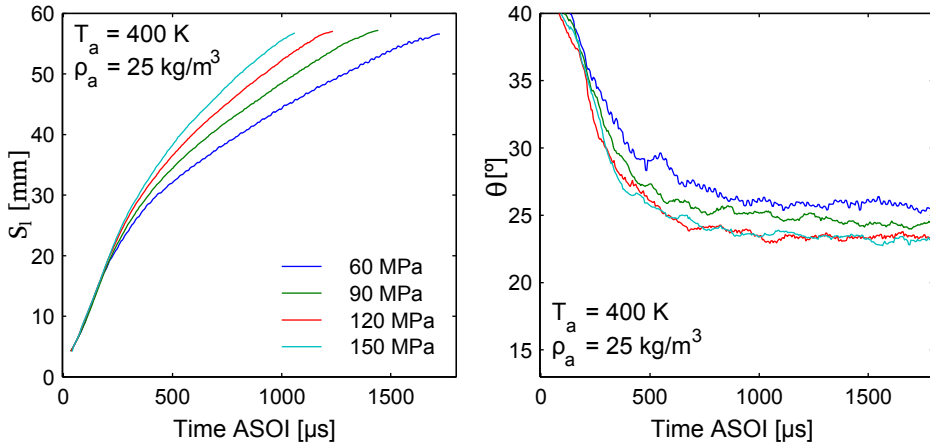
Figure 5.16: Effect of p_i on the spray penetration (right) and spreading angle (left) (7-spray average); $T_a = 400$ K, $\rho_a = 19.2$ kg/m³, $Ch =$ high.

in injection pressure produces an increase in the penetration rate. These results qualitatively agree with those previously obtained for the momentum flux and the known relation between mass flow rate, momentum flux and outlet velocity (see Sec. 3.3) [2, 26]. Nonetheless, the injection pressure effect is noticeable only after the spray has penetrated to a certain extent, since at the beginning of the injection the spray development is very similar. The right plot shows also another significant feature: the spreading angle decreases $1 - 2°$ passing from $p_i = 60$ to 150 MPa. This effect, also observed by other authors [30, 31] is likely due to the fact that an increase in the injection pressure induces modifications in the internal flow pattern that have repercussions on the spray formation.

Fig. 5.17 illustrates the influence of injector charge level in conventional *square* injection profiles. Likewise with the injection pressure, an increase in Ch causes an increase in the spray momentum and then in the penetration rate [32]. Nevertheless, there is a slight difference between the injection pressure and the piezo-stack charge level effects, and it is noticeable at the start of the injection. As discussed in Sec. 5.2, the opening of the nozzle of the *CDA* injector is directly controlled by the piezo-stack deformation through the leverage mechanism, while the fuel pressure has a contrasting effect. Coherently with what observed in Fig. 5.4, at the beginning of the injection, the spray penetration is more dependent on the injector charge than on p_i. This further result confirms that the needle lift plays a key role in both the transient and the steady stages of the injection process.

The effect of partial needle lift can be observed also in the spreading angle: Fig. 5.17-right shows that, decreasing the needle lift, θ increases of about 5°.
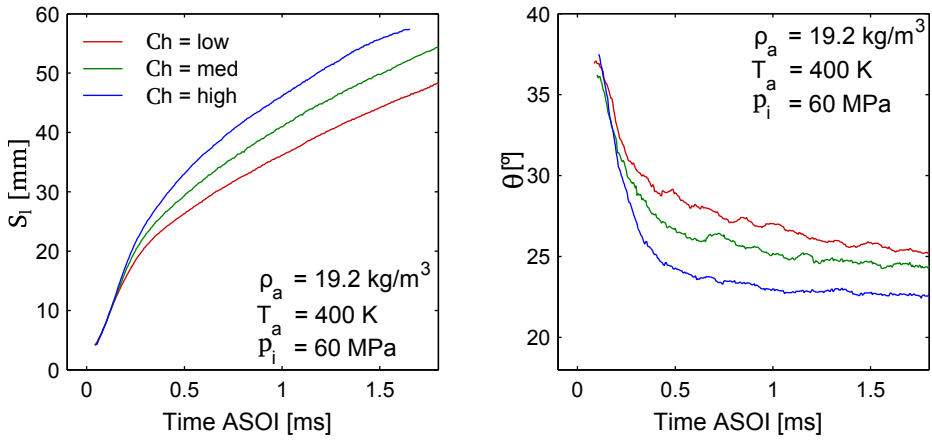
Figure 5.17: Effect of Ch on the spray penetration (left) and spreading angle (right)(7-spray average); $T_a = 400\,\mathrm{K}$, $\rho_a = 19.2\,\mathrm{kg/m^3}$, $p_i = 60\,\mathrm{MPa}$.
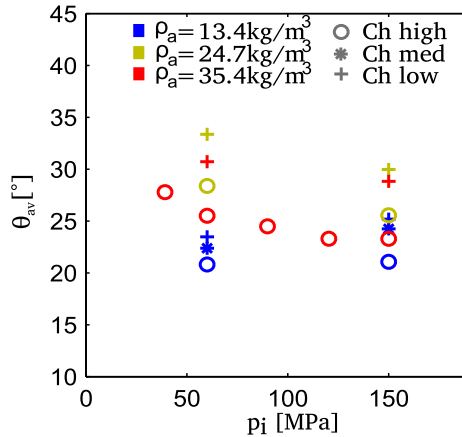
Figure 5.18: Average spreading angle at different test conditions; $T_a = 400\,\mathrm{K}$.

This observation is of great importance since it creates a link with the hydraulic characterization results (Sec. 5.2): reducing the injector *charge*, modifications in the internal flow take place as proven by the variation measured in C_A and C_v. The variations observed in the spreading angle suggest that these modifications are propagated downstream and affect the spray development and the mixture formation [24, 33].

Effect of injection rate shaping

Fig. 5.19-left compares spray penetration using three different injection rate profiles: with reference to Tab. 5.1, the injection profiles named *boot1* and *ramp2* are compared to the reference *square* injection profile (*Ch* = *high*). The comparison highlights a significant impact of the injection rate profile on the penetration rate: *boot* and *ramp* at the beginning of the injection penetrate slower than the *square* profile. The *ROI* increase characterizing the *boot* profile is readily reflected as an increase in the penetration rate at about 1.5 ms. On the other hand, in the *ramp* case the spray penetration, lower at the beginning, keeps growing with quasi-linear dependence on time as a consequence of the increasing *ROI* and finally penetrates faster than the *square* case.

Also in this case, the spreading angle depends on the flow throttling actuated by the needle. Coherently, Fig. 5.19-right shows that the angle varies accordingly to the instantaneous mass flow rate: during the *foot* stage the spreading angle is higher and at the end of the injection (when the mass flow rate is the same for the three cases) the spreading angles measured are very close.

These results confirm the capability of the *CDA* to control the spray formation, causing a modification of the penetration rate when applying *boot* or *ramp* profiles. This fact proves the versatility of the injector and adds new possible injection strategies for the engine designers [34].

Although this is a direct consequence of the capability of controlling the spray momentum flux [32], it is important to underline the novelty of this measurement, since the effect of injection rate shaping on spray development has been investigated only in few cases [35, 36], and none of them using the direct acting technology.

Another interesting qualitative measurement provided by the Mie imaging is calculated dividing the spray volume (V_s), obtained from the spray contours, by the total amount of fuel injected at the correspondent instant ($\int \dot{m}dt$). This quantity ($v_{f,av}$) represents the average fuel specific volume within the spray region, and therefore it is an indicator of the fuel-air mixing [1]. $v_{f,av}$ is presented in Fig. 5.20 at different injection cases: the plot clearly indicates that the increasing mass
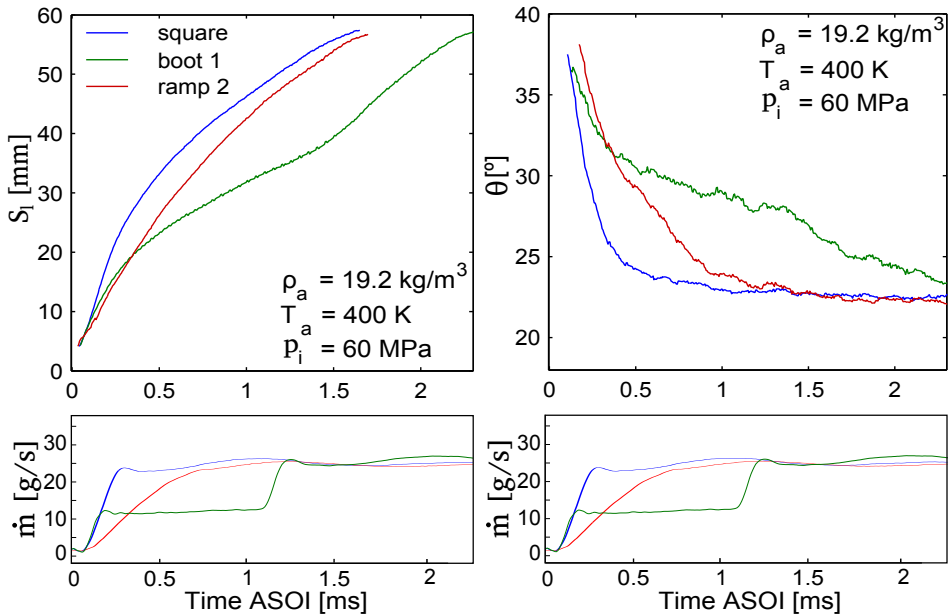
Figure 5.19: Effect of injection rate shape on the spray penetration (right) and spreading angle (left). $\rho_a = 19.2\,^{kg}/_{m^3}$, $T_a = 400\,K$, $p_i = 60\,MPa$.

flow rate characterizing the *ramp* injection or the transition occurring in the *boot* case causes a substantial decrease of $v_{f,av}$. As mentioned in the description of the mixing limited spray-interpretation, an increase in the mass flow rate causes a transient momentum and mass accumulation within the spray, until this wave is not transmitted to the spray tip. On the other hand, the small difference observed between the two *square* injection is likely due, in part to the lower spreading angle measured at $p_i = 150\,MPa$ and, in part, to the longer *ROI* ramp up characterizing this conditions (c.f. Fig.5.4) and, therefore, to the aforementioned mass accumulation.

5.3.2 Spray axis

The partial needle lift is expected to increase the asymmetries in the fuel flow within the nozzle: as shown by Martinez [13], in a micro-sac configuration the perturbations caused by the restriction at the needle seat increase the fuel velocities in the sac and modify the flow pattern at the orifice inlet. However, the variations expected could be observed in the plane on which the orifice and the
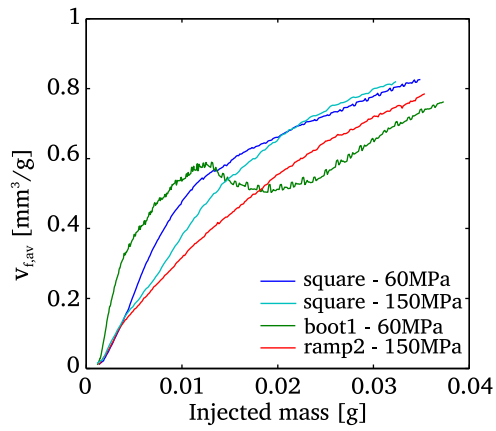
Figure 5.20: Average fuel specific volume obtained at different injection conditions; $\rho_a = 19.2\,\mathrm{kg/m^3}$, $T_a = 400\,\mathrm{K}$.
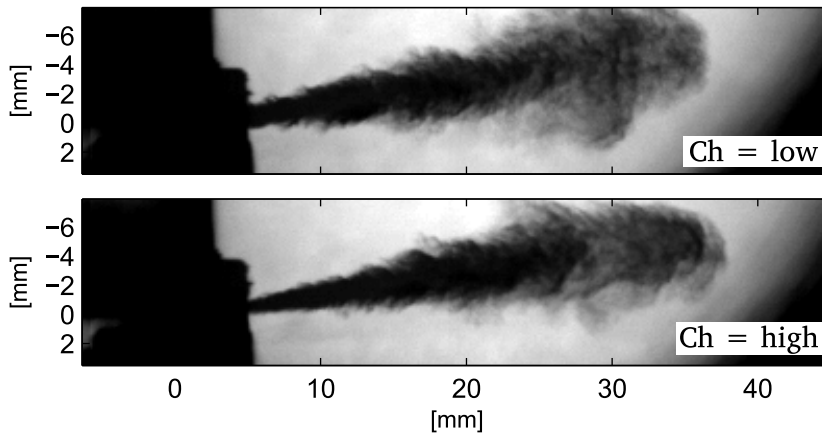
Figure 5.21: Sample raw images obtained using the DBI *setup for different value of* Ch *at similar spray penetration; $\rho_a = 19.2\,\mathrm{kg/m^3}$, $T_a = 500\,\mathrm{K}$.*

injector axis are lying and, therefore, the frontal visualization setup used in the previous tests cannot clarify this issue.

Tho this end, the *DBI* imaging setup described in Sec.4.5.3 was used to observe the development of a single spray along the convenient direction. In Fig. 5.21 two sample raw images are presented.

As a result of the processing applied, *2-D* extinction maps can be obtained [37]: Fig. 5.22 shows the time-averaged extinction maps obtained at two different charge levels. Even if the measurement cannot be considered quantitative due to the limitations of the technique (Sec. 4.5.3, [37]), the results provide important insight about the morphology of the spray.
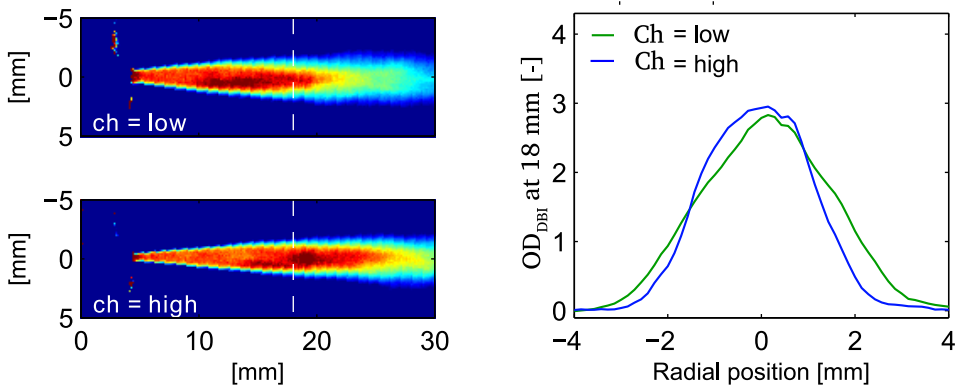
Figure 5.22: Spray optical depth obtained by DBI *technique;* $\rho_a = 19.2\,{}^{\mathrm{kg}}\!/\mathrm{m^3}$, $T_a = 500\,\mathrm{K}$, $p_i = 60\,\mathrm{MPa}$.

Also from this point of view, at different *charge* the spray shape changes: even without measuring the spreading angle, at low charge, the spray appears wider (Fig.5.21). The radial profiles of the *DBI* derived optical depth (OD_{DBI}) reveals another important feature (Fig. 5.22 right): at low injection *charge*, the equivalent extinction profile is asymmetric and the curve is slightly *shifted* on one side. In order to globally evaluate this effect, the spray axis was calculated connecting the orifice outlet to the spray centroid obtained based on OD_{DBI}. The deviation of the spray axis from the nominal orifice axis is indicated by the angle γ.

Fig. 5.23 shows, at two different injection pressures, that at *low* charge γ increases with respect to the *high* charge case. As shown by Martinez in [13] and presented in Fig. 3.26, at partial needle lift, the velocity profile at the orifice outlet is modified: at partial needle lift, the velocities of the flow in the needle seat
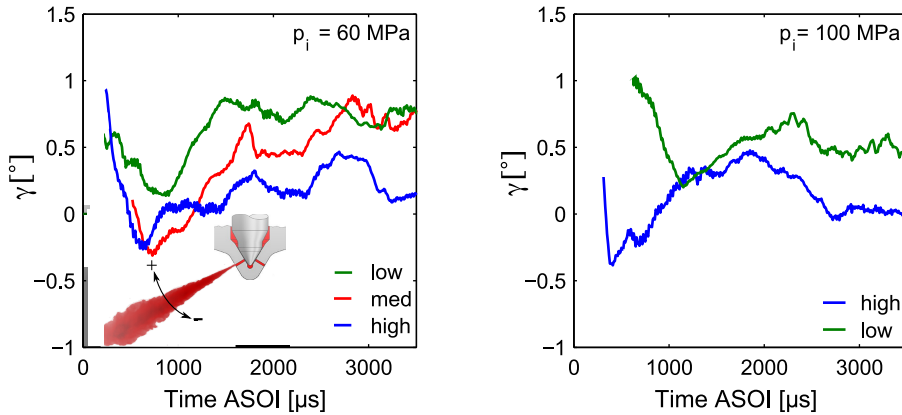
Figure 5.23: Spray axis inclination obtained from lateral spray imaging; the sketch on the plot indicate the sense of the rotation; $\rho_a = 19.2 \, \mathrm{kg/m^3}$, $T_a = 500 \, \mathrm{K}$.

are significantly increased with the consequent generation of asymmetries in the flow within the orifice. Therefore, this phenomenon is suspected to affect the spray formation and the fuel distribution within the spray. To the author's knowledge, exhaustive computational works investigating the relationship between the velocity profile at the orifice outlet cannot be found in the literature.

5.3.3 Transient behaviors

The results presented up to this point give a description of the global behavior of the spray; however, the time resolution of the data obtained is not fine enough to catch transient spray features associated to fluctuation in the mass flow rate or the penetration rate at the start of the injection [25, 30]. In fact, despite the fine pixel resolution (a pixel of the camera corresponds to about 0.18 mm), the frame rate is relatively low (20*kfps*) does not allow to study fast transients. In order to overcome this problem, some tests were specifically performed reducing the camera field of view and increasing the acquisition rate (64 × 64 pix centered on the nozzle at 320*kfps*).

At the high acquisition rate employed, the spray penetration and the spreading angle can be measured accurately in the region analyzed, adding the fundamental advantage of the improved time accuracy. The sample images of the start of the injection shown in Fig. 5.24 show important differences between the sprays in terms of timing and shape. To better understand this hole-to-hole dispersion

p_i = 60MPa – high

p_i = 150MPa – high

p_i = 60MPa – low

p_i = 60MPa – ramp 2
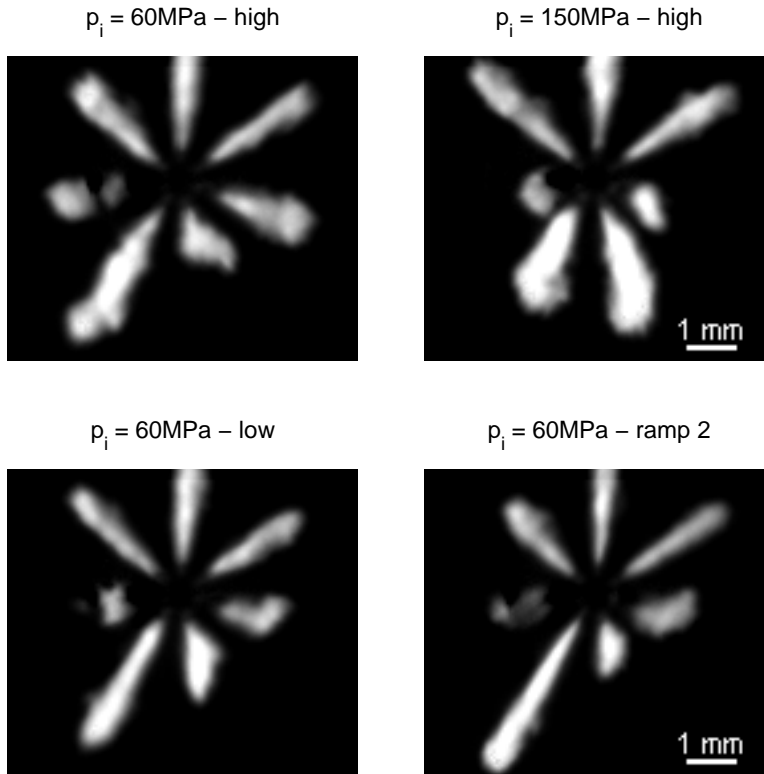
Figure 5.24: Sample images of the nozzle region at SOI*; T_a = 870 K, ρ_a = 19.2 kg/m³.*

the penetration and spreading angle measured in these tests will be carefully discussed.

The four plots of Fig. 5.25 present the average penetration obtained for the different sprays at different injection conditions. The hole-to-hole penetration difference suggests that, at lower *charge*, the difference between the spray plumes increases. This fact relates the hole-to-hole dispersion (at least at the very beginning of the injection) to the needle position. This hypothesis is enforced by the dispersion of the data observed in the *ramp* case: decreasing the velocity of the needle lift, the difference between the sprays increases further and, also, a significant difference in the timing at which each spray appears can be observed. On the other hand, an increase in p_i does not show any significant effect on the hole-to-hole dispersion. Even tough the nozzle seat is *micro-sac* type, the flow through the orifices at the start of the injection is not symmetric [38]. Kastengren
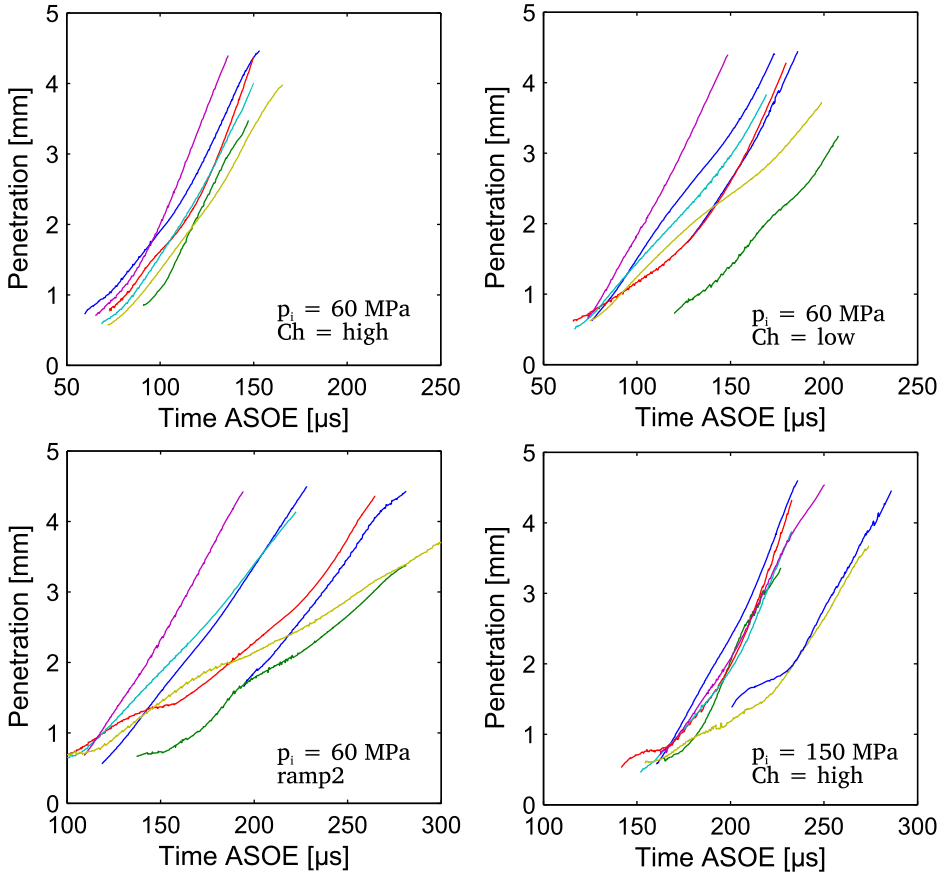
Figure 5.25: *Penetration results from the 7 sprays obtained for different cases. The colors indicate the different sprays;* $\rho_a = 19.2\,\mathrm{kg/m^3}$, $T_a = 870\,\mathrm{K}$.

et al. [39] used X-ray imaging to characterize the needle movement in a single-hole axis-symmetric nozzle and observed that the needle has repetitive off-axis movements during the injection: the same behavior may be the cause of the hole-to-hole differences observed in these tests [40]. It is also interesting to notice that the slope of the penetration curves, in some cases, increases with time. To investigate this behavior, the spray tip velocity was calculated, based on the penetration data [23, 30]. The tip velocity curves presented in Fig. 5.26 for different injection conditions show an interesting feature: during the opening transient the tip velocity shows a local minimum and then, it continues increasing, at least until the spray tip exits from the field of view. In the author's opinion, this behavior, consistent in the different injection cases, is associated to the sac-pressure that is

increasing during the needle opening. In fact, during this period there are impor-
tant head losses at the needle seat combined with the increasing available volume
due to displacement of the needle [13, 41]. Therefore, during this period the sac
pressure is the resultant from a complex phenomenon and it is not expected to be
steady: the tip velocity, still increasing at 5 mm indicates that at that point the sac
pressure has not reached its maximum yet. This hypothesis has been proposed
also by Pickett et al. [42] studying mass flow rate at the injector opening.

Finally, comparing the different injection cases it is also interesting to notice
how the tip velocity in the first millimeters results more affected by the injector
charge (or injection rate profile) rather than the injection pressure: this result is
in accordance with the *ROI* measurements (c.f. Fig. 5.4).
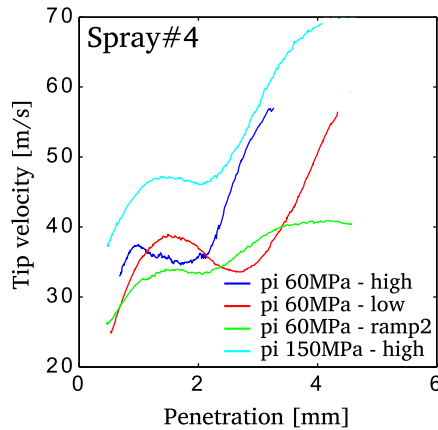
Figure 5.26: Spray tip velocity at different test condition for one sample spray;
$\rho_a = 19.2\,\text{kg/m}^3$, $T_a = 870\,\text{K}$

To draw a global comparison of this first transient of the sprays development,
the time employed by each spray to reach the penetration $S_l = 3\,\text{mm}$ was eval-
uated for different cases and the hole-to-hole and the shot-to-shot dispersion of
this measurement is presented in Tab. 5.2. This data clearly indicates that, in all
the cases, the repeatability of the injector is high; on the other hand, the hole-to-
hole dispersion is consistently high meaning that there is a systematic difference
in the sprays. As a last remark, the hole-to-hole dispersion is significantly higher
for *ramp* injections, as a consequence of the slow needle movement during the
opening.

The spreading angle measured in the nozzle near-field for the different sprays
is plotted together with the related mass flow rate (figures 5.27 and 5.28). In

	low		high	
	hole	shot	hole	shot
$p_i = 60\,\text{MPa}$ - *square*	24.8	3.7	10.2	3.3
$p_i = 150\,\text{MPa}$ - *square*	33.8	4.1	22.4	5.4
$p_i = 60\,\text{MPa}$ - *ramp2*			47.3	7.1
$p_i = 150\,\text{MPa}$ - *ramp2*			109.8	11.2

Table 5.2: Shot-to-shot and hole-to-hole standard deviation when measuring the time needed for the spray to reach $S_l = 3\,\text{mm}$. Values are expressed in μs.
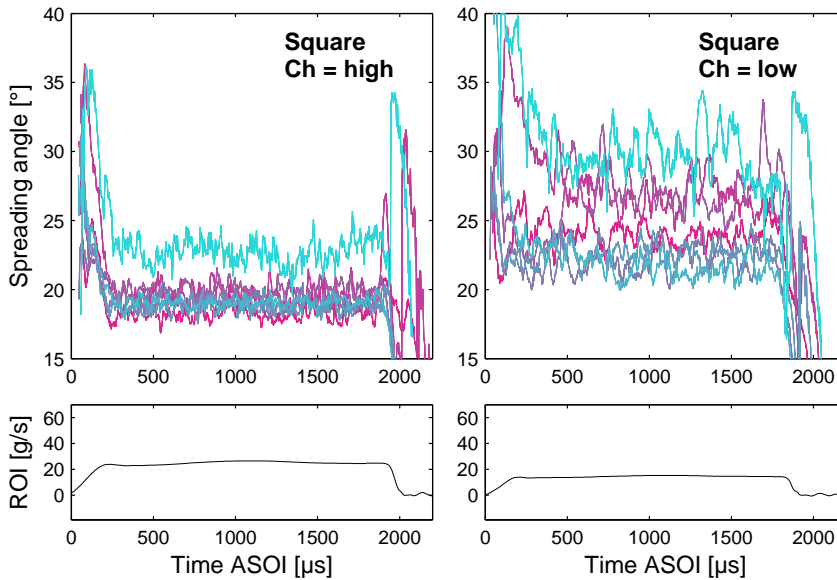
Figure 5.27: 1-repetition angle comparison measured via high speed Mie setup. Each color corresponds to a different spray; $p_i = 60\,\text{MPa}$, $\rho_a = 19.2\,\text{kg/m}^3$, $T_a = 870\,\text{K}$.
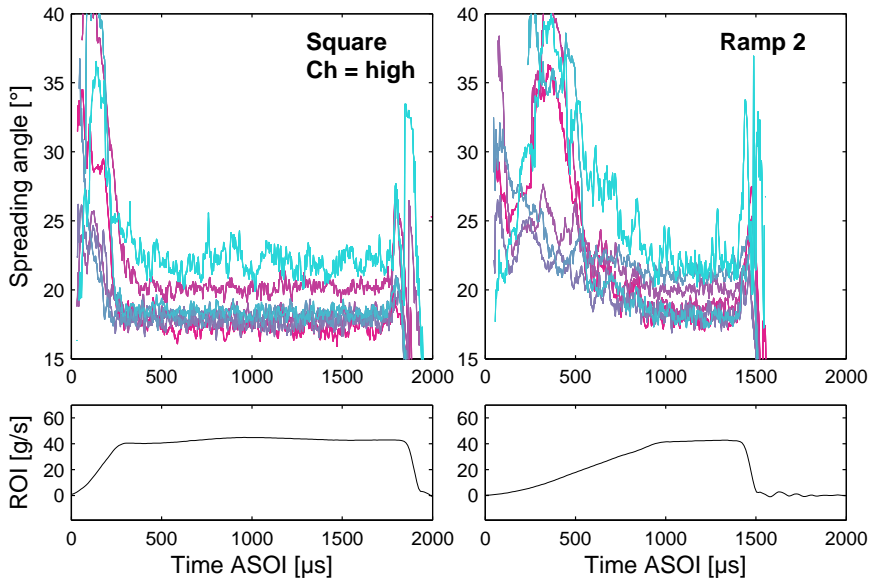
Figure 5.28: 1-repetition angle comparison measured via high speed Mie setup. Each color corresponds to a different spray; $\rho_a = 19.2\,\mathrm{kg/m^3}$, $T_a = 870\,\mathrm{K}$, $p_i = 150\,\mathrm{MPa}$.

order to prevent the long-pass filtering deriving by the repetition-averaging, the data from only 1 repetition is studied. The comparison performed for different cases highlights important features:

- the injection pressure has a secondary effect on the spreading angle for the *high-Charge* case, where the needle effect on the flow should be negligible; this is consistent with what was observed in previous tests and in other works found in the literature [43, 44];

- a reduction in the charge causes an increase of the measured spreading angle, confirming the measurements obtained in the spray far field, and of the related hole-to-hole dispersion;

- the effect of the needle lift is observed at steady (*square* profiles) and at transient conditions (*ramp2* profile).

Observing more in details the fluctuations in Fig. 5.27 the comparison suggests that there are periodic oscillations in the near field spray at about $7.5 - 8.5\,\mathrm{kHz}$. In Fig. 5.29, the results related to the steady part of the injection are presented, shifting arbitrarily each spray on the Y-axis in order to distinguish the behavior
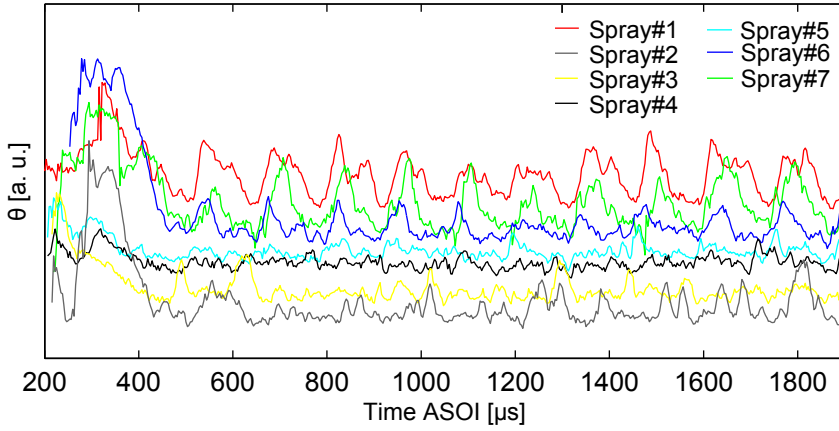
Figure 5.29: 1-repetition angle comparison measured via high speed Mie setup. Each color corresponds to a different spray and each curve has been shifted vertically to highlight the transient behavior; $\rho_a = 19.2\,\mathrm{kg/m^3}$, $T_a = 870\,\mathrm{K}$, $p_i = 150\,\mathrm{MPa}$.
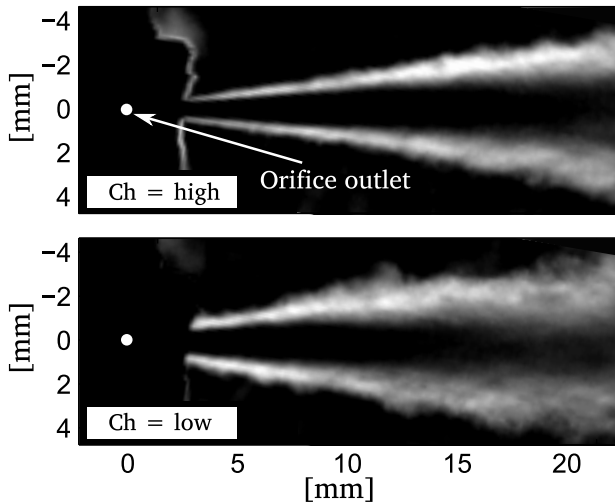
Figure 5.30: Standard deviation maps obtained by DBI images; $p_a = 3.1\,\mathrm{MPa}$, $T_a = 500\,\mathrm{K}$ and $p_i = 60\,\mathrm{MPa}$.

of each spray. The comparison suggests that the fluctuations are consistent be-
tween the different sprays and that they have the same period but differ in phase
and amplitude; this fact implies that the observed phenomenon is not caused by
turbulence produced within the orifice, but to larger scale perturbations taking
place within the sac. However, no relationship between the relative position of
the orifice in the nozzle and the phase of the oscillation on the nozzle was found.

Finally, a further technique was employed to stress the spray fluctuations: the
images obtained in the *DBI* setup were studied also to investigate possible fluctu-
ations in the spray boundaries. Using the frames captured during the steady part
of the injection $(2000 - 2700\,\mu s$ ASOI), it is possible to obtain the standard devi-
ation image, describing the statistical variation of each pixel intensity. Fig. 5.30
presents the result obtained at *high* and *low* charge: at low charge the area charac-
terized by fluctuation in intensity is substantially wider and it highlights important
variations in the spray contours.

5.4   Spray development at evaporative conditions

In this section, the liquid phase penetration results obtained at evaporative con-
ditions via Mie scattering (*LL*) are presented and compared to the vapor phase
penetration data (S_v) measured via Schlieren technique.
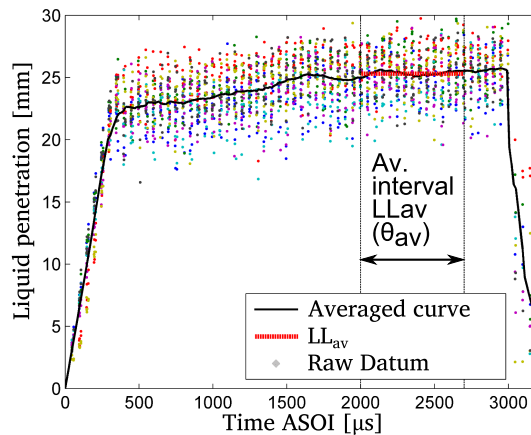
*Figure 5.31: Raw liquid phase penetration measurements and average value; the
dots represent the raw data (different colors refer to different sprays) and the black
solid line is the average curve. In the plot it is presented also the parameter LL_{av} and
the related averaging interval; $p_a = 5\,MPa$, $T_a = 870\,K$, $p_i = 60\,MPa$, Ch = high.*

5.4.1 Effect of boundary conditions

In Fig. 5.31, the *7-spray* average liquid phase penetration is plotted together with the raw data and the characteristic shape of liquid phase penetration at evaporative conditions can be observed [17–19]: in the first transient the sprays penetrate into the test chamber until a certain distance is reached. At that distance, the enthalpy supplied by the entrained gas is enough to evaporate the fuel to completion [1]. The dots plotted on the same axes represents the raw data measured for each spray and each repetition; the big area covered by the points cloud is mainly due to two factors:

- the intrinsic behavior of the liquid length: it is related to the perturbations within the nozzle orifices and fluctuations in the mass flow rate are eventually reflected on the spray structure;

- hole-to-hole discrepancies: as shown in the previous section the flow through the orifices is not completely symmetric and therefore some differences are expected also in the liquid phase penetration.

In order to understand the general behavior of the injector, this part of the analysis is focused on the *7-spray* averaged data while the discussion related to the hole-to-hole dispersion is left to a separate section.
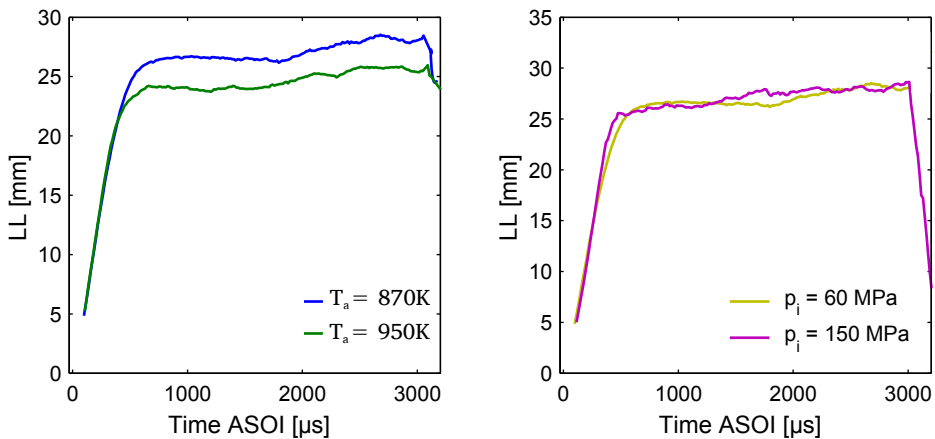
Figure 5.32: Liquid phase penetration at different test conditions: effect of ambient temperature (left) and of rail pressure (right); $p_a = 5$ MPa, Ch = high.

Fig. 5.32-left presents the liquid phase penetration measured at two different ambient temperatures. As expected, both curves overlap in the first transient part

since ambient density is very similar in the two cases but it stabilizes at different values as a consequence of the higher temperature of the ambient gas [1, 17, 19]. On the other hand, the comparison drawn on Fig. 5.32-right shows liquid phase penetration at two different injection pressures and presents an opposite scenario: during the transient part, higher injection pressure contributes to a faster penetration, as a consequence of a higher velocity at the orifice outlet. On the other hand, the effect on the steady LL is negligible: this fact has already been observed by other authors [17, 19, 28] and it is in agreement to the mixing-limited approach (see Sec.3.3.2)[1].
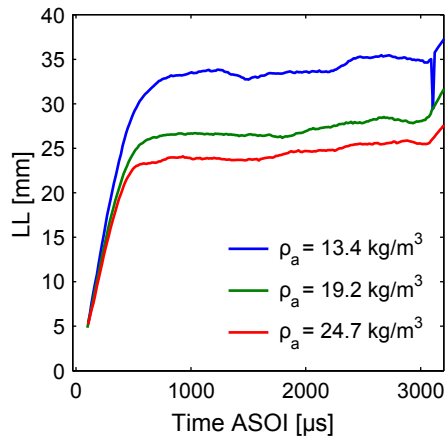
Figure 5.33: Liquid phase penetration at different test conditions: effect of ambient density; $T_a = 870$ K, $p_i = 60$ MPa, Ch = high.

Also, as a consequence of the mixing-limited approach, p_a is not expected to have a significant impact on LL; however, if ambient pressure is varied keeping constant T_a, the density of the ambient gases changes and this effect can be observed in Fig. 5.33. At higher ρ_a, liquid phase penetrations is reduced in both the transient and the steady period; two factors are contributing to this result:

- the spreading angle has been experimentally observed to increase at higher ambient densities, increasing the mass of hot gas entrained in the spray [23–25];

- as already discussed when presenting the results at isothermal conditions, the higher density of the gas *introduces* more inertia into the spray and thus the spray penetrates more slowly [24].

Even if the effects described above are already known and they are widely described in the literature [17, 28, 45], these comparisons are important since they give a quantitative guidance for a future use of the injector in a real engine and, at the same time, they confirm the reliability of the experimental methodology employed.

Observing the plots presented in figures 5.32 and 5.33, LL always shows a slight positive slope, even after the first transient. As discussed by other authors [19, 39], there are two factors that likely contribute to this effect: i) for long injections, low temperature fuel-air mix is re-entrained in the spray causing thus, a decrease in the effective ambient temperature and an increment in liquid length; ii) during the injection the fuel flowing from upstream of the sac cools down the injector tip. This way, the temperature of the fuel at the orifice outlet is decreasing during the injection and this is reflected on liquid length [19, 46].
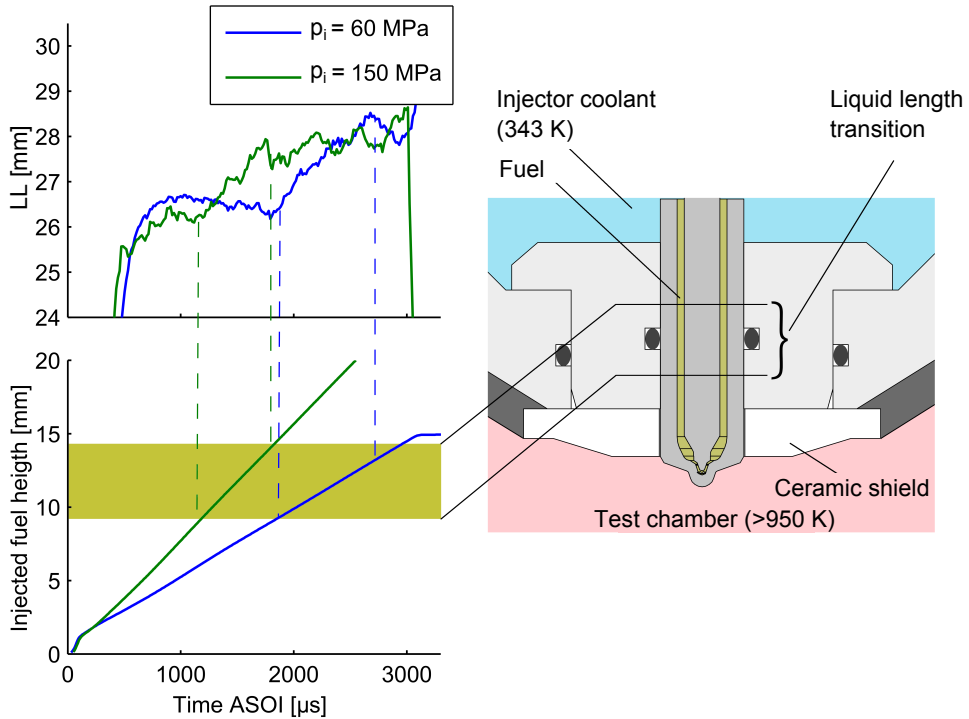
Figure 5.34: *Transient liquid length compared to the fuel position in the sac before the injection (Injectionheigth);* $T_a = 950\,\mathrm{K}$, Ch = high, $p_a = 5\,\mathrm{MPa}$.

Considering the large size of the chamber and the fact that the slope seems to decrease at the end of the injection, this second hypothesis is considered the most

likely cause of the phenomenon observed. Moreover, in the steady period of the curves, it is possible to distinguish a knee corresponding to the definitive stabilization of the penetration: in other words, at a certain moment after the start of the injection, the liquid length definitively stops growing (c.f. Fig. 5.32). Moreover, the timing of this event depends on p_i and Ch. When the liquid phase penetration slope is compared to the total volume of fuel injected, a further confirmation to this hypothesis is found. In fact, due to the relatively long interval between two consecutive injections (close to 3 s), the fuel within the injector is considered to reach the same temperature of nozzle. Therefore, if the temperature of the nozzle is not homogeneous (see Fig.4.9), the temperature of the fuel in the nozzle will not be constant either. Considering the nozzle temperature constant at each axial position, along the injector axial coordinate correspondent to the location of the fuel before the start of the injection can be related to the instantaneous temperature of the fuel injected: this axial coordinate has been plotted in Fig. 5.34 in parallel to the liquid phase penetration curve (the $y - axis$ scale is adjusted to highlight the LL increase). The plot shows that at both injection pressure the increase in liquid length stops when a certain volume of fuel has been injected and the axial coordinate corresponding to this volume is the same in the two cases. This result enforces the interpretation discussed earlier, that relates the positive slope in the liquid phase penetration with a variation in the instantaneous temperature of the fuel injected. Using the *1D* model developed by Pastor et al. [1], the results indicate that the fuel temperature variation needed to increase the LL of 2 mm is between $35-40$ K: the nozzle temperature measurements presented in Fig. 4.9 show that moving from 0 to 15 mm from the nozzle tip, the temperature decreases of about 30 K. The consistency between these two results confirms that the increase observed in the stabilized LL is related to the variation of the fuel temperature during the injection event.

5.4.2 Global analysis

For a global comparison of the data, the parameter LL_{av} is plotted versus ambient temperature and ambient density respectively in Fig. 5.35 and Fig. 5.36. The effect of injection pressure is negligible at full needle lift; moreover, an increase in T_a at full needle lift has the same effect on LL_{av} at both injection pressures. On the other hand, when the charge applied to the piezo-stack is reduced two main effects are evident:

- the injection pressure is affecting LL_{av} and the ambient temperature effect is quantitatively different at different p_i. This can be explained by the fact that the variation in charge applied at the different injection pressure corresponds to different needle throttling λ;

- reducing the needle lift, LL_{av} is significantly shorter. If the partial needle lift affected only the fuel pressure upstream of the orifice, LL_{av} would not be expected to change. However, the important reduction in liquid length caused by partial needle lift means that the internal flow is somehow changing and this is affecting the spray development and, as a matter of fact, confirms the relationship previously described between needle lift, area coefficient and spreading angle.
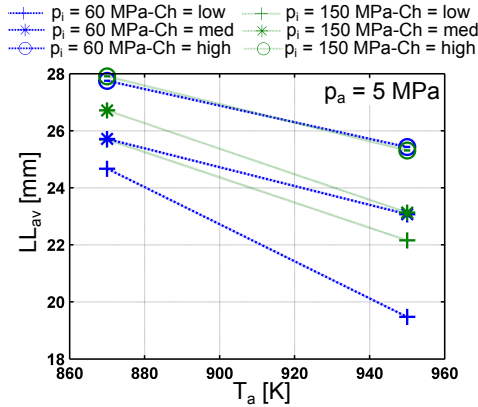
Figure 5.35: Effect of test conditions on the average liquid length (LL_{av}); $p_a = 5$ MPa.
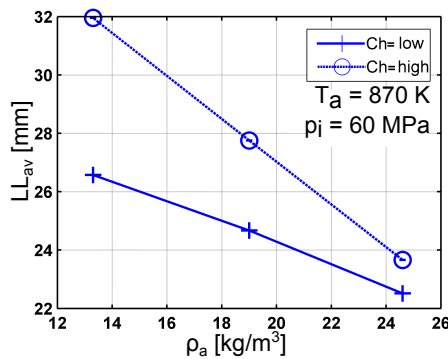
Figure 5.36: Effect of test conditions on the average liquid length (LL_{av}); $T_a = 870$ K, $p_i = 150$ MPa.

Fig. 5.36 summarizes the effect of ambient density on *LL* [1, 17] and remarks the same point: a reduction in the needle lift causes a significant reduction in liquid length also at different ambient density.

When LL_{av} is related to λ, a linear relationship between these two magnitudes can be observed and this relationship is consistent at two different injection pressures creating a link among the results presented in Fig. 5.35. The variable λ seems to control LL_{av} and the more the needle throttles the fuel flow, the more the liquid penetration is reduced.
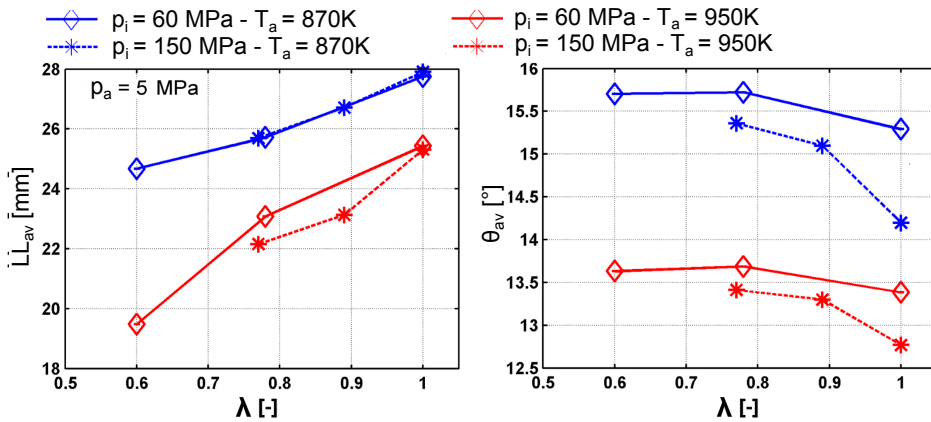
*Figure 5.37: Effect of λ on the average liquid length (*LL$_{av}$*); $p_a = 5$ MPa.*

As shown by *ROI* measurements, the *CDA* injector is capable of performing advanced and adjustable injection rate shapes. When the liquid phase penetration is measured at evaporative conditions, the results are consistent with what discussed before: Fig. 5.38-left shows that in the *ramp* case the liquid length continuously increases until the *ROI* has not reached its maximum and in the *boot* case (Fig.5.38-right) a two-steps liquid length profile was measured. Again, this confirms the behavior discussed in the previous section: when the needle is throttling the fuel flow, *LL* is shorter.

As for the experiments at isothermal conditions, specific tests were performed to measure *LL* at high time resolution (68 kHz). In order to evaluate the fluctuations at the spray boundaries, the spray width at 9 mm from the orifice outlet was measured: this measurement was preferred to the spreading angle because it provides a better response to the temporal fluctuations. In fact, the spreading angle measurement evaluates a certain portion of the spray contour and for this reason it smooths possible fluctuations.
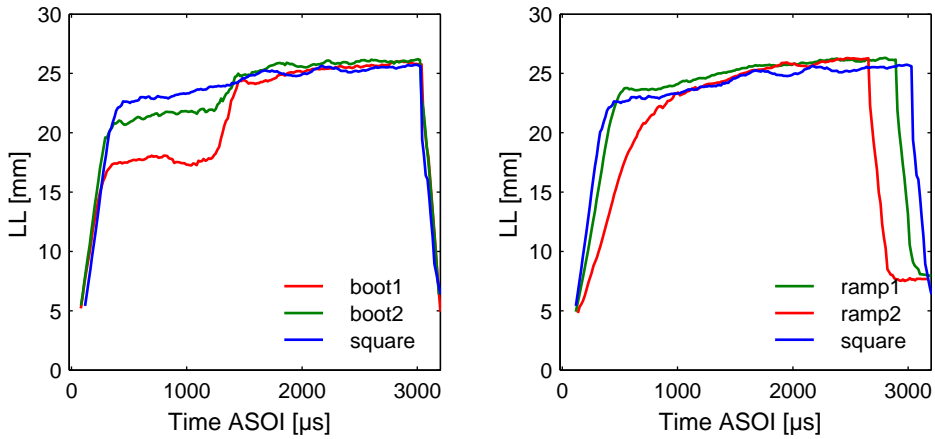
Figure 5.38: Effect of injection rate shaping on LL. Ramp shaped injection profiles (left) and boot *shaped injection profiles (right); $T_a = 950$ K, $p_a = 5$ MPa, $p_i = 150$ MPa.*

Fig. 5.39 presents iquid phase penetration and spray width 1-repetition results: on one side, the plot confirms the relationship between charge and *LL*; on the other, it shows that when needle lift is throttling the flow, also in this case, higher fluctuations can be observed in terms of spray width and *LL*. On the top part of the same figure, the comparison between spray images at *high* and *low* injector *charge* gives another confirmation of the unsteadiness of the flow. Even though it cannot be considered a quantitative measurement, the distribution of the scattered light intensity suggests that, at lower charge, the axial distribution of the fuel in the spray is less homogeneous. This can be considered a further insight of the unsteadiness of the fuel flow.

The impact of the inhomogeneities of the illumination system on the *LL* [47] was assessed performing a further test: liquid penetration was measured rotating the injector of 90° around its axis and maintaining the same optical configuration.

The modification in the injector orientation has only a slight effect on the LL_{av}: considering the tests performed at $T_a = 870$ K, $\rho_a = 19.2$ kg/m³ and $p_i = 60$ MPa the value of LL_{av} obtained at *high* and *low charge* was respectively 27.7 and 24.6 mm while, in the modified injector position, at the same test condition it was obtained 28.1 and 23.8 mm that is considered below the test uncertainties. However, since the rotation of the injector axis is considered to mostly affect the measurement of each single spray more than the global average, in Fig. 5.40, the LL_{av} obtained for each single spray is presented. The plot shows that the result obtained depends only slightly on the injector orientation and the same pattern
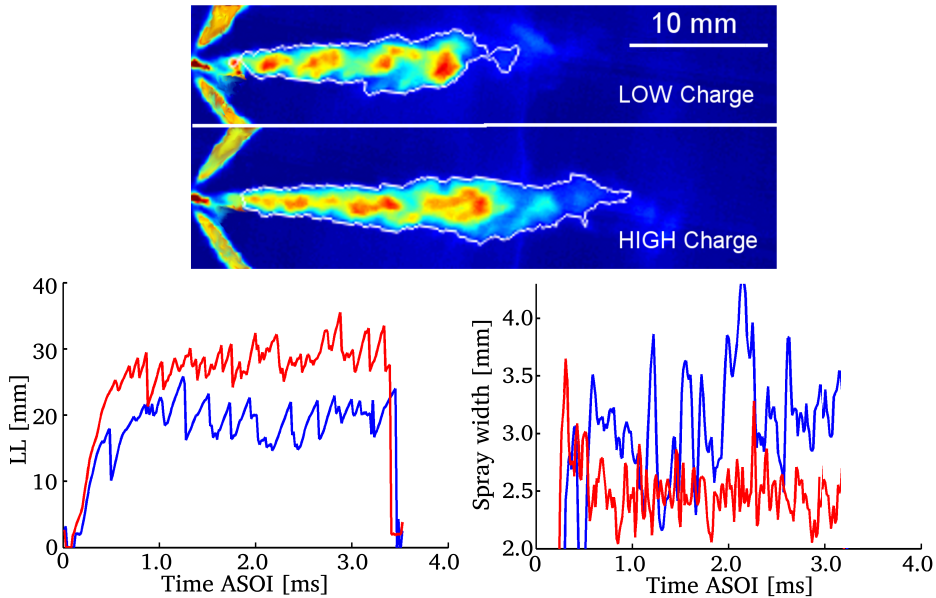
Figure 5.39: 1-repetition angle comparison measured via high speed Mie setup. Each color corresponds to a different spray; $\rho_a = 19.2\,\mathrm{kg/m^3}$, $T_a = 870\,\mathrm{K}$, $p_i = 150\,\mathrm{MPa}$.

is obtained in both cases. As a consequence of that, the robustness of the results is proven since the *LL* hole-to-hole dispersion observed is not dependent on the light orientation.

5.4.3   Liquid- and Vapor-phase penetration.

The Schlieren technique was employed in this work to measure the vapor phase penetration of the sprays at evaporative conditions (S_v) [48, 49]. The results confirm what was observed in the experiments at isothermal conditions, providing similar results. In this section, the results from additional tests are presented together with some sample comparison with liquid phase penetration.

As demonstrated for isothermal conditions, the injector charge acts on penetration similarly to a variation in injection pressure: by reducing the injector *charge*, the throttling effect of the needle on the fuel flow reduces the spray momentum and hence, the spray penetrates slower in the chamber [1]. The plots on Fig. 5.41 include more injection pressure and charge variations and it shows that controlling *Ch* it is possible to regulate the spray penetration rate in a nearly continuous range. Another important detail emerging from the plot is the modest
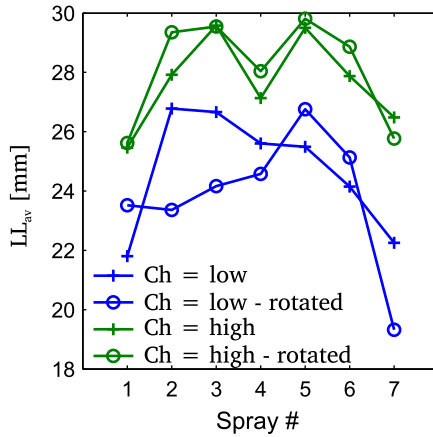
*Figure 5.40: Average liquid length (*LL$_{av}$*) measured for the different spray at two different injector orientations.* $p_a = 5\,\mathrm{MPa}$

difference between the curves obtained at $Ch = 100\%$ and $Ch = 115\%$: when Ch is above the maximum nominal value, the effect of the injector *charge* on S_v is very low. This fact is consistent with the spray momentum flux measurements, showing only a slight effect of the *charge* on $\dot{M}_{av}$ when the *charge* is above the nominal maximum [4].
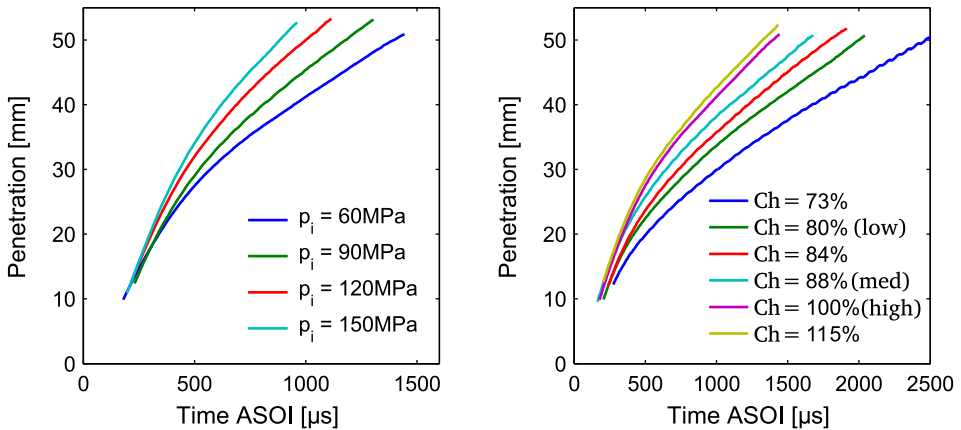
Figure 5.41: Spray penetration measured via Schlieren techniques. Effect of p_i at $Ch = \mathrm{high}$ *on the left and effect of injector* charge *at* $p_i = 60\,\mathrm{MPa}$ *on the right;* $\rho_a = 17.5\,\mathrm{kg/m^3}$, $T_a = 950\,\mathrm{K}$.

The comparison between liquid and vapor phase penetration presented in Fig.5.42 shows that both measurements are identical during the first transient state but, when the *LL* stabilizes, S_v continues penetrating like at isothermal conditions [1, 49]. The effect of injection rate shaping is successfully reflected on the spray penetration also at evaporative conditions. The plots presented in figures 5.42 and 5.43 show the impact on penetration of, respectively, boot and ramp shaped injection profiles at different injection pressure. The comparison between the two boot and ramp typologies give a further idea of the precision of the injector and its capability to modulate the flow. It is important to observe that the penetration curves obtained in the *boot* cases at $p_i = 150$ MPa are representative only of the *foot* stage of the injection, since, when the *ROI* increases, the spray plumes are almost at the visualization limit and the effect observed in the curves is similar to the one caused by a reduction in injector *charge*.

The *ramp* shaped injection profile, on the other hand, has a different effect on penetration: the reduction in the slope of the *ROI ramp-up* is reflected in a slower penetration along the first millimeters. In a conventional *square* injection the spray penetration velocity decreases during the injection due to the increasing amount of entrained air: the *ramp* shaped injection profile compensates this decrease in the spray penetration velocity increasing the mass flow rate and the measured penetration is nearly linear with time. Also in this case, the different settings between *ramp1* and *ramp2* are coherently reflected on the penetration curves, proving the great flexibility of the injector.
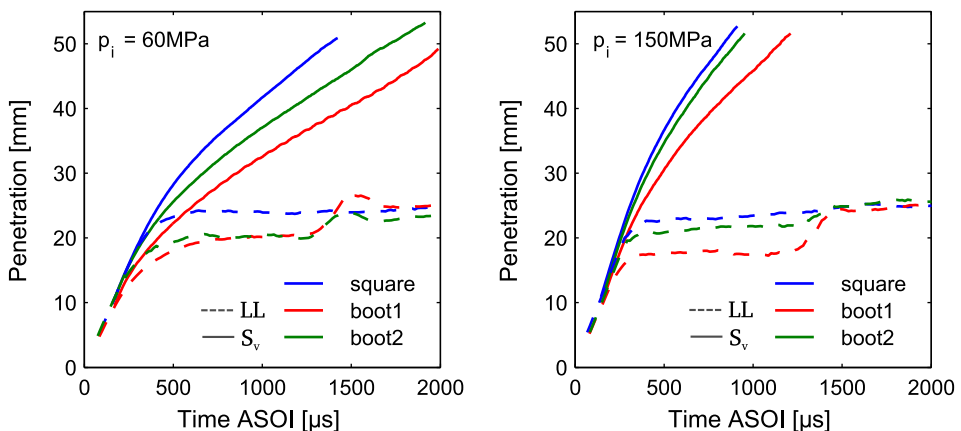
Figure 5.42: Effect of boot *profiles on S_v at $p_i = 60$ MPa (left) and at $p_i = 150$ MPa (right). The dashed lines indicate the liquid phase penetration; $\rho_a = 17.5\,\mathrm{kg/m^3}$, $T_a = 950$ K.*
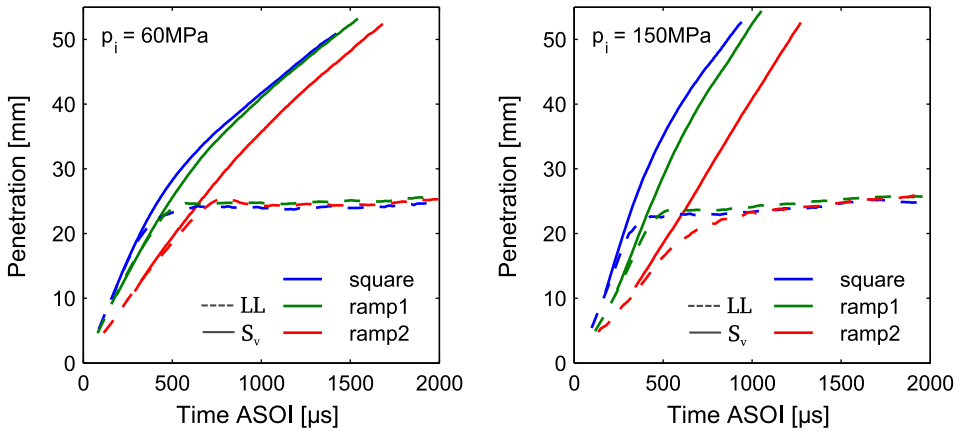
Figure 5.43: Effect of ramp profiles on S_v at $p_i = 60$ MPa (left) and at $p_i = 150$ MPa (right). The dashed lines indicate the liquid phase penetration; $\rho_a = 17.5 \, \text{kg/m}^3$, $T_a = 950$ K.

As discussed in Sec.3.3 and observed experimentally, ambient temperature is not expected to affect the spray penetration if ρ_a is kept constant [1, 24]. However, other researchers experimentally observed that a reduction in ambient temperature or a variation in ambient composition have some effect on the spray penetration [23, 50] and pointed out that, in this region characterized by important velocity gradients, the viscous forces depending on the gas proprieties might have an important effect on this first phase of the penetration.

In this optics, the ambient temperature impact can be explained, since the temperature affects the viscosity of the air and the droplets diameter [51]: in fact, when the ambient temperature is increased the droplet diameter is reduced due to fuel evaporation and due to a reduction in fuel surface tension. Fig. 5.44 confirms these observations, showing the differences observed between S_v measured at $T_a = 950$ K and S_l measured via Mie scattering at $T_a = 400$ K. The two curves show a significant difference and at $T_a = 400$ K the spray penetrates faster than at high temperature. However, if a time shift is applied, this differences are related only to the first part (about 25 mm) while, in a second stage, the two curves overlap [23].

5.5 Hole-to-hole dispersion and repeatability

The statistical dispersion of the measurements was studied observing the standard deviation. In order to separate the contribution of the hole-to-hole dispersion
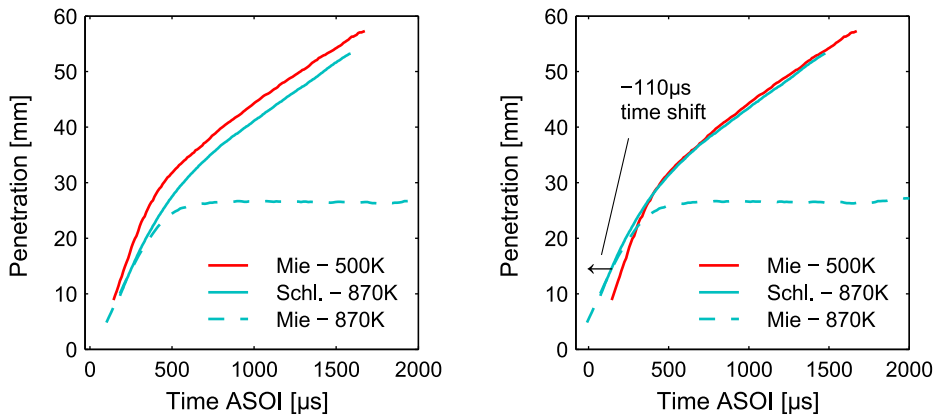
Figure 5.44: Spray penetration measured via schlieren and Mie scattering techniques. In the right plot the penetration data at high temperature has been shifted on the time axis; $\rho_a = 19.2\,^{kg}/m^3$, $T_a = 870\,K$, $p_i = 600\,MPa$, $Ch = high$.

from the test repeatability (shot-to-shot dispersion), the standard deviation was obtained in two different ways: calculating the dispersion of the average orifice values (hole-to-hole) and the average of the shot-to-shot dispersion measured in each orifice (shot-to-shot). Both measurements are a fundamental indicator of the injector performances.

Even if the standard deviation of the measurements is strongly affected by the setup employed, this analysis allows, on the one hand, to have an idea of the reliability of the results and, on the other, to observe if partial needle lift affects the injector performances in terms of control.

In Tab. 5.3, the standard deviations obtained in the different experiments are presented for comparison. Generally, the standard deviation indicates good consistency of the results in terms of repeatability and hole-to-hole dispersion. The highest hole-to-hole standard deviations are obtained for LL_{av} and θ_{av}: in both cases the dispersion is associated to setup issues (illumination and background homogeneity) as already discussed by other authors -[21, 47, 52]. Moreover, the shot-to-shot dispersion of the same measurements is also relatively high, but for different reasons: *LL* in Diesel spray is normally oscillating around an average value as a consequence of the atomization related and nozzle flow turbulences [53]. The same consideration holds for the spreading angle, even if, in this case, there is a strong component of the uncertainty of the measurement, as discussed earlier (Sec.5.3).

When comparing different test conditions another important result emerges: decreasing the injector charge (needle lift), increases the hole-to-hole dispersion in all the measurements performed, confirming and extending what observed in micro-visualization tests. Therefore, when the needle is throttling the flow, the sac pressure and velocity fields increase their asymmetries that are propagated in the spray formation and mixing process. On the other hand, the general behavior observed for the repeatability does not show a clear relationship with the injector charge and remains almost constant underlining that, at partial needle lift, the injector repeatability is not affected

| | $p_i = 60\,\text{MPa}$ | | | | | | $p_i = 150\,\text{MPa}$ | | | | | |
| | low | | med | | high | | low | | med | | high | |
	hole	shot	hole	shot	hole	shot	hole	shot	hole	shot	hole	shot
LL_{av} (at 870 K)	10	3.0	6.9	2.7	3.7	2.0	7.3	2.2	6.1	2.6	3.9	2.3
θ_{av} (at 400 K)	16	4.2	14	5.9	6.0	4.8	7.4	6.3	5.3	4.2	5.1	3.8
$\dot{M}_{av}$ (at 870 K)	4.6	2.2	2.9	2.1	2.5	1.8	6.0	2.0	2.2	1.7	2.4	1.8
S_l (at 30 mm)	5.9	5.8	5.1	3.1	2.5	2.7	3.2	4.2	2.4	2.7	2.7	2.6

Table 5.3: Percentual shot-to-shot and hole-to-hole standard deviation obtained in different measurements.

5.6 Summary of the results

From the experimental observations presented in this chapter, the following main conclusions are drawn:

- all the measurements showed typical behavior when studying the effect of conventional boundary conditions (ambient parameters and injection pressure) proving the reliability of the diagnostics;

- the *CDA* injector is fully capable of throttling the fuel flow in steady and transient conditions and, therefore, it is capable to perform injection rate shaping;

- partial needle lift, either in steady or transient conditions, causes modifications in the flow within the nozzle and in the spray development. At partial needle lift, the effective area at the orifice outlet is lower and the spray spreading angle is higher, with a consequent increase of the air-entrainment and reduction of the liquid length.

- the partial needle lift also causes a slight deviation of the spray axis as a consequence of the asymmetries of the flow at the orifice inlet;

- transient fluctuations in the quantities measured (spreading angle and liquid-length) indicate that the partial needle lift causes unsteadiness in the flow, reflected in higher fluctuation in LL and θ; this fluctuations are considered to further promote the air entrainment.

The interactions between the fuel flow and the injector needle are causing the needle itself to vibrate and these vibrations might be the origin of the flow unsteadiness, as observed by other authors [39, 54]. Moreover, the onset of cavitation might occur in the needle seat, as observed by Martinez [13]. Several studies demonstrated that fuel cavitation within the orifice is linked to an increase of the spray spreading angle [7, 48]. Both the explications above, in author's opinion, concur in modifying the spray development and are both consistent with all the observation presented.

The results obtained clearly show that the needle lift control operated by the *CDA* is a very strong tool to manage the spray development, producing effects that were not possible to get with conventional injectors. The significant effect on *ROI*, vapor- and liquid-phase penetration can be employed for the development of new engine strategies: in this scenario also liquid length can be controlled and varied during the injection by acting on the needle position. For example, to reduce the mass flow rate in the first part of the injection reducing its needle lift would have a double positive effect: to control the mass of fuel injected before the ignition and, to reduce the wall impingement as a consequence of a shorter liquid length.

5.7   Discussion and analysis

In this last part of this section, the *1D* spray model (*1DM*) developed by Pastor et al. [1] is employed, on the one hand, to understand the physics behind the observations previously presented and, on the other hand, to calibrate the model and to gain access to the spray variables (fuel mass fraction, local velocity etc.) that will be essential for the interpretation of the results at reacting conditions.

As already discussed in this chapter, the measurement of the spreading angle is always affected by high uncertainties, in part due to the optical arrangement and in part to the image processing applied. Moreover, the results presented showed that a completely steady spreading angle is very difficult to be measured, and that the field of view, in some way affects the spreading angle. Besides, the spray penetration can be measured with more accuracy, since its determination is less ambiguous and less affected by the technique employed.

The *1DM* was used to obtain indirectly the spray spreading angle. The spreading angle derived by the *1DM* (θ_{th}) is obtained as the value that, given the mass flow rate and the area coefficient, allows to have the best match of the spray penetration and liquid length data. This method is particularly interesting since it gives a value of the spreading angle based, not on direct observations, but on the resultant features of the mixing process. In Fig. 5.45 the vapor- and the liquid-phase penetration obtained experimentally are compared to the results obtained from the *1DM*. By adjusting the spreading angle, the model *predictions* match the experimental liquid and vapor phase penetration results.
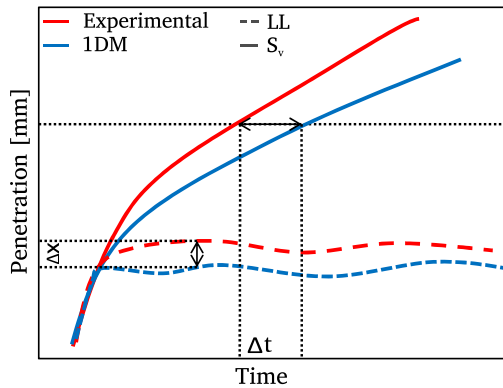
Figure 5.45: Determination of the spreading angle through the 1DM. The θ_{th} input in the model is adjusted until the best match with S_v and LL is reached.

The procedure shown in Fig. 5.45 was repeated for all the *square* injections: in Tab. 5.4 the results obtained at $T_a = 870\,\mathrm{K}$ and $\rho_a = 19.2\,\mathrm{kg/m^3}$ are presented and compare to the experimental values.

	low		*med*		*high*	
	1DM	*Mie*	*1DM*	*Mie*	*1DM*	*Mie*
$p_i = 60\,\mathrm{MPa}$	20.5	25.3	20.2	24.1	19.7	22.5
$p_i = 150\,\mathrm{MPa}$	21.1	24.6	20.5	21.8	18.5	21.0

Table 5.4: Spreading angle obtained by direct measurement and by the 1DM. The values are expressed in °. $T_a = 870\,\mathrm{K}$, $\rho_a = 19.2\,\mathrm{kg/m^3}$.

In Tab. 5.4, the spreading angle obtained from the *1DM* is compared to the one measured experimentally. The comparison confirms the relationship between the spreading angle and *Ch* obtained by the direct measurements: decreasing the

needle lift, the spreading angle increases. However, the spreading angle obtained with this methodology shows less sensitivity to the boundary conditions (Ch and p_i) than the one obtained via direct measurement. This is probably related to the fact that the *steady* spreading angle is difficult to obtain experimentally: in the cases tested (figures 5.16 and 5.17), even at 2 ms ASOI, the spreading angle shows, a dependence on time, indicating that more time is needed to obtain a steady value.

In order to obtain more insight about the angle results, a statistical analysis was carried out. To this end, an exponential equation, based on the studies performed by Hiroyasu and Arai [33] is fitted to the experimental data, including the parameters affecting the spreading angle:

$$\theta = k \cdot C_A^a \cdot \rho_a^b \cdot p_i^c \ , \tag{5.3}$$

where k, a, b and c are the parameters adjusted in the regression. In this case, the area coefficient C_A is used to represent indirectly the effect of needle throttling: in fact, Raitz and Bracco, in their work[20], found a relationship between this quantity and the spreading angle. In this case, the needle throttling λ, is the only quantity affecting significantly the area coefficient. For sake of consistency, the regression was performed using different sets of data. On one side, the spreading angle obtained using the *1DM* (θ_{th}), on the other, the spreading angle obtained experimentally using two different methodologies: the area method employed by Naber and Siebers [24], and the fitting method used by Pastor et al. [52].

Tab. 5.5 presents the results of the regressions and indicates the exponent values together with the the related confidence intervals [55]. The low values of R^2 ($R^2 \approx 70\%$) indicate a low accuracy of the fit [55]. This aspect is mostly related to the nature of the spreading angle and to the difficulties in its prediction and measurement [20, 33, 56]. However, the results of the regressions suggest some important conclusions:

- qualitatively, a clear effect of the C_A and ρ_a is detected in the three datasets: spreading angle increases with ρ_a and decreases with C_A. Moreover, the three regressions do not catch any clear effect of the injection pressure (the confidence interval is above and below 0) and indicate a negligible impact of p_i, since the confidence interval ranges between very low values;

- from all the analysis the value of a (C_A exponent) is high, suggesting a significant impact of this quantity on the spreading angle and, consequently, the relationship between needle lift and spreading angle;

- the two methods used to measure experimentally the spreading angle (area and fitting methods), even though provide different results, are consistent in their variation and relationship with the boundary conditions;

- the values of the ambient density exponent b obtained experimentally is close to the one found by Hiroyasu and Arai [33] ($b = 0.26$), proving a good consistency with the literature.

		k	a	b	c	R2
1DM	Coefficient	13,7	-1,7	0,131	0,009	74%
	Conf. interval	11,3/16,2	-2,3/-1,04	0,09 / 0,16	-0,03/0,01	
Fit Method	Coefficient	11,3	-4,7	0,29	-0,039	79%
	Conf. interval	6,2/16,3	-6,4/-3,0	0,19/0,38	-0,10/0,03	
Area Method	Coefficient	10,25	-5,75	0,31	-0,03	78%
	Conf. interval	4,8/15,6	-7,7/-3,7	0,20/0,42	-0,11/0,04	

Table 5.5: Coefficient obtained by the regression of Eq. (5.3) spreading angle.

The discrepancies in the values as well as in the trends of experimental measurements and *1DM* derived angles, underline the weakness of the spreading angle measuring techniques or, at least, something missing in the relationship between penetration and spreading angle as it is described by the *1DM* (at the basis of the *1DM* angle calculation) [22]. In this sense, it is worth to mention the contribution presented by Pickett et al. [42] characterizing the spray shape by means of two different angles: one for the near field and another for the spray far field (see Fig.5.46). Despite the encouraging results obtained, a consistent methodology to determine the two spreading angles was not indicated and, in this specific discussion, a superficial analysis of the penetration results through the double-angle approach will bring only further questions. Due to the global interest of this thesis, it has been preferred to leave the double-angle analysis to further more specific studies.

The discussion about the spreading angle is continued performing the analysis of the penetration data. A statistical analysis of the spray penetration obtained in the Mie scattering tests is performed. The set of tests include the variation of several boundary conditions: ambient temperature, ambient density, injection pressure, and injector charge. The equation used for the regression takes into
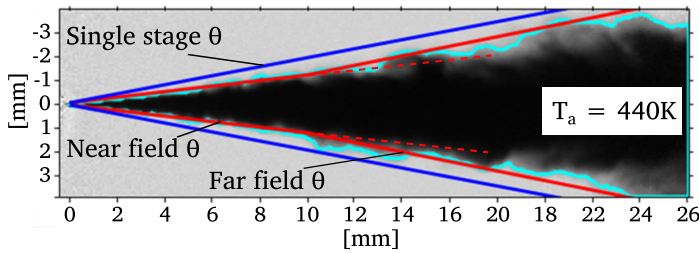
Figure 5.46: Near- and far-field spreading angle as proposed by Pickett et al. [42].

account the controlled variables, as in the works carried out by other authors ([23, 57]):

$$S = K(C_A \cdot D_0)^{0.5} \cdot \dot{M}_{av}^a \cdot \rho_a^b \cdot \left(tan\left(\frac{\theta}{2} \right) \right)^c \cdot t^{0.5} \, , \qquad (5.4)$$

being K, a, b and c the parameters obtained from the regression. In this approach, the effect of injection pressure and injection charge is studied using the quantities spray momentum, spreading angle ($tan\left(\frac{\theta}{2} \right)$), and area coefficient. The exponent of the area coefficient C_A and of the time t is fixed at 0.5 as indicated by the dimensional analysis [7, 24].

The spreading angle results were evaluated including in the analysis alternatively the values obtained experimentally as well as the ones derived from the *1DM*. Moreover, as commented in Sec. 3.3, the penetration of the spray can be divided in two stages: a first one, characterized by a linear relationship between penetration and time and, a second one, in which the penetration is proportional to the square root of time [23, 24, 28]. In this analysis, only the second stage of the spray penetration is taken into account, since during this stage the results are less dependent on the injector dynamic and more consistent results can be found in the literature [23, 24, 28].

The related results are presented in Tab. 5.6. As a general comment, it can be observed that in both the cases a good fit to the experimental data is found, confirming the exponents of C_A and t assumed *a priori*. In all the cases the exponent referred to the spray momentum a is very close to the exponent derived from the dimensional analysis ($a = 0.25$) [11], underlining the consistency of the results presented. On the other hand, when comparing the coefficients b and c different considerations are needed. The values of b and c obtained using θ_{th} are both very close to the dimensional analysis results ($b = -0.25$ and $c = -0.5$). This fact is not surprising: in fact, the method used to determine the spreading

angle itself calibrate θ_{th} to adjust the *1DM* to the experimental data and, therefore, they includes in the results the theoretical dependencies on the boundary conditions. However, the high R^2 indicates the consistency of the methodology and the functionality of the results obtained.

The results related to the spreading angle obtained experimentally are characterized by a higher difference from dimensional analysis results. In specific, the value of c indicates a very low impact of θ on penetration, and the related confidence interval reveals that the effect of this parameter is not caught clearly by the regression. Based on this fact, the spreading angle measured in these experiments is not considered accurate for the description of the mixing process. The exponent of ρ_a ($b = -0.31$), even though close to the dimensional analysis value, is higher. Probably, the effect of the spreading angle, not caught by the regression, is partially transferred on the ambient density [55]. In fact, as a shown in Tab.5.5, spreading angle and ambient density are mutually related. It is also interesting to observe, that similar values for b were obtained in other studies including in the regression the experimental mesured spreading angle ($b = -0.34$ by Desantes et al. [58] and $b = -0.33$ by Payri et al. [23]).

	a	b	c	R^2
θ fit meth.	0.248	−0.310	0.0076	98.1
θ area meth.	0.246	−0.306	−0.018	97.8
θ_{th}	0.232	−0.249	−0.517	99.1
Dim analysis [7, 24, 59]	0.25	−0.25	0.50	
Empiric (Payri et al. [23])	0.24	−0.33	−0.09	

Table 5.6: Exponents obtained from the regression to Eq. (5.4) to the experimental data. The results obtained from dimensional analysis and from other authors are presented for reference.

Finally, it is worth to underline, that the considerations about the measured spreading angle should not be considered with a general extent. In particular, even after a fine tuning of the image processing technique, the field of view employed in the experiments and the test conditions studied are considered to have a significant impact on the reliability of the angle measured since, depending on these factors, the difference in the spreading angle may be found.

References

[1] Pastor, J., J. López, J. García-Oliver, and J. Pastor. "A 1D model for the description of mixing-controlled inert diesel sprays". *Fuel* 87.13 (2008), pp. 2871–2885.

[2] Payri, R., J. Garcia, F. Salvador, and J. Gimeno. "Using spray momentum flux measurements to understand the influence of diesel nozzle geometry on spray characteristics". *Fuel* 84.5 (2005), pp. 551–561.

[3] Payri, R., C. Guardiola, F. Salvador, and J. Gimeno. "Critical cavitation number determination in diesel injection nozzles". *Experimental Techniques* 28.3 (2004), pp. 49–52.

[4] Payri, R., J. Gimeno, O. Venegas, and A. H. Plazas-Torres. "Experimental and computational study of the influence of partial needle lift on nozzle flowin diesel fuel injectors". *Atomization and Sprays* 22.8 (2012).

[5] Ferrari, A. and A. Mittica. "FEM modeling of the piezoelectric driving system in the design of direct-acting diesel injectors". *Applied Energy* 99 (2012), pp. 471–483.

[6] Schmidt, D. P. and M. L. Corradini. "The internal flow of diesel fuel injector nozzles: A review". *International Journal of Engine Research* 2.1 (2001), pp. 1–22.

[7] Payri, F., V. Bermudez, R. Payri, and F. Salvador. "The influence of cavitation on the internal flow and the spray characteristics in diesel injection nozzles". *Fuel* 83.4 (2004), pp. 419–431.

[8] Payri, R., F. Salvador, P. Marti-Aldaravi, and J. Martínez-López. "Using one-dimensional modeling to analyse the influence of the use of biodiesels on the dynamic behavior of solenoid-operated injectors in common rail systems: Detailed injection system model". *Energy Conversion and Management* 54.1 (2012), pp. 90–99.

[9] Manin, J., M. Bardi, L. Pickett, and R. Payri. "Boundary condition and fuel composition effects on injection processes of diesel sprays at the microscopic level". *ILASS Europe* 2013-457 (2013).

[10] Benajes, J., J. Pastor, R. Payri, and A. Plazas. "Analysis of the influence of diesel nozzle geometry in the injection rate characteristic". *Journal of fluids engineering* 126.1 (2004), pp. 63–71.

[11] Gimeno, J. "Desarrollo y aplicación de la medida de flujo de cantidad de movimiento de un chorro Diesel". PhD thesis. E.T.S. Ingenieros Industriales. Universidad Politécnica de Valencia, 2008.

[12] CHAVES, H., M. KNAPP, A. KUBITZEK, and F. OBERMEIER. "Experimental study of cavitation in the nozzle hole of diesel injectors using transparent nozzles". *SAE Paper* 950290 (1995).

[13] MARTÍNEZ LÓPEZ, J. "Estudio Computacional De La Influencia Del Levantamiento De Aguja Sobre El Flujo Interno Y El Fenómeno De La Cavitación En Toberas De Inyección Diesel". PhD thesis. E.T.S. Ingenieros Industriales. Universidad Politécnica de Valencia, 2013.

[14] PAYRI, F., R. PAYRI, F. SALVADOR, and J. MARTÍNEZ-LÓPEZ. "A contribution to the understanding of cavitation effects in diesel injector nozzles through a combined experimental and computational investigation". *Computers & Fluids* 58 (2012), pp. 88–101.

[15] PAYRI, R., J. GIMENO, J. P. VIERA, and A. H. PLAZAS. "Needle lift profile influence on the vapor phase penetration for a prototype diesel direct acting piezoelectric injector". *Fuel* 113 (2013), pp. 257–265.

[16] BRUNEAUX, G. "Development of optical diagnostic techniques to correlate mixing and auto-ignition processes in high pressure Diesel jets". *Oil and Gas Science and Technology-Revue de l'IFP* 63.4 (2008), pp. 461–477.

[17] SIEBERS, D. "Liquid-phase fuel penetration in Diesel sprays". *SAE transactions* 107.3 (1998), pp. 1205–1227.

[18] MARTINEZ, S., F. SANCHEZ-CRUZ, J. RIESCO, J. GALLEGOS, and S. ACEVES. "Liquid penetration length in direct diesel fuel injection". *Applied Thermal Engineering* 28 (2008), pp. 1756–1762.

[19] PAYRI, R., J. M. GARCÍA-OLIVER, M. BARDI, and J. MANIN. "Fuel temperature influence on diesel sprays in inert and reacting conditions". *Applied Thermal Engineering* 35 (2012), pp. 185–195.

[20] REITZ, R. and F. BRACCO. "On the dependence of spray angle and other spray parameters on nozzle design and operating conditions". *SAE Paper* 790494 (1979).

[21] MACIAN, V., R. PAYRI, A. GARCIA, and M. BARDI. "Experimental Evaluation of the Best Approach for Diesel Spray Images Segmentation". *Experimental Techniques* 36.6 (2012), pp. 26–34.

[22] PICKETT, L. M. et al. "Relationship Between Diesel Fuel Spray Vapor Penetration/Dispersion and Local Fuel Mixture Fraction". *SAE International Journal of Engines* 4.1 (2011), pp. 764–799.

[23]   PAYRI, F., R. PAYRI, M. BARDI, and M. CARRERES. "Engine combustion network: Influence of the gas properties on the spray penetration and spreading angle". *Experimental Thermal and Fluid Science* 53 (2014), pp. 236–243.

[24]   NABER, J. and D. SIEBERS. "Effects of gas density and vaporization on penetration and dispersion of diesel sprays". *SAE Paper* 960034 (1996).

[25]   ARANEO, L. "Prediction of Diesel spray penetration with short injections in low density gas". *Proceedings of Conference on Thermo-and Fluid-Dynamic Processes in Diesel Engines, THIESEL, Spain*. 2004.

[26]   DESANTES, J., R. PAYRI, F. SALVADOR, and A. GIL. "Development and validation of a theoretical model for diesel spray penetration". *Fuel* 85 (2006), pp. 910–917.

[27]   PENG, D.-Y. and D. B. ROBINSON. "A New Two-Constant Equation of State". *Industrial & Engineering Chemistry Fundamentals* 15.1 (1976), pp. 59–64.

[28]   DESANTES, J., J. PASTOR, R. PAYRI, and J. PASTOR. "Experimental characterization of internal nozzle flow and diesel spray behavior. part II: Evaporative conditions". *Atomization and sprays* 15.5 (2005), pp. 517–543.

[29]   ROISMAN, I., L. ARANEO, and C. TROPEA. "Effect of ambient pressure on penetration of a diesel spray". *International journal of multiphase flow* 33.8 (2007), pp. 904–920.

[30]   MANIN, J., M. BARDI, L. PICKETT, R. DAHMS, and J. OEFELEIN. "Development and mixing of diesel sprays at the microscopic level from low to high temperature and pressure conditions". *THIESEL 2012 Conference on Thermo-and Fluid Dynamic Processes in Direct Injection Engines*. 2012.

[31]   ALLOCCA, L., S. DABAGOV, D. HAMPAI, L. MARCHITTO, and S. ALFUSO. "Tomography of a GDI Spray by PolyCO Based X-Ray Technique". *SAE Paper* 2013-24-0040 (2013).

[32]   PAYRI, R., S. RUIZ, F. SALVADOR, and J. GIMENO. "On the dependence of spray momentum flux in spray penetration: Momentum flux packets penetration model". English. *Journal of Mechanical Science and Technology* 21.7 (2007), pp. 1100–1111.

[33]   HIROYASU, H. "Experimental and theoretical studies on the structure of fuel sprays in diesel engines". *ICLASS-91, Gaithersburg, USA* (1991), pp. 17–31.

[34] DOHLE, U., S. KAMPMANN, T. WINTRICH, and C. HINRICHSEN. "Advanced Diesel Common Rail Systems for Future Emission Legislation". *International Conference on Automotive Technologies-ICAT*. 2004, pp. 109–113.

[35] BENAJES, J., R. PAYRI, S. MOLINA, and V. SOARE. "Investigation of the influence of injection rate shaping on the spray characteristics in a diesel common rail system equipped with a piston amplifier". *Journal of fluids engineering* 127.6 (2005), pp. 1102–1110.

[36] STEGEMANN, J., J. SEEBODE, J. BALTES, C. BAUMGARTEN, and G. MERKER. "Influence of throttle effects at the needle seat on the spray characteristics of a multihole injection nozzle". *ILASS Europe* (2002).

[37] MANIN, J., M. BARDI, and M. PICKETT L. "Evaluation of the liquid length via diffused back-illumination imaging in vaporizing Diesel sprays". *COMODIA* 6 (2012).

[38] PAYRI, R., F. SALVADOR, J. GIMENO, and J. DE LA MORENA. "Effects of nozzle geometry on direct injection diesel engine combustion process". *Applied Thermal Engineering* 29.10 (2009), pp. 2051–2060.

[39] KASTENGREN, A. L. et al. "Engine Combustion Network (ECN): measurements of nozzle geometry and hydraulic behavior". *Atomization and Sprays* 22.12 (2012), pp. 1011–1052.

[40] CHIAVOLA, O. and F. PALMIERI. "Modeling needle motion influence on nozzle flow in high pressure injection system". *SAE Paper* 2007-01-0250 (2007).

[41] KASTENGREN, A. L., F. Z. TILOCCO, and C. F. POWELL. "Initial Evaluation of Engine Combustion Network Injectors with X-Ray Diagnostics". *ILASS Americas* 2011-101 (2011).

[42] PICKETT, L. M., J. MANIN, R. PAYRI, M. BARDI, and J. GIMENO. "Transient rate of injection effects on spray development". *SAE Paper* 2013-24-0001 (2013).

[43] DESANTES, J., R. PAYRI, J. GARCIA, and F. SALVADOR. "A contribution to the understanding of isothermal diesel spray dynamics". *Fuel* 86.7 (2007), pp. 1093–1101.

[44] DE LA MORENA, J. "Estudio de la influencia de las características del flujo interno en toberas sobre el proceso de inyección Diesel en campo próximo". PhD thesis. Universidad Politécnica de Valencia, 2011.

[45] MANCARUSO, E. and B. M. VAGLIECO. "Optical investigation of the combustion behaviour inside the engine operating in HCCI mode and using alternative diesel fuel". *Experimental Thermal and Fluid Science* 34.3 (2010), pp. 346–351.

[46] SIEBERS, D. L. "Scaling liquid-phase fuel penetration in diesel sprays based on mixing-limited vaporization". *SAE Paper* 1999-01-0528 (1999).

[47] PICKETT, L. M., C. L. GENZALE, J. MANIN, L. MALBEC, and L. HERMANT. "Measurement uncertainty of liquid penetration in evaporating diesel sprays". *ILASS Americas* 2011-111 (2011).

[48] MYONG, K., M. ARAI, H. SUZUKI, J. SENDA, and H. FUJIMOTO. "Vaporization characteristics and liquid-phase penetration for multi-component fuels". *SAE Paper* 2004-01-0529 (2004).

[49] PASTOR, J. V, R. PAYRI, J. M. GARCIA-OLIVER, and F. J. BRICENO. "Analysis of transient liquid and vapor phase penetration for diesel sprays under variable injection conditions". *Atomization and Sprays* 21.6 (2011).

[50] ALLOCCA, L., E. MANCARUSO, A. MONTANARO, and B. M. VAGLIECO. "Use of Mineral Diesel, First-, and Second-Generation Biodiesels in Modern Common Rail Injection Systems under Nonevaporative and Evaporative Conditions". *Atomization and Sprays* 22.2 (2012).

[51] PAYRI, R., B. TORMOS, F. SALVADOR, and L. ARANEO. "Spray droplet velocity characterization for convergent nozzles with three different diameters". *Fuel* 87.15 (2008), pp. 3176–3182.

[52] PASTOR, J. V, J. ARRÈGLE, and A. PALOMARES. "Diesel Spray Image Segmentation With a Likelihood Ratio Test". *Appl. Opt.* 40.17 (June 2001), pp. 2876–2885.

[53] PICKETT, L. M. et al. "Comparison of diesel spray combustion in different high-temperature, high-pressure facilities". *SAE Paper* 2010-01-2106 (2010).

[54] MANIN, J., A. KASTENGREN, and R. PAYRI. "Understanding the Acoustic Oscillations Observed in the Injection Rate of a Common-Rail Direct Injection Diesel Injector". *Journal of Engineering for Gas Turbines and Power* 134.12, 122801 (2012), pp. 122–132.

[55] HUNTER, W. G. and J. S. HUNTER. "Statistics for experimenters". *Interscience, New York* (1978).

[56] RANZ, W. E. "Some experiments on orifice sprays". *The Canadian Journal of Chemical Engineering* 36.4 (1958), pp. 175–181.

[57] PAYRI, R., F. J. SALVADOR, J. GIMENO, and V. SOARE. "Determination of Diesel Spray Characteristics in Real Rngine In-Cylinder air Density and Presure Conditions". *Journal of Mechanical Science and technology* 19 (2005), pp. 2040–2052.

[58] DESANTES, J., R. PAYRI, F. SALVADOR, and J. DE LA MORENA. "Influence of cavitation phenomenon on primary break-up and spray behavior at stationary conditions". *Fuel* 89.10 (2010), pp. 3033–3041.

[59] DENT, J. *A basis for the comparison of various experimental methods for studying spray penetration*. Society of Automotive Engineers, 1971.

Chapter 6

Results and discussion: spray ignition and combustion

This chapter presents the results related to the combustion of the sprays produced by the *CDA* injector based on the chemiluminescence tests and on the 2-color optical pyrometry. The relationship between the quantities measured and the test conditions is discussed presenting qualitative comparisons, as well as extracting characteristic combustion parameters (e.g. ignition delay, lift-off length etc.). The *1DM* [1], calibrated at evaporative conditions in the previous chapter, will be employed for a deeper interpretation of the results.

6.1 *CH** and *OH** chemiluminescence imaging

In this section, the results related to the *CH** and *OH** radical chemiluminescence are presented starting from a general description of the raw images obtained and presenting the radicals related contour maps.

6.1.1 *CH** and *OH** appearance

Figures 6.1 and 6.2 present the image-sequences recorded by the two cameras for a sample test condition and give an overall description of the features captured during the tests. Moreover, the presentation of the images is convenient to point out the technical approach followed for the results analysis. *CH** emissions arise earlier than *OH**'s and are evenly distributed in the spray regions. The shape of the area where CH* chemiluminescence is observed recalls the shape of the

sprays, and, as observed by other authors, it overlaps the regions where fuel is vaporized [2–4]. However, the *CH** intensity is very low and it is right above the camera sensor noise level [5, 6]. The *CH** chemiluminescence intensity increases progressively up to the second stage ignition (τ_{SSI}), when intensity suddenly rises about three orders of magnitude; afterward, it is not possible to relate the signal recorded with *CH** emissions anymore, because they are disguised by broadband high temperature chemiluminescence and early soot incandescence [5, 7]. On the other hand, the *OH** radicals appearance has different features: the *OH** emissions start growing from separated nucleus and the intensity of the signal rises sharply at the beginning, and stabilizes at a certain level. The nuclei are observed at the same time and in the same regions where the *CH*-camera detects the abrupt increase in the intensity, confirming that *OH** chemiluminescence is a good marker for high temperature reactions but, also, that after second stage ignition the spectrum of the light emissions is wider [2, 5, 8]. Finally, the diffusive phase of the flame takes place and the flame front stabilizes at a certain distance from the nozzle outlet (lift of length or *LOL*) [3, 9]. The camera intensifier tends to increase its noise level when the signal intensity gets stronger: in the images presented in figures 6.1 and 6.2, the combustion causes the noise level to increase in the entire image. The same effect is caused by the background reflections that, in the same way, falsely increase the signal in some areas of the images. This fact has to be taken into account in order to understand correctly the results and to avoid misinterpretation of the data.

In the following section the *CH*/ OH** chemiluminescence results are presented by means of the contour maps described in Sec. 4.5.4 [10]; in this way, the distinctive features of each test condition can be easily pointed out without dispersive presentations of raw images. This section is divided into two sub-parts: the first, presenting the relationship between the ignition event and the ambient parameters and, the second, studying the effects of the injection parameters with special focus on the unique features of the *CDA* injector.

6.1.2   Effect of boundary conditions

As described earlier, the images obtained in the tests were re-elaborated and condensed into maps relating the intensity of the chemiluminescence radiation with the time *ASOI* and its axial [I] position. In this figures the images' field of view and the acquisition interval limits are indicated by gray straight lines (see Fig.6.3). Liquid- and vapor-phase penetration data, available from the tests at inert conditions, are presented on the same plot: these references can be particularly useful

---

[I]As discussed in Ch. 4, the adjective *axial* refers to the spray axis and the *axial distance* refers to the distance from the orifice outlet.
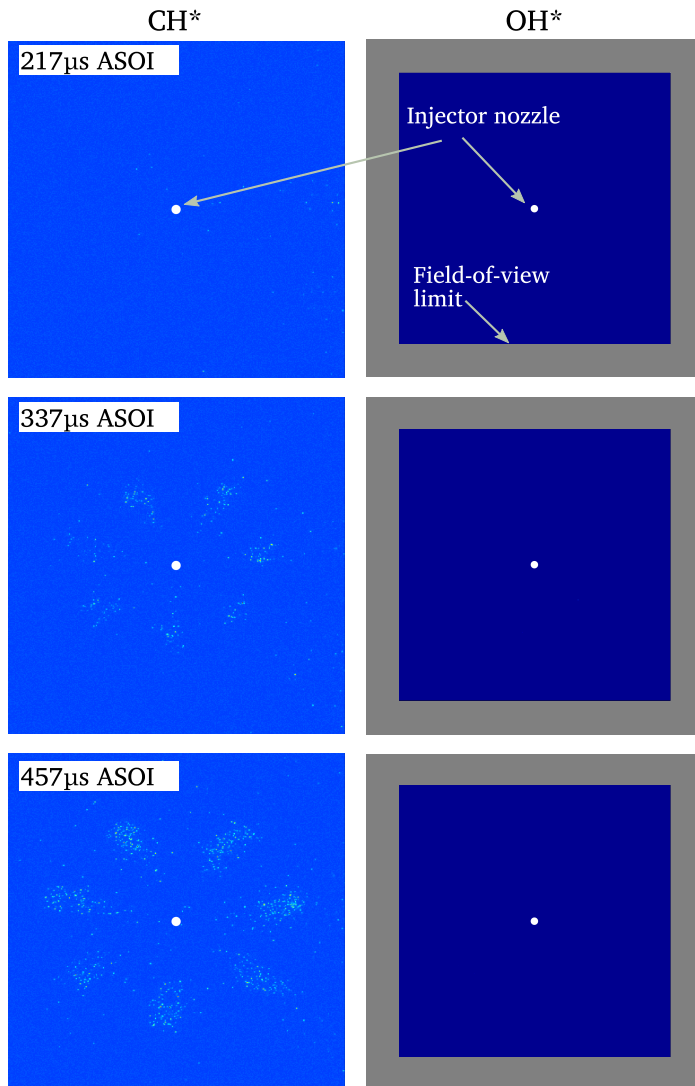
Figure 6.1: CH* and OH* formation. *Time-sequence of images captured simultaneously by the two intensified cameras. The gray area on the* OH* *images indicates the region out of the camera field of view.* $O_2\% = 16\%$, $T_a = 935\,\mathrm{K}$, $p_i = 60\,\mathrm{MPa}$, Ch = high.
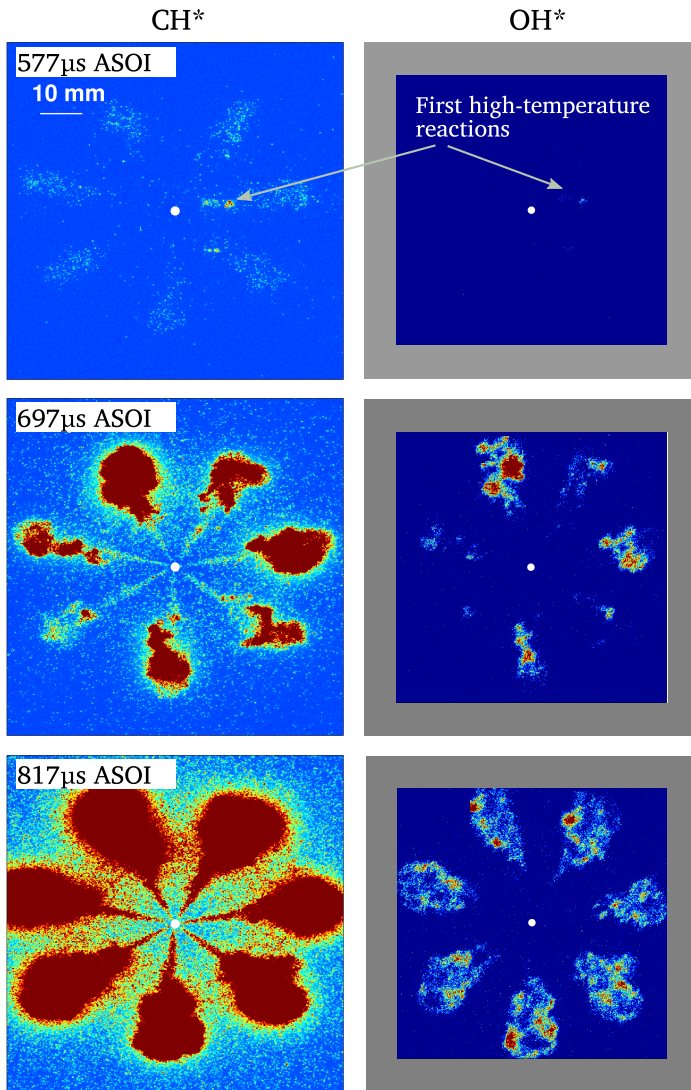
Figure 6.2: CH* and OH* *formation. Time-sequence of images captured simultaneously by the two intensified cameras. The gray area on the* OH* *images indicates the region out of the camera field of view.* $O_2\% = 16\%$, $T_a = 935\,K$, $p_i = 60\,MPa$, $Ch = high$.

to have a more global understanding of the results. The conditions tested in the liquid- and vapor-phase measurement are identical to the ones tested in this work except for two aspects:

- in the liquid- and vapor-phase penetration tests, the combustion of the fuel was prevented, by injecting in nitrogen atmosphere, in order to focus the measurement on the spray development;

- the only ambient temperatures tested at inert conditions were 870 and 950 K whereas the tests at reacting conditions were performed at $T_a = 870$ and 935 K. This second case will be compared to the data at inert conditions at $T_a = 950$ K.

The bias introduced in the data by the differences mentioned above is considered negligible [11, 12], particularly for the extent of the qualitative description performed in this section, which has only a reference purpose.

In Fig. 6.3 the color-maps obtained from *CH** and *OH** chemiluminescence are presented for different cases, where the only test condition differing is the ambient oxygen concentration. The differences between the *CH** and *OH** chemiluminescence onset described observing the raw images, is confirmed by the color maps: *CH** emissions appears smoothly (note the color scale of plots) and distributed in a wide region that starts very close to the spray tip. The maps highlight a relationship between the *CH** chemiluminescence and the region included between the vapor and the liquid phase penetration even though the background reflections combined with the intensifier noise avoids an accurate detection of the boundaries of the chemiluminescence emission region; on the other hand, the *OH** chemiluminescence appears later and the transition of the signal intensity from its appearance to its maximum is faster. Ambient oxygen content has a different impact on the *OH** and *CH** development: reminding that *CH** measurement can be related to this radical only before the onset of high temperature reactions (i.e. *OH** apparition), the timing and the position of its detection is barely affected by the oxygen concentration [13]; differently, an increase from 12 to 21% of the oxygen content, causes a faster onset of the *OH** radicals and moves the reaction region closer to the nozzle tip; the *OH** chemiluminescence intensity is also strongly linked to the oxygen concentration and increases with the oxygen content [13–15].

Fig. 6.4 shows the impact of the ambient temperature on the measured variables. As in the previous case, *CH** chemiluminescence appears close to the spray tip and it extends to the spray region while the *OH** signal appears well behind the vapor penetration boundary. A reduction in the ambient temperature delays the
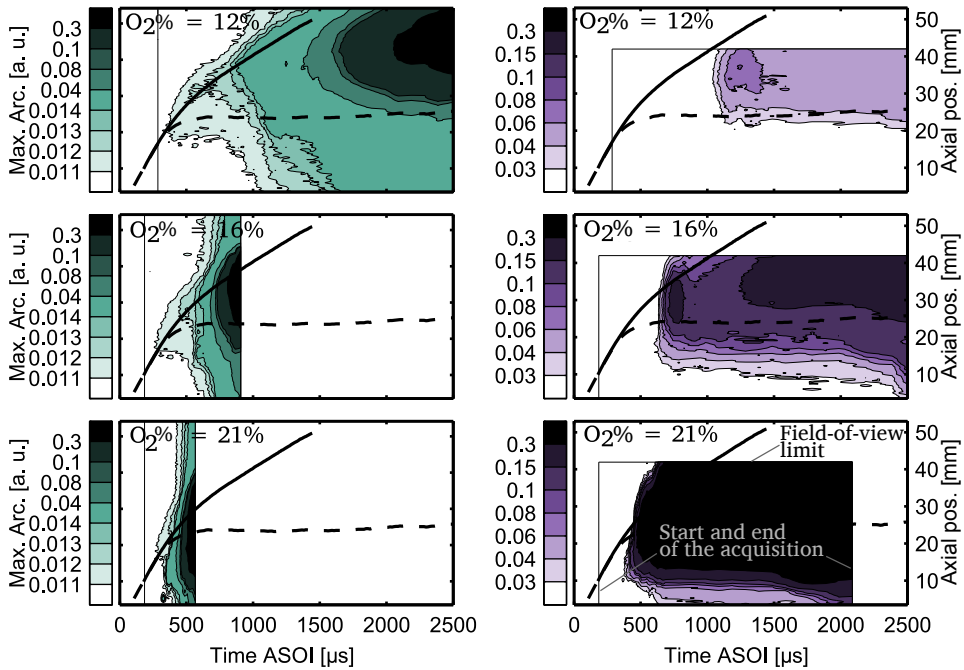
Figure 6.3: Effect of oxygen concentration. Contour maps for CH* (left) and OH* (right) chemiluminescence emissions at different oxygen concentration. The related liquid and vapor phase penetration are indicated respectively by the dashed and solid lines. $T_a = 935$ K, $p_a = 5$ MPa, $p_i = 60$ MPa, Ch = high.

onset of *OH** radicals [13–15] but, in this case, differently from the effect of oxygen concentration, the *CH** chemiluminescence apparition is delayed in a similar way. No significant changes are observed in the intensity of both chemiluminescence signals. The color-maps presented in Fig. 6.4 also show another important feature that was not readily apparent in the previous figure: right after its first onset, the *OH** chemiluminescence features a local maximum in the intensity. This feature, observed also by other authors [16, 17], is related to the premixed phase of combustion: the location and the magnitude of this local maximum will be further analyzed in the next sections.

6.1.3   Effect of injection parameters

The dependence of the ignition process on the injection parameters was studied focusing on two points:
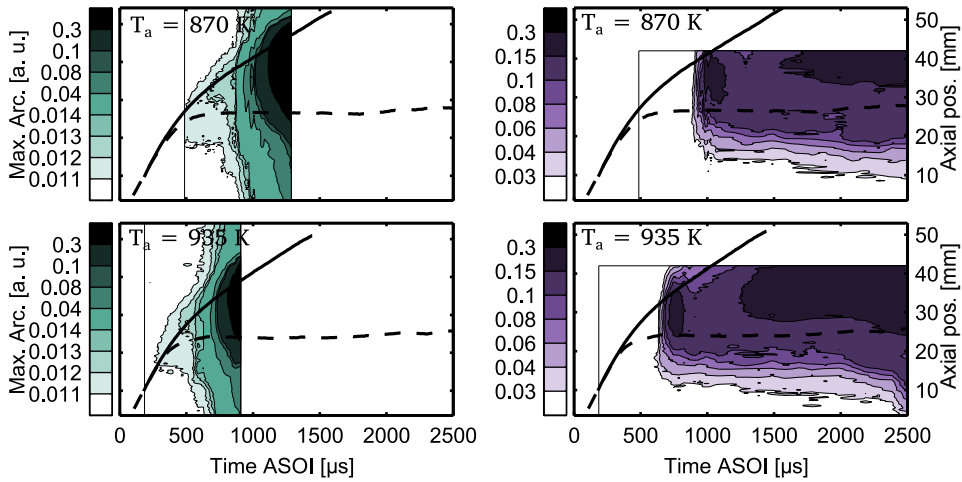
Figure 6.4: Effect of ambient temperature. Contour maps for CH* *(left) and* OH*
*(right) chemiluminescence emissions at different ambient temperature. The related
liquid and vapor phase penetration are indicated respectively by the dashed and
solid lines.* $O_2\% = 16\%$, $p_a = 5\,\text{MPa}$, $p_i = 60\,\text{MPa}$, Ch = high.

- the comparison between the effect of a reduction in mass flow rate due to a reduction in p_i and a reduction in mass flow rate due to the partial needle lift (lower *Ch*);

- the effect of a modification of the mass flow rate in the first part of the injection, fixing the final mass flow rate by performing rate shaping.

In the first comparison, a reduction in mass flow rate from a reference test condition ($p_i = 150\,\text{MPa}$, *Ch = high*, Fig. 6.5-top) was obtained in two different ways: reducing the injection pressure, while maintaining the maximum needle lift ($p_i = 60\,\text{MPa}$, *Ch = high*, Fig. 6.5-middle), and reducing the needle lift while maintaining the injection pressure ($p_i = 150\,\text{MPa}$, *Ch = low*, Fig. 6.5-bottom). The comparison shows that the main effect on the measured variables of a decrease in mass flow rate is the reduction of the axial position of the chemiluminescence. The *CH** emissions, as discussed earlier, are strongly related to the spray penetration, which depends on spray momentum and then, on mass flow rate [1, 11, 18]. However, it is important to notice that the axial position of the first *CH** detection is similar in the three cases compared, while the first *OH** detection is farther from the nozzle tip at high mass flow rate. The similitude to the gas-jet [1] offers a path to understand this phenomenon: following this interpretation of

the Diesel spray, a modification in the mass flow rate does not affect the spatial domain of the mixing field, but it only contracts or dilates the time scale; in other words, even changing the mass flow rate, at a datum spray penetration, the mixing field is identical (this is true if the spreading angle is not changing, but at this degree of approximation, it can be considered constant). The fact that the *CH** radicals location is not affected by injection parameters links this measurement to the mixing field. On the other hand, *OH** chemiluminescence has to be interpretated as the final stage of the pre-reactions: the time needed for the pre-reactions to be completed, mainly depends on the chemical/physical condition of the mixture. This lapse of time is approximately constant for the different injection cases compared in Fig. 6.5. However, due to the different velocities characterizing the three cases, in the high-p_i and -Ch case, the second stage ignition takes place at a farther location.
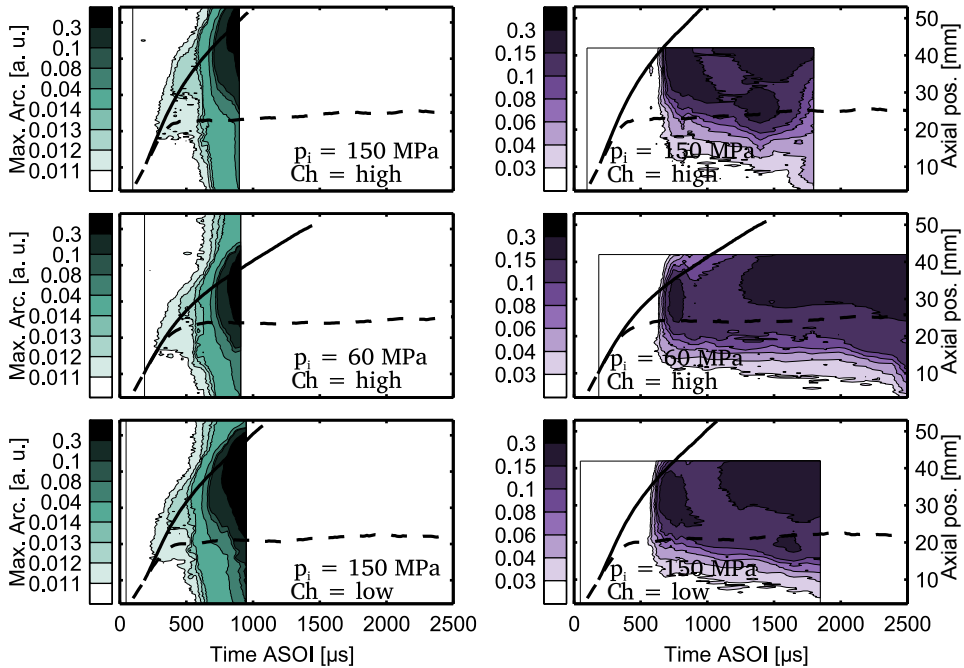
Figure 6.5: Effect of p_i and Ch. Contours maps for CH* (left) and OH* (right) chemiluminescence emissions at different injection conditions. The related liquid and vapor phase penetration are indicated respectively by the dashed and solid lines. $O_2\% = 16\%$, $T_a = 935\,\mathrm{K}$, $p_a = 5\,\mathrm{MPa}$.

In the following comparison the injection rate shape was modified, reducing the mass flow rate during the first part of the injection, and reaching the same level

during the final stage. The related injection rate profiles are plotted in Fig. 6.6 for reference.
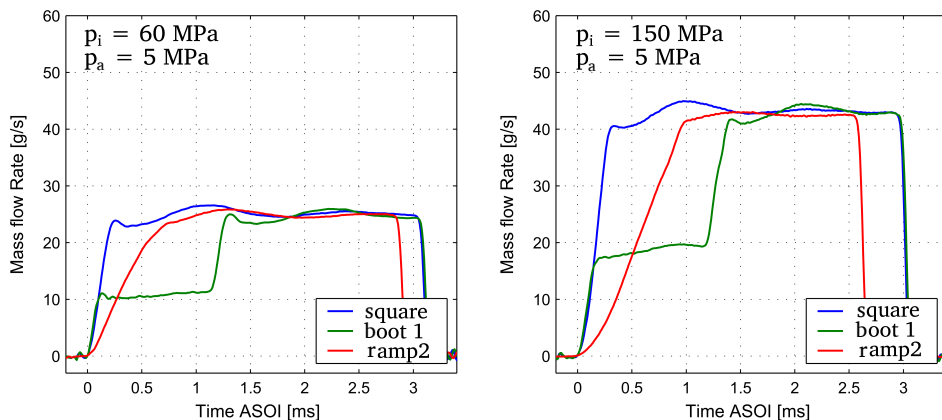
Figure 6.6: Square, boot1 *and* ramp2 *mass flow rate at* $p_i = 60\,\text{MPa}$ *(left) and* $p_i = 150\,\text{MPa}$ *(right);* $p_b = 5\,\text{MPa}$.

Besides the modification in the liquid- and vapor-phase penetration associated to the injection rate shaping (see Ch. 5), the main differences caused by the alternative injection rate shapes concern the location and the intensity of the peak observed at the ignition. This fact enforces the hypothesis that this peak is related to the premixed phase of the Diesel combustion: in fact, in the boot and in the ramp injection, due to the particular injection rate shape, the amount of fuel injected before the combustion is lower and, as a consequence of that, the premixed phase of the combustion will be lower [19–21]. This combustion phase is strongly related to the peak in the rate of heat release that is the responsible of the noise problems related to the Diesel engine. Moreover, the formation of extended high temperature regions during this phase is responsible for the production of NO_x [20, 22]. The reduction in the intensity peak observed is an encouraging insight of the usefulness of these injection strategies.

In the next section, the data showed in the color maps will be summarized in some key parameters, enabling the presentation of a global picture of the results.

6.2   First- and second-stage ignition characterization

The results presented in the previous section helped understand the implications that the variation of each test condition has on the ignition process. However, the contour-maps are effective to compare only a limited number of test conditions
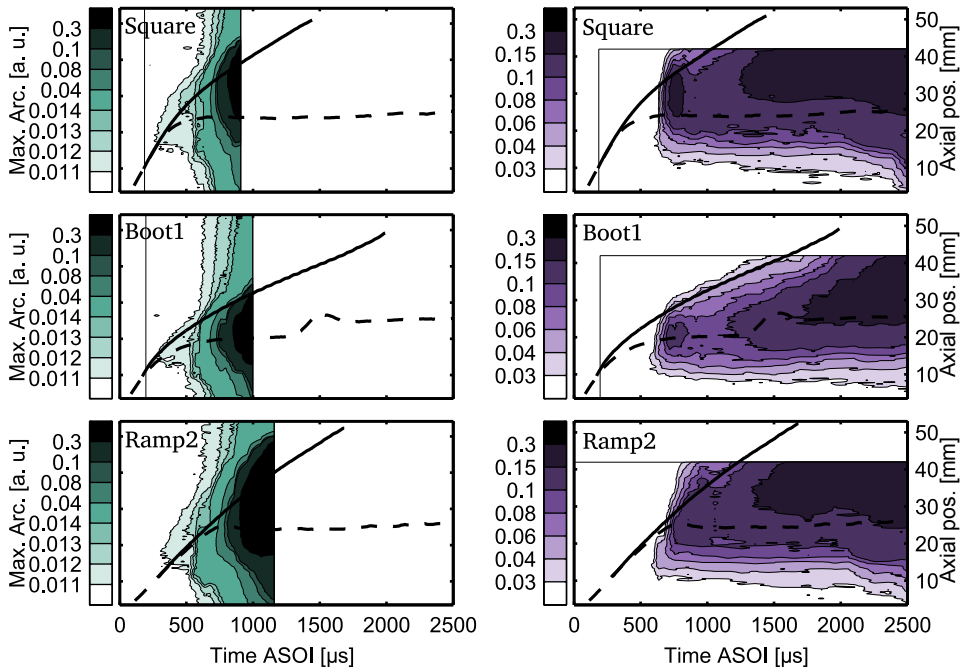
Figure 6.7: Effect of injection rate shape. Contours maps for CH* (left) and OH* (right) chemiluminescence emissions at different injection conditions. The related liquid- and vapor-phase penetration are indicated respectively by the dashed and solid lines. $O_2\% = 16\%$, $T_a = 935\,\mathrm{K}$, $p_a = 5\,\mathrm{MPa}$ and $p_i = 60\,\mathrm{MPa}$.

and it is hard to present a global picture of the results. In this section, the parameters describing the main features of the contour maps are presented, in order to observe the global trends of the results. As in the previous sections, the ambient and injection parameters will be discussed separately.

6.2.1 Effect of ambient parameters

The first parameters of interest are τ_{CF} and τ_{SSI} that, as previously discussed, are representative of the time at which, respectively, first- and second-stage ignition begin [3, 9]. The plots presented in Fig. 6.8 show and relate with each other the effect that $O_2\%$, T_a, and p_a have on the ignition process, fixing the injection parameters. The comparison confirms and extends the observations done before:

- an increase in ambient temperature and pressure causes a similar decrease in τ_{CF} and as in τ_{SSI};

- oxygen concentration affects mainly τ_{SSI}, while it has only a second order effect on τ_{CF}.

The dwell time between τ_{CF} and τ_{SSI} in Fig. 6.9 is coherent with the previous observations but offers a different point of view: $O_2\%$ and p_a are the main drivers for this parameter, while ambient temperature impact is substantially lower. These observations are deeply related to the physical and chemical processes taking place in the Diesel spray and are in accordance with what found in other works [13, 16]. The results presented achieve two goals: they confirm what found in other works while adding new information related to the specific conditions tested, and they prove the reliability of the techniques employed, that will give further support to the evaluation of the direct-acting injector capabilities.
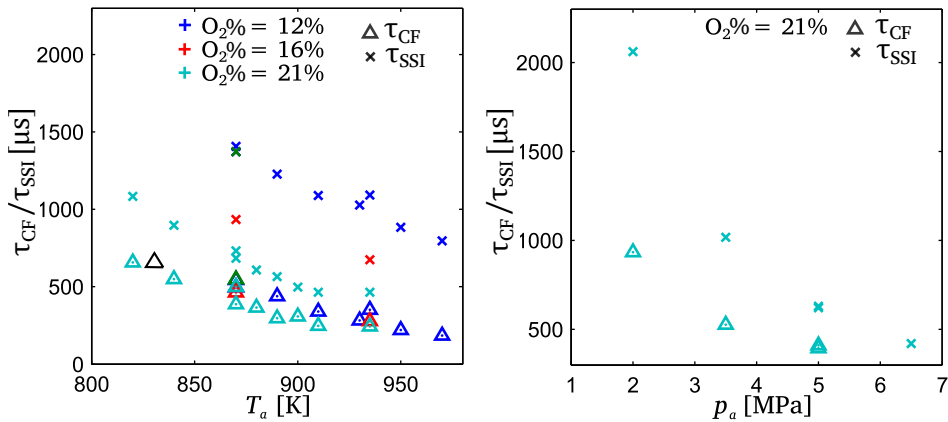
Figure 6.8: τ_{CF} and τ_{SSI} at different test conditions. On the left plot the data are plotted versus ambient temperature at fixed back pressure ($p_a = 5$ MPa) while in the right plot the ambient temperature and the oxygen content are fixed ($O_2\% = 21\%$, $T_a = 935$ K). In all the cases the same injection has been tested: $p_i = 60$ MPa, Ch = high.

6.2.2 Effect of injection parameters

In this section, the effect of injection parameters on the ignition process are presented. In order to quantify the effect of the needle lift, the approach presented in Ch. 5 is followed employing the non-dimensional parameter λ.

In this way, it is possible to compare the conventional injections at different *charge* levels together with the boot type injections. In fact, considering that in
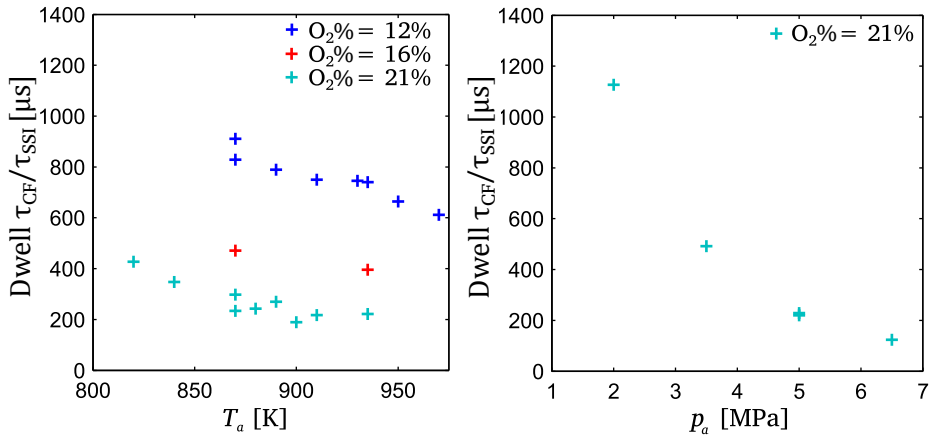
Figure 6.9: τ_{CF}/τ_{SSI} dwell time at different test conditions. On the left plot the data are plotted versus ambient temperature at fixed back pressure ($p_a = 5$ MPa) while in the right plot the ambient temperature and the oxygen content are fixed ($O_2\% = 21\%$, $T_a = 935$ K). In all the cases the same injection has been tested: $p_i = 60$ MPa, Ch $=$ high.

most of the cases the ignition delay (τ_{SSI}) is lower than 1 μs (that means, before the transition from *foot* to *leg* stage) the boot injection can be treated as an injection at low needle lift; the results related to the ramp shaped injections, will be added on the same plot for reference, with an indication on the x-axis.

The effect of injection parameter on τ_{SSI} is limited (see Fig. 6.10), and the variations observed fall within the limit of the experimental accuracy. However, in the conventional square injections some slight trends can be captured:

- injection pressure tends to reduce the τ_{SSI} due to his enhancing effect on the mixing process; this effect has already been observed in other works [7, 13, 23];

- the needle fuel throttling has a small effect in reducing the τ_{SSI}.

Even if this second effect is small, it is interesting to underline that this effect can be explained only assuming that reducing the needle lift, the spray development is modified. In fact, if the spray development at reduced needle lift was the same as at *Ch = high*, the effect of the fuel throttling should be similar to the one of a reduction in injection pressure, causing a longer τ_{SSI} [9, 23]. However, the trend observed is the opposite. This fact can be explained by the observations
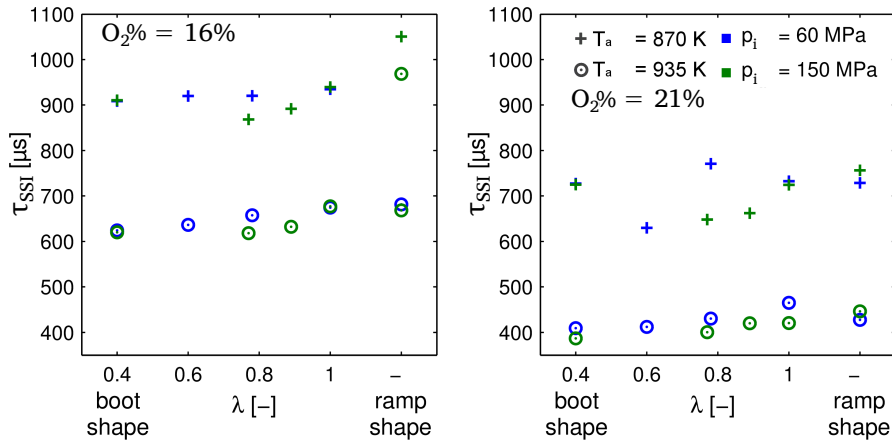
Figure 6.10: τ_{SSI} *at different test conditions. Each plot presents the effect of the injection parameters at different ambient conditions.* $p_a = 5\,\text{MPa}$.

presented in the inert spray characterization: the fuel throttling operated by the nozzle needle has consequences on the fuel flow through the nozzle orifices which are reflected on the spray development as an increase of the spray spreading angle and a reduction in the area coefficient. The increase in the spreading angle enhances the mixing process, and it gives an explanation to the reduction in the τ_{SSI} observed at partial needle lift.

Another interesting feature appearing in the contour maps is the peak in the intensity that has been observed right after the second stage ignition. As mentioned earlier in this section, this characteristic is linked to the premixed phase of the Diesel combustion and, therefore, to the injection parameters that control the amount of ignitable mixture formed at the moment of the ignition. The measurement of OH_{peak} is meaningful only in the case that the premixed combustion takes place entirely in the field of view: analyzing the images of the tests, it was observed that for some test conditions (e.g. $T_a = 870\,\text{K}$ and $p_i = 150\,\text{MPa}$) the premixed combustion was partially out of the field of view, and the results related to these tests were not reliable. For this reason, they are not included in the plot. The results in Fig. 6.11 confirmed that reducing the mass flow rate (either by reducing the injection pressure or by partial needle lift) produces a reduction in OH_{peak}. Moreover, it is worth mentioning that, for all the ambient conditions presented in the plot, the lowest OH_{peak} is achieved using the non-conventional injection rate shapes (either *boot* or *ramp*). Therefore, the reduction in the mass flow rate before the ignition, obtained by modifying the mass-flow rate profile, has interesting consequences on the ignition event. This observation is also sustained
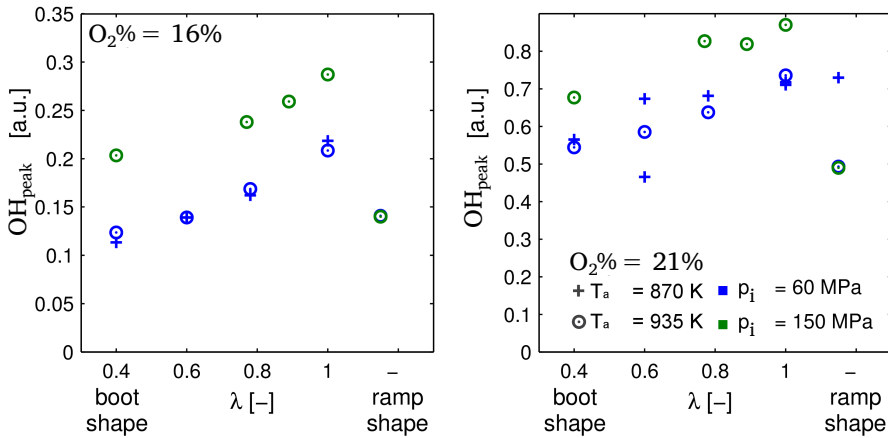
Figure 6.11: OH* *chemiluminescence peak intensity at different test conditions. Each plot presents the effect of the injection parameters at different ambient conditions.* $p_a = 5\,\text{MPa}$.

by the calculation of the mass injected at the moment of the ignition (m_{SSI}): this parameter, obtained relating τ_{SSI} and the mass flow rate measured for the same injection condition, shows the same behavior of OH_{peak} and, therefore, it confirms the hypothesis of the relationship between OH_{peak} and the premixed combustion. The calculation of m_{SSI} (Fig. 6.12) is a further confirmation that the employment of *boot* and *ramp* shaped injection profiles helps controlling the premixed phase of the combustion.

The axial location where the ignition takes place (x_{SSI}) is another fundamental measurement when evaluating the Diesel ignition [19, 24]. In fact, in a Diesel engine, the location of the ignition can determine radical changes in the thermodynamic conditions of the mixture, especially when it occurs in the proximity of the piston bowl [25, 26]. In this case, even though the fuel sprays are injected in free field conditions (the test chamber is big compared to the spray), this parameter helps to investigate the injection rate shaping capabilities of controlling the ignition location. x_{SSI} of the ignition location increases with λ: either a decrease in injection pressure or in piezo-stack charge causes the fuel to ignite closer to the injector tip. Moreover, the mass flow rate profile at the start of the injection has the most significant impact on this parameter, allowing a substantial reduction of this distance without modifying neither the injection pressure nor the mass flow rate at the end of the injection.

As commented for the previous graphics, modifying either the injection pressure or the needle lift has similar effect on the mass flow rate, and this effect is
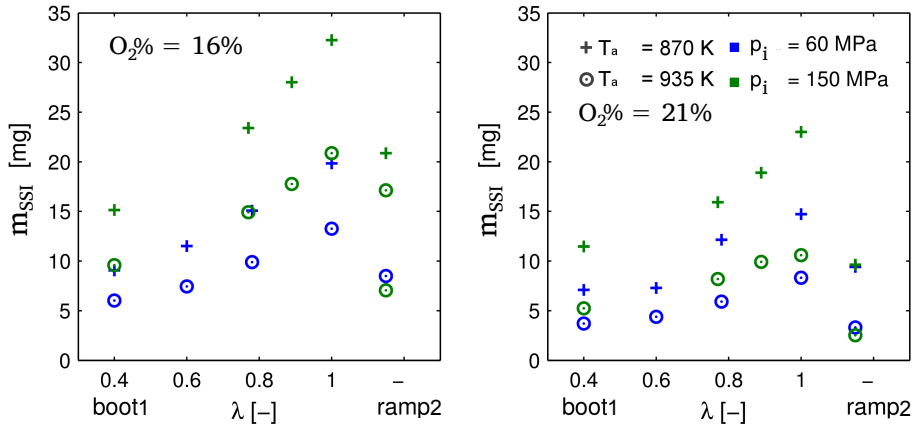
Figure 6.12: Mass of fuel injected at τ_{SSI} at different test conditions. Each plot presents the effect of the injection parameters at different ambient conditions. $p_a = 5\,\text{MPa}$.
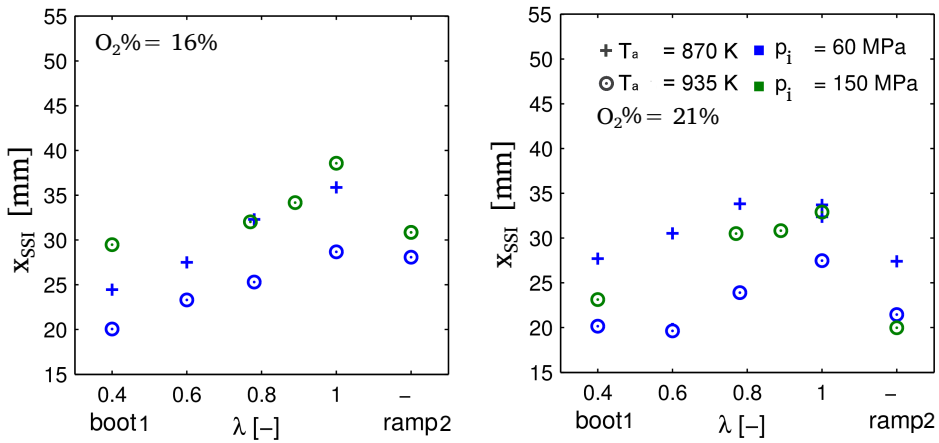
Figure 6.13: Axial position of the second stage ignition x_{SSI} at different test conditions. Each plot presents the effect of the injection parameters at different ambient conditions. $p_a = 5\,\text{MPa}$.

evenly reflected on the OH_{peak} and its location. However, it has also been pointed out that the flow throttling operated by the needle (e.g. at low values of λ), modifies the spray development enhancing the mixing process. τ_{SSI} results confirmed these observations even though the differences observed fall in the range of the measurement uncertainties. Fig. 6.14 compares the m_{SSI} and x_{SSI}, based on the average mass flow rate. In this way, the effect on these measurements caused by the injection pressure and the needle lift can be compared. The plots remark that the injection parameter that mainly drives these magnitudes is the average mass flow rate, since the points at different needle lift and injection pressure lie on the same line. Only at a closer look, it can be observed that the points at partial needle lift (*low* and *med* piezo-stack charge) are not well aligned to the line connecting the points at full needle lift, suggesting that the effect of the two injection parameters compared is not exactly the same. However, the differences observed are very small and cannot be considered conclusive.
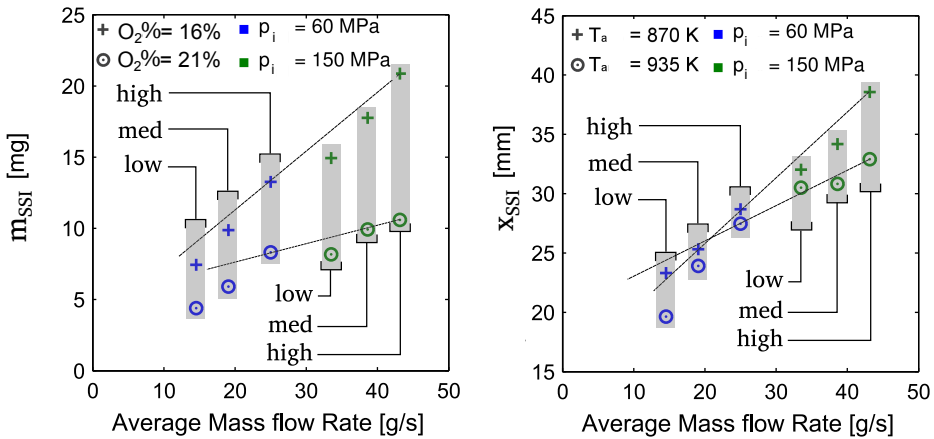
Figure 6.14: m_{SSI} (left) and x_{SSI} (right) at different test conditions. $p_a = 5\,\text{MPa}$, $O_2\% = 21\%$.

6.2.3   General comparison

The effect of the test conditions on the measured quantities are summarized in figures 6.15, 6.16 and 6.17.

The second stage ignition delay (τ_{SSI}) is mainly driven by the ambient conditions (see Fig.6.15). The injection parameters only have a second order effect on this measurement. Only the ramp injection seems to have an important impact on τ_{SSI} in some conditions: after the ramp-up period, the spray produced in the

ramp case behaves as the square case adding an initial delay. If the τ_{SSI} is longer than the ramp up period this delay will be entirely transferred on the ignition timing.

On the other hand, the quantity m_{SSI} is significantly affected by ambient and injection parameters (Fig.6.16). A decrease in ambient temperature and oxygen concentration causes m_{SSI} to be smaller. In this case, the effect of injection parameters is of similar extent: increasing injection pressure or *Ch*, produces a significant increment in m_{SSI}. In the same way, the introduction of *boot* and *ramp* injections causes a reduction in this parameter. The advantage of *ramp* injection, compared to the *square* case, is more significant in cases characterized by short τ_{SSI} (high oxygen concentration and ambient temperature). On the other hand, the effect of boot shape is more or less constant at all the conditions tested.
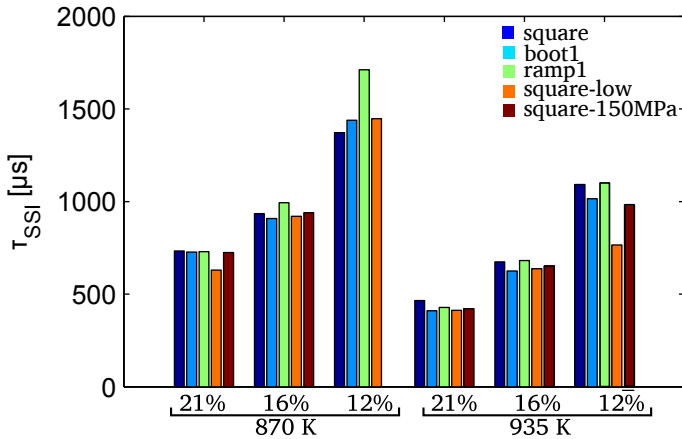
Figure 6.15: *Average* τ_{SSI} *obtained at different conditions.* $p_a = 5\,MPa$, $p_i = 60\,MPa$.

As for m_{SSI}, the quantity x_{SSI} represented in Fig.6.17 is affected by both, ambient and injection parameters. Generally, the longer the τ_{SSI} is (low O_2% and low T_a), the farther is the ignition location. However, in this case, a lower mass flow rate (low p_i and low *Ch*) also causes a significant reduction in x_{SSI}. Additionally, the advantage obtained using the *ramp* injection is important only at conditions characterized by short τ_{SSI}, while the impact of *boot* injection is the same at all the conditions.

The different impact of *ramp* or *boot* injections put emphasis on the fact that the injection rate profile has to be chosen depending on the in-cylinder conditions, paying particular attention to the second-stage ignition delay.
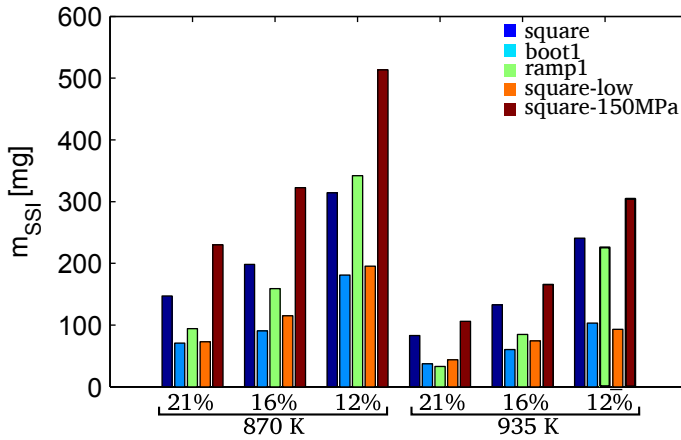
Figure 6.16: Average m_{SSI} obtained at different conditions. $p_a = 5\,\mathrm{MPa}$, $p_i = 60\,\mathrm{MPa}$.

Generally, in a Diesel engine, high temperature and high oxygen concentration conditions are typical of high-load engine conditions: therefore, based on the results presented above, the introduction of *ramp* injection profiles is more appropriate at high-load conditions while *boot* injections is more convenient at medium- and low-load. However, a further fine tuning on the duration of the *leg* stage or the slope of the *ramp* profile could provide the optimum injection shape for all the engine load conditions.

6.3 Lift-off length: steady and transient behavior.

6.3.1 *Square injections*

The lift-off length of the sprays was measured in two different ways: 1) by the processing the *OH** still images (the same images used to determine the ignition delay) and 2) by performing additional tests in which *OH** time averaged images were acquired. The first analysis provides the transient lift-off length, while the second provides only one value representative of the test condition (LOL_{av}) [13, 27]. Although this second method provides less information than the first, it is normally preferred, since the time-averaging helps reducing the dispersion of the measurement and guarantees robust results [6, 28]. As described in Sec. 4.5.4, the shutter-interval for the time-averaged images was chosen between $880-1380\,\mu s$ ASOI in order to exclude the ignition and the end-of-injection (*EOI*) transients. As observed in the previous section, there are various cases in which
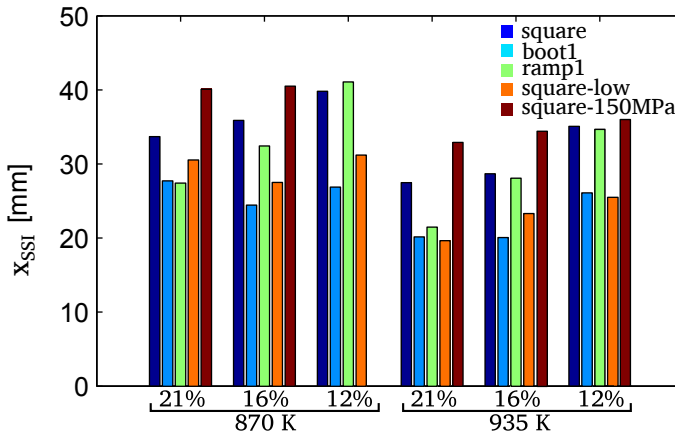
Figure 6.17: Average x_{SSI} obtained at different conditions. $p_a = 5$ MPa, $p_i = 60$ MPa.

τ_{SSI} falls within or after this interval. However, considering the purposes of this comparison, it was preferred to maintain the shutter-interval constant . Figures 6.18 and 6.19 present the comparison between transient versus time averaged *LOL* at different conditions.

Fig. 6.18 compares the effect of *Ch* at $p_i = 60$ MPa (left) and at $p_i = 150$ MPa (right). Generally, the lift-off length increases with the outlet velocity, either due to an increase in p_i or *Ch*. This is consistent with other results found in the literature [13, 27, 29, 30] and also with the gas jet theory presented in Sec. 3.5.3 [31]. Because of the highly reacting environment ($T_a = 935$ K and $O_2\% = 21\%$), the ignition takes place well before the shuttering interval, and during this interval the flame front is well established at the *LOL*. As a consequence of that, LOL_{av} is very close to the transient value and both techniques provide consistent results. Moreover, before the end of the injection (the *EOI* is indicated by a black tick on each curve) the transient lift-off length does not show any significant variation until the quick decrease taking place at the *EOI*. The shortening of the lift-off length at the end of the injection is a typical phenomenon occurring in highly reacting environment (e.g. high temperature or high oxygen concentration), related to the combustion of the lean mixture forming at the *EOI* [32, 33].

Fig.6.19 presents the results at lower ambient temperature $T_a = 870$ K. In the cases presented on the left-hand side plot ($O_2\% = 21\%$) the shutter-interval includes the ignition transient, and in the right-hand side plot ($O_2\% = 16\%$) τ_{SSI} is even longer. As a consequence of that, a significant discrepancies are observed between the transient and time-averaged *LOL* results. Even though, both
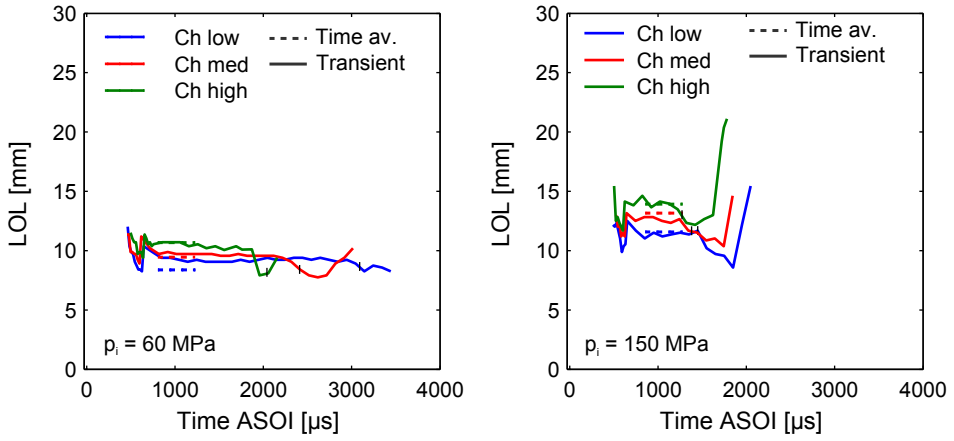
Figure 6.18: *Time averaged and transient* LOL. *Effect of* Ch *and* p_i. $p_a = 5$ MPa, $O_2\% = 21\%$ *and* $T_a = 935$ K.
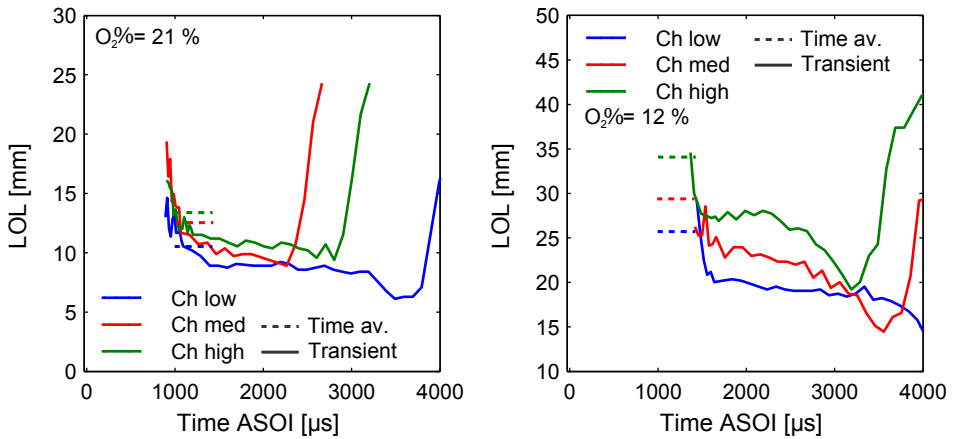
Figure 6.19: *Time averaged and transient* LOL. *Effect of* Ch *and* $O_2\%$. $p_a = 5$ MPa, $T_a = 870$ K *and* $p_i = 60$ MPa.

the measurements catch the same trends, LOL_{av} is generally higher than the transient measurement. This fact is consistent to the behavior of the transient lift-off length: at these conditions the *LOL* last longer in reaching a steady value, and continue decreasing until the *EOI*. It is important to underline, that even adjusting the shutter-interval at these conditions the calculation of a time-averaged lift-off length would excessively simplify the process, missing important information. As a further remark, it has to be said that the time averaged image alone does not reveal any insight of the *transition* of the *LOL*, and, therefore, would lead to incorrect results.
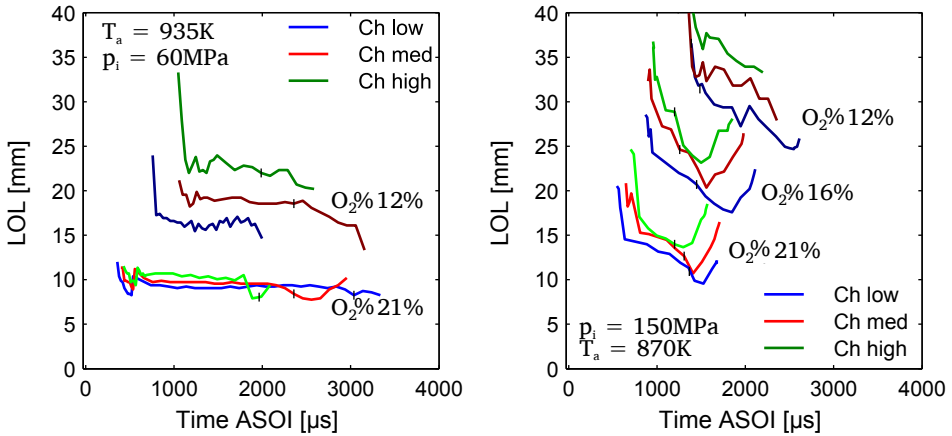
Figure 6.20: *Transient* LOL. *Effect of* Ch *and* O_2%. *The black ticks indicate the end of injection for each case.* $p_a = 5\,\text{MPa}$.

Finally, Fig. 6.20 shows the behavior of the *LOL* at different test conditions. In these cases, the time averaged results are not plotted. A global evaluation of the results suggests that, in some cases, the *LOL* is almost steady during the whole combustion event while, in other cases, the *LOL* varies during the whole injection without reaching a steady value. Assuming that, for very long injections, the lift-off length always tends to an asymptotic steady value [34], it is the author opinion, that this fact is related, on one side, to the relationship between ignition location and the hypothetical steady *LOL* value and, on the other, on the velocity of the response of the lift-off length in modifying its position. This last point will be better explored when presenting the effect of injection rate shaping. In light of the highly transient behavior of the lift-off length at most of the conditions tested, a steady value was calculated averaging the transient results during a convenient time interval and only in the cases in which the *LOL* variation was limited. This

value has been called LOL_{std}. Fig. 6.21 shows the difference between the ignition location and the LOL_{std} (Δx) suggesting the following comments:

- at all the conditions tested Δx is positive, as typical for Diesel combustion [14];

- at high ambient temperature Δx decreases. However, this effect is significant at $O_2\% = 21\%$ and it is lower at lower oxygen concentration.

- this difference decreases at low oxygen content .

Moreover, Fig. 6.21 shows that the fuel outlet velocity is a driving parameter for Δx; increasing the injection pressure or the injector *charge* a significant increase in Δx can be observed.

Due to the complex relationship between Δx and the boundary conditions and the limitation of the present data-set it has been preferred to leave the investigation of this feature of the combustion to a more specific study. To this end, a wider range of test conditions and the use of longer injections should helps the robustness of the conclusions. However, the comparison highlights features that are rarely discussed in the literature [34]. Moreover, these results underline that, when trying to translate the results to a real engine, a time averaged *LOL* might not be appropriate and, even more, when applying strategies with short injection durations and high rail pressures.
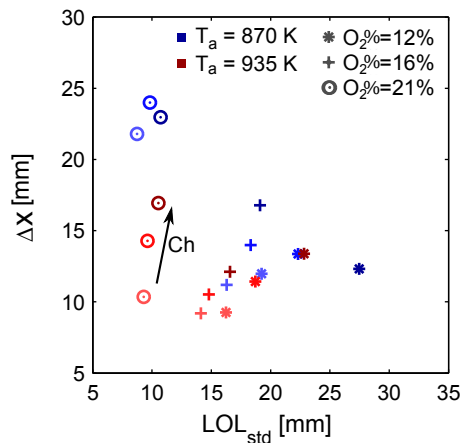
Figure 6.21: Distance between ignition location and steady lift-off length. $p_a = 5\,\mathrm{MPa}$, $p_i = 60\,\mathrm{MPa}$.

6.3.2 Effect of injection rate shaping

The effect of injection rate shaping can also be observed on the transient lift-off length curves. Many authors highlighted the relationship between *LOL* and the fuel outlet velocity [13, 31, 35]. Being *ramp* or *boot* injections characterized by the fuel outlet velocity varying with time, it is not surprising to observe variations in the *LOL* when modifying the injection rate shape. However, this effect has to be carefully related to the ambient boundary conditions.

Fig. 6.22 presents the effect of *boot* injection rate profile on *LOL*. Coherently with the lower fuel outlet velocity characterizing the *foot* stage, right after the ignition the *LOL* is shorter than in the following stage, appearing in the order *boot1 < boot2 < square*. Even though this effect is consistent at all the conditions tested, it is substantially higher at lower oxygen concentration. In other words, the longer is x_{SSI}, the greater is the impact of using a *boot* injection. At $p_i = 60$ MPa, the *foot/leg* transition can be recognized on the *LOL* curve. On the other hand, at $p_i = 150$ MPa the transition is harder to see: in this case, it could be said that the boot injection rate shape, help to partially compensate the *LOL* decrease characterizing the *square* injections.
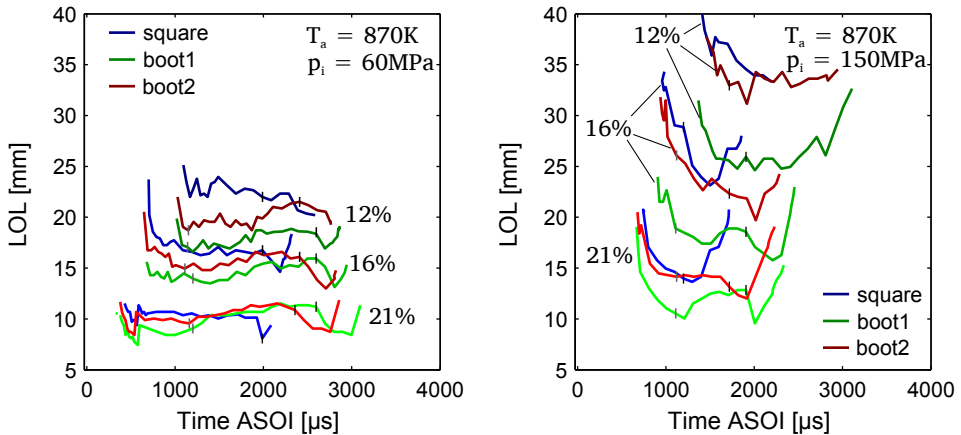
Figure 6.22: Transient LOL*. Effect of* boot *injection rate profile and* O_2%. *The black ticks indicate the end of injection and the* foot/leg *transition for each case.* $p_a = 5$ MPa.

Different considerations should be drawn for *ramp* injection profiles. The plot in Fig. 6.23 show a slight effect of the injection rate profile shape on the transient *LOL*. In fact, even though the *ramp* injections allow to reduce x_{SSI} (c.f. Fig.6.11), the mass flow rate grows faster than in the *boot* case. For this reason,

it is worth to remind the parameter t_{open} describing the slope of the *ROI* ramp-up (t_{open} is the time needed for the *ROI* rate to reach the 90% of its steady value). At $p_i = 60\,\text{MPa}$, t_{open} for the two *ramp* injections is 0.34 and 0.61 ms while at $p_i = 150\,\text{MPa}$ this value is 0.51 and 1.10 ms. These values help understanding the measured transient *LOL*. Differently from the cases at $p_i = 150\,\text{MPa}$, at $p_i = 60\,\text{MPa}$, the *LOL* is measured only after the ramp-up period.
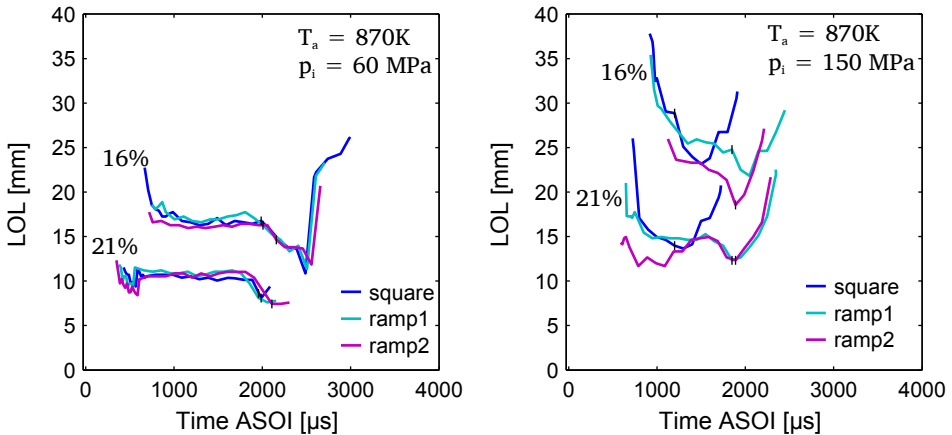
Figure 6.23: Transient LOL. *Effect of* ramp *injection rate profile and* O_2%. *The black ticks indicate the end of injection for each case.* $p_a = 5\,\text{MPa}$.

Finally, the transient lift-off length has been used to obtain the average Φ_{eq} at the *LOL*. This measurement is an important indicator to investigate the impact of the boundary conditions on the combustion event. The Φ_{eq} was obtained using the results obtained by the *1DM*, following the approach followed by Garcia in his Ph.D. thesis [36]: the experimental value of the lift-off length was compared to the maps provided by the *1DM* for each specific test conditions: the fuel-air equivalence ratio Φ_{eq} is among the results provided by the calculation [1]. With the aim of calculating a parameter representative of each specific test condition, the value of Φ_{eq} is averaged along the whole duration of the injection. Fig. 6.24 presents the results obtained for this parameter at different test conditions. An increase on T_a causes an increase in Φ_{eq} since, as previously observed, at higher temperature the lift-off length is shorter. However, a decrease in O_2% is more complex: even though lower O_2% produces an increase in *LOL* and more gas entrainment before the *LOL*, the total mass of oxygen entrained might be lower, due to its lower concentration [9, 36, 37]. Lower injection pressure and *Ch* are characterized by shorter lift-off length: coherently the fuel-air equivalence ratio obtained is lower. As for the ignition parameters (m_{SSI} and x_{SSI}), both *boot* and

ramp injections have an effect on Φ_{eq}. Also in this case, the effect of the *ramp* injection is remarkable only at high $O_2\%$ and T_a conditions, while the *boot* effect is persistent at all the conditions tested.
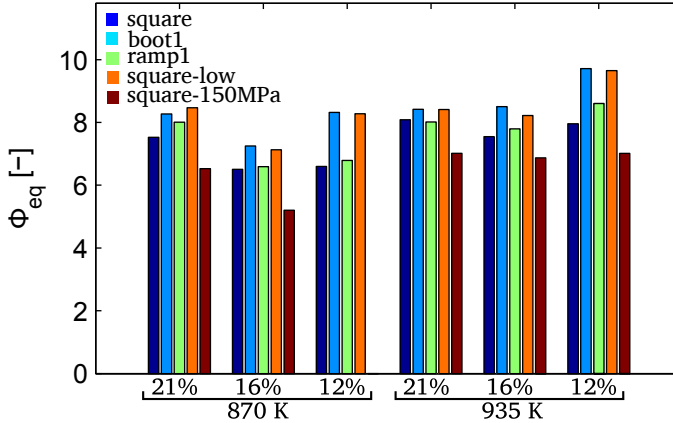
Figure 6.24: Average Φ_{eq} obtained at different conditions. $p_a = 5\,\text{MPa}$, $p_i = 60\,\text{MPa}$.

6.4 Statistical analysis

The broad range of conditions tested provides a solid base to perform a statistical analysis and to increase the reliability of the results. A least-square regression has been performed to have an analytical description of the relationship between the test conditions and the measurements performed. The equations used have been chosen depending on the parameter analyzed. On the one hand, τ_{SSI}, which is directly related to the combustion chemistry, is fitted to an Arrhenius type equation (Eq.(6.1)) [13, 14, 38]; on the other, x_{SSI} and *LOL* are strongly linked to the spray development and therefore an exponential equation is preferred (Eq.(6.3)) following other examples in the literature [13, 23, 35]. To employ the same equations used by other authors will give the advantage of performing direct comparisons. In order to obtain results consistent with the literature, only the results related to conventional injections were been included in the analysis. While in the cases of τ_{SSI} and x_{SSI}, there is a wide data set on which to base the regression, it is important to remind that only few data are available for the LOL measurement: in part, because the transient *LOL* was performed only for a limited number of conditions and, in part because many cases have been discarded, including only

the cases at which the *LOL* was reasonably steady. Also, considering that the variation in density related to the *LOL* was limited ($17.8-19.5 \, \mathrm{kg/m^3}$), the dependence on this variable was fixed.

$$\tau_{SSI} \propto \exp\left(\frac{A}{T}\right) \cdot \rho_a^a \cdot p_i^b \cdot O_2\%^c \cdot \lambda^d \ , \tag{6.1}$$

$$x_{SSI} \propto T_a^z \cdot \rho_a^a \cdot u_{eff}^b \cdot O_2\%^c \ , \tag{6.2}$$

$$LOL \propto T_a^z \cdot \rho_a^{-1} \cdot u_{eff}^b \cdot O_2\%^c \ . \tag{6.3}$$

	Exp.	Conf. Int.	Pickett et al. [14]	Benajes et al. [13]
A	6120	5831/6409	6534	7216
a	−1.39	−1.66/ − 1.12	−0.96	−0.93
b	−0.04	−0.13/0.05	−	−0.09
c	−1.44	−1.58/ − 1.30	−1	−1.25
d	0.12	0.23/0.01	−	−
R^2	99.1%			

Table 6.1: Exponents obtained from the regression to Eq. (6.1) to the experimental data.

Tab.6.1 shows part of the results from the statistical analysis performed. The results related to τ_{SSI} show relatively good agreement with the results from Pickett et al. [14] and Benajes et al [13]. Although small differences appear, the general trend is very close and the high R^2 found proves the good precision of the tests and the reliability of the results. Moreover, the constant A, related to the effect of the ambient temperature, is affected by the fuel employed: interestingly, the result obtained is closer to the values obtained by Pickett et al. testing with *DR2* reference fuel [14] rather than to the result obtained by Benajes et al. using n-dodecane [13]. The similar characteristics of *DR2* fuel and the one employed in this work (commercial fuel, EU standard EN590) is probably the reason of this result. The results also remark the different effect of injection pressure and injector charge: increasing the injection pressure or the injection charge (λ) the mass flow rate increases as well. However, in the first case, the τ_{SSI} decreases ($b = -0.04$) while in the second τ_{SSI} increases ($d = 0.120$).

The regression related to x_{SSI} is characterized by a lower precision $R^2 = 90.2\%$ (Tab.6.2). This fact is probably linked to the criterion chosen for the x_{SSI} measurement: despite the method has been applied consistently to all the conditions

	Exp.	Conf. Int.
z	−3.10	−3.70/ − 2.50
a	−0.61	−0.74/ − 0.48
b	0.46	0.56/0.36
c	−0.4	−0.49/ − 0.31
d	−0.02	−0.18/0.14
R^2	90.2%	

Table 6.2: Exponents obtained from the regression to Eq. (6.2) to the experimental data.

tested, some lack of accuracy might have been introduced by the limited field of view or the hole-to-hole dispersion. However, the regression highlights clearly the parameters mostly affecting the variable studied.

	Exp.	Conf. Int.	Pickett et al. [14]	Benajes et al. [13]
z	−2.61	−3.76/ − 1.46	−3.74	−3.89
a	−1	−	−0.85	−1
b	0.43	0.29/0.55	1	0.54
c	−1.32	−1.49/ − 1.15	−1	−1
R^2	95.1%			

Table 6.3: Exponents obtained from the regression to Eq. (6.3) to the experimental data. The results obtained from dimensional analysis and from other authors are presented for reference.

The results related to the *LOL* (Tab.6.3) are slightly better in terms of precision of the fit ($R^2 = 95.1\%$). In this case, the limited number of tests represents an important drawback. However, the exponents obtained by the regression are in good agreement with the results found by Benajes et al. [13], in particular for the exponent b related to the effective velocity.

Finally, it is important to remind that, when testing with a multi-hole injector, some interaction of the sprays with the wall boundary layer should be expected. In fact, due to the wide included angle of the nozzle (156°), the separation by the chamber wall is gradual. As a consequence of that, some temperature inhomogeneity is expected in the air entrained, especially in the proximity of the nozzle, where the sprays are closer to the chamber wall. This fact might, in part, justify the small discrepancies with respect to the literature observed in the exponents concerning the ambient temperature and, therefore, the ambient density.

6.5   Hole-to-hole dispersion
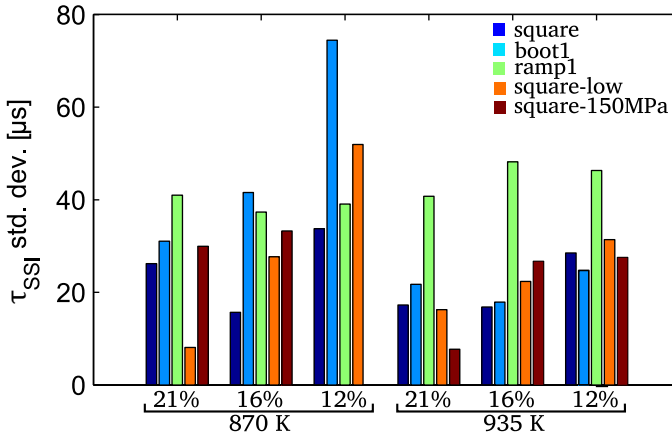
Figure 6.25: τ_{SSI} hole-to-hole dispersion measured at different conditions. $p_a = 5\,\text{MPa}$, $p_i = 60\,\text{MPa}$.
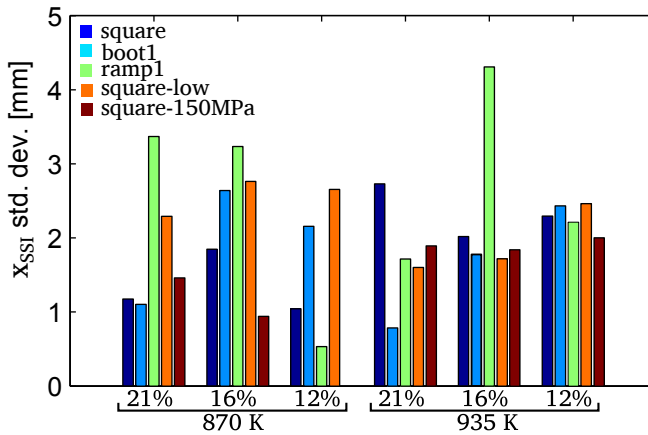
Figure 6.26: x_{SSI} hole-to-hole dispersion measured at different conditions. $p_a = 5\,\text{MPa}$, $p_i = 60\,\text{MPa}$.

In Ch.5 it has been demonstrated that at reduced needle lift the hole-to-hole dispersion is higher. The hole-to-hole dispersion of two combustion indicators (τ_{SSI} and x_{SSI}) was measured and the results are presented in figures 6.25 and 6.26. Comparing the *low* and the *high charge* cases, the same trend can be observed for the two parameters: at low charge, the hole-to-hole dispersion is higher.

The same can be said for *boot* and *ramp* shaped injections characterized by a higher dispersion than the square case. It is interesting to notice that the difference between *ramp* and square case is higher for the cases characterized by short ignition (high T_a and O_2%). In fact, in *ramp* injections, the needle throttles the flow only for a short period and, after that, the flow behaves as in the *high* charge case, compensating the initial dispersion. Differently, in *boot* injection, the needle throttles the flow for a longer period and, therefore, the increase in τ_{SSI} and x_{SSI} dispersion is observed to a greater extent at long ignition delay conditions (low T_a and O_2%). The results at reacting conditions are therefore consistent with the spray development results.

6.6   Soot production and flame temperature analysis

The 2-color optical pyrometry was employed to investigate the impact of the injection characteristics on the flame temperature and soot production [39, 40]. As was done for the *CH*/OH** chemiluminescence, the section begins with a general description of the results obtained (T_f and *KL 2D* maps) and continues with a qualitative comparison presenting the contour maps in order to highlight the effect of the boundary conditions. Finally, some characteristic parameters will be calculated to enable a global comparison of the results.

The *2C* is a powerful technique that offers a large amount of results with a relatively easy setup. However, as discussed by other authors, other tests should be performed to investigate the accuracy of the technique, in particular, when aiming to use the data provided for comparisons with *CFD* models [40, 41]. In this case, it was not possible to apply any other technique, to verify the results obtained. Therefore, considering the high number of works found in the literature supporting the effectiveness of this methodology [15, 40, 42–44], the results are trusted for a comparative extent, aiming at understanding the effect of test conditions on the measured variables. On the other hand, less attention should be paid to their quantitative meaning.

Finally, it has to be said that the results of these tests, in some cases, present features that are not ascribable to the physics of the process: this artifacts of the measurement will be pointed out during the presentation of the results putting the emphasis only on the results considered to be reliable.

6.6.1   Effect of ambient parameters

Fig.6.27 presents the *2D* maps obtained for flame temperature (T_f) and *KL* at different oxygen concentration. The comparison shows clearly that, a reduction in
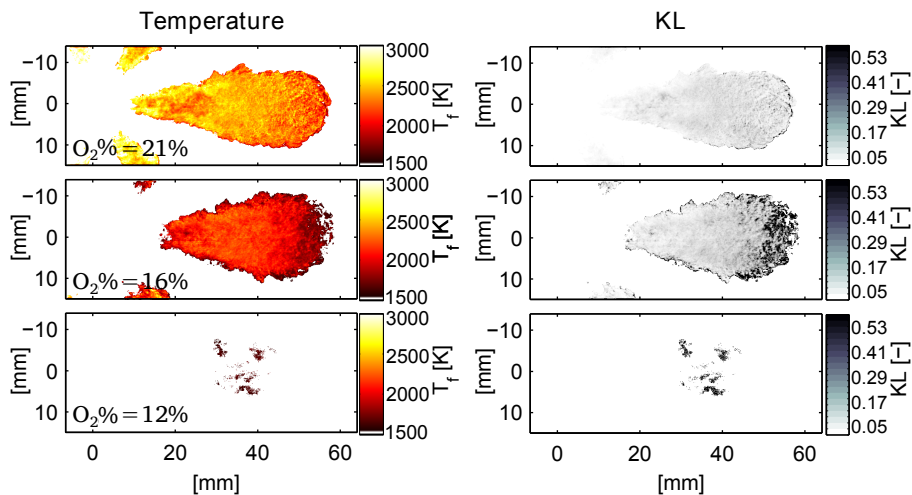
Figure 6.27: Effect of oxygen concentration. Flame temperature (left) and KL *2D maps at different ambient oxygen concentration.* $p_a = 5\,\mathrm{MPa}$, $T_a = 950\,\mathrm{K}$, $p_i = 60\,\mathrm{MPa}$, Ch = high.

the oxygen content (from 21 to 16% O_2%) produces a significant decrease in the flame temperature and an increase in *KL*. On the other hand, the low soot incandescence measured at O_2% = 12% is at the limit of the sensitivity of the cameras sensor: the related results are characterized by a very high spatial incoherence and, therefore, they are not considered reliable.

The decrease in flame temperature is related to simple combustion chemistry: the reduction in oxygen concentration implies an increase in the mass of the partial combustion products [37]. On the other hand the increase of *KL* observed need a more complex explanation. To this end, the equivalent ratio calculated through the *1DM* along the axial and radial direction of the spray is presented in Fig.6.29 for the two conditions. Even though the equivalent ratio at the *LOL* is similar in both cases (see Fig. 6.24) the oxidation process takes more time (or axial distance) at O_2 = 16% due to the lower oxygen content of the gas entrained. This fact results in the progressively higher *KL* measured along the axial direction Fig.6.29.

As discussed by Dec in [9], during the diffusive phase of the combustion, the soot is *contained* within the stoichiometric surface ($\Phi_{eq} = 1$). This means that the flame will penetrate into the chamber only until Φ_{eq} on the centerline is above 1. The fuel-air equivalence ratio calculated on the center-line by the *1DM* indicates that this limit is reached by the spray out of the field-of-view since at its limit
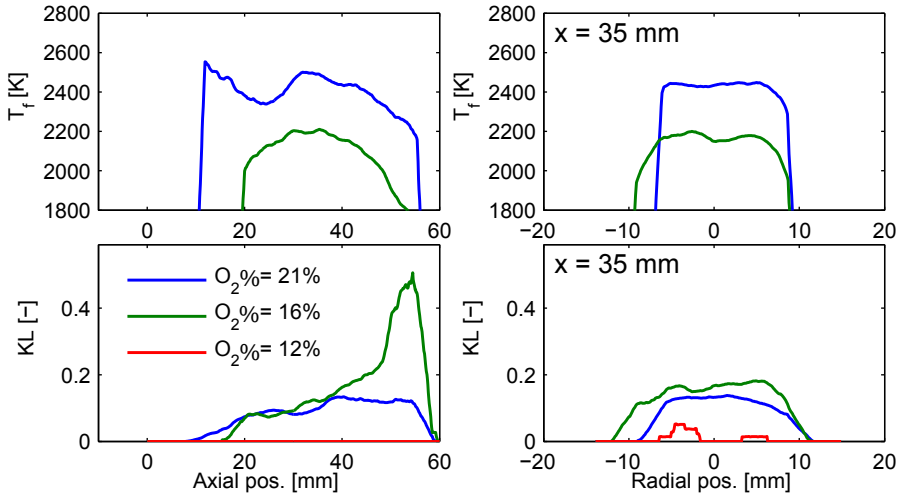
Figure 6.28: Effect of oxygen concentration. Spray axial (left) and radial (right) profiles of flame temperature and KL at different ambient oxygen concentration. $p_a = 5\,\text{MPa}$, $T_a = 950\,\text{K}$, $p_i = 60\,\text{MPa}$, Ch = high.
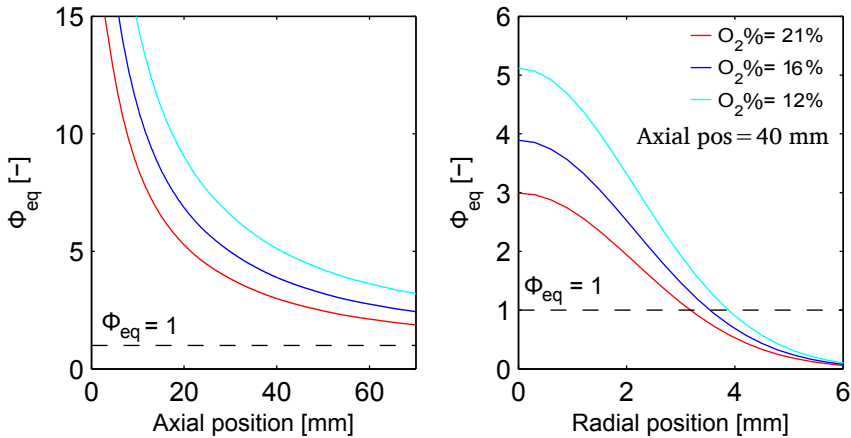
Figure 6.29: Spray axial and radial fuel-air equivalence ratio obtained from the 1DM for a steady spray at different oxygen concentrations . $p_a = 5\,\text{MPa}$, $p_i = 150\,\text{MPa}$, Ch = high.

(63 mm from the orifice) Φ_{eq} is well over 1. Consequently, this feature of the flame cannot be measured in the present experiments. Moreover, the *1DM* results indicate that a reduction in the gas oxygen content causes Φ_{eq} radial profile to be wider. This fact is observed experimentally by a lengthen of the flame (Fig. 6.29).
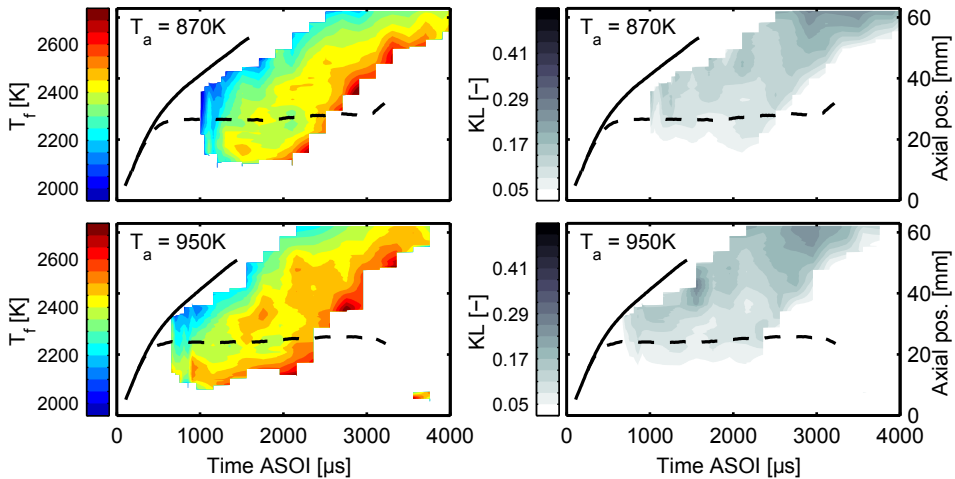
Figure 6.30: Effect of ambient temperature. Flame temperature (left) and KL *(right) at different T_a. The related liquid- and vapor-phase penetration are indicated respectively by the dashed and solid lines. $p_a = 5$ MPa, $O_2\% = 21\%$, $p_i = 60$ MPa, Ch = high.*

An increase in ambient temperature produces an increase in T_f and a slight increase in *KL*: this fact, hard to distinguish in the contour maps, can be observed in the axial profiles showed in Fig.6.29. As previously discussed, an increase in ambient temperature causes a reduction in the x_{SSI} and *LOL*, producing a higher Φ_{eq} in the premixed region of the flame. Coherently with what discussed by other authors [9, 36], this fact is reflected in a higher *KL* in the diffusive region of the flame.

The flame temperature results presented in the contour maps (Fig.6.30), as well as in the axial profiles (Fig.6.31), reveal a local minimum consistently appearing in the region of the liquid length. It is not clear if this might be considered or not an artifact of the measurement. On the one hand, the minimum observed could be considered as a consequence of the fuel evaporation: while there is liquid fuel, part of the heat produced by the combustion is employed for its evaporation. On the other, the liquid itself might absorb part of the soot radiation, altering the results. The same effect can be observed in the spray radial profile calculated at 25 mm, characterized by a minimum close to the flame axis.
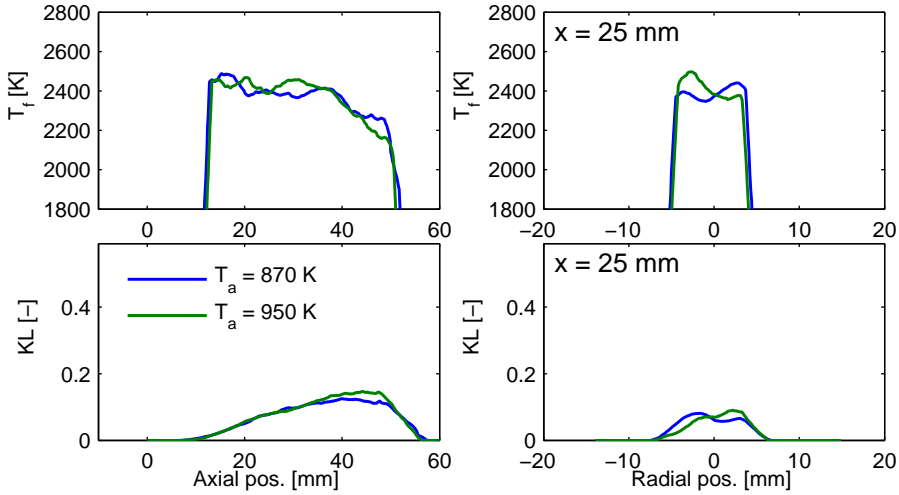
Figure 6.31: Effect of ambient temperature. Axial (left) and radial (right) profiles of flame temperature (top) and KL. $p_a = 5$ MPa, $O_2\% = 21\%$, $p_i = 60$ MPa, Ch = high.

It has also to be remarked, that non-physical features appears in the measurements. For example, the peaks in the *KL* spray radial profiles appearing close to the flame boundaries cannot be considered physical, since, being the flame approximately axis-symmetric, the *KL* at the borders should be lower than along the center-line [40]. Finally, the effect of the ambient temperature on T_f would be expected to increase progressively with the axial distance, since moving farther from the orifice, it increases the amount of air entrained. However, observing the T_f axial profile in Fig.6.31, this trend is not clear, underlining the lack in accuracy of the *2C* flame temperature measurement.

6.6.2 Effect of injection parameters

Despite the *2D* maps provide much information, also in this case it is preferred to describe the results through the contour maps, in order to present the transient evolution of the flame.
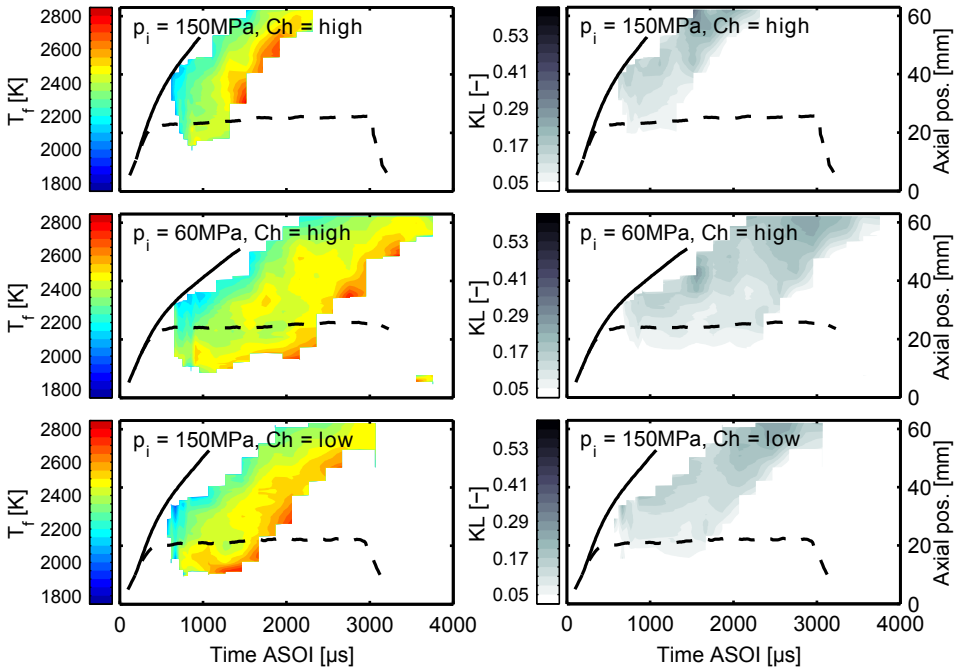
Figure 6.32: Effect of injection settings. Flame temperature (left) and KL (right) at different setting of the injection system. The related liquid and vapor phase penetration are indicated respectively by the dashed and solid lines. $O_2\% = 21\%$, $p_a = 5\,\mathrm{MPa}$, $T_a = 950\,\mathrm{K}$.

The effect of a variation in the injection settings is presented in figures 6.32 and 6.33. Reducing injection pressure or *Ch* the causes a substantial increase in the *KL*: this fact is coherent with the equivalence ratio at the lift-off length obtained by previous calculations. Decreasing either the injection pressure or *Ch*, the *LOL* is shorter and, therefore, Φ_{eq} is higher. However, no clear effect is observed in T_f. It is also interesting to note, that at $Ch = low$, having $LL \approx 20\,\mathrm{mm}$, the spray radial profile is flat, remarking the relation between flame temperature and liquid length mentioned before.

The impact of injection rate shape is presented on figures 6.34 and 6.35: a part of the modifications in the flame shape related to the spray development,
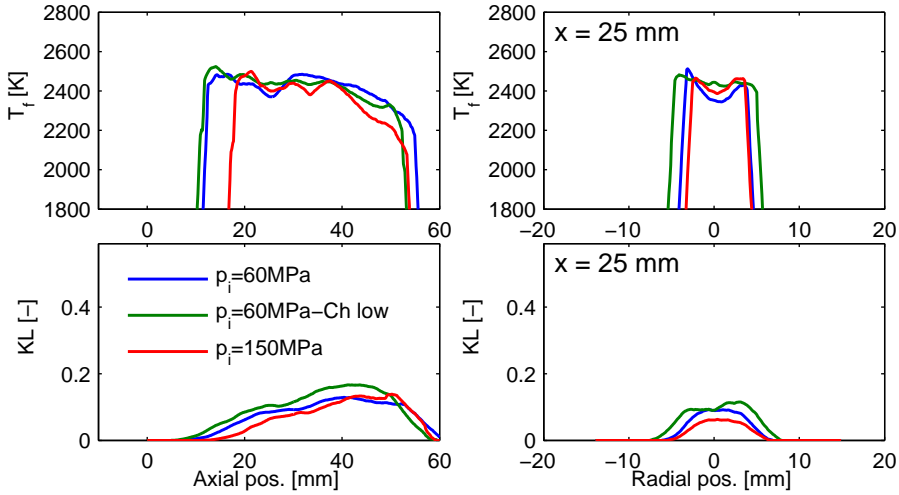
Figure 6.33: Effect of injection settings. Axial (left) and radial (right) profiles of flame temperature (top) and KL. $O_2\% = 21\%$, $p_a = 5\,\mathrm{MPa}$, $T_a = 950\,\mathrm{K}$.

the results appears difficult to understand. Consistently with what discussed previously, the shorter x_{SSI} (axial position of the ignition location) characterizing the *ramp* and boot injections at these conditions causes a higher Φ_{eq}. However the effect on the soot production is difficult to be observed on the axial profile. Moreover, during the *leg* stage, the *boot* injection is characterized by a very high flame temperature and very low soot production. This fact cannot be understood completely, either. However, two possible interpretations are given: i) the high fluctuations characterizing the flow at this stage of the injection could produce an air entrainment higher than the expectations (the calculation of Φ_{eq} presented earlier does not consider fluctuations in the mass flow rate) [32], resulting in a reduction of the Φ_{eq}. This fact could explain the differences in temperature and *KL* observed; ii) in this case the ignition is taking place very close to the nozzle: in this area the soot incandescence radiation, reflected by the background, could have a higher impact on the images and on the following calculations.
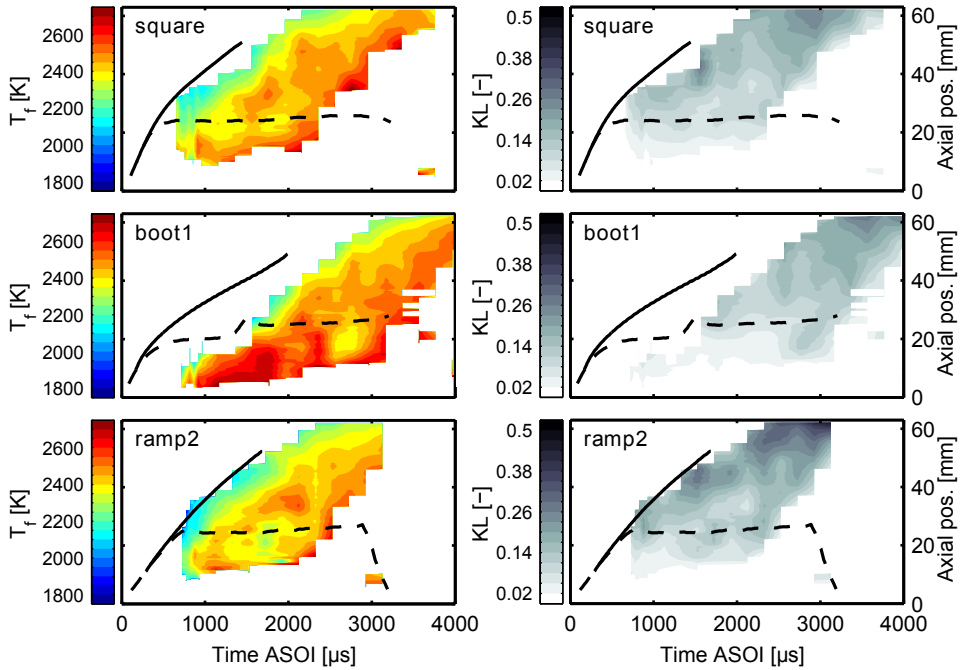
Figure 6.34: Effect of injection rate shape. Flame temperature (left) and KL (right) at different injection rate shape. The related liquid and vapor phase penetration are indicated respectively by the dashed and solid lines. $O_2\% = 21\%$, $T_a = 950\,\mathrm{K}$, $p_a = 5\,\mathrm{MPa}$, $p_i = 60\,\mathrm{MPa}$.
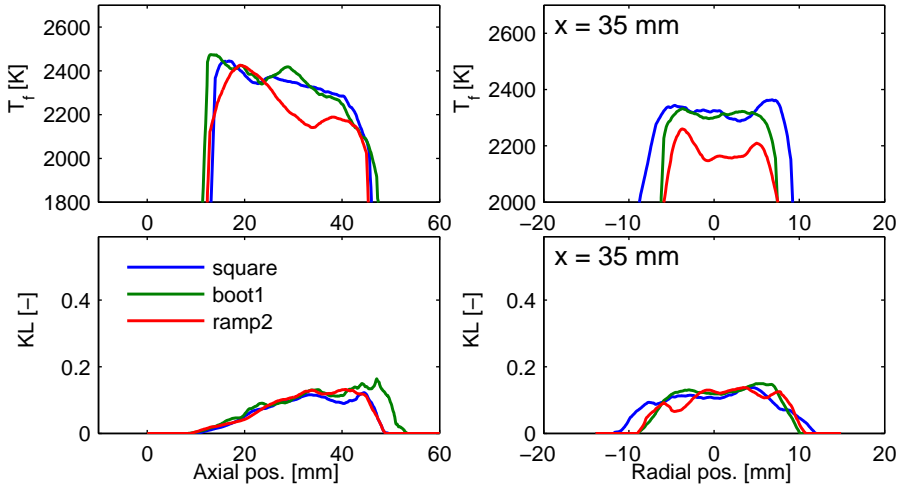
Figure 6.35: Effect of injection rate shape. Axial (left) and radial (right) profiles of flame temperature (top) and KL. *$O_2\% = 21\%$, $T_a = 950\,K$, $p_a = 5\,MPa$, $p_i = 60\,MPa$.*

With the aim of summarizing the results obtained by the *2C* method, a characteristic value for the *KL* and the flame temperature was extracted for each test condition. This value was obtained from the contour maps, calculating the median of the measurements obtained between 35 and 55 mm on the contour maps: in this region, the combustion is well developed for all the cases evaluated, being far enough from the lift-off length. This way, the parameter obtained allows consistent comparison among the different cases. Moreover, the artifacts at the border of the flame were not considered, excluding the data at less than 5 mm from the flame contours.

The results are presented in figures 6.36 and 6.37. Oxygen concentration and, to a lesser extent, ambient temperature are the main drivers for flame temperature. On the other hand, injection parameters have a secondary effect on the flame temperature. Similarly, a reduction in oxygen concentration causes a significant increase of *KL* while, when increasing ambient temperature, a slightly higher *KL* is measured. In this case, injection parameters have an important impact on *KL*: generally at lower injection pressure and charge the *KL* measured is higher as a consequence of the lower Φ_{eq} measured at the *LOL* [9]. However, the impact of the injection shape changes at different test conditions: generally, the use of *boot* or *ramp* injections cause an increase of *KL*. However, the impact of the *ramp* injection is more pronounced in the cases characterized by short τ_{SSI} ($O_2\% = 21\%$). On the other hand, the impact of the *boot* injection on *KL* increases

as much as τ_{SSI} becomes longer ($O_2\% = 16\%$, $T_a = 870\,\text{K}$). This fact is consistent with the lift-off length measured, and the average equivalence ratio obtained for the different conditions (c.f. Fig.6.24).
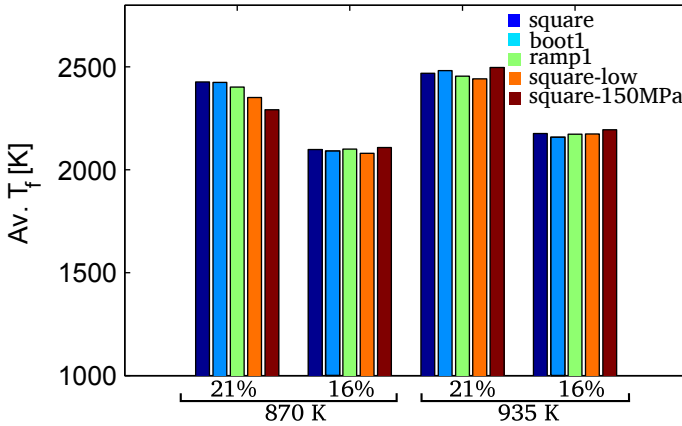
Figure 6.36: *Average T_f obtained at different conditions.* $p_a = 5\,\text{MPa}$, $p_i = 60\,\text{MPa}$.
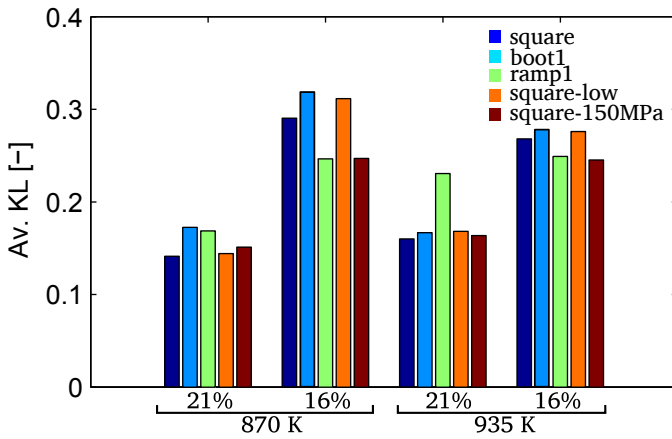
Figure 6.37: *Average KL obtained at different conditions.* $p_a = 5\,\text{MPa}$, $p_i = 60\,\text{MPa}$.

6.6.3 General comments about the *2C*

After the presentation of the results obtained by the *2C* method some conclusions should be drawn:

- the spread of the values obtained for *KL* as for T_f underlines the need of improving the test methodology. First of all the number of test repetitions should be increased, as well as the time resolution of the experiments.

- cameras with higher sensitivity could improve the accuracy of the results: the regions characterized by lower soot incandescence intensity go along with non physical features in the results. This would allow to explore more conditions characterized by lower soot incandescence intensity (i.e. low oxygen concentration) and to have a more accurate description of the first transient of the combustion;

- the *KL* results generally show good consistency with the other measurements and with the theoretical expectations;

- the interpretation of the flame temperature measurements is more complicated. In particular, in the view of real engine applications, the interest of knowing the flame temperature is related specifically to the premixed phase and region of the combustion. However, during the premixed phase of the combustion, the soot incandescence is still too weak and the related results could not be considered reliable. On the other hand, during the diffusive phase, the premixed region of the flame is hard to analyze. Also in this case, it is difficult to draw clear conclusions, since, due to the short injection duration the lift-off length stabilizes only during a limited period, and moreover, being this region very close to the upstream limit of the flame, artifacts are often appearing in the results;

- in order to have accurate measurements of the premixed phase and region of the combustion, specific studies should be performed to understand if there is any overlap with the chemiluminescence emissions. In fact, in this cases the soot emission is generally lower and, at the same time, the chemiluminescence emissions are intense. Even though the filters used (550 and 650 nm cwl) should exclude a wide part of the chemiluminescence contribution, a deeper understanding on this aspect should be reached.

References

[1] PASTOR, J., J. LÓPEZ, J. GARCÍA-OLIVER, and J. PASTOR. "A 1D model for the description of mixing-controlled inert diesel sprays". *Fuel* 87.13 (2008), pp. 2871–2885.

[2] DEC, J. and E. COY. *OH radical imaging in a DI diesel engine and the structure of the early diffusion flame*. Tech. rep. Sandia National Labs., Albuquerque, NM (United States), 1996.

[3] AGGARWAL, S. "A review of spray ignition phenomena: present status and future research". *Progress in Energy and Combustion Science* 24.6 (1998), pp. 565–600.

[4] PAYRI, R., F. SALVADOR, J. GIMENO, and J. DE LA MORENA. "Effects of nozzle geometry on direct injection diesel engine combustion process". *Applied Thermal Engineering* 29.10 (2009), pp. 2051–2060.

[5] LILLO, P., L. PICKETT, H. PERSSON, O. ANDERSSON, and S. KOOK. "Diesel Spray Ignition Detection and Spatial/Temporal Correction". *SAE International Journal of Engines* 5.3 (2012), pp. 1330–1346.

[6] BARDI, M. et al. "Engine Combustion Network: comparison of spray development, vaporization, and combustion in different combustion vessels". *Atomization and Sprays* 22.10 (2012), pp. 807–842.

[7] DEC, J. and C. ESPEY. "Chemiluminescence imaging of autoignition in a DI diesel engine". *SAE Paper* 982685 (1998).

[8] GAYDON, A. *The spectroscopy of flames*. Chapman & Hall London, 1957.

[9] DEC, J. *A conceptual model of DI diesel combustion based on laser-sheet imaging*. Society of Automotive Engineers Warrendale, PA, 1997.

[10] MACIAN, V., R. PAYRI, S. RUIZ, M. BARDI, and A. H. PLAZAS. "Experimental study of the relationship between injection rate shape and Diesel ignition using a novel piezo-actuated direct-acting injector". *Applied Energy* 118 (2014), pp. 100–113.

[11] NABER, J. and D. SIEBERS. "Effects of gas density and vaporization on penetration and dispersion of diesel sprays". *SAE Paper* 960034 (1996).

[12] SIEBERS, D. "Liquid-phase fuel penetration in Diesel sprays". *SAE transactions* 107.3 (1998), pp. 1205–1227.

[13] BENAJES, J., R. PAYRI, M. BARDI, and P. MARTI-ALDARAVI. "Experimental characterization of diesel ignition and lift-off length using a single-hole ECN injector". *Applied Thermal Engineering* 58.1-2 (2013), pp. 554–563.

[14]   PICKETT, L. M., D. L. SIEBERS, and C. A. IDICHERIA. "Relationship Between Ignition Processes and the Lift-Off Length of Diesel Fuel Jets". *SAE Paper* 2005-01-3843 (2005).

[15]   MANCARUSO, E. and B. M. VAGLIECO. "Optical investigation of the combustion behaviour inside the engine operating in HCCI mode and using alternative diesel fuel". *Experimental Thermal and Fluid Science* 34.3 (2010), pp. 346–351.

[16]   HIGGINS, B., D. SIEBERS, and A. ARADI. "Diesel-spray ignition and premixed-burn behavior". *SAE Paper* 2000-01-0940 (2000).

[17]   PAYRI, R., J. M. GARCÍA-OLIVER, M. BARDI, and J. MANIN. "Fuel temperature influence on diesel sprays in inert and reacting conditions". *Applied Thermal Engineering* 35 (2012), pp. 185–195.

[18]   DESANTES, J., R. PAYRI, F. SALVADOR, and A. GIL. "Development and validation of a theoretical model for diesel spray penetration". *Fuel* 85 (2006), pp. 910–917.

[19]   DOHLE, U., S. KAMPMANN, T. WINTRICH, and C. HINRICHSEN. "Advanced Diesel Common Rail Systems for Future Emission Legislation". *International Conference on Automotive Technologies-ICAT*. 2004, pp. 109–113.

[20]   DOBER, G. et al. "The impact of injection strategies on emissions reduction and power output of future diesel engines". *SAE Paper* 2008-01-0941 (2008).

[21]   MENDEZ, S. and B. THIROUARD. "Using multiple injection strategies in diesel combustion: potential to improve emissions, noise and fuel economy trade-off in low CR engines". *Technology* 2013 (2008), pp. 04–08.

[22]   ROLLBUSCH, C. "Effects of hydraulic nozzle flow rate and high injection pressure on mixture formation, combustion and emissions on a single-cylinder DI light-duty diesel engine". *International Journal of Engine Research* 13.4 (2012), pp. 323–339.

[23]   PAYRI, R., F. SALVADOR, J. GIMENO, and J. DE LA MORENA. "Influence of injector technology on injection and combustion development - Part 2: combustion analysis". *Applied Energy* 88.4 (2011), pp. 1130–1139.

[24]   VALENTINO, G., L. ALLOCCA, S. IANNUZZI, and A. MONTANARO. "Biodiesel/mineral diesel fuel mixtures: Spray evolution and engine performance and emissions characterization". *Energy* 36.6 (2011), pp. 3924–3932.

[25] KATSURA, N., M. SAITO, and J. SENDA. "Characteristics of a diesel spray impinging on a flat wall". *International Symposium COMODIA*. Vol. 90. 1990, pp. 193–198.

[26] BRUNEAUX, G. "Combustion structure of free and wall-impinging diesel jets by simultaneous laser-induced fluorescence of formaldehyde, poly-aromatic hydrocarbons, and hydroxides". *International Journal of Engine Research* 9.3 (2008), pp. 249–265.

[27] SIEBERS, D. L. and B. HIGGINS. "Flame lift-off on direct-injection diesel sprays under quiescent conditions". *SAE Paper* 2001-01-0530 (2001).

[28] HIGGINS, B. and D. SIEBERS. "Measurement of the flame lift-off location on DI diesel sprays using OH chemiluminescence". *SAE Paper* 2001-01-0918 (2001).

[29] KALGHATGI, G. T. "Lift-off heights and visible lengths of vertical turbulent jet diffusion flames in still air". *Combustion Science and Technology* 41.1-2 (1984).

[30] CHOMIAK, J. and A. KARLSSON. "Flame lift-off in diesel sprays". *Symposium (International) on Combustion* 26.2 (1996), pp. 2557–2564.

[31] PETERS, N. *Turbulent combustion*. Cambridge university press, 2000.

[32] MUSCULUS, M., T. LACHAUX, L. PICKETT, and C. IDICHERIA. "End-of-injection over-mixing and unburned hydrocarbon emissions in low-temperature-combustion diesel engines". *SAE Paper* 2007-01-0907 (2007).

[33] KOOK, S., L. PICKETT, and M. MUSCULUS. "Influence of diesel injection parameters on end-of-injection liquid length recession". *SAE International Journal of Engines* 2.1 (2009), pp. 1194–1210.

[34] PICKETT, L., S. KOOK, H. PERSSON, and O. ANDERSSON. "Diesel fuel jet lift-off stabilization in the presence of laser-induced plasma ignition". *Proceedings of the Combustion Institute* 32.2 (2009), pp. 2793–2800.

[35] SIEBERS, D. and B. HIGGINS. "Effects of injector conditions on the flame lift-off length of DI diesel spray". *Thermo-and fluid Dynamic Processes in Diesel Engines* (2000), pp. 253–277.

[36] GARCÍA, J. M. "Aportaciones al estudio del proceso de combustión turbulenta de chorros en motores diesel de inyección directa". PhD thesis. Valencia: E.T.S. Ingenieros Industriales. Universidad Politécnica de Valencia, 2004.

[37] DESANTES, J., J. PASTOR, J. GARCIA-OLIVER, and J. PASTOR. "A 1D model for the description of mixing-controlled reacting diesel sprays". *Combustion and Flame* 156.1 (2009), pp. 234–249.

[38] PISCHINGER, F., U. REUTER, and E. SCHEID. *Self ignition of diesel sprays and its dependence on fuel properties and injection parameters*. Tech. rep. American Society of Mechanical Engineers, New York, NY, 1988.

[39] MATSUI, Y., T. KAMIMOTO, and S. MATSUOKA. "A study on the time and space resolved measurement of flame temperature and soot concentration in a DI diesel engine by the two-color method". *SAE Paper* 790491 (1979).

[40] PAYRI, F., J. V. PASTOR, J. M. GARCÍA, and J. M. PASTOR. "Contribution to the application of two-colour imaging to diesel combustion". *Measurement Science and Technology* 18.8 (2007), p. 2579.

[41] MUSCULUS, M. P. B., S. SINGH, and R. D. REITZ. "Gradient effects on two-color soot optical pyrometry in a heavy-duty DI diesel engine". *Combustion and Flame* 153.100962 (2008), pp. 216–227.

[42] DISTASIO, S. and P. MASSOLI. "Influence of the soot property uncertainties in temperature and volume-fraction measurements by two-colour pyrometry". *Measurement Science and Technology* 5.12 (1994), p. 1453.

[43] MUSCULUS, M. P. B. "Measurements of the Influence of Soot Radiation on In-Cylinder Temperatures and Exhaust NOx in a Heavy-Duty DI Diesel Engine". *SAE Paper* 2005-01-0925 (2005).

[44] BARRO, C., F. TSCHANZ, P. OBRECHT, and K. BOULOUCHOS. "Influence of post-injection parameters on soot formation and oxidation in a common-rail-diesel engine using multi-colour-pyrometry". *ASME 2012 Internal Combustion Engine Division Fall Technical Conference ICEF*. 2012, pp. 23–26.

Chapter 7

Conclusions and future directions

7.1   Introduction

This chapter aims at drawing the main conclusions with respect to the work carried out along this thesis. The main goals reached in this investigation are presented relating the results obtained in the different phases of the investigation and putting them in a wider context.

The last section of this chapter proposes a list of the potential developments of the present work, indicating directions for new studies and possible improvements to the quality of the results presented in this thesis.

7.2   Summary and conclusions

The present thesis investigated the effect of the partial needle lift and injection rate shaping on the whole injection event. This work starts from the initial requirement by *General Motors* to characterize a novel injector prototype designed by Continental. This injector features the so called *direct-acting* system, where a piezo-actuator (stack) is mechanically coupled to the injector needle, having direct control on its position: this technological achievement enables a fast and precise control on the position of the needle and, therefore, on the fuel flow through the injector nozzle. In this way, without modifying the rail pressure, the fuel mass flow rate can be controlled, even in the short time scale of the injection event, enabling alternative injection rate profiles (*injection rate shaping*).

The nozzle internal flow, the fuel spray development and combustion have been investigated applying a wide range of experimental techniques:

- rate of injection and rate of momentum measurements for the characterization of the internal flow;

- Mie scattering at isothermal and evaporative conditions, diffused back-light illumination (*DBI*) and Schlieren technique to investigate the spray development and evaporation;

- radicals chemiluminescence imaging and 2-color optical pyrometry to investigate the sprays combustion.

All the imaging tests have been performed in a state-of-the-art high-pressure high-temperature facility, capable of reproducing the typical Diesel engine in-cylinder conditions, in a wide and optical accessible test chamber. The wide section of the chamber allows to study the injection event in free field-like conditions, avoiding the direct interaction between the spray plumes and the surrounding walls, which introduces higher uncertainties in the results.

The experiments performed in this thesis are the first to be carried out in the department using the high-temperature high-pressure facility. For this reason, different modifications were implemented to the test rig for the fulfillment of the experiments. In particular:

- the design of a system for the control of the injector temperature during the tests;

- the design and implementation of a new buffer system to improve the efficiency of the gas-flow movement within the test chamber;

- the development of a methodology for the temperature measurement within the test chamber;

- the design of a high temperature mirror, to be used within the chamber for the application of the double-pass Schlieren technique.

7.2.1   Injector capabilities

The internal flow characterization proved the capability of the injector of controlling the fuel flow by means of partial needle lift: controlling the electronic signal to the piezo-actuator (applied voltage), the injector is fully capable of throttling the fuel flow in steady and transient conditions and, therefore, it is capable to

perform injection rate shaping. The results obtained indicate a very fast and accurate response on a wide range of conditions, even when performing injection rate shaping.

The main findings about the injector behavior are listed below:

- in this injector design, the only force lifting the needle is produced by the piezo actuator deformation and to the leverage system acting directly on the needle. The fuel pressure, pushing the needle against the seat also persist during the injection. For this reason, to the contrary of traditional injectors, higher injection pressure causes longer hydraulic delays, and longer transients to reach the steady mass flow rate;

- the fuel mass flow rate through the nozzle, can be reduced by means of partial needle lift down to a minimum of $50 - 80\%$ of the mass flow rate obtained at maximum needle lift. Below this limit the injector behavior is unstable (very high shot-to-shot dispersion). The bottom limit mentioned above increases with the injection pressure, for the reasons explained in the previous point;

- at partial needle lift a higher shot-to-shot dispersion is measured, in terms of mass injected per cycle;

- at partial needle lift an important increase of the hole-to-hole dispersion is observed in terms of spray momentum, spray penetration, and liquid phase penetration.

7.2.2 Partial needle lift, fuel flow and spray development

All the tests performed indicate that the reduction in the mass flow rate obtained by reducing the needle lift has consequences on the internal flow and on the consequent spray development. In particular, reducing the needle lift the following effects have been observed:

- the effective area at the orifice outlet is reduced;

- the spray spreading angle is wider;

- both the previous effects concur in increasing the air-entrainment causing a reduction of the liquid length;

- transient fluctuations in the quantities measured (spreading angle and liquid-length). Moreover these fluctuations have been observed to be coherent in the different orifices;

- a deviation of the spray axis. This deviation could be observed on the plane containing the spray and the injector axis. It is probably related to high asymmetries of the flow in at the orifice entrance related to the acceleration of the fuel flow at the needle seat.

The previous observations indicate that partial needle lift causes significant modification of the fuel flow at the orifice inlet: the increase of the flow velocity produced at the needle seat, is propagated in the sac until the orifice inlet. The variation of the flow in this region are considered to be the cause of the reduction in the area coefficient and the deviation of the spray axis and probably of the spreading angle.

However, it is not excluded that cavitation takes place in the needle seat and the fuel vapor bubble are dragged until the nozzle orifice: this phenomenon would be consistent with all the previous observations including the transient fluctuations and the increase of the spreading angle.

Finally, the interaction between the needle and the cavitating flow, might cause the needle to vibrate with a consequent amplification of the previous effects.

From the engine point of view, the relationship between the needle lift, spreading angle and liquid length provides a new strategy to control the mixing process and to reduce the liquid fuel impingement on the piston bowl.

7.2.3   Injection rate profile and spray combustion

The increase in spreading angle measured at partial needle lift has only a secondary effect on the measured combustion parameters: however, a slight reduction in the ignition delay has been measured at low needle lift. This fact is consistent with the increase in spreading angle. A part of that, all the measured variables follow the normal trends generally described in the literature. The ignition delay increases at lower ambient temperature, ambient density and oxygen concentration while it decreases slightly at higher injection pressure. The lift-off length and the ignition location decrease with ambient temperature, ambient density and oxygen concentration and they increase with the fuel effective velocity at the orifice outlet. These dependencies have been investigated by performing statistical analysis and good agreement with other studies in the literature were found.

The introduction of non-conventional injection rate profiles (*boot* and *ramp*) has a significant impact on the premixed phase of the combustion (reducing the mass injected before the ignition and the peak in chemiluminescence intensity

related to this phase) and on the ignition location (reducing the distance from the nozzle of the fuel ignition). However, the extent of these effects changes depending on the ambient conditions: in particular, the impact of the *ramp* injection profile is more evident at conditions characterized by short ignition delay while the *boot* injection effect is similar at all the conditions tested. This fact is clearly linked to the rate of injection before the fuel ignition.

In this sense, the injection rate shaping confirms a great potential for the employment in real engines: the control on the premixed phase of combustion is fundamental for the reduction of engine noise and NO_x emissions.

On the other hand, the soot formation during the diffusive combustion, is related to the fuel-air equivalence ratio at the lift-off length: consistently with this fact the measurements performed remark that the *ramp* and *boot* injections, characterized by shorter lift-off length, present a higher soot formation (*KL*).

The results obtained underline the need of the correct selection of the shape of the injection profile in order to find the correct trade-off between soot production and NO_x/combustion noise.

Finally, the higher hole-to-hole dispersion measured at partial needle lift represents a limitation in the control of the combustion affecting also the results related to *boot* and *ramp* injections.

7.3 Future directions

The present thesis represents the first experimental investigation focused on the effect of partial needle lift and injection rate shaping using a direct acting injector. For this reason, a wide range of tests were performed evaluating several aspects of the injection event. Even though in many cases the injector behavior have been completely understood, certain features should be further investigated. Here below, a list of further studies is provided:

- study of the flow within the nozzle. Despite different hypothesis have been presented, a definitive conclusion about the processes taking place upstream of the orifice could not be drawn. The employment of X-ray diagnostics would allow the study of the flow within the nozzle revealing whether there is or not cavitation. Moreover, this technique would permit to determine the real position and the movements of the needle: the knowledge of the complete geometry in steady and transient conditions, would allow further studies by means of *CFD* simulations. A part of giving a better understanding of the flow in this specific nozzle, the results might be

extended to more general conclusions about the relationship between the geometry upstream of the orifice and spray characteristics;

- extension of the injection duration at reacting conditions. In general, the test at reacting conditions, are characterized by short injection duration, that prevent from measuring the parameters characteristics of a steady flame. In these tests, the maximum amount of fuel injected per cycle was limited by the mechanical resistance of the inner window of the chamber. A new design of these components could solve this problem, allowing a more accurate characterization of the combustion parameters.

- improve the 2-color optical pyrometry measurements. The results from 2-color optical pyrometry revealed weakness, in part due to the sensitivity of the cameras, in part to the low number of test repetitions performed. In particular, a specific objective of these new tests should be to assess the impact on the soot formation of an increase in the mass flow rate after the ignition. To this end the tests might be repeated with longer injection duration and higher time resolution with faster high speed cameras;

- investigation of the optimum injection rate shape. The combustion parameters presented in this work should be measured performing parametric variations of the injection rate shape, aiming at understanding which is the most suitable injection rate profile for each combination of ambient conditions.

- investigation of the injector behavior in a single cylinder engine. This study should attempt to transfer the knowledge about the injector capabilities acquired in the high-temperature high-pressure facility to a real engine, evaluating similarities and differences.

Bibliography

ADLER, D. and W. LYN. "The evaporation and mixing of a liquid fuel spray in a diesel air swirl". *Proceedings of the Institution of Mechanical Engineers, Conference Proceedings*. Vol. 184. 10. SAGE Publications. 1969, pp. 171–180, (*it appears in: Chap.3-[71]*).

AGGARWAL, S. "A review of spray ignition phenomena: present status and future research". *Progress in Energy and Combustion Science* 24.6 (1998), pp. 565–600, (*it appears in: Chap.3-[75], Chap.6-[212,220]*).

ALLOCCA, L., S. DABAGOV, D. HAMPAI, L. MARCHITTO, and S. ALFUSO. "Tomography of a GDI Spray by PolyCO Based X-Ray Technique". *SAE Paper* 2013-24-0040 (2013), (*it appears in: Chap.5-[171]*).

ALLOCCA, L., E. MANCARUSO, A. MONTANARO, and B. M. VAGLIECO. "Use of Mineral Diesel, First-, and Second-Generation Biodiesels in Modern Common Rail Injection Systems under Nonevaporative and Evaporative Conditions". *Atomization and Sprays* 22.2 (2012), (*it appears in: Chap.5-[195]*).

ALTIERI, L. and A. TONOLI. "Piezoelectric Injectors for Automotive Applications: Modeling and Experimental Validation of Hysteretic Behavior and Temperature Effects". *Journal of Dynamic Systems, Measurement, and Control* 135 (2013), pp. 011005–1, (*it appears in: Chap.2-[24]*).

ANEJA, R. and J. ABRAHAM. "How far does the liquid penetrate in a diesel engine: Computed results vs. measurements?" *Combustion Science and Technology* 138.1-6 (1998), pp. 233–255, (*it appears in: Chap.3-[67]*).

ARANEO, L. "Prediction of Diesel spray penetration with short injections in low density gas". *Proceedings of Conference on Thermo-and Fluid-Dynamic Processes in Diesel Engines, THIESEL, Spain*. 2004, (*it appears in: Chap.5-[169,177,186]*).

ARCOUMANIS, C., H. FLORA, M. GAVAISES, N. KAMPANIS, and R. HORROCKS. "Investigation of cavitation in a vertical multi-hole Diesel injector". *SAE Paper* 1999-01-0524 (1999), (*it appears in: Chap.3-[82]*).

ARCOUMANIS, C., J. WHITELAW, and K. WONG. *Gaseous simulation of diesel-type sprays in a motored engine*. Tech. rep. Warrendale, PA; Society of Automotive Engineers, 1989, (*it appears in: Chap.3-[56]*).

ARGUEYROLLES, B., S. DEHOUX, P. GASTALDI, L. GROSJEAN, et al. "Influence of injector nozzle design and cavitation on coking phenomenon". *Small* 2013 (2007), pp. 09–03, (*it appears in: Chap.3-[41]*).

ARREGLE, J. and J. V. PASTOR. "The influence of injection parameters on diesel spray characteristics". *SAE Paper* 1999-01-0200 (1999), (*it appears in: Chap.3-[70]*).

BADOCK, C., R. WIRTH, A. FATH, and A. LEIPERTZ. "Investigation of cavitation in real size diesel injection nozzles". *International Journal of Heat and Fluid Flow* 20.5 (1999), pp. 538–544, (*it appears in: Chap.3-[83]*).

BAE, C., J. YU, J. KANG, J. KONG, and K. O. LEE. "Effect of nozzle geometry on the common-rail diesel spray". *SAE Paper* 2002-01-1625 (2002), (*it appears in: Chap.3-[35]*).

BAERT, R., P. FRIJTERS, B. SOMERS, C. LUIJTEN, and W. DE BOER. "Design and operation of a high pressure, high temperature cell for HD diesel spray diagnostics: guidelines and results". *SAE Paper* 2009-01-0649 (2009), (*it appears in: Chap.1-[3,4], Chap.4-[102,109]*).

BARDI, M. et al. "Engine Combustion Network: comparison of spray development, vaporization, and combustion in different combustion vessels". *Atomization and Sprays* 22.10 (2012), pp. 807–842, (*it appears in: Chap.4-[137], Chap.6-[212,228]*).

BARRO, C., F. TSCHANZ, P. OBRECHT, and K. BOULOUCHOS. "Influence of post-injection parameters on soot formation and oxidation in a common-rail-diesel engine using multi-colour-pyrometry". *ASME 2012 Internal Combustion Engine Division Fall Technical Conference ICEF*. 2012, pp. 23–26, (*it appears in: Chap.6-[239]*).

BENAJES, J., J. PASTOR, R. PAYRI, and A. PLAZAS. "Analysis of the influence of diesel nozzle geometry in the injection rate characteristic". *Journal of fluids engineering* 126.1 (2004), pp. 63–71, (*it appears in: Chap.5-[158]*).

BENAJES, J., R. PAYRI, M. BARDI, and P. MARTI-ALDARAVI. "Experimental characterization of diesel ignition and lift-off length using a single-hole ECN injector". *Applied Thermal Engineering* 58.1-2 (2013), pp. 554–563, (*it appears in: Chap.3-[76], Chap.4-[137,139], Chap.6-[215,216,221,222,228,229,233,235,236,237]*).

BENAJES, J., R. PAYRI, S. MOLINA, and V. SOARE. "Investigation of the influence of injection rate shaping on the spray characteristics in a diesel common rail system equipped with a piston amplifier". *Journal of fluids engineering* 127.6 (2005), pp. 1102–1110, (*it appears in: Chap.2-[21], Chap.5-[173]*).

BERGWERK, W. "Flow pattern in diesel nozzle spray holes". *Proceedings of the Institution of Mechanical Engineers* 173.1 (1959), pp. 655–660, (*it appears in: Chap.3-[36,40]*).

BIANCHI, G. M., S. FALFARI, M. PAROTTO, and G. OSBAT. "Advanced modeling of common rail injector dynamics and comparison with experiments". *SAE transactions* 112.3 (2003), pp. 55–72, (*it appears in: Chap.3-[34]*).

BLESSING, M., G. KONIG, C. KRUGER, U. MICHELS, and V. SCHWARTZ. "Analysis of Flow and Cavitation Phenomena in Diesel Injection Nozzles and Its Effects on Spray and Mixture Formation". *SAE Paper* 2003-01-1358 (2003), (*it appears in: Chap.2-[21], Chap.3-[83,86]*).

BOEHNER, D. W. "Common rail injection system for commercial diesel vehicles" (1997), (*it appears in: Chap.2-[15]*).

BOGUE, D. "Entrance effects and prediction of turbulence in non-Newtonian flow". *Industrial & Engineering Chemistry* 51.7 (1959), pp. 874–878, (*it appears in: Chap.3-[36]*).

BORÉE, J., N. ATASSI, G. CHARNAY, and L. TAUBERT. "Measurements and image analysis of the turbulent field in an axisymmetric jet subject to a sudden velocity decrease". *Experimental thermal and fluid science* 14.1 (1997), pp. 45–51, (*it appears in: Chap.3-[59]*).

BOSCH, W. "Fuel Rate Indicator Is a New Measuring Instrument for Display of the Characteristics of Individual Injection". *SAE Paper* 660749 (1966), (*it appears in: Chap.4-[105]*).

BRACCO, F. *Modeling of engine sprays*. Tech. rep. Princeton Univ., NJ (USA). Dept. of Mechanical and Aerospace Engineering, 1985, (*it appears in: Chap.3-[67]*).

BRUNEAUX, G. "Combustion structure of free and wall-impinging diesel jets by simultaneous laser-induced fluorescence of formaldehyde, poly-aromatic hydrocarbons, and hydroxides". *International Journal of Engine Research* 9.3 (2008), pp. 249–265, (*it appears in: Chap.6-[224]*).

BRUNEAUX, G. "Liquid and vapor spray structure in high-pressure common rail diesel injection". *Atomization and Sprays* 11.5 (2001), (*it appears in: Chap.3-[50]*).

BRUNEAUX, G. "Development of optical diagnostic techniques to correlate mixing and auto-ignition processes in high pressure Diesel jets". *Oil and Gas Science and Technology-Revue de l'IFP* 63.4 (2008), pp. 461–477, (*it appears in: Chap.2-[12], Chap.3-[75], Chap.5-[167]*).

BUCKINGHAM, E. "Model experiments and the form of empirical equations." *Trans. ASME*. 1915, (*it appears in: Chap.3-[54]*).

CAO, Z.-M., K. NISHINO, S. MIZUNO, and K. TORII. "PIV measurement of internal structure of diesel fuel spray". *Experiments in fluids* 29.1 (2000), S211–S219, (*it appears in: Chap.3-[71]*).

CHARLES B. BRIGHT, J. C. G. "Very high speed rate shaping fuel injector". US7255290 B2. 2007, (*it appears in: Chap.1-[3]*).

CHAVES, H., M. KNAPP, A. KUBITZEK, and F. OBERMEIER. "Experimental study of cavitation in the nozzle hole of diesel injectors using transparent nozzles". *SAE Paper* 950290 (1995), (*it appears in: Chap.5-[162]*).

CHEHROUDI, B., S. CHEN, F. BRACCO, and Y. ONUMA. *On the intact core of full-cone sprays*. Tech. rep. Instrument Society of America, Research Triangle Park, NC, 1985, (*it appears in: Chap.3-[67]*).

CHIAVOLA, O. and F. PALMIERI. "Modeling needle motion influence on nozzle flow in high pressure injection system". *SAE Paper* 2007-01-0250 (2007), (*it appears in: Chap.3-[84,85], Chap.5-[179]*).

CHOMIAK, J. and A. KARLSSON. "Flame lift-off in diesel sprays". *Symposium (International) on Combustion* 26.2 (1996), pp. 2557–2564, (*it appears in: Chap.6-[229]*).

CMT-motores termicos web-page. last access 15/02/2014. URL: http://www.cmt.upv.es/, (*it appears in: Chap.1-[4]*).

COLEBROOK, C. F. "Turbulent Flow in Pipes, with particular reference to the Transition Region between the Smooth and Rough Pipe Laws." *Journal of the ICE* 11.4 (1939), pp. 133–156, (*it appears in: Chap.3-[34,36]*).

COPPO, M., C. DONGIOVANNI, and C. NEGRI. "Numerical analysis and experimental investigation of a common rail-type diesel injector". *Journal of engineering for gas turbines and power* 126.4 (2004), pp. 874–885, (*it appears in: Chap.3-[35]*).

Correas, D. "Estudio teórico-experimental del chorro libre diesel isotermo". PhD thesis. Tesis doctoral, Depto. de Máquinas y Motores Térmicos, Universidad Politécnica de Valencia, España, 1998, (*it appears in: Chap.3-[61,63,71]*).

De la Morena, J. "Estudio de la influencia de las características del flujo interno en toberas sobre el proceso de inyección Diesel en campo próximo". PhD thesis. Universidad Politécnica de Valencia, 2011, (*it appears in: Chap.3-[68], Chap.5-[182]*).

Dec, E. J. "Advanced compression-ignition engines-understanding the in-cylinder processes". *Proceedings of the Combustion Institute* 32.2 (2009), pp. 2727–2742, (*it appears in: Chap.2-[13]*).

Dec, J. E. and R. E. Canaan. "PLIF Imaging of NO Formation in a DI Diesel Engine1". *SAE Paper* 980147 (1998), (*it appears in: Chap.3-[77]*).

Dec, J. *A conceptual model of DI diesel combustion based on laser-sheet imaging*. Society of Automotive Engineers Warrendale, PA, 1997, (*it appears in: Chap.1-[1], Chap.3-[76,77,78], Chap.4-[132], Chap.6-[212,220,222,234,240,242,247]*).

Dec, J. and E. Coy. *OH radical imaging in a DI diesel engine and the structure of the early diffusion flame*. Tech. rep. Sandia National Labs., Albuquerque, NM (United States), 1996, (*it appears in: Chap.3-[77,79,80], Chap.4-[132], Chap.6-[212]*).

Dec, J. and C. Espey. "Chemiluminescence imaging of autoignition in a DI diesel engine". *SAE Paper* 982685 (1998), (*it appears in: Chap.3-[72,74], Chap.4-[131], Chap.6-[212,222]*).

Delacourt, E., B. Desmet, and B. Besson. "Characterisation of very high pressure diesel sprays using digital imaging techniques". *Fuel* 84.7 (2005), pp. 859–867, (*it appears in: Chap.3-[65]*).

Delphi. *Direct acting light-duty diesel CR system*. Tech. rep. Delphi Automotive, 2008, (*it appears in: Chap.2-[22,23]*).

Dent, J. *A basis for the comparison of various experimental methods for studying spray penetration*. Society of Automotive Engineers, 1971, (*it appears in: Chap.3-[63], Chap.5-[203]*).

Desantes, J., J. Pastor, J. Garcia-Oliver, and J. Pastor. "A 1D model for the description of mixing-controlled reacting diesel sprays". *Combustion and Flame* 156.1 (2009), pp. 234–249, (*it appears in: Chap.3-[58,61,76], Chap.6-[234,240]*).

DESANTES, J., J. PASTOR, R. PAYRI, and J. PASTOR. "Experimental characterization of internal nozzle flow and diesel spray behavior. part II: Evaporative conditions". *Atomization and sprays* 15.5 (2005), pp. 517–543, (*it appears in: Chap.3-[65,67], Chap.5-[169,186,187,202]*).

DESANTES, J., R. PAYRI, J. GARCIA, and F. SALVADOR. "A contribution to the understanding of isothermal diesel spray dynamics". *Fuel* 86.7 (2007), pp. 1093–1101, (*it appears in: Chap.3-[71], Chap.5-[182]*).

DESANTES, J., R. PAYRI, F. SALVADOR, and J. DE LA MORENA. "Influence of cavitation phenomenon on primary break-up and spray behavior at stationary conditions". *Fuel* 89.10 (2010), pp. 3033–3041, (*it appears in: Chap.5-[203]*).

DESANTES, J., R. PAYRI, F. SALVADOR, and A. GIL. "Development and validation of a theoretical model for diesel spray penetration". *Fuel* 85 (2006), pp. 910–917, (*it appears in: Chap.3-[71], Chap.4-[126], Chap.5-[169,171], Chap.6-[217]*).

DESANTES, J. M., J. J. LOPEZ, J. M. GARCIA, and J. M. PASTOR. "Evaporative diesel spray modeling". *Atomization and Sprays* 17.3 (2007), (*it appears in: Chap.3-[58]*).

DESANTES, J. M., J. J. LOPEZ, J. M. GARCIA, and J. M. PASTOR. "Evaporative diesel spray modeling". *Atomization and Sprays* 17.3 (2007), (*it appears in: Chap.1-[2]*).

DIGIORGIO, F., D. LAFORGIA, and V. DAMIANI. "Investigation on drop size distribution in the spray of a five-hole vco nozzle at high feeding pressure". *SAE transactions* 104.3 (1995), pp. 205–219, (*it appears in: Chap.3-[70]*).

DISTASIO, S. and P. MASSOLI. "Influence of the soot property uncertainties in temperature and volume-fraction measurements by two-colour pyrometry". *Measurement Science and Technology* 5.12 (1994), p. 1453, (*it appears in: Chap.4-[141,142], Chap.6-[239]*).

DOBER, G. et al. "The impact of injection strategies on emissions reduction and power output of future diesel engines". *SAE Paper* 2008-01-0941 (2008), (*it appears in: Chap.1-[2], Chap.2-[20], Chap.6-[219]*).

DOHLE, U., S. KAMPMANN, T. WINTRICH, and C. HINRICHSEN. "Advanced Diesel Common Rail Systems for Future Emission Legislation". *International Conference on Automotive Technologies-ICAT*. 2004, pp. 109–113, (*it appears in: Chap.2-[14,20,21], Chap.5-[173], Chap.6-[219,224]*).

Engine Combustion Network web-page. last access 15/02/2014. URL: http://www.sandia.gov/ecn/, (*it appears in: Chap.1-[2]*).

ESPEY, C., J. E. DEC, T. A. LITZINGER, and D. A. SANTAVICCA. "Planar laser Rayleigh scattering for quantitative vapor-fuel imaging in a diesel jet". *Combustion and Flame* 109.1 (1997), pp. 65–86, (*it appears in: Chap.3-[71,80]*).

European Parliament and the Council of the European Union, Regulation (EC) No 595/2009. June 2009, (*it appears in: Chap.1-[1]*).

FAETH, G. "Evaporation and combustion of sprays". *Progress in Energy and Combustion Science* 9.1 (1983), pp. 1–76, (*it appears in: Chap.3-[56,59]*).

FAVENNEC, A.-G. and D. FRUMAN. "Effect of the needle position on the cavitation of Diesel injectors". *Proceedings of the 3rd ASME-JSME Joint Fluids engineering conference* FEDSM99-7044 (1999), (*it appears in: Chap.3-[82]*).

FERRARI, A. and A. MITTICA. "FEM modeling of the piezoelectric driving system in the design of direct-acting diesel injectors". *Applied Energy* 99 (2012), pp. 471–483, (*it appears in: Chap.1-[3], Chap.2-[24], Chap.5-[155,157]*).

FLAIG, U., W. POLACH, and G. ZIEGLER. "Common Rail System (CR-System) for passenger car DI diesel engines; Experiences with applications for series production projects". *SAE Paper* 1999-01-0191 (1999), (*it appears in: Chap.2-[14]*).

FLYNN, P. F. et al. "Diesel combustion: an integrated view combining laser diagnostics, chemical kinetics, and empirical validation" (1999), (*it appears in: Chap.1-[1], Chap.3-[30,76,78,79]*).

FORSTALL, W. and A. SHAPIRO. "Momentum and mass transfer in coaxial gas jets". *J. Appl. Mech.* 72 (1950), pp. 399–408, (*it appears in: Chap.3-[63]*).

FUSTER, D. et al. "Simulation of primary atomization with an octree adaptive mesh refinement and VOF method". *International Journal of Multiphase Flow* 35.6 (2009), pp. 550–565, (*it appears in: Chap.3-[67]*).

GARCÍA, J. M. "Aportaciones al estudio del proceso de combustión turbulenta de chorros en motores diesel de inyección directa". PhD thesis. Valencia: E.T.S. Ingenieros Industriales. Universidad Politécnica de Valencia, 2004, (*it appears in: Chap.1-[1,4], Chap.2-[12,13], Chap.3-[57], Chap.4-[102], Chap.6-[234,242]*).

GAVAISES, M., A. ANDRIOTIS, D. PAPOULIAS, N. MITROGLOU, and A. THEODOR-AKAKOS. "Characterization of string cavitation in large-scale Diesel nozzles with tapered holes". *Physics of fluids* 21 (2009), p. 052107, (*it appears in: Chap.3-[35]*).

GAYDON, A. *The spectroscopy of flames*. Chapman & Hall London, 1957, (*it appears in: Chap.3-[74], Chap.4-[131,132,134], Chap.6-[212]*).

GHANDHI, J. B. and D. M. HEIM. "An optimized optical system for backlit imaging". *Review of Scientific Instruments* 80.5 (2009), pages, (*it appears in: Chap.4-[130,131]*).

GIMENO, J. "Desarrollo y aplicación de la medida de flujo de cantidad de movimiento de un chorro Diesel". PhD thesis. E.T.S. Ingenieros Industriales. Universidad Politécnica de Valencia, 2008, (*it appears in: Chap.1-[1,4], Chap.2-[18], Chap.3-[42,43,44,45,46,48], Chap.4-[101,107], Chap.5-[160,202]*).

GLASSEY, S. and A. STOCKNER. "HEUI-A new direction for diesel engine fuel systems" (1993), (*it appears in: Chap.2-[21,22]*).

GRANT, R. P. and S. MIDDLEMAN. "Newtonian jet stability". *AIChE Journal* 12.4 (1966), pp. 669–678, (*it appears in: Chap.3-[52,53]*).

GRAVESEN, P., J. BRANEBJERG, and O. S. JENSEN. "Microfluidics-a review". *Journal of Micromechanics and Microengineering* 3.4 (1993), p. 168, (*it appears in: Chap.3-[39]*).

GUIDE, O. U. "Version 16". *Chicago, IL: SPSS Inc* (1990), (*it appears in: Chap.3-[84]*).

GUILDENBECHER, D., C. LÓPEZ-RIVERA, and P. SOJKA. "Secondary atomization". English. *Experiments in Fluids* 46.3 (2009), pp. 371–402, (*it appears in: Chap.3-[55]*).

HAN, J. and G. TRYGGVASON. "Secondary breakup of axisymmetric liquid drops. I. Acceleration by a constant body force". *Physics of fluids* 11 (1999), p. 3650, (*it appears in: Chap.3-[55]*).

HAY, N. and P. JONES. *Comparison of the various correlations for spray penetration*. Society of Automotive Engineers, 1972, (*it appears in: Chap.3-[63]*).

HEILIG, A., M. KAISER, and F. DINKELACKER. "Near Nozzle High-Speed Measurements of the Intact Core for Diesel Spray". *ICLASS* (2012), (*it appears in: Chap.3-[68]*).

HERNÁNDEZ, J., J. SANZ-ARGENT, J. CAROT, and J. JABALOYES. "Ignition delay time correlations for a diesel fuel with application to engine combustion modelling". *International Journal of Engine Research* 11.3 (2010), pp. 199–206, (*it appears in: Chap.3-[75]*).

HERNÁNDEZ, J., J. SANZ-ARGENT, J. CAROT, and J. JABALOYES. "Modelling of the auto-ignition angle in diesel HCCI engines through D-optimal design". *Fuel* 89.9 (2010), pp. 2561–2568, (*it appears in: Chap.1-[2]*).

HEYWOOD, J. "Internal combustion engine fundamentals". *Mc Graw Hill, Inc. -* (1998), pages, (*it appears in: Chap.1-[1], Chap.2-[11]*).

HEYWOOD, J. B. and O. Z. WELLING. "Trends in performance characteristics of modern automobile SI and diesel engines". *SAE International Journal of Engines* 2.1 (2009), pp. 1650–1662, (*it appears in: Chap.3-[29]*).

HIGGINS, B., D. SIEBERS, and A. ARADI. "Diesel-spray ignition and premixed-burn behavior". *SAE Paper* 2000-01-0940 (2000), (*it appears in: Chap.3-[72,73,74,75], Chap.6-[216,221]*).

HIGGINS, B. and D. SIEBERS. "Measurement of the flame lift-off location on DI diesel sprays using OH chemiluminescence". *SAE Paper* 2001-01-0918 (2001), (*it appears in: Chap.3-[76], Chap.4-[134,138], Chap.6-[228]*).

HIROYASU, H. "Experimental and theoretical studies on the structure of fuel sprays in diesel engines". *ICLASS-91, Gaithersburg, USA* (1991), pp. 17–31, (*it appears in: Chap.3-[56], Chap.5-[173,200,201]*).

HIROYASU, H. and M. ARAI. "Structures of fuel sprays in diesel engines". *SAE transactions* 99.3 (1990), pp. 1050–1061, (*it appears in: Chap.3-[61,63,65,86]*).

HIROYASU, H., M. ARAI, and M. TABATA. "Empirical equations for the Sauter mean diameter of a Diesel spray". *SAE Paper* 890464 (1989), (*it appears in: Chap.3-[70]*).

HUESTIS, E., P. A. ERICKSON, and M. P. MUSCULUS. "In-cylinder and exhaust soot in low-temperature combustion using a wide-range of EGR in a heavy-duty diesel engine". *Training* 2013 (2007), pp. 12–05, (*it appears in: Chap.4-[139]*).

HUNTER, W. G. and J. S. HUNTER. "Statistics for experimenters". *Interscience, New York* (1978), (*it appears in: Chap.5-[200,203]*).

HURN, R. and K. HUGHES. "Combustion characteristics of diesel fuels as measured in a constant-volume bomb". *SAE transactions* 6 (1952), pp. 24–35, (*it appears in: Chap.3-[72]*).

INCROPERA, F. P., A. S. LAVINE, and D. P. DEWITT. *Fundamentals of heat and mass transfer*. John Wiley & Sons Incorporated, 2011, (*it appears in: Chap.4-[116]*).

IYER, V., J. ABRAHAM, and V. MAGI. "Exploring injected droplet size effects on steady liquid penetration in a Diesel spray with a two-fluid model". *International Journal of Heat and Mass Transfer* 45.3 (2002), pp. 519–531, (*it appears in: Chap.3-[56]*).

JICHA, M., J. JEDELSKY, J. OTAHAL, and J. SLAMA. "Influence of some geometrical parameters on the characteristics of effervescent atomization". *ILASS Europe* (2002), (*it appears in: Chap.3-[69]*).

JOHNSON, J. E. et al. "Characteristics of 3000 bar Diesel Spray Injection under Non-Vaporizing and Vaporizing Conditions". *ICLASS* (2012), (*it appears in: Chap.2-[16]*).

JOHNSON, T. V. "Review of diesel emissions and control". *International Journal of Engine Research* 10.5 (2009), pp. 275–285, (*it appears in: Chap.1-[1], Chap.3-[29]*).

JUNEJA, H., Y. RA, and R. REITZ. "Optimization of injection rate shape using active control of fuel injection". *SAE Paper* 2004-01-0530 (2004), (*it appears in: Chap.1-[3], Chap.3-[87]*).

KALGHATGI, G. T. "Lift-off heights and visible lengths of vertical turbulent jet diffusion flames in still air". *Combustion Science and Technology* 41.1-2 (1984), (*it appears in: Chap.3-[79], Chap.6-[229]*).

KAMIMOTO, T., H. YOKOTA, and H. KOBAYASHI. *Effect of high pressure injection on soot formation processes in a rapid compression machine to simulate diesel flames*. Tech. rep. Society of Automotive Engineers, Warrendale, PA, 1987, (*it appears in: Chap.3-[72]*).

KAMPMANN, S., B. DITTUS, P. MATTES, and M. KIRNER. "The influence of hydro grinding at VCO nozzles on the mixture preparation in a DI diesel engine". *SAE transactions* 105.3 (1996), pp. 1329–1339, (*it appears in: Chap.3-[66]*).

KASTENGREN, A. L., F. Z. TILOCCO, and C. F. POWELL. "Initial Evaluation of Engine Combustion Network Injectors with X-Ray Diagnostics". *ILASS Americas* 2011-101 (2011), (*it appears in: Chap.5-[180]*).

KASTENGREN, A. L. et al. "Engine Combustion Network (ECN): measurements of nozzle geometry and hydraulic behavior". *Atomization and Sprays* 22.12 (2012), pp. 1011–1052, (*it appears in: Chap.5-[179,187,198]*).

KASTENGREN, A. and C. POWELL. "Spray density measurements using X-ray radiography". *Proceedings of the Institution of Mechanical Engineers, Part D: Journal of Automobile Engineering* 221.6 (2007), pp. 653–662, (*it appears in: Chap.3-[49]*).

KASTNER, O., F. ATZLER, C. JUVENELLE, R. ROTONDI, and A. WEIGAND. "Directly actuated piezo injector for advanced injection strategies towards cleaner diesel engines". *7th Int. symposium towards cleaner diesel engine TDCE*. 2009, (*it appears in: Chap.1-[3]*).

KATSURA, N., M. SAITO, and J. SENDA. "Characteristics of a diesel spray impinging on a flat wall". *International Symposium COMODIA*. Vol. 90. 1990, pp. 193–198, (*it appears in: Chap.6-[224]*).

KOBORI, S., T. KAMIMOTO, and A. ARADI. "A study of ignition delay of diesel fuel sprays". *International Journal of Engine Research* 1.1 (2000), pp. 29–39, (*it appears in: Chap.3-[75]*).

KOOK, S., L. PICKETT, and M. MUSCULUS. "Influence of diesel injection parameters on end-of-injection liquid length recession". *SAE International Journal of Engines* 2.1 (2009), pp. 1194–1210, (*it appears in: Chap.6-[229]*).

KOSAKA, H. et al. "Simultaneous 2-D imaging of OH radicals and soot in a diesel flame by laser sheet techniques". *SAE Paper* 960834 (1996), (*it appears in: Chap.3-[79]*).

KRISTENSSON, E. et al. "Analysis of multiple scattering suppression using structured laser illumination planar imaging in scattering and fluorescing media". *Opt. Express* 19 (2011), pp. 13647–13663, (*it appears in: Chap.3-[69]*).

LAPUERTA, M., O. ARMAS, J. J. HERNÁNDEZ, and A. TSOLAKIS. "Potential for reducing emissions in a diesel engine by fuelling with conventional biodiesel and Fischer–Tropsch diesel". *Fuel* 89.10 (2010), pp. 3106–3113, (*it appears in: Chap.1-[2]*).

LARSSON, A. "Optical studies in a DI diesel engine". *SAE transactions* 108.4 (1999), pp. 2137–2155, (*it appears in: Chap.3-[80]*).

LEBAS, R., T. MENARD, P. BEAU, A. BERLEMONT, and F.-X. DEMOULIN. "Numerical simulation of primary break-up and atomization: DNS and modelling study". *International Journal of Multiphase Flow* 35.3 (2009), pp. 247–260, (*it appears in: Chap.3-[67]*).

LEE, J. et al. "Effect of piezo-driven and solenoid-driven needle opening of common-rail diesel injectors on internal nozzle flow and spray development". *International Journal of Engine Research* 7.6 (2006), pp. 489–502, (*it appears in: Chap.2-[18], Chap.3-[84]*).

LICHTAROWICZ, A., R. DUGGINS, and E. MARKLAND. "Discharge coefficients for incompressible non-cavitating flow through long orifices". *Journal of Mechanical Engineering Science* 7.2 (1965), pp. 210–219, (*it appears in: Chap.3-[41]*).

LILLO, P, L. PICKETT, H. PERSSON, O. ANDERSSON, and S. KOOK. "Diesel Spray Ignition Detection and Spatial/Temporal Correction". *SAE International Journal of Engines* 5.3 (2012), pp. 1330–1346, (*it appears in: Chap.3-[72], Chap.4-[137,138], Chap.6-[212]*).

LIN, S. and R. REITZ. "Drop and spray formation from a liquid jet". *Annual Review of Fluid Mechanics* 30.1 (1998), pp. 85–105, (*it appears in: Chap.3-[30]*).

LINNE, M. "Imaging in the optically dense regions of a spray: A review of developing techniques". *Progress in Energy and Combustion Science* 39.5 (2013), pp. 403–440, (*it appears in: Chap.1-[1,2], Chap.3-[49]*).

LINNE, M., M. PACIARONI, T. HALL, and T. PARKER. "Ballistic imaging of the near field in a diesel spray". *Experiments in fluids* 40.6 (2006), pp. 836–846, (*it appears in: Chap.3-[49,50]*).

MACIÁN, V., V. BERMÚDEZ, R. PAYRI, and J. GIMENO. "New technique for determination of internal geometry of a diesel nozzle with the use of silicone methodology". *Experimental techniques* 27.2 (2003), pp. 39–43, (*it appears in: Chap.3-[42]*).

MACIAN, V, R. PAYRI, A. GARCIA, and M. BARDI. "Experimental Evaluation of the Best Approach for Diesel Spray Images Segmentation". *Experimental Techniques* 36.6 (2012), pp. 26–34, (*it appears in: Chap.3-[66], Chap.4-[121,123], Chap.5-[168,196]*).

MACIAN, V., R. PAYRI, S. RUIZ, M. BARDI, and A. H. PLAZAS. "Experimental study of the relationship between injection rate shape and Diesel ignition using a novel piezo-actuated direct-acting injector". *Applied Energy* 118 (2014), pp. 100–113, (*it appears in: Chap.1-[5], Chap.6-[212]*).

MACPHEE, A. G. et al. "X-ray imaging of shock waves generated by high-pressure fuel sprays". *Science* 295.5558 (2002), pp. 1261–1263, (*it appears in: Chap.3-[49]*).

MAJEWSKI, W. A. and M. K. KHAIR. *Diesel emissions and their control*. Society of Automotive Engineers, 2006, (*it appears in: Chap.1-[1], Chap.2-[13], Chap.3-[29]*).

MANCARUSO, E. and B. M. VAGLIECO. "Optical investigation of the combustion behaviour inside the engine operating in HCCI mode and using alternative diesel fuel". *Experimental Thermal and Fluid Science* 34.3 (2010), pp. 346–351, (*it appears in: Chap.2-[12], Chap.4-[139], Chap.5-[187], Chap.6-[215,216,239]*).

MANIN, J., M. BARDI, L. PICKETT, R. DAHMS, and J. OEFELEIN. "Development and mixing of diesel sprays at the microscopic level from low to high temperature and pressure conditions". *THIESEL 2012 Conference on Thermo-and Fluid Dynamic Processes in Direct Injection Engines*. 2012, (*it appears in: Chap.1-[3], Chap.3-[68], Chap.5-[171,177,179]*).

MANIN, J., M. BARDI, L. PICKETT, and R. PAYRI. "Boundary condition and fuel composition effects on injection processes of diesel sprays at the microscopic level". *ILASS Europe* 2013-457 (2013), (*it appears in: Chap.3-[68,84], Chap.5-[158]*).

MANIN, J., M. BARDI, and M. PICKETT L. "Evaluation of the liquid length via diffused back-illumination imaging in vaporizing Diesel sprays". *COMODIA* 6 (2012), (*it appears in: Chap.4-[130,131], Chap.5-[176]*).

MANIN, J., A. KASTENGREN, and R. PAYRI. "Understanding the Acoustic Oscillations Observed in the Injection Rate of a Common-Rail Direct Injection Diesel Injector". *Journal of Engineering for Gas Turbines and Power* 134.12, 122801 (2012), pp. 122–132.

MANIN, J. "Analysis of Mixing Processes in Liquid and Vaporized Diesel Sprays through LIF and Rayleigh Scattering Measurements". PhD thesis. E.T.S. Ingenieros Industriales. Universitat Politécnica de Valéncia, 2011, (*it appears in: Chap.2-[17]*).

MARTÍNEZ LÓPEZ, J. "Estudio Computacional De La Influencia Del Levantamiento De Aguja Sobre El Flujo Interno Y El Fenómeno De La Cavitación En Toberas De Inyección Diesel". PhD thesis. E.T.S. Ingenieros Industriales. Universidad Politécnica de Valencia, 2013, (*it appears in: Chap.3-[30,84,86], Chap.4-[130], Chap.5-[163,174,176,180,198]*).

MARTINEZ, S., F. SANCHEZ-CRUZ, J. RIESCO, J. GALLEGOS, and S. ACEVES. "Liquid penetration length in direct diesel fuel injection". *Applied Thermal Engineering* 28 (2008), pp. 1756–1762, (*it appears in: Chap.5-[167,185]*).

MASUDA, R. "Validation of diesel fuel spray and mixture formation from nozzle internal flow calculation". *SAE Paper* 2005-01-2098 (2005), (*it appears in: Chap.3-[84]*).

MATSUI, Y., T. KAMIMOTO, and S. MATSUOKA. "A study on the time and space resolved measurement of flame temperature and soot concentration in a DI diesel engine by the two-color method". *SAE Paper* 790491 (1979), (*it appears in: Chap.4-[140], Chap.6-[239]*).

MENDEZ, S. and B. THIROUARD. "Using multiple injection strategies in diesel combustion: potential to improve emissions, noise and fuel economy trade-off in low CR engines". *Technology* 2013 (2008), pp. 04–08, (*it appears in: Chap.1-[1], Chap.3-[82], Chap.6-[219]*).

MICHALSKI, L., K. ECKERSDORF, J. KUCHARSKI, and J. MCGHEE. "Temperature Measurement, John Wiley & Sons". *Chichester, Great Britain -* (2001), pages, (*it appears in: Chap.4-[116]*).

MIE, G. "Beiträge zur Optik trüber Medien, speziell kolloidaler Metallösungen". *Annalen der physik* 330.3 (1908), pp. 377–445, (*it appears in: Chap.4-[119]*).

MIESSE, C. "Correlation of experimental data on the disintegration of liquid jets". *Industrial & Engineering Chemistry* 47.9 (1955), pp. 1690–1701, (*it appears in: Chap.3-[56]*).

MILLER, C. R., D. J. WALDMAN, and S. F. SHAFER. *Direct operated check HEUI injector*. US Patent 5,651,345. July 1997, (*it appears in: Chap.2-[22]*).

MIRANDA, R., H. CHAVES, U. MARTIN, and F. OBERMEIER. "Cavitation in a transparent real size VCO injection nozzle". *Proceedings of ICLASS, Sorrento Italy* (2003), (*it appears in: Chap.3-[83]*).

MUGELE, R. and H. EVANS. "Droplet size distribution in sprays". *Industrial & Engineering Chemistry* 43.6 (1951), pp. 1317–1324, (*it appears in: Chap.3-[69,70]*).

MUNIZ, L. and M. MUNGAL. "Effects of heat release and buoyancy on flow structure and entrainment in turbulent nonpremixed flames". *Combustion and Flame* 126.1 (2001), pp. 1402–1420, (*it appears in: Chap.3-[59]*).

MUSCULUS, M. P. B. "Measurements of the Influence of Soot Radiation on In-Cylinder Temperatures and Exhaust NOx in a Heavy-Duty DI Diesel Engine". *SAE Paper* 2005-01-0925 (2005), (*it appears in: Chap.4-[141,142], Chap.6-[239]*).

MUSCULUS, M. P. B., M. P. C., and L. M. PICKETT. "Conceptual models for low-load, single-injection, EGR-diluted, partially premixed low-temperature DI diesel combustion". *Progress in Energy and Combustion science* (2013), (*it appears in: Chap.3-[30,79]*).

MUSCULUS, M. P. B., S. SINGH, and R. D. REITZ. "Gradient effects on two-color soot optical pyrometry in a heavy-duty DI diesel engine". *Combustion and Flame* 153.100962 (2008), pp. 216–227, (*it appears in: Chap.6-[239]*).

MUSCULUS, M., T. LACHAUX, L. PICKETT, and C. IDICHERIA. "End-of-injection overmixing and unburned hydrocarbon emissions in low-temperature-combustion diesel engines". *SAE Paper* 2007-01-0907 (2007), (*it appears in: Chap.3-[79], Chap.6-[229,245]*).

MUSCULUS, M. and K. KATTKE. "Entrainment waves in diesel jets". *SAE International Journal of Engines* 2.1 (2009), pp. 1170–1193, (*it appears in: Chap.3-[56,58]*).

MYONG, K., M. ARAI, H. SUZUKI, J. SENDA, and H. FUJIMOTO. "Vaporization characteristics and liquid-phase penetration for multi-component fuels". *SAE Paper* 2004-01-0529 (2004), (*it appears in: Chap.3-[67], Chap.5-[192,198]*).

NABER, J. and D. SIEBERS. "Effects of gas density and vaporization on penetration and dispersion of diesel sprays". *SAE Paper* 960034 (1996), (*it appears in: Chap.3-[46,61,63,64,65,66,71], Chap.4-[102,123,126], Chap.5-[169,173,186,195,200,202,203], Chap.6-[215,217]*).

NABI, M. N., M. S. AKHTER, and M. M. ZAGLUL SHAHADAT. "Improvement of engine emissions with conventional diesel fuel and diesel–biodiesel blends". *Biore-source Technology* 97.3 (2006), pp. 372–378, (*it appears in: Chap.1-[2]*).

PASTOR, J. V., J. ARRÈGLE, and A. PALOMARES. "Diesel Spray Image Segmentation With a Likelihood Ratio Test". *Appl. Opt.* 40.17 (June 2001), pp. 2876–2885, (*it appears in: Chap.3-[66], Chap.4-[121], Chap.5-[196,200]*).

PASTOR, J. V., R. PAYRI, J. M. GARCIA-OLIVER, and F. J. BRICENO. "Analysis of transient liquid and vapor phase penetration for diesel sprays under variable injection conditions". *Atomization and Sprays* 21.6 (2011), (*it appears in: Chap.4-[126], Chap.5-[192,194]*).

PASTOR, J., J. LÓPEZ, J. GARCÍA-OLIVER, and J. PASTOR. "A 1D model for the description of mixing-controlled inert diesel sprays". *Fuel* 87.13 (2008), pp. 2871–2885, (*it appears in: Chap.1-[5], Chap.3-[56,57,58,61,67], Chap.5-[153,165,168,173,185,186,188,190,192,194,195,198], Chap.6-[211,217,234]*).

PAYRI, F., V. BERMUDEZ, R. PAYRI, and F. SALVADOR. "The influence of cavitation on the internal flow and the spray characteristics in diesel injection nozzles". *Fuel* 83.4 (2004), pp. 419–431, (*it appears in: Chap.1-[3], Chap.3-[35,63], Chap.5-[156,198,202,203]*).

PAYRI, F. and J. DESANTES. *Motores de combustión interna alternativos*. Editorial Reverté, 2011, (*it appears in: Chap.1-[4], Chap.2-[11]*).

PAYRI, F., J. V. PASTOR, J. M. GARCÍA, and J. M. PASTOR. "Contribution to the application of two-colour imaging to diesel combustion". *Measurement Science and Technology* 18.8 (2007), p. 2579, (*it appears in: Chap.4-[139,143,145], Chap.6-[239,243]*).

PAYRI, F., R. PAYRI, M. BARDI, and M. CARRERES. "Engine combustion network: Influence of the gas properties on the spray penetration and spreading angle". *Experimental Thermal and Fluid Science* 53 (2014), pp. 236–243, (*it appears in: Chap.5-[168,169,179,186,195,202,203]*).

PAYRI, F., R. PAYRI, F. SALVADOR, and J. MARTÍNEZ-LÓPEZ. "A contribution to the understanding of cavitation effects in diesel injector nozzles through a combined experimental and computational investigation". *Computers & Fluids* 58 (2012), pp. 88–101, (*it appears in: Chap.5-[165]*).

PAYRI, R., L. ARANEO, J. SHAKAL, and V. SOARE. "Phase doppler measurements: system set-up optimization for characterization of a diesel nozzle". *Journal of mechanical science and technology* 22.8 (2008), pp. 1620–1632, (*it appears in: Chap.3-[70]*).

Payri, R., J. Garcia, F. Salvador, and J. Gimeno. "Using spray momentum flux measurements to understand the influence of diesel nozzle geometry on spray characteristics". *Fuel* 84.5 (2005), pp. 551–561, (*it appears in: Chap.3-[46], Chap.5-[153,171]*).

Payri, R., J. Gimeno, P. Martí-Aldaví, and O. Venegas. "Study of the influence of internal flow on the spray behavior under cavitating conditions using a transparent nozzle". *ICLASS 2012* (2012), (*it appears in: Chap.3-[66]*).

Payri, R., J. Gimeno, J. P. Viera, and A. H. Plazas. "Needle lift profile influence on the vapor phase penetration for a prototype diesel direct acting piezoelectric injector". *Fuel* 113 (2013), pp. 257–265, (*it appears in: Chap.1-[5], Chap.4-[128], Chap.5-[165]*).

Payri, R., C. Guardiola, F. Salvador, and J. Gimeno. "Critical cavitation number determination in diesel injection nozzles". *Experimental Techniques* 28.3 (2004), pp. 49–52, (*it appears in: Chap.3-[37], Chap.5-[154,155,162]*).

Payri, R., S. Ruiz, F. Salvador, and J. Gimeno. "On the dependence of spray momentum flux in spray penetration: Momentum flux packets penetration model". English. *Journal of Mechanical Science and Technology* 21.7 (2007), pp. 1100–1111.

Payri, R., F. J. Salvador, J. Gimeno, and G. Bracho. "A new methodology for correcting the signal cumulative phenomenon on injection rate measurements". *Experimental Techniques* 32.1 (2008), pp. 46–49, (*it appears in: Chap.4-[106,107,109]*).

Payri, R., F. J. Salvador, J. Gimeno, and V. Soare. "Determination of Diesel Spray Characteristics in Real Rngine In-Cylinder air Density and Presure Conditions". *Journal of Mechanical Science and technology* 19 (2005), pp. 2040–2052, (*it appears in: Chap.3-[64], Chap.5-[202]*).

Payri, R., F. Salvador, J. Gimeno, and J. De la Morena. "Effects of nozzle geometry on direct injection diesel engine combustion process". *Applied Thermal Engineering* 29.10 (2009), pp. 2051–2060, (*it appears in: Chap.2-[12], Chap.4-[132,133], Chap.5-[178], Chap.6-[212]*).

Payri, R., F. Salvador, J. Gimeno, and J. De la Morena. "Study of cavitation phenomena based on a technique for visualizing bubbles in a liquid pressurized chamber". *International Journal of Heat and Fluid Flow* 30.4 (2009), pp. 768–777, (*it appears in: Chap.3-[42]*).

Payri, R., F. Salvador, J. Gimeno, and J. De la Morena. "Influence of injector technology on injection and combustion development - Part 2: combustion analysis". *Applied Energy* 88.4 (2011), pp. 1130–1139, (*it appears in: Chap.3-[75,76], Chap.6-[222,235]*).

PAYRI, R., F. SALVADOR, J. GIMENO, and L. ZAPATA. "Diesel nozzle geometry influence on spray liquid-phase fuel penetration in evaporative conditions". *Fuel* 87.7 (2008), pp. 1165–1176, (*it appears in: Chap.3-[46,67], Chap.4-[119]*).

PAYRI, R., F. SALVADOR, P. MARTI-ALDARAVI, and J. MARTÍNEZ-LÓPEZ. "Using one-dimensional modeling to analyse the influence of the use of biodiesels on the dynamic behavior of solenoid-operated injectors in common rail systems: Detailed injection system model". *Energy Conversion and Management* 54.1 (2012), pp. 90–99, (*it appears in: Chap.5-[158]*).

PAYRI, R., B. TORMOS, F. SALVADOR, and L. ARANEO. "Spray droplet velocity characterization for convergent nozzles with three different diameters". *Fuel* 87.15 (2008), pp. 3176–3182, (*it appears in: Chap.5-[195]*).

PAYRI, R., B. TORMOS, F. SALVADOR, and A. PLAZAS. "Using one-dimensional modelling codes to analyse the influence of diesel nozzle geometry on injection rate characteristics". *International journal of vehicle design* 38.1 (2005), pp. 58–78, (*it appears in: Chap.2-[14,15]*).

PAYRI, R., J. M. GARCÍA-OLIVER, M. BARDI, and J. MANIN. "Fuel temperature influence on diesel sprays in inert and reacting conditions". *Applied Thermal Engineering* 35 (2012), pp. 185–195, (*it appears in: Chap.1-[4], Chap.3-[67,76], Chap.4-[132], Chap.5-[167,185,186,187], Chap.6-[216]*).

PAYRI, R., J. GIMENO, M. BARDI, and A. H. PLAZAS. "Study liquid length penetration results obtained with a direct acting piezo electric injector". *Applied Energy* 106 (2013), pp. 152–162, (*it appears in: Chap.1-[5], Chap.4-[125]*).

PAYRI, R., J. GIMENO, O. VENEGAS, and A. H. PLAZAS-TORRES. "Experimental and computational study of the influence of partial needle lift on nozzle flowin diesel fuel injectors". *Atomization and Sprays* 22.8 (2012), (*it appears in: Chap.1-[5], Chap.5-[154,155,193]*).

PENG, D.-Y. and D. B. ROBINSON. "A New Two-Constant Equation of State". *Industrial & Engineering Chemistry Fundamentals* 15.1 (1976), pp. 59–64, (*it appears in: Chap.4-[146], Chap.5-[169]*).

PETERS, N. *Turbulent combustion*. Cambridge university press, 2000, (*it appears in: Chap.3-[79,81], Chap.6-[229,233]*).

PICKETT, L. M., D. L. SIEBERS, and C. A. IDICHERIA. "Relationship Between Ignition Processes and the Lift-Off Length of Diesel Fuel Jets". *SAE Paper* 2005-01-3843 (2005), (*it appears in: Chap.1-[3], Chap.3-[74,75,79], Chap.6-[215,216,232,235,236,237]*).

PICKETT, L., S. KOOK, H. PERSSON, and O. ANDERSSON. "Diesel fuel jet lift-off stabilization in the presence of laser-induced plasma ignition". *Proceedings of the Combustion Institute* 32.2 (2009), pp. 2793–2800, (*it appears in: Chap.6-[231,232]*).

PICKETT, L. and D. L. SIEBERS. "Soot in diesel fuel jets: effects of ambient temperature, ambient density, and injection pressure". *Combustion and Flame* 138 (2004), pp. 114–135, (*it appears in: Chap.4-[140]*).

PICKETT, L. M., C. L. GENZALE, J. MANIN, L. MALBEC, and L. HERMANT. "Measurement uncertainty of liquid penetration in evaporating diesel sprays". *ILASS Americas* 2011-111 (2011), (*it appears in: Chap.4-[119,120,121], Chap.5-[191,196]*).

PICKETT, L. M., J. MANIN, R. PAYRI, M. BARDI, and J. GIMENO. "Transient rate of injection effects on spray development". *SAE Paper* 2013-24-0001 (2013), (*it appears in: Chap.3-[61], Chap.5-[180,201,202]*).

PICKETT, L. M. et al. "Comparison of diesel spray combustion in different high-temperature, high-pressure facilities". *SAE Paper* 2010-01-2106 (2010), (*it appears in: Chap.4-[132], Chap.5-[196]*).

PICKETT, L. M. et al. "Relationship Between Diesel Fuel Spray Vapor Penetration/Dispersion and Local Fuel Mixture Fraction". *SAE International Journal of Engines* 4.1 (2011), pp. 764–799, (*it appears in: Chap.3-[50], Chap.5-[168,201]*).

PILCH, M. and C. ERDMAN. "Use of breakup time data and velocity history data to predict the maximum size of stable fragments for acceleration-induced breakup of a liquid drop". *International Journal of Multiphase Flow* 13.6 (1987), pp. 741–757, (*it appears in: Chap.3-[55]*).

PISCHINGER, F, U. REUTER, and E. SCHEID. *Self ignition of diesel sprays and its dependence on fuel properties and injection parameters*. Tech. rep. American Society of Mechanical Engineers, New York, NY, 1988, (*it appears in: Chap.6-[235]*).

PITTS, W. M. et al. "Temperature uncertainties for bare-bead and aspirated thermocouple measurements in fire environments". *ASTM Special Technical Publication* 1427 (2003), pp. 3–15, (*it appears in: Chap.4-[116]*).

PLAZAS, A. H. "Modelado unidimensional de inyectores common-rail Diesel". PhD thesis. Valencia: E.T.S. Ingenieros Industriales. Universidad Politécnica de Valencia, 2005, (*it appears in: Chap.2-[15]*).

POTZ, D., W. CHRIST, and B. DITTUS. "Diesel nozzle-the determining interface between injection system and combustion chamber". *Thermo-and Fluid-dynamic Processes in Diesel Engines: Selected Papers from the THIESEL 2000 Conference Held in Valencia, Spain, September 13-15, 2000*. Springer Verlag. 2002, p. 133, (*it appears in: Chap.3-[37,41]*).

POTZ, D., W. CHRIST, and B. DITTUS. "Diesel nozzle-the determining interface between injection system and combustion chamber". *Thermo-and Fluid-dynamic Processes in Diesel Engines: Selected Papers from the THIESEL 2000 Conference Held in Valencia, Spain, September 13-15, 2000*. Springer Verlag. 2002, p. 133.

PRASAD, C. V. and S. KAR. "An investigation on the diffusion of momentum and mass of fuel in a diesel fuel spray". *Journal of Engineering for Power* 99 (1977), p. 225, (*it appears in: Chap.3-[71]*).

RANZ, W. E. "Some experiments on orifice sprays". *The Canadian Journal of Chemical Engineering* 36.4 (1958), pp. 175–181, (*it appears in: Chap.3-[56,65], Chap.5-[200]*).

REITZ, R. and F. BRACCO. "On the dependence of spray angle and other spray parameters on nozzle design and operating conditions". *SAE Paper* 790494 (1979), (*it appears in: Chap.3-[65], Chap.5-[168,200]*).

REITZ, R. and F. BRACCO. "Mechanisms of breakup of round liquid jets". *Encyclopedia of fluid mechanics* 3 (1986), pp. 233–249, (*it appears in: Chap.3-[53,54,55]*).

REITZ, R. D. "Atomization and other breakup regimes of a liquid jet". PhD thesis. Princeton Univ., NJ, 1978, (*it appears in: Chap.3-[51,55,56,67]*).

REYNOLDS, O. "An experimental investigation of the circumstances which determine whether the motion of water shall be direct or sinuous, and of the law of resistance in parallel channels." *Proceedings of the Royal Society of London* 35.224-226 (1883), pp. 84–99, (*it appears in: Chap.3-[32]*).

RIPOLL, A. B. and M. P.-S. SÁNCHEZ-PASTOR. *Fundamentos y aplicaciones de la Mecánica de Fluidos*. McGraw-Hill Interamericana de España, 2005, (*it appears in: Chap.3-[39,42]*).

ROISMAN, I., L. ARANEO, and C. TROPEA. "Effect of ambient pressure on penetration of a diesel spray". *International journal of multiphase flow* 33.8 (2007), pp. 904–920, (*it appears in: Chap.5-[169]*).

ROLLBUSCH, C. "Effects of hydraulic nozzle flow rate and high injection pressure on mixture formation, combustion and emissions on a single-cylinder DI light-duty diesel engine". *International Journal of Engine Research* 13.4 (2012), pp. 323–339, (*it appears in: Chap.6-[219]*).

SALVADOR, F., J. GIMENO, J. D. LA MORENA, and M. CARRERES. "Using one-dimensional modeling to analyze the influence of the use of biodiesels on the dynamic behavior of solenoid-operated injectors in common rail systems: Results of the simulations and discussion". *Energy Conversion and Management* 54.1 (2012), pp. 122–132, (*it appears in: Chap.3-[34]*).

SALVADOR, F. J., A. H. PLAZAS, J. GIMENO, and M. CARRERES. "Complete modelling of a piezo actuator last-generation injector for diesel injection systems". *International Journal of Engine Research* 15.1 (2014), pp. 3–19, (*it appears in: Chap.2-[18,19], Chap.3-[32,34]*).

SALVADOR, F. J. "Estudio teórico experimental de la influencia de la geometría de toberas de inyección Diesel sobre las características del flujo interno y del chorro". PhD thesis. Valencia: E.T.S. Ingenieros Industriales. Universidad Politécnica de Valencia, 2003, (*it appears in: Chap.1-[4], Chap.3-[66]*).

SÁNCHEZ, J. J. L. *Estudio teórico-experimental del chorro libre diesel no evaporativo y de su interacción con el movimiento del aire*. Reverté, 2005, (*it appears in: Chap.4-[102]*).

SCHLICHTING, H., J. KESTIN, H. SCHLICHTING, and H. SCHLICHTING. *Boundary-layer theory*. Vol. 539. McGraw-Hill New York, 1968, (*it appears in: Chap.3-[39]*).

SCHMIDT, D. P. and M. L. CORRADINI. "The internal flow of diesel fuel injector nozzles: A review". *International Journal of Engine Research* 2.1 (2001), pp. 1–22, (*it appears in: Chap.1-[1], Chap.3-[30], Chap.5-[155]*).

SCHMIDT, D. P. and M. CORRADINI. "The internal flow of diesel fuel injector nozzles: a review". *International Journal of Engine Research* 2.1 (2001), pp. 1–22, (*it appears in: Chap.3-[30]*).

SCHNEIDER, B. M. "Experimentelle Untersuchungen zur Spraystruktur in transienten, verdampfenden und nicht verdampfenden Brennstoffstrahlen unter Hochdruck". *Ph. D. Thesis* (2003), (*it appears in: Chap.3-[53,67]*).

SCHÖPPE, D. et al. "Delphi Common Rail system with direct acting injector". English. *MTZ worldwide* 69.10 (2008), pp. 32–38, (*it appears in: Chap.2-[22,23]*).

SETTLES, G. S. *Schlieren and shadowgraph techniques: visualizing phenomena in transparent media*. Springer Verlag, 2001, (*it appears in: Chap.4-[126]*).

SIEBERS, D. L. "Scaling liquid-phase fuel penetration in diesel sprays based on mixing-limited vaporization". *SAE Paper* 1999-01-0528 (1999), (*it appears in: Chap.3-[58], Chap.5-[187]*).

SIEBERS, D. L. and B. HIGGINS. "Flame lift-off on direct-injection diesel sprays under quiescent conditions". *SAE Paper* 2001-01-0530 (2001), (*it appears in: Chap.3-[80,81], Chap.6-[228,229]*).

SIEBERS, D. "Liquid-phase fuel penetration in Diesel sprays". *SAE transactions* 107.3 (1998), pp. 1205–1227, (*it appears in: Chap.1-[3], Chap.3-[67], Chap.4-[119,121], Chap.5-[167,185,186,187,190], Chap.6-[215]*).

SIEBERS, D. and B. HIGGINS. "Effects of injector conditions on the flame lift-off length of DI diesel spray". *Thermo-and fluid Dynamic Processes in Diesel Engines* (2000), pp. 253–277, (*it appears in: Chap.3-[81], Chap.4-[138], Chap.6-[233,235]*).

SOTERIOU, C., M. LAMBERT, S. ZUELCH, and D. PASSEREL. "The flow characteristics of high efficiency Diesel nozzles with enhanced geometry holes". *Proc. THIESEL International Conference on Thermo-and Fluid Dynamic Processes in Diesel Engines. Valencia, Spain*. 2006, (*it appears in: Chap.3-[41]*).

SOU A.AND MAULANA, M., K. ISOZAKI, S. HOSOKAWA, and A. TOMIYAMA. "Effects of nozzle geometry on cavitation in nozzles of pressure atomizers". *Journal of Fluid Science and Tachnology* 3 (2008), pp. 622–632, (*it appears in: Chap.3-[66]*).

SPALDING, D. B. *Combustion and mass transfer: a textbook with multiple-choice exercises for engineering students*. Pergamon Press Oxford, 1979, (*it appears in: Chap.3-[71]*).

STEGEMANN, J., J. SEEBODE, J. BALTES, C. BAUMGARTEN, and G. MERKER. "Influence of throttle effects at the needle seat on the spray characteristics of a multihole injection nozzle". *ILASS Europe* (2002), (*it appears in: Chap.3-[85], Chap.5-[173]*).

STERLING, A. M. and C. SLEICHER. "The instability of capillary jets". *J. Fluid Mech* 68.3 (1975), pp. 477–495, (*it appears in: Chap.3-[56]*).

STOKES, G. G. *On the effect of the internal friction of fluids on the motion of pendulums*. Vol. 9. Pitt Press, 1851, (*it appears in: Chap.3-[32]*).

SUH, H. K. and C. S. LEE. "Effect of cavitation in nozzle orifice on the diesel fuel atomization characteristics". *International Journal of Heat and Fluid Flow* 29.4 (2008), pp. 1001–1009, (*it appears in: Chap.3-[40]*).

Summary of current and historical light-duty vehicle emissions standards. Tech. rep. 2010, (*it appears in: Chap.1-[1]*).

TANAKA, T., A. ANDO, and K. ISHIZAKA. "Study on pilot injection of DI diesel engine using common-rail injection system". *JSAE Review* 23.3 (2002), pp. 297–302, (*it appears in: Chap.1-[3]*).

TANG, J. et al. "Coking Phenomena in Nozzle Orifices of DI-Diesel Engines". *SAE International Journal of Fuels and Lubricants* 2.1 (2009), pp. 259–272, (*it appears in: Chap.3-[41]*).

VALENTINO, G., L. ALLOCCA, S. IANNUZZI, and A. MONTANARO. "Biodiesel/mineral diesel fuel mixtures: Spray evolution and engine performance and emissions characterization". *Energy* 36.6 (2011), pp. 3924–3932, (*it appears in: Chap.1-[2], Chap.6-[224]*).

VEDALDI, A. and B. FULKERSON. *VLFeat: An Open and Portable Library of Computer Vision Algorithms*. 2008, (*it appears in: Chap.4-[145]*).

WAKURI, Y., M. FUJII, T. AMITANI, and R. TSUNEYA. "Studies on the penetration of fuel spray in a diesel engine". *Bulletin of JSME* 3.9 (1960), pp. 123–130, (*it appears in: Chap.3-[63,64]*).

WAN, Y. and N. PETERS. "Scaling of spray penetration with evaporation". *Atomization and sprays* 9.2 (1999), (*it appears in: Chap.3-[56,63]*).

WESTBROOK, C. K. et al. "The effects of pressure, temperature, and concentration on the reactivity of alkanes: Experiments and modeling in a rapid compression machine". *Symposium (International) on Combustion*. 1998, pp. 371–378, (*it appears in: Chap.3-[72]*).

WHITE, F. M. *Fluid mechanics, WCB*. 1999, (*it appears in: Chap.3-[39]*).

WINKLHOFER, E. "An experimental database for diesel spray combustion". *Symposium (International) on Combustion*. Vol. 26. 2. Elsevier. 1996, pp. 2541–2547, (*it appears in: Chap.3-[80]*).

WINTERBOURN, M., D. HOPLEY, C. SOTERIOU, and S. ZUELCH. "Development of the New Delphi Diesel Direct Acting Piezo Injector (DFI3) Using Simulation". *Thiesel* 5 (2008), p. 232, (*it appears in: Chap.2-[23]*).

WRIGHT, Y., G. DE PAOLA, K. BOULOUCHOS, and E. MASTORAKOS. "Simulations of spray autoignition and flame establishment with two-dimensional CMC". *Combustion and Flame* 143.4 (2005), pp. 402–419, (*it appears in: Chap.1-[2]*).

YUE, Y., C. F. POWELL, R. POOLA, J. WANG, and J. K. SCHALLER. "Quantitative measurements of diesel fuel spray characteristics in the near-nozzle region using X-ray absorption". *Atomization and sprays* 11.4 (2001), (*it appears in: Chap.3-[49]*).

ZHAO, H. and N. LADOMMATOS. "Optical diagnostics for soot and temperature measurement in diesel engines". *Progress in Energy and Combustion Science* 24.3 (1998), pp. 221–255, (*it appears in: Chap.1-[2], Chap.4-[141]*).